CHARACTERIZATION OF THE STELLAR / SUBSTELLAR BOUNDARY

by

SERGIO BONUCCI DIETERICH

Under the Direction of Todd J. Henry

ABSTRACT

The aim of this dissertation is to address the topic of distinguishing very low mass stars from brown dwarfs through observational means. To that end, we seek to better characterize both populations and establish mechanisms that facilitate establishing an individual object's membership in either the very low mass star or the brown dwarf populations. The dissertation is composed of three separate observational studies.

In the first study we report on our analysis of *HST/NICMOS* snapshot high resolution images of 255 stars in 201 systems within ∼10 parsecs of the Sun. We establish magnitude and separation limits for which companions can be ruled out for each star in the sample, and then perform a comprehensive sensitivity and completeness analysis for the subsample of 138

M dwarfs in 126 systems. We calculate a multiplicity fraction of $0.0^{+3.5}_{-0.0}\%$ for L companions to M dwarfs in the separation range of 5 to 70 AU, and $2.3^{+5.0}_{-0.7}\%$ for L and T companions to M dwarfs in the separation range of 10 to 70 AU. Considering these results and results from several other studies, we argue that the so-called "brown dwarf desert" extends to binary systems with low mass primaries and is largely independent of primary mass, mass ratio, and separation.

In the second study we construct a Hertzsprung-Russell diagram for the stellar/substellar boundary based on a sample of 63 objects ranging in spectral type from M6V to L4. We report new *VRI* photometry for 63 objects and new trigonometric parallaxes for 37 objects. We employ a novel SED fitting algorithm to determine effective temperatures, bolometric luminosities, and radii. We find evidence for the local minimum in the radius−temperature and radius−luminosity trends that may indicate the end of the stellar main sequence and the start of the brown dwarf sequence at $T_{\rm eff} \sim 2075K$, $\log(L/L_{\odot}) \sim -3.9$, and $(R/R_{\odot}) \sim 0.086$.

The third study is a pilot study for future work and part of a long term search for astrometric binaries that have the potential to yield dynamical masses. We report the discovery of five new multiple systems and discuss their potential for determining dynamical masses: LHS 2071AB, GJ 1215 ABC, LTT 7434 AB, LHS 501 AC, and LHS 3738 AB.

INDEX WORDS: Astronomy, Binaries: close, Brown dwarfs, Galactic structure, Hertzsprung-Russell and C-M diagrams, Infrared: stars, Parallaxes, Solar neighborhood, Stars: fundamental parameters, Stars: low-mass, Stars: statistics

CHARACTERIZATION OF THE STELLAR / SUBSTELLAR BOUNDARY

by

SERGIO BONUCCI DIETERICH

A Dissertation Submitted in Partial Fulfillment of the Requirements for the Degree of

Doctor of Philosophy

in the College of Arts and Sciences

Georgia State University

2013

CHARACTERIZATION OF THE STELLAR / SUBSTELLAR BOUNDARY

by

SERGIO BONUCCI DIETERICH

Committee Chair:	Todd J. Henry
Committee:	Adam Burgasser
	Douglas R. Gies
	Gary Hastings
	Sebastien Lepine
	Russel J. White

Electronic Version Approved:

Office of Graduate Studies

College of Arts and Sciences

Georgia State University

December 2013

DEDICATION

This dissertation is dedicated to the strongest person I know, my wife Bonny Dieterich, and to her physician, Dr. Stephen Szabo. Through the challenges life threw at us in the course of my graduate studies, Bonny showed unimaginable strength and positive thinking, and Dr. Szabo was there to guide and help us every step of the way.

ACKNOWLEDGMENTS

Special Thanks goes to:

My advisor Dr. Todd Henry, who was there to guide me every step of the way and help make this project a reality.

To my colleagues Adric Riedel, Jen Winters, Wei-Chun Jao, Mark Boyd, Altonio Hosey, and John Lurie. Through the course of our work, my problems often became their problems, and our successes were mutually celebrated.

To the other members of my dissertation committee, who were there to guide me and at times rein in some crazy ideas: Adam Burgasser, Douglas Gies, Gary Hastings, Sebastien Lepine, and Russel White.

To my mother, my sisters, brothers-in-law, nieces, and nephews, who shared the excitement of every development and discovery, no matter how small.

To Alvin Das, who a long long time ago constructed a LATEX package for GSU dissertation preparation, and to Adric Riedel for being its most recent curator. A generation of Astronomy Ph.D. students is indebted to Alvin for this work.

TABLE OF CONTENTS

LIST OF TABLES

LIST OF FIGURES

LIST OF ABBREVIATIONS

2MASS 2 Micron All Sky Survey. An all sky survey in the infrared bands J, H, and K_s that is the major source for the discovery of field brown dwarfs and VLM stars.

ALTAIR ALTtitude conjugate Adaptive optics for the InfraRed. The infrared AO module on Gemini North. ALTAIR is used to feed a wavefront corrected beam to Gemini's science instruments.

AO Adaptive Optics. A system for correcting the effect of atmospheric disturbance and obtaining sharper images.

AU Astronomical Unit. The mean radius of Earth's orbit, equivalent to 149,603,500 km.

CCD Charge-Coupled Device. The most common imaging device for modern optical astronomy.

CHARA Center for High Angular Resolution Astronomy. The CHARA Array is a long baseline optical interferometer constructed and operated by the Georgia State University Center for High Angular Resolution Astronomy.

CMD Color-Magnitude Diagram. An observational HR diagram where photometric colors are plotted against absolute magnitudes.

CMF Companion Mass Function. For a given (sub)stellar population, the probability of finding companions as a function of the companion's mass.

CTIOPI Cerro Tololo Inter-American Observatory Parallax Investigation. A large astrometric program run by the RECONS group on CTIO's 0.9m telescope.

CTIO Cerro Tololo Inter-American Observatory. The NOAO southern hemisphere observatory in Chile.

DeNIS Deep Near Infrared Southern sky survey. An European survey of the southern sky in the far red and near infrared bands.

EOS Equation of State. A relationship relating temperature, pressure, and volume for a given substance.

FGS Fine Guidance Sensors. An optical interferometer on board HST that is used for acquiring and keeping the telescope's position with respect to guide stars. As a science instrument, it can be used to probe stellar multiplicity by producing an interferogram of the science target.

HST Hubble Space Telescope. NASA's multi-purpose space telescope capable of high resolution imaging in infrared, visible, and ultraviolet light.

HBMM Hydrogen Burning Minimum Mass. The lowest possible mass for a stellar object.

HR Hertzsprung−Russell (Diagram). A diagram where temperature is plotted against luminosity for a stellar population. The Hertzsprung−Russell Diagram is one of the most basic tools of stellar astronomy.

IDL Interactive Data Language. A computer language useful for scientific data analysis.

IMF Initial Mass Function. The rate of (sub)stellar formation as a function of mass.

IRAF Image Reduction and Analysis Facility. A versatile computer environment for processing astronomical images developed by NOAO.

LF Luminosity Function. The space density of objects as a function of luminosity. Absolute magnitude or spectral types are often used as proxies for luminosity in the Luminosity Function.

MF Mass Function. The space density of objects as a function of the object's mass.

MuF Multiplicity Fraction. For a given stellar population, the number of star systems containing more than one star or brown dwarf.

$\mathbf{M}_J$ Jupiter Mass. Equivalent to 1.90×10^{27} kg or 9.55×10^{-4} $M_\odot$.

MLAR Mass-Luminosity-Age Relation. For substellar objects, a relation indicating mass as a function of luminosity and age.

MLR Mass-Luminosity Relation. For main sequence stellar objects, a relation linking observed luminosity to mass.

$\mathbf{M}_\odot$ Solar Mass. 1.99×10^{30} kg.

MMT Multiple Mirror Telescope. A 6.5m telescope located on Mt. Hopkins, Arizona.

NaCo The AO system for VLT telescope UT4.

NIC2 NICMOS Camera 2. One of three cameras on board the NICMOS

instrument in the Hubble Space Telescope.

NICMOS Near Infrared Camera and Multi-Object Spectrometer. A second generation near infrared instrument in the Hubble Space Telescope.

NIRI Near Infra-Red Imager. An imager and low resolution spectrograph used on the Gemini North telescope. NIRI is capable of diffraction limited imaging in the near infrared when coupled with ALTAIR.

NOAO National Optical Astronomy Observatories. The U.S. institution that coordinates national public effort in astronomy and runs Kitt Peak National Observatory as well as CTIO.

PSF Point Spread Function. The pattern of light from an unresolved point source formed in an astronomical light detector.

RECONS REsearch Consortium On Nearby Stars. A research group led by Todd Henry at Georgia State University that aims to characterize the population of the solar neighborhood.

RMR Radius-Mass Relation. A relation relating the object's radius to it is mass.

RV Radial Velocity. The component of an object's velocity along the line of sight to that object. Measured through spectroscopic Doppler shift.

SDSS Sloan Digital Sky Survey. An optical survey using the *ugriz* filter system. Its field consisted mostly of the northern sky.

SED Spectral Energy Distribution. An expression of flux as a function of

wavelength, mapping out the entire energy output of an astronomical body.

SOAR Southern Astrophysics Research telescope. A 4.1 meter telescope located in Cerro Pachon, Chile, and manged by NOAO on behalf of the SOAR Consortium.

SOI SOAR Optical Imager. The main imaging instrument used on SOAR for optical wavelengths.

VLM Very Low Mass. A term used in referring to stars whose masses are near the end of the stellar main sequence. Usually applied to spectral types M6V and later.

VLT Very Large Telescope(s). Four 8.2m telescopes located on Cerro Paranal, Chile, and operated by the European Southern Observatory.

WISE Wide-field Infrared Survey Explorer. A satellite that mapped the entire sky providing mid-infrared photometry in four bands ranging from 3.4 to 22μm.

CHAPTER 1
INTRODUCTION AND MOTIVATION

The overarching theme of this dissertation is the study of the stellar/substellar boundary in the context of the stellar population of the solar neighborhood, defined for this purpose as the stellar and substellar objects within 25 pc of the Sun. We know that most of the stars in the Galaxy are smaller than the Sun and that stars comprising the least luminous M spectral class account for >70% of the stars in the solar neighborhood (Henry et al. 2006). However, where the end of the stellar main sequence lies with respect to mass, luminosity, spectral type, and effective temperature is a question that has thus far been addressed by theoretical models of stellar evolution, but has been only loosely constrained by observations. Theory predicts that objects with masses less than $\sim 0.075 M_{\odot}$ lack the interior temperature and pressure necessary to ignite the fusion of hydrogen (e.g., Burrows et al. 1993, 1997; Baraffe et al. 1998). These substellar objects are the *brown dwarfs*, which look very much like their stellar cousins during their youth, but enter a constant cooling curve rather than the main sequence where true stars reside in the Hertsprung-Russell (HR) diagram. Despite the sophistication of stellar and substellar structure and evolution models (e.g., Burrows et al. 1997; Baraffe et al. 1998; Chabrier et al. 2000; Baraffe et al. 2003), distinguishing a *Very Low Mass* (VLM) *star* from a high mass *brown dwarf* through observations is still challenging but made easier by the studies described in this dissertation.

The complication stems from the fact that brown dwarfs shine much like stars during their early lives mostly due to to release of gravitational energy before each object cools

to temperatures that are distinctly substellar, with the precise cooling rate depending on both mass and metallicity. Objects belonging to the late M and early L spectral classes are therefore thought to comprise a mixture of VLM stars and brown dwarfs of different ages and masses.

1.1 A Basic Overview of What is a star and What is a Brown Dwarf

Several aspects of the physics of stars and brown dwarfs are discussed throughout this dissertation. Section 5.1.1 discusses possible ways of distinguishing the two classes of objects in detail. A brief discussion of the aspects most relevant to understanding the nature of these distinct categories is given here to motivate the subject.

The early stellar formation process can essentially be described as localized contraction of gas and dust inside a giant molecular cloud (e.g. Shu et al. 1987; Bate 2009, 2011). The process is a positive feedback loop in the sense that initial heterogeneities in the cloud's gravitational potential serve as sink points for contraction, which in turn increase the gravitational pull of the region in question on the surrounding gas. If at some point during the contraction process the resulting macroscopic body of condensed matter achieves the core temperature and pressure necessary for the fusion of light hydrogen (i.e., hydrogen-1, a single proton) *and hydrostatic equilibrium is achieved* between the inward force of gravity and the outward thermal pressure caused as a result of fusion, a star is born. Hydrostatic equilibrium is then maintained so long as hydrogen-1 is available for fusion, and the star enters a prolonged period of stability during which its characteristics change little, known

as the main sequence stage.

If for some reason the accretion process is stopped before the proto-stellar object has gained enough mass to ignite the sustainable core fusion of hydrogen-1, a substellar *brown dwarf* is born. Several mechanisms have been proposed for the cessation of accretion before the stellar minimum mass is reached, and some of those mechanisms are explored in §4.6.2. Because both stars and brown dwarfs have heat of formation and deuterium burning as the primary sources of luminosity during the first few million years of their lives, the two classes of objects largely resemble each other from the observational perspective (Burrows et al. 1997; Baraffe et al. 1998, 2002). After ∼1 Gyr the difference in luminosity between VLM stars and high mass brown dwarfs becomes more pronounced. However, because the ages of astronomical bodies can in most cases be only poorly constrained, and because it is often difficult to infer the observable photospheric properties arising from a given bolometric luminosity, there may still be substantial uncertainty in characterizing the stellar or substellar nature of a given object. Traditionally, the late M dwarfs are thought to consist of main sequence age VLM stars as well as young brown dwarfs, whereas the early to mid L dwarfs are thought to comprise a mixture of VLM stars, young and low mass brown dwarfs, as well as high mass and older (few Gyr) brown dwarfs (Kirkpatrick 2005). The T and Y spectral classes are thought to be comprised exclusively of substellar objects. In all cases, brown dwarfs enter a cooling curve that makes them evolve through these cool spectral classes on a time scale of billions of years. The effect of continuous cooling is that whereas stars follow a *Mass−Luminosity Relation* (MLR) with metallicity and magnetism playing only secondary

roles, luminosity is also a function of age for brown dwarfs, therefore forming a complex *Mass−Luminosity−Age* Relation (MLAR).

1.2 The M, L, T, and Y Spectral Classes

The work to be described in this dissertation is observational in its nature. It is therefore important to describe the basics of what VLM stars and brown dwarfs look like to an astronomer without regard to the incompletely understood underlying theory. The MK spectral classification system is well suited for this end in the sense that objects are classified solely with regard to the appearance of their spectra, so as to form a sequence of continuously changing spectral types. Each class is divided into usually ten subtypes, with 0 denoting the hottest subtype and 9 denoting the coolest. Hotter spectral types and subtypes are referred to as "early" types relative to cooler, "late" types. While the work presented here does not have an emphasis on spectroscopy, the prevalence of the spectral classification system in this field of study makes a brief review of its cooler classes necessary.

The M spectral class constitutes the coolest of the seven original spectral classes (O, B, A, F, G, K, M), with effective temperatures in the range of ∼3800K−2500K. M dwarf spectra are characterized mainly by the presence of absorption bands due to oxide molecules such as TiO and VO, with the latter becoming more prominent in the cooler subtypes. The blackbody continuum present in earlier spectral types is not easily distinguished in M dwarfs due to heavy absorption by a wide array of chemical species, creating the phenomenon of "line blanketing" and making the interpretation of the underlying physics a complex task.

More recently, three additional spectral types were added to the MK system to accommodate observations of objects even cooler than the M dwarfs. The L spectral class (Kirkpatrick et al. 1999) is characterized by the gradual disappearance of spectral signatures due to metal oxides (e.g., TiO, VO), the strengthening of absorption features due to metal hydrides, and absorption due to neutral alkali metals. L dwarfs range in effective temperature from $\sim$2500K$-$1500K. The T spectral class (Burgasser et al. 2003a) denotes objects where absorption by CH_4 and H_2O dominate the overall morphology of the spectra. Photometrically, the late Ls and early Ts are characterized by a strong shift towards bluer infrared colors in a spectral range where effective temperature changes little (Figure 3.5) This complex "L-T transition" (e.g., Leggett et al. 2005) is thought to correspond to the breakup and eventual collapse of dust clouds that provide uniform coverage in the earlier L dwarfs. The lack of a thick dust coverage then allows flux from deeper and hotter layers to emerge. T dwarfs range in effective temperature from $\sim$1500K$-$500K. Very recently, the first objects belonging to the still cooler Y tentative spectral class have been characterized (Cushing et al. 2011) and there is ongoing work aimed at understanding these objects.

1.3 Motivation

Aside from being a problem of fundamental importance in stellar astrophysics, distinguishing stars from brown dwarfs has practical implications for many fields of astronomy. Whereas a VLM star is expected to stay on the main sequence for a time longer than the current age of the Universe, brown dwarfs gradually cool with time. Just where in the luminosity

and temperature sequence the dividing line between stars and brown dwarfs is found has implications for determining the mass-luminosity ratio of the Galaxy and of the Universe. The problem is also of fundamental importance in the search for life in the Universe. Due to their long lifetimes and low ionizing fluxes, VLM stars are thought to be good hosts to habitable planets. On the other hand, the fact that a brown dwarf cools down in a time scale comparable to the potential time scale of biological evolution poses severe challenges to the idea of life evolving in a brown dwarf system. In practical terms for current exoplanet searches, the radial velocity, transiting, and astrometric signatures of a planet are all easier to detect around VLM stars than in systems with more massive stars so long as the faint star is not so faint as to limit the necessary signal to noise for the observations. Further, a transiting planet around a VLM star has a greater likelihood of being in the habitable zone when compared to transits around hotter and more massive stars. Determining the boundary between stars and brown dwarfs is therefore of importance to planet hunting surveys because it may indicate which spectral type marks the boundary between a good candidate and a poor candidate for habitability.

1.4 Three Interconnected Studies

This dissertation consists of three distinct observational studies. The first study, called the *HST/NICMOS Multiplicity of M Dwarfs* study, establishes the frequency of substellar companions to VLM stars, and provides context for testing different stellar and substellar formation scenarios. It provides constraints on our ability to study substellar objects through

targeted searches for stellar/substellar binary systems, where the properties of the substellar component can be partially inferred from the better understood stellar component.

The second and largest of the three studies, called the *HLIMIT Survey*, is a comprehensive effort to establish the morphology of the HR diagram at the stellar/substellar boundary. By combining astrometric and photometric observations with the latest available atmospheric models, the *HLIMIT Survey* establishes the radii, luminosities, and effective temperatures for a sequence of 62 objects on either side of the stellar/substellar boundary. The *HLIMIT Survey* probes the luminosity, effective temperature, and radius corresponding to the stellar/substellar boundary for the solar neighborhood population by detecting the local minimum in the luminosity−radius and temperature−radius trends. These local minima indicate the changes in the internal physics of objects from thermal pressure support to partial electron degeneracy, thus signaling the end of the stellar main sequence and the start of the brown dwarf cooling curve.

The third study is a pilot effort called the *Gemini-AO Search for Dynamical Masses* and is part of a longer term study to resolve VLM binary systems that have the potential to yield dynamical masses for individual components and determine their observational properties. It focused mainly on targets whose multiplicity was originally discovered due to astrometric perturbations in the parallax solution. We identify five newly discovered binaries and provide an overview of the observations and the science potential of this ongoing work.

CHAPTER 2

History and Overview of the Field

This chapter aims to give the reader a brief overview of the field of very low mass stars and brown dwarfs. The discussion is organized both around chronological and topical lines. It is meant to serve as background for the work to be described in subsequent chapters and is by no means a complete treatment. The reader who wishes a more in depth treatment may refer to the several good review articles on the subject, amongst which are: Chabrier & Baraffe (2000); Burrows et al. (2001); Chabrier et al. (2005); Kirkpatrick (2005); Burgasser et al. (2007); Chabrier et al. (2009); Luhman (2012); Duchêne & Kraus (2013), and Torres (2013).

2.1 Postulation and Early Searches

The existence of the substellar objects we now call brown dwarfs, as well as the idea that there exists a mass limit separating stars from brown dwarfs on physical grounds were first proposed independently by Kumar (1963) and by Hayashi & Nakano (1963). These early studies examined pre-main sequence evolution, and demonstrated that for objects below a certain mass, the gravitational contraction of a proto-stellar core could be halted by electron degeneracy pressure before high enough temperature and pressure were achieved to ignite the fusion of light hydrogen (H^1). Kumar (1963) in particular demonstrated that the critical mass for the onset of core degeneracy, the *Hydrogen Burning Minimum Mass* (HBMM), is dependent on the chemical composition of the stellar body. He calculated that a *Population I* star with a chemical composition of $X = 0.62$, $Y = 0.35$, and $Z = 0.03$, where X, Y, and Z are respectively the mass fractions of H, He, and all other elements, would have *HBMM*

$\sim 0.07 M_{\odot}$ and a radius $R \sim 0.068 R_{\odot}$. For an older *Population II* star with $X = 0.90$, $Y = 0.09$, and $Z = 0.01$ the same calculations yielded $HBMM \sim 0.09 M_{\odot}$ and $R \sim 0.081 R_{\odot}$. While today's models predict larger radii, the idea of the mass boundary between stellar and substellar objects being close to $0.07 M_{\odot}$ for Population I compositions is still thought to be largely correct (Table 6.6). Kumar (1963) referred to the newly postulated substellar objects as *black dwarfs*. The term *brown dwarf* was coined by Jill Tarter in 1975 as part of her Ph.D. thesis, and reflected the fact that little was known about their colors other than the fact that these objects, if in fact they existed, would be very dim.

After the initial theoretical postulation in 1963, observational efforts to find brown dwarfs and to characterize the nearby VLM stellar population were hindered by their intrinsic faintness for more than two decades. Observing prospects improved in the mid-to-late 1980s with the introduction of the *Charge-Coupled Device* (CCD), and later, infrared arrays, as alternatives to photography, which is most sensitive in blue wavelengths. Because the older photographic sky surveys were not sensitive enough to allow for a systematic survey of the field for brown dwarfs, early searches focused exclusively on detecting substellar companions to known nearby stars. We now know that such searches were bound to have low success rate due to the so-called *brown dwarf desert* around main sequence stars, which states that the rate of occurrence of stellar/substellar binaries, known as the *Multiplicity Fraction* (MuF), is on the order of only $\sim$2%, regardless of mass ratio or the separation being probed (§ 4.4).

Despite the low success rate of companion searches, interesting objects were found, and these objects are now the prototypes upon which substellar classification is based. The first of

these objects, GD 165B, was discovered as an extremely red companion to the white dwarf GD 165 in 1988 (Becklin & Zuckerman 1988). Follow-up spectroscopy (Kirkpatrick et al. 1993) revealed a spectrum distinct from those of known M dwarfs, and yet lacking the CH_4 absorption bands thought to be the hallmark of brown dwarf atmospheres. While the substellar nature of GD 165B was not clear, it was clear that its atmospheric properties did not conform to any known spectral class (§ 1.2). Today GD 165B is considered the prototype of the L spectral class, and is classified as an L4 dwarf (Kirkpatrick 2005). The discovery of GD 165B was followed by the discovery of GJ 229B in 1995 by a coronagraphic companion search (Nakajima et al. 1995). Unlike GD 165B, GJ 229B has clear spectrophotometric signatures of CH_4. GJ 229B has spectral type T6, and is the prototype of the T spectral class.

2.2 Large Sky Surveys

The number of known L and T dwarfs quickly grew starting at the turn of the century due to the advent of large digital sky surveys. Most notably, the *Two Micron All Sky Survey* (2MASS) in the near infrared (Skrutskie et al. 2006) and the *Sloan Digital Sky Survey* (SDSS) in the optical (York et al. 2000) identified several hundred VLM stars and brown dwarfs that were later confirmed through spectroscopic observations (e.g Kirkpatrick et al. 1999, 2000; Burgasser et al. 2002; Geballe et al. 2002; Hawley et al. 2002; Cruz et al. 2003; Burgasser et al. 2004; Knapp et al. 2004). The European *Deep Near Infrared Survey of the southern sky* (DeNIS) produced results similar to 2MASS in the southern sky, but also

explored the far red optical I band. Data mining of these large sky surveys is a continuing effort, and has thus far yielded the vast majority of all known L and T dwarfs. As of November 6, 2012, 918 L dwarfs and 355 T dwarfs were listed at dwarfarchives.org, an online compilation whose goal is to maintain a list of all known L, T, and Y dwarfs.

2.3 Theoretical Developments

In parallel to the observational work, the theory of VLM stars and brown dwarfs also developed rapidly in the late 1990s and early 2000s. Most of the theoretical work was carried out by two distinct research groups, both of which sought to create comprehensive structure and evolution as well as atmospheric models. One group was led by Adam Burrows at the University of Arizona, and became known as the Tucson group. The second group was led by Isabelle Baraffe and France Allard at École Normale Supérieure de Lyon, and became known as the Lyon group. In 1993 the Tucson group was the first to publish detailed structure and evolution models for VLM stars and high mass brown dwarfs, with a particular emphasis on identifying the set of parameters producing the HBMM (Burrows et al. 1993). That work found HBMM $= 0.0767 M_{\odot}$ for solar metallicity and HBMM $= 0.094 M_{\odot}$ in the extreme case of zero metallicity[1]. The work was extended four years later (Burrows et al. 1997) to include evolutionary tracks ranging from VLM stars to planetary mass objects in an unified treatment based on a more sophisticated treatment of atmospheric opacity. The results reported in Burrows et al. (1997), which include the previous results from Burrows et al. (1993) became

[1]The detailed predictions of several models regarding the hydrogen burning limit are discussed in §6.7.3 and summarized in Table 6.6.

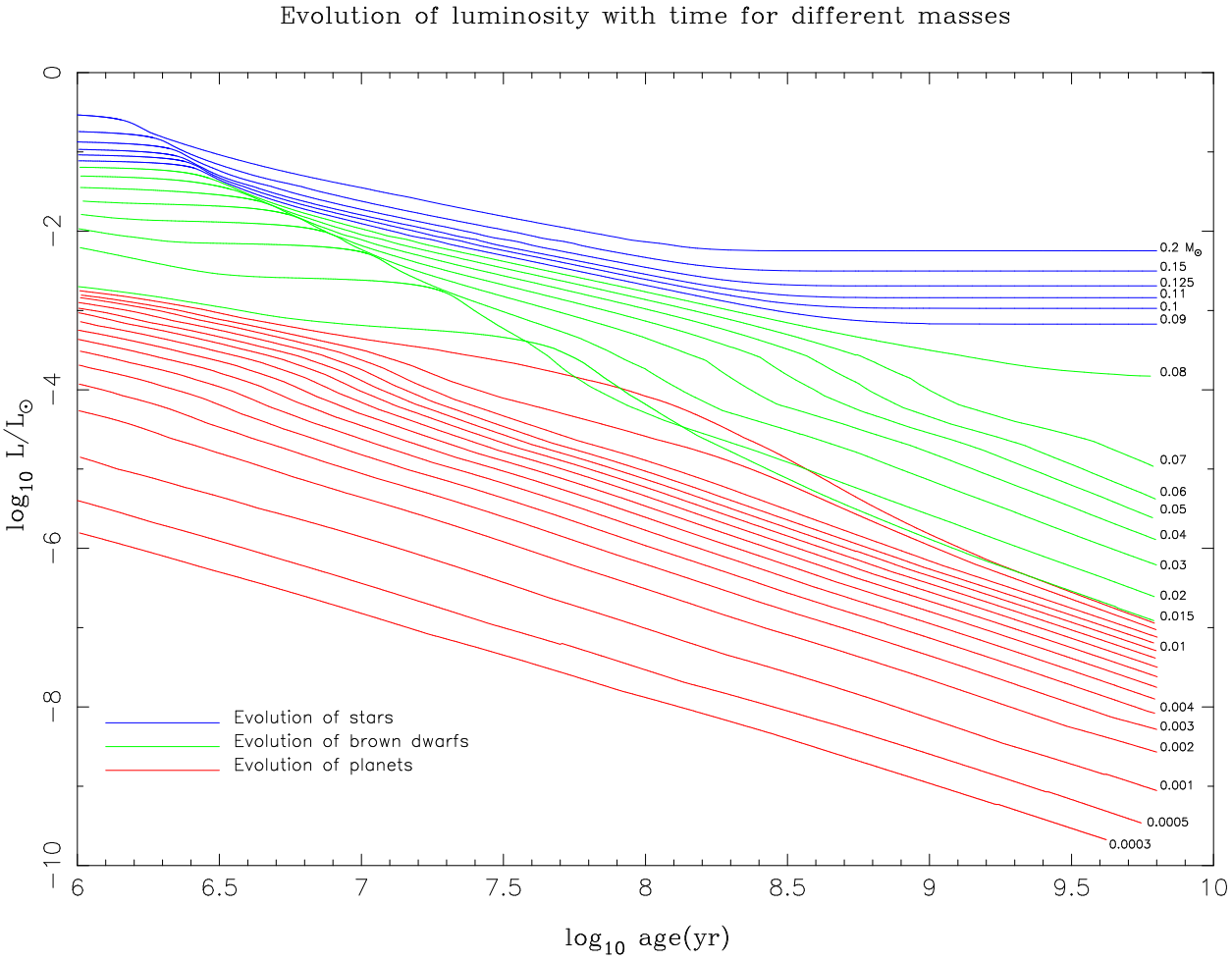

Figure 2.1 The Burrows evolutionary tracks for low mass stars, brown dwarfs, and planetary mass objects (Burrows et al. 1997). The difference in luminosity between stars and brown dwarfs is more pronounced for $t > 1\ Gyr$ than at earlier ages. Stars and brown dwarfs show an early period of stability due to deuterium burning. After deuterium runs out, stars eventually stabilize again in the main sequence, whereas brown dwarfs enter a continuous cooling curve. Image courtesy of Adam Burrows.

known as the "Burrows models", or the "Tucson models", and are still widely referenced today. Figure 2.1 is the classic diagram of the Burrows models, showing evolutionary tracks for VLM stars, brown dwarfs, and planetary mass objects.

In the meantime, across the Atlantic the Lyon group was also developing their evolutionary models, but taking a different approach to the problem. All interior structure and evolution models must rely on an atmospheric model that places a boundary condition at

the surface of the object in question. Whereas the Tucson group developed atmospheric models as an integral part of their interior structure and evolution models, the Lyon group developed their atmospheric models independently, and then later incorporated them into evolutionary models. The approach taken by the Lyon group has led to a greater diversity of models, with each of them working best in a particular temperature regime. In particular, the early models of Baraffe et al. (1998) were soon after developed into the "DUSTY" version (Chabrier et al. 2000) and the "COND" version (Baraffe et al. 2003). These two versions are different in their treatments of atmospheric dust formation, which becomes relevant at temperatures $\lesssim$ 2600 K. In the "DUSTY" scenario dust grains are left in the atmosphere and provide a significant source of additional opacity, whereas in the "COND" scenario the grains condense and settle below the photosphere, and in so doing also deplete the atmosphere of metals. While neither of these two extreme cases has been shown to match observations for a wide range of temperatures, the "DUSTY" models appear better suited in replicating early to mid L dwarf atmospheres, whereas the "COND" models do a better job in replicating T dwarf observations. Modeling the transition from L dwarfs to T dwarfs remains problematic.

Significant progress was made by the Lyon group recently with the publication of the *BT-Settl* atmospheric models (Allard et al. 2012, 2013). The *BT-Settl* models use a non-equilibrium inter-phase approach to treating the problem of grain formation and sedimentation in cool atmospheres. The models provide a grid of synthetic spectra with effective temperatures ranging from solar ($\sim$5800 K) down to planetary temperatures of a few hundred Kelvins. Variations in metallicity and gravity make the grid three-dimensional. These

models have greatly facilitated the determination of fundamental atmospheric parameters by comparison of observed spectra and photometry to synthetic spectra. The *BT-Settl* results are particularly relevant in the modeling of L dwarf atmospheres, where the treatment of grain sedimentation requires sophisticated modeling. §§5.5 and 5.6 describe how the *BT-Settl* spectra were used to determine fundamental atmospheric parameters in the context of this dissertation. The research community that studies low mass stars and brown dwarfs eagerly awaits the publication of new evolutionary models that incorporate *BT-Settl* as a boundary condition[2].

2.4 The Diversity of M, L, and T dwarfs

In this section we review discoveries over the past ∼10 years that highlight the current breadth and scope of the field from the observational perspective. This treatment is brief and not meant as all-inclusive.

Surface Gravity. Surface gravity is an important consideration in the treatment of VLM stars and brown dwarfs due to their small radii and compact nature. While surface gravity and its diagnostic features in higher mass stars are useful for distinguishing main sequence stars from evolved giant stars, giant L and T dwarfs are generally not thought to exist. Variations in surface gravity occur mainly as a result of early contraction, with low gravity being associated with youth. Gravity considerations are particularly relevant for L dwarfs, where depending on mass, age, and metallicity, a given spectral subtype may

[2]The ongoing development of evolutionary models incorporating *BT-Settl* was announced by F. Allard in June of 2012 during *Cool Stars 17* in Barcelona.

correspond to a stellar object, an intermediate age high mass brown dwarf, a young low mass brown dwarf, or even a very young planetary mass object.

The use of gravity sensitive spectral features for identifying youth in brown dwarfs was first demonstrated by Martín et al. (1999) and emphasized by McGovern et al. (2004), who analyzed the infrared and optical spectra of the young brown dwarfs G196-3B, KPNO Tau 4, σ Ori 47, and σ Ori 51. They note that the widths of absorption lines due to neutral alkali elements, in particular K, Na, Cs, Rb, as well as the strengths of absorption bands due to VO, TiO, CaH, and other metal hydrides can be used as relative measures of surface gravity, and hence youth. Because of the important role of surface gravity in determining the nature of L dwarfs, Cruz et al. (2009) have proposed a two-dimensional spectral typing sequence from L0 to L5 where the suffixes α, β, and γ indicate normal gravity, low gravity, and very low gravity, respectively. The L0 to L5 spectral range is extremely diverse as far as the nature of its members is concerned, and a two-dimensional classification scheme such as the ones proposed by Kirkpatrick (2005), Cruz et al. (2009), and Allers & Liu (2013) would be of significant value in linking spectral classification to underlying physics. Unfortunately, this scheme has not been universally adopted. Comparison to model atmospheres (e.g. Allard et al. 2013) indicates that "normal" L dwarfs have surface gravities $\log\ g \sim 5.0$ (where g is the acceleration due to gravity in cgs units), whereas very low gravity (i.e., young) objects may have surface gravities as low as $\log\ g \sim 3.5$.

Metallicity. Several metal-poor L subdwarfs have been identified to date (e.g., Burgasser et al. 2003b, 2008b, 2009; Cushing et al. 2009; Sivarani et al. 2009; Lodieu et al. 2010). These ob-

jects appear to be analogous to subdwarfs of earlier spectral classes, where low metallicity is usually observed along with kinematics indicative of an older population. As an example, 2MASS J0616-6407, an sdL5 (Cushing et al. 2009), has spectroscopic signatures of low metal content and an impressive radial velocity of 454 ± 15 km s^{-1}. There have also been suggestions of particularly metal-rich L dwarfs (e.g., Looper et al. 2008), in which the spectroscopic effects of high metallicity may mimic the effects of low surface gravity.

The Blue L Dwarfs. Several L dwarfs have unusually blue near infrared spectra, and comprise a distinct group known as the blue L dwarfs (e.g., Cruz et al. 2007; Burgasser et al. 2008a; Bowler et al. 2010; Schmidt et al. 2010; Cushing et al. 2010). The blue excess in the infrared is most likely due to a thinner than usual cloud layer, which is likely the result of low metallicity, high surface gravity causing high sedimentation rate, high vertical mixing in the atmosphere, or a combination of these factors (Cushing et al. 2010). The blue L dwarfs highlight how grain formation and sedimentation produce complex atmospheric physics, and how the effects of these basic parameters are manifested in interconnected ways.

Multiplicity. Multiplicity across the stellar/substellar boundary is one of the main topics of this thesis. In keeping with this section's goal of highlighting the diversity of VLM stars and brown dwarfs, an overview of the topic is presented here. A detailed discussion of topics such as the "brown dwarf desert" including presentation of new results, is found in Chapter 4. The results discussed there can be summarized by stating that binaries in which the primary component is of spectral type M or earlier and the secondary component is an L or a T dwarf are infrequent, with an occurrence rate of only a few percent. This

result is largely invariant across different stellar ages, mass ratios, and separations. In the following discussion we also include the M dwarfs because many multiplicity studies have focused simply on low mass objects, which includes the M, L, and T dwarfs.

Early infrared speckle studies established the multiplicity of stellar companions around M dwarfs to be 32±11% (Henry & McCarthy 1990; Henry 1991). Subsequent work by Fischer & Marcy (1992) indicated a slightly higher multiplicity rate of 42±9%. In a synthesis of several multiplicity studies (Reid & Gizis 1997; Oppenheimer et al. 2001; Hinz et al. 2002; Reid et al. 2003; Delfosse et al. 2004), Burgasser et al. (2007) derive an overall *Multiplicity Fraction* (MuF) of 27^{+5}_{-4}% for M dwarfs. The same study finds that the observed MuF for VLM systems with primaries of spectral type M6V or later is ∼20%; however, they note that due to to selection effects the real MuF is likely somewhat lower. Taking the results of several studies into consideration, Burgasser et al. (2007) note that the MuF for VLM stars and brown dwarfs could range from as low as 10% to as high as 30%, and that the binary population is characterized by closely separated and nearly equal mass systems. In particular, they note that 93% of the systems have separation <20 AU, and 77% have mass ratios > 0.8, where 1.0 denotes an equal mass binary.

In addition to the general population trends described above, there are also noteworthy subsets of very widely separated binaries and very widely separated hierarchical higher order multiples. The contrast between these subsets and the main binary population described above may shed light into brown dwarf formation scenarios (§4.6.2). As an example of one study, Faherty et al. (2010) find that widely separated binaries with separations as large as

$\sim$25000 AU may survive dynamic interactions in the young cluster environment and form stable field-aged systems. These systems have binding energies that are close to the limit for bound systems (Close et al. 2007). Several studies also note a disproportionate number of systems where two closely separated, nearly equal mass brown dwarfs are in a wide hierarchical orbit around a more massive main sequence star (e.g., Golimowski et al. 2004a; Burgasser et al. 2005; Caballero 2007; Law et al. 2010; Faherty et al. 2010). In particular, Faherty et al. (2010) note that the ratio of triple systems to binary systems is 2.4 times higher for VLM objects than for the general field population. It has also been noted that the reverse configuration, where the central star is a close binary and those two components are orbited by a single wide separation low mass companion, is also common (Allen et al. 2012). That study has suggested that formation scenarios based on conservation of angular momentum where angular momentum is transferred from the binary component to the isolated wide component, therefore decreasing the separation of the binary component, are likely responsible for the high occurrence of triple systems.

Finally, very close binaries have also been detected via spectroscopic observations. Shkolnik et al. (2010) report an overall spectroscopic binary fraction of 16% for M dwarfs. More specifically, Blake et al. (2010) report the late M and L dwarf binary fraction to be $2.5^{+8.6}_{-1.6}$% for separations smaller than 1.0 AU and Clark et al. (2012) report the binary fraction for M dwarfs with separations smaller than 0.4 AU to be 3% to 4%.

Galactic Kinematics. Studies of the Galactic kinematics of L and T dwarfs have been primarily concerned with determining the sample's age based on its Galactic velocity

distribution. The method relies on the idea that stars are born in a cluster environment with a small velocity dispersion, which then gradually increases as stars travel through the Galaxy and undergo dynamical interactions with other objects. The age dependence of the velocity dispersion can be modeled as a power law of the form t^{α} with $\alpha \sim 0.33$ for the solar neighborhood (Binney et al. 2000). Because the calculation of three-dimensional Galactic velocities must rely on known tangential velocities from trigonometric parallax observations as well as spectroscopic radial velocities, only a small subset of the known L and T dwarfs can be completely characterized at this time. Many more have been studied in a more restricted sense through the determination of proper motion only (Schmidt et al. 2007; Faherty et al. 2009).

There have been conflicting results in the literature regarding age determination through kinematic means. Zapatero Osorio et al. (2007) examined the space motions of 21 L and T dwarfs and concluded that the kinematics of these objects most closely resemble those of hot F type stars. From the comparison, they derive ages ranging from 0.5−4 Gyr for the substellar population, which is lower than the accepted age for low mass stars in the solar neighborhood. In contrast, subsequent larger studies have found no clear evidence that the low mass stellar population and the VLM and substellar populations are characterized by different ages. Schmidt et al. (2010) determined the three-dimensional Galactic velocities of 306 L dwarfs and concluded that while the population is best characterized by a mix of a younger component and an older component, the overall characteristics are no different than those noted for M dwarfs. Schmidt et al. (2010) find the mean tangential velocity to

be $V_{tan} = 28$ km s^{-1} with a dispersion of $\sigma_{tan} = 25$ km s^{-1}. Seifahrt et al. (2010) examined a sample of 43 L dwarfs with three-dimensional velocities and derived an age of $\sim$3 Gyr for the L dwarfs, which is comparable to the accepted age for late M dwarfs in the solar neighborhood (Reiners & Basri 2009).

As pointed out by Seifahrt et al. (2010), the derivation of an age for the L dwarf population that is comparable to the age of the M dwarf population, as in Seifahrt et al. (2010) and Schmidt et al. (2010), poses problems for the interpretation of substellar evolution. Even without detailed knowledge of the spectral sub-type corresponding to the HBMM, it is accepted that the L dwarf population constitutes a mix of stellar and substellar objects. Because L type brown dwarfs comprise the hotter component of a permanently cooling population, they should be on average younger than the stellar population, which does not cool with time. Seifahrt et al. (2010) speculate that perhaps their observed sample is not adequate for statistical treatment due to the non-Gaussian nature of their velocity dispersion, or that perhaps the initial velocity dispersion of substellar objects is higher than that of stellar objects. The latter consideration would mean that a different zero point velocity dispersion is necessary when estimating the age of brown dwarfs, and is consistent with the ejection scenario of brown dwarf formation (§4.6.2).

2.5 Trigonometric Parallaxes

The list of late M, L, T, and now Y dwarfs with trigonometric parallaxes has been steadily growing over the last fifteen years. A compendium of all VLM stars and brown dwarfs with

parallaxes was initially published in Dupuy & Liu (2012) and continues to be periodically updated by T. Dupuy at

https://www.cfa.harvard.edu/∼tdupuy/plx/Database_of_Ultracool_Parallaxes.html.

As of December 1, 2013, the list contains 411 objects with trigonometric parallaxes. An additional 37 trigonometric parallaxes are being published in association with this dissertation. There now exists a robust sample of objects with trigonometric parallaxes for statistical purposes. A more thorough discussion of trigonometric parallaxes is reserved for §6.2.

2.6 M Dwarfs in the Solar Neighborhood

Most of the stars in the Galaxy are M dwarfs, and yet they have been somewhat neglected by those searching the databases of large surveys, who tend to concentrate on discovering L and T dwarfs. In addition to neglecting more than 70% of the stars in the Galaxy (Henry et al. 2006), not focusing on M dwarfs prevents a thorough understanding of the stellar formation process and how brown dwarfs form because the ubiquity of M dwarfs must be the principal prediction of any comprehensive theoretical formation scenario.

Over the past decade, the search for nearby M dwarfs has been carried out mostly by the RECONS group through proper motion searches of the SuperCOSMOS Sky Survey. Subsets of this search have concentrated on specific proper motion regimes, and now cover the entire proper motion range for $\mu \geq 0.18''/yr$. The results of these searches have been published in several articles of *The Solar Neighborhood* series in the *Astronomical Journal* [3]. The search is sensitive to magnitudes $I \sim 19$, $R \sim 20$, and $B \sim 21$ and newly discovered stars are denom-

[3] www.recons.org

inated SuperCOSMOS RECONS (SCR) stars. The requirement that a target be detected in all three filters effectively limits the search for the faintest M dwarfs to distances closer than 10 pc. In addition to the SuperCOSMOS search, many other late M dwarfs discovered through the 2MASS search or other sky searches were placed in the CTIOPI/RECONS parallax program for astrometric and photometric characterization (§5.2). Because some M dwarfs are past the SuperCOSMOS detection limit in the B band, and because we require detection in all three SuperCOSMOS bands, it is not possible to say that the census of nearby M dwarfs is complete at this point; however we believe that any new additions will only marginally change the population properties. The search for the "missing" nearby M dwarf continues with the extension of RECONS work to 25 pc. M dwarf multiplicity is also being investigated by RECONS through the REDDOT project led by Jennifer Winters, which aims to obtain a census of all nearby M dwarfs with stellar companions.

2.7 The Luminosity Function and the Mass Function

The *Luminosity Function* (LF) is defined as the space density of objects as a function of luminosity, which is usually represented by absolute magnitude or spectral type. In a similar manner, the *Mass Function* (MF) expresses the space density of objects as a function of the object's mass. The *Initial Mass Function* (IMF) is defined as the rate of creation of new objects per unit volume, without regard to the elapsed age of a population or the object's lifetime. For substellar objects, the LF is a convolution of the IMF and the cooling rate that causes those objects to advance to cooler spectral types.

Both the LF and the MF are difficult quantities to establish due to the requirement that all objects within a certain pre-determined volume be counted. This requires reliable distance measurements and a sky survey of enough sensitivity to detect all objects within that volume. Further, determining the MF requires a relation between luminosity and mass, the Mass-Luminosity Relation (MLR), because mass is not directly measurable except in the case of close binaries. In the case of constantly cooling brown dwarfs, the MLF becomes the Mass-Luminosity-Age Relation (MLAR). The current lack of volume-complete samples for which all distances are established through trigonometric parallax makes a rigorous determination of the LF and MF impossible for now. In practice, the LF can be estimated based on photometric field surveys and spectrophotometric distance estimates. However, estimates of the MF are still for the most part based on models of (sub)stellar structure and evolution.

The luminosity function for field VLM stars and L dwarfs within 20 pc was estimated by Cruz et al. (2007) based on targets detected by 2MASS and follow-up spectroscopy. That work found a space density of 4.9×10^{-3} pc^{-3} for spectral types between M7V and M9.5V and a lower limit of 3.8×10^{-3} pc^{-3} for L dwarfs down to subtype L8. Figure 2.2 shows the spectral type breakdown of the sample. More recently, Kirkpatrick et al. (2012) used the results of the WISE survey and spectrophotometric distance estimates to estimate the luminosity function of objects of all spectral types within an 8 pc radius. That study found 7 objects with spectral types between M7V and M9.5V, 3 L dwarfs, 22 T dwarfs, and 8 Y dwarfs. Given the small number of L dwarfs within 8 pc, any statistical interpretation of the 8 pc sample must be made with caution.

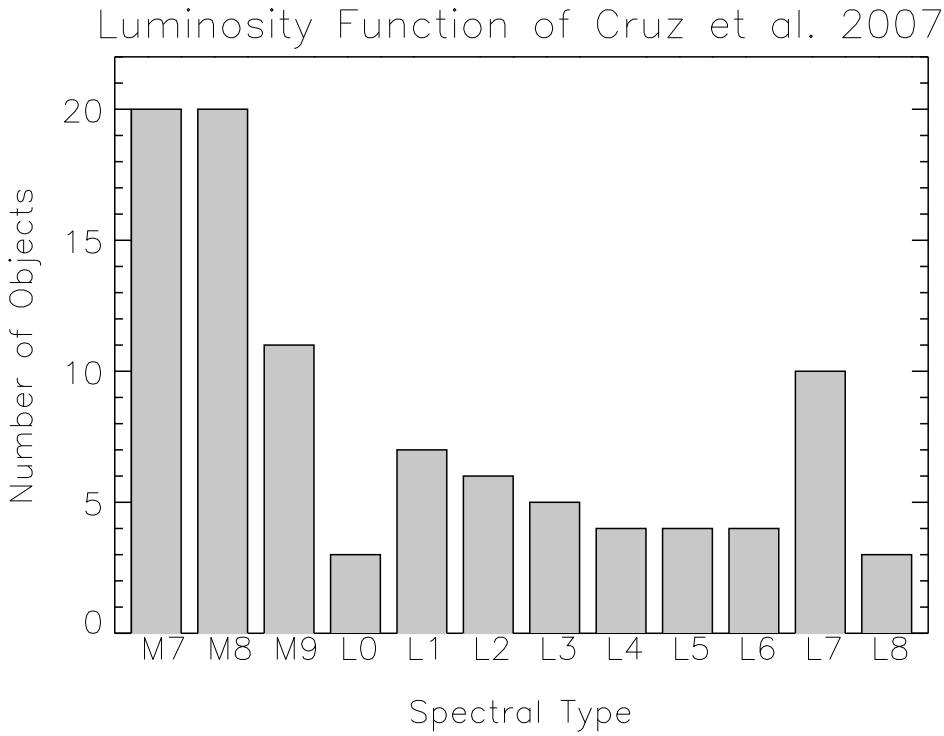

Figure 2.2 The 20 pc Luminosity Function of Cruz et al. (2007). Distances were obtained both through trigonometric parallax and spectrophotometric distance estimates. The numbers are lower limits for L dwarfs.

Predictions of the MF and the resulting LF have been done based on the substellar cooling rates predicted by models and assuming several different forms for the IMF (Burgasser 2004; Allen et al. 2005). The results of those studies are discussed in detail in light of the results of this dissertation in §6.7.3. Both studies predict a local minimum in the luminosity function for early Ls, which is attributed to the onset of the brown dwarf cooling curve. For most forms of the IMF, these studies also predict that objects with $T_{\rm eff} < 1000$ K, the T and Y dwarfs, should outnumber the stellar objects. This prediction is contrary to the previously mentioned WISE results, which suggest that stars outnumber brown dwarfs by about six to one. The theoretical MF and observational results could be reconciled if the IMF is somehow truncated or has a sharp slope somewhere between the mid M and mid L spectral types.

CHAPTER 3

Overview of the HST/NICMOS Multiplicity Study

This chapter and Chapter 4 are based on "*The Solar Neighborhood, XXVIII: The Multiplicity Fraction of Nearby Stars From 5 to 70 AU and the Brown Dwarf Desert Around M Dwarfs*", by Dieterich et al. (2012). The study described there was originally conceived by Todd Henry, David Golimowski, and John Krist in the late 1990s. The observing strategy and target selection was done by those collaborators at that time, and is included here for completeness. The search for faint companions in the reduced images and the statistical analysis on the results of that search constitutes original research by the author. The current chapter contains an introduction to the topic, a description of the observations and data analysis, and a general description of the results. Chapter 4 contains a detailed analysis in the context of VLM binaries and the stellar/substellar MuF.

3.1 Introduction

The Mass Function (MF), Multiplicity Fraction (MuF), and the Mass−Luminosity Relation (MLR) are three of the most important characteristics of a stellar or substellar population. However, all three remain poorly constrained for VLM stars. Although the lowest mass stars, the M dwarfs, dominate the Galaxy in numbers and comprise the majority of our stellar neighbors (Henry et al. 2006), not a single M dwarf is visible to the naked eye. Over the last two decades, advances in observational astronomy have made a thorough study of these faint stars possible. Empirical mass-luminosity relations (Henry & McCarthy 1993; Henry et al. 1999; Delfosse et al. 2000) have achieved a high degree of reliability for early to

mid M dwarfs, with progress continuing for later M dwarfs at the end of the main sequence. Large sky surveys such as 2MASS in the near infrared (Skrutskie et al. 2006) and SDSS in the optical (York et al. 2000) (§2.2) have provided a wealth of new data for population studies, but lack the angular resolution necessary to investigate the MuF and the *Companion Mass Function* (CMF) at separations corresponding to the short periods necessary for determining dynamical masses.

The discovery of GL 229B, the first unequivocal brown dwarf (Nakajima et al. 1995) (§2.1), followed by hundreds of others, raised fundamental questions about our understanding of low mass star formation. Are VLM stars and brown dwarfs products of a single mechanism of (sub)stellar formation applicable to a wide range of masses? Or, do brown dwarfs constitute a fundamentally different population? What do multiplicity properties, such as the overall multiplicity fraction and the separation distribution, tell us about the environments in which VLM stars and brown dwarfs were born? These are some of the fundamental questions that have only recently been addressed through a combination of sky surveys (e.g., Bochanski et al. 2010), wide separation common proper motion searches (e.g., Allen et al. 2007; Allen & Reid 2008), high resolution multiplicity surveys (e.g., Reid & Gizis 1997; Close et al. 2003; Gizis et al. 2003; Lowrance et al. 2005; Reid et al. 2008; Metchev & Hillenbrand 2009) and the establishment of trigonometric parallaxes for a large sample of objects (e.g., Dahn et al. 2002; Henry et al. 2006, §6.2).

Thorough characterization of any stellar population requires the study of a volume limited sample. In an effort to better understand these properties, collaborators Henry, Golimowski,

and Krist conducted an HST/*NICMOS* snapshot program imaging 255 objects in 201 star systems with trigonometric parallaxes placing them within ∼10 pc of the Sun (Table 3.1). The survey used the technique of methane imaging (Rosenthal et al. 1996; Tinney et al. 2005) to clearly distinguish cool brown dwarf companions. In 2004 we reported the detection of four M dwarf companions and one binary L dwarf in a triple system (Golimowski et al. 2004a). With small infrared contrasts ranging from ∼0 magnitudes (GJ 1001BC) to 4.5 magnitudes (GJ 84AB), the companions we reported in 2004 were relatively bright. We have since carried out a deeper search of the data, establishing formal sensitivity limits for the detection of companions in the field of each primary target and extending the limiting magnitude differences routinely to 11 at separations of 3.0″, 8 at 1.0″, 4 at 0.4″, and 2 at 0.2″ (§3.4). Having completed the deeper search of the data with no further detections, I now report on the magnitude and separation limits to which we can rule out companions for each object in our sample. What the lack of additional brown dwarf detections tells us about the multiplicity fraction of systems with VLM secondaries in these mass and separation regimes is discussed in Chapter 4.

3.2 General Characteristics of the Sample

The target list was designed to provide a sample that is representative of the solar neighborhood. Because this survey was an HST snapshot program, the targets were pulled from a large pool of selected targets in order to fill small gaps in HST's observing schedule. The RECONS 10 pc sample was used as a starting list for the search and allowed the HST snap-

shot scheduling process to select a random subsample from the 10 pc sample[1]. In order to be a member of the RECONS 10 pc sample, an object must have a trigonometric parallax greater than 100 mas, with an error smaller than 10 mas. Table 3.1 summarizes several tallies of the observed sample. These observations comprise 69% of the RECONS 10 pc sample (epoch 2012.0), including main sequence stars, white dwarfs, L and T dwarfs, but excluding extrasolar planets. Because trigonometric parallaxes for nearby stars are constantly being updated, 17 objects in 13 systems originally included in our search are no longer members of the 10 pc sample. We still include their data as individual stars in this paper, but exclude them from statistical considerations in order to keep the sample volume limited. Table 3.4, located at the end of this chapter, provides a complete list of all objects observed along with the sensitivity to companions around each object (§3.4)

Table 3.1: Summary Tallies of HST/NICMOS Search

Sub-sample	Tally
HST Visits	217
Total Targets Believed to be Single	233
Total Unresolved Known Multiples	22
Total Star Systems[a]	201
Single targets within 10 pc	218
Unresolved Known Multiples within 10 pc	21
Star Systems within 10 pc[a]	188
Single M Dwarfs within 10 pc	141
Systems with M Dwarf Primary within 10 pc[a]	126
Single Targets beyond 10 pc	15
Unresolved Known Multiples beyond 10 pc	1
Star Systems beyond 10 pc[a]	13

[1]Because all observations consisted of an identical observing sequence, the (equal) duration of each visit did not create a selection effect.

[a]Denotes known physical association at any physical separation, including systems comprising multiple fields of view.

Figure 3.1 shows the spectral type distribution of the NICMOS snapshot sample. Out of the 218 resolved objects within 10 pc we observed, 138, or 63%, are M dwarfs. This number is a very close match to the M dwarf fraction in the RECONS 10 pc sample, which is 248 out of 357 objects, or 69% (epoch 2012.0). The preponderance of M dwarfs in the sample means that even though the sample is a random representation of the solar neighborhood, it focuses on the spectral type that is least scrutinized by *Radial Velocity* (RV) companion searches and open cluster imaging searches. By studying nearby M dwarfs, which comprise a disk rather than cluster population, the survey maps the brown dwarf desert in a largely unexplored region.

3.3 Observations and Data Reduction

Golimowski et al. (2004a) describe technical aspects of the observations in detail. We give a brief summary here and highlight the aspects that are most relevant in achieving the sensitivities we later quote for each individual target.

The survey obtained direct images of each target using *NICMOS Camera 2* (NIC2) through four near infrared filters during cycles 7 (1997−1998) and 11 (2002−2003). NIC2 has a plate scale of $0.076''\text{pixel}^{-1}$ and a field of view of $19.5''\times19.5''$ (Viana et al. 2009; Thatte et al. 2009)[2]. Targets were imaged through the *F110W*, *F180M*, *F207M*, and *F222M* filters, centered at 1.10μm, 1.80μm, 2.07μm, and 2.22μm, respectively. Because HST observations are not subject to atmospheric absorption, the NICMOS filters are not defined to sample

[2] HST/NICMOS documentation, including the *NICMOS Instrument Handbook* and the *NICMOS Data Handbook*, is currently available from the Space Telescope Science Institute at www.stsci.edu/hst/nicmos

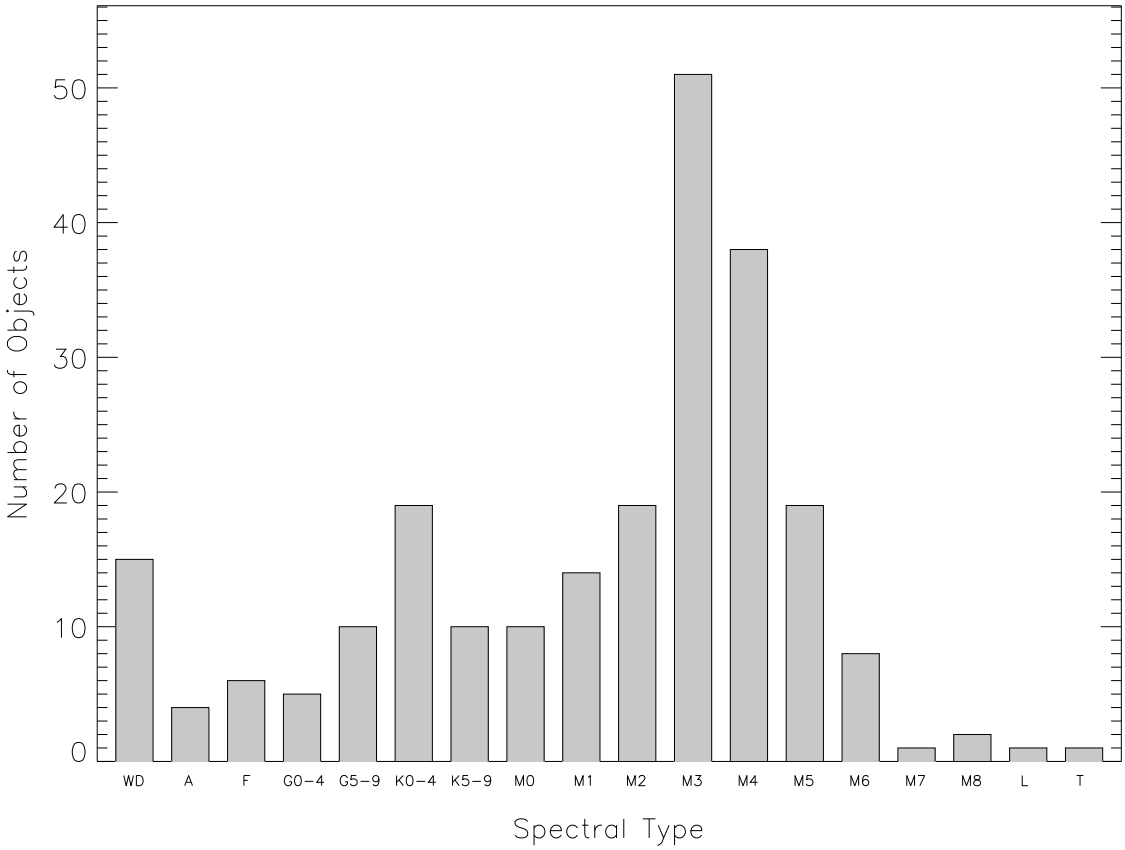

Figure 3.1 Spectral type distribution of the 239 targets within 10 pc in the HST/NICMOS sample. The sample constitutes 69% of the RECONS 10 pc sample (epoch 2012.0). 63% of the targets are M dwarfs, which is in close agreement with the M dwarf distribution of the 10 pc sample, 69% (epoch 2012.0).

atmospheric transmission windows in the way that ground based near infrared filters are. The resulting filter set is non-standard when compared to ground based systems, but allows the user to construct a color scheme that is more suitable for the underlying physics being investigated. Figure 3.2 shows the transmission curves for the selected NICMOS filters, with the 2MASS *J, H,* and K_S filters also plotted for comparison. The four filters used in this survey were selected to detect the strong CH_4 absorption bands observed in T dwarf spectra at 1.7μm and 2.2μm, in effect imaging in and out of these absorption bands. Depending on

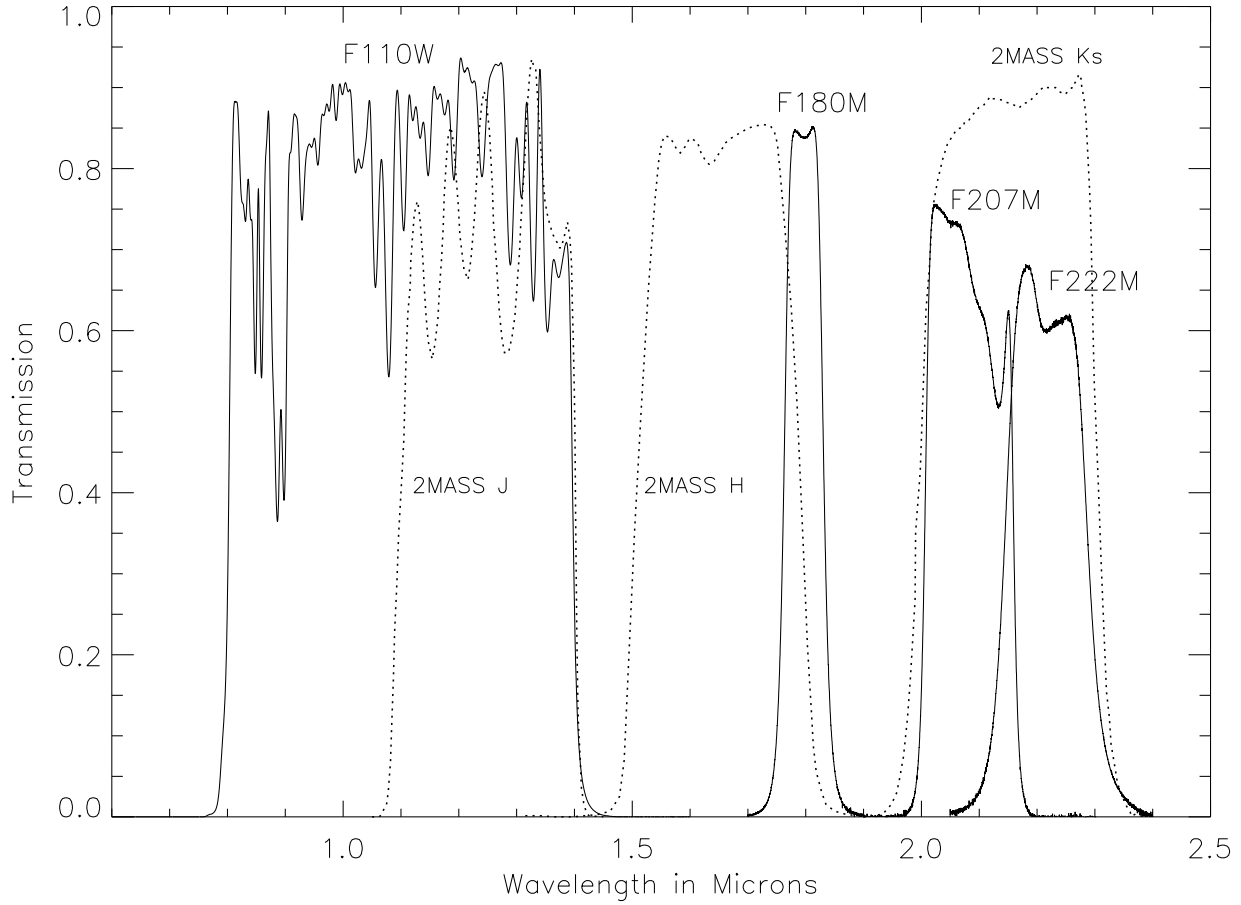

Figure 3.2 Transmission curves for the four NICMOS filters used in the survey. The 2MASS filters are plotted with dotted lines for comparison. Although no individual NICMOS filter is a close match to a ground-based equivalent, together they cover nearly the same wavelength range of ground-based near-infrared color systems.

the filter choice, there is a drastic color shift of up to three magnitudes for T dwarfs. A late T dwarf appears blue in *F110W−F180M* (0.0 to −1.0, Figure 3.5(a)) whereas it is red in *F180M−F207M* (1.0 to 2.0, Figure 3.5(c)). Because no background source is likely to have such a strong color shift, T dwarfs are readily identified in this color scheme. This technique is commonly known as methane imaging and has been used to successfully identify brown dwarfs in photometric observations (Rosenthal et al. 1996; Tinney et al. 2005).

By centering the targets on the detector, it was possible to search for companions within a

radius of 9.5″, except for a small (∼1″ in diameter) artifact due to the coronagraphic hole on the upper left quadrant of the detector[3]. A few targets had large coordinate uncertainties, in most cases due to poorly constrained high proper motions. These targets were not properly centered in the field of view, and are specified in the notes to Table 3.4. Although some of the primary targets are very bright (e.g., Sirius, Vega, Procyon), we did not use the coronagraph because it would make the acquisition process too long for a snapshot program and its peripheral position in the detector would severely limit the search radius. Placing the primary target behind the coronagraph would also add uncertainty to the measurement of the position angle and separation of any binary systems. Even with saturated central targets, we could still search for companions, albeit with a lower sensitivity closer to the central target (Table 3.4).

Two sets of exposures for each target were co-added, resulting in a total exposure time of 64 s for the *F110W* and *F180M* filters and 128 s for the *F207M* and *F222M* filters. Saturation of bright targets and cosmic ray hits were minimized by using NICMOS's multi-accumulate mode, which reads the detector in a non-destructive manner at predetermined time intervals. In the event of saturation or a cosmic ray hit, the NICMOS pipeline scales the value from unaffected readouts so as to obtain the approximate value due to the astronomical source. Only pixels that saturate or are hit by a cosmic ray before the first readout at 0.303 s are lost. For targets that were bright enough to saturate during the first readout, we obtained photometry by using *Point Spread Function* (PSF) fits based on the unsaturated portion of

[3]HST's roll orientation during a given exposure is constrained by the need to keep the solar arrays facing the Sun. Consequently, the position angle of the coronagraphic hole with respect to celestial north, as well as the image's overall orientation, varies widely among the images of our targets.

the PSF.

Because there is no background atmospheric glow, the extended PSF of the primary target is the dominant source of background flux obscuring any fainter objects in the field of view. The properly scaled PSF of another star of similar spectral type and brightness was subtracted from the PSF of each target. A detailed discussion of the PSF subtraction process is given in Krist et al. (1998). The quality of the subtraction varied from target to target and depends primarily on whether or not a good PSF match could be obtained. The PSF varies with target color, telescope focus, and the position of the NICMOS cold mask (Krist et al. 1998). It was always possible to find an isolated star whose PSF was used as the reference for PSF subtraction. If the PSF reference had been a close binary or if it had been contaminated by background sources, we would have noticed a physically unrealistic negative PSF in the subtracted image. We then performed aperture photometry on the primary target as well as any other sources in the field of view using standard *IRAF* routines and the aperture corrections for encircled energy fraction listed in Table 2 of Krist et al. (1998). To verify the validity of the aperture corrections, the photometry of the crowded field of LHS 288 (31 sources, Figure 3.3) was performed varying the aperture from three to six pixels ($0.23''$ to $0.46''$). The photometry agreed to $\lesssim$0.03 magnitudes in all bands, regardless of aperture. The final photometry was done using a six pixel aperture, except in cases when a crowded field or a source near the edge of the field required a smaller aperture.

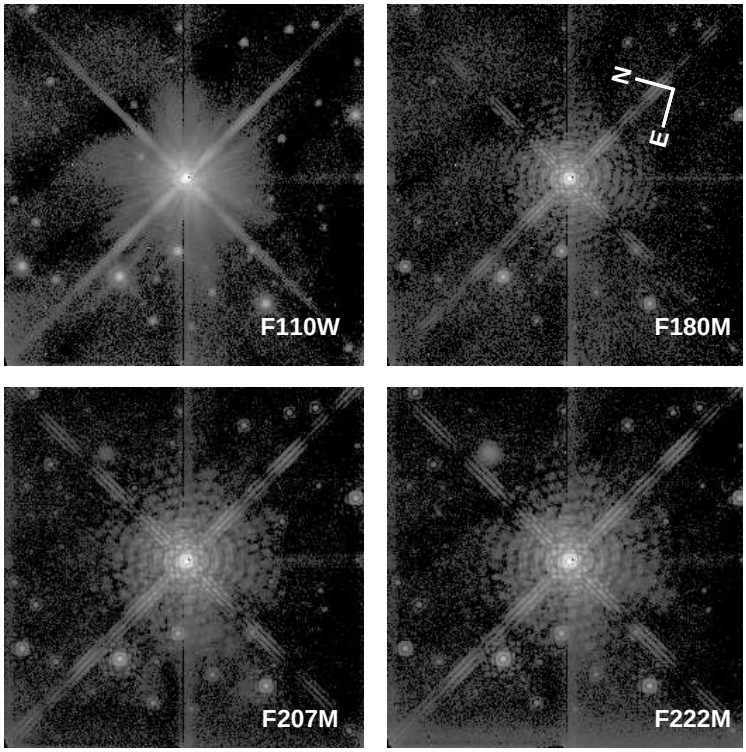

(a)

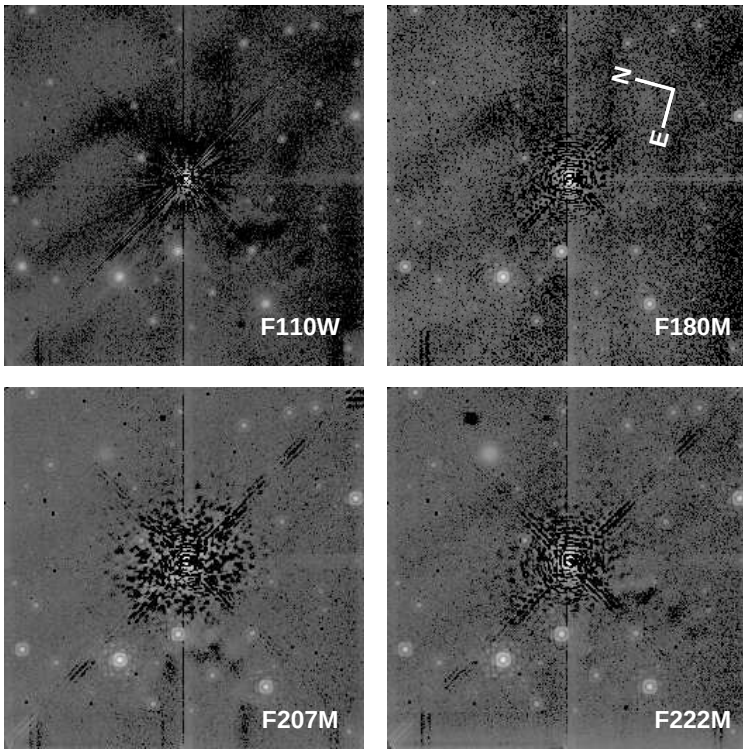

(b)

Figure 3.3 Survey images for LHS 288 (M5.5V) using logarithmic scaling. The frames illustrate typical survey images both before (a) and after (b) PSF subtraction. The ghost-like coronagraphic artifact is visible in the upper left hand corner, particularly in the *F222M* images. The highly structured PSF of the primary target dominates the field before PSF subtraction.

3.4 Determining the Sensitivity of the Search

We define the "sensitivity" of the search as the extent to which we can detect or rule out the existence of a companion to a given star at a given separation and image contrast Δm. The sensitivity varies from target to target and is influenced by the overall brightness of the primary target, the quality of the PSF subtraction, the image filter, intrinsic detector noise, and the prominence of detector artifacts. For each image these factors interact in a complex way, thus making it difficult to draw generalizations about instrumental sensitivity for the survey as a whole. We have therefore devised a method to measure the sensitivity achieved for each target at various separations, and quote individual results in Table 3.4.

Because HST is not subject to atmospheric effects, its images are inherently stable, thus facilitating PSF modeling. We used *Tiny Tim 6.3* (Krist & Hook 1997) to simulate generic NIC2 stellar PSFs through the four filters used in the search. The properly scaled model PSFs were inserted into the PSF subtracted images of the primary targets to test our ability to detect companions at a range of contrasts and separations using a customized IDL code. At sub-arcsecond separations, we inserted a single companion at separations of 0.2″, 0.4″, 0.6″, and 0.8″ and a varying range of contrasts at random position angles (Figure 3.5.1(a)). The PSF insertion code automatically excluded the strong diffraction spikes present in well-exposed NICMOS images at 45°, 135°, 225°, and 315°. The residual flux from the PSF subtracted primary target was set to zero at a radius interior to the position of the artificially inserted companion to facilitate visual inspection. At separations of 1.0″ or greater, we produced an image where artificial companions were arranged in a radial pattern around the

PSF subtracted primary (Figure 3.5.1(b)). This pattern tested the sensitivity at separations of 1.0″, 2.0″, 3.0″, and 4.0″ at contrasts typically incremented from 6 to 13 magnitudes. The simulated images and their surface plots were then visually inspected. In both regimes, an artificially inserted companion was considered detectable if it was visible in the simulated image and if a surface plot around the companion indicated that the artificial PSF retained its characteristic stellar shape, with its peak clearly above the background noise, corresponding to a typical signal-to-noise of 3−5. Although automating the PSF recovery process (e.g., by using a cross-correlation algorithm) would have saved a considerable amount of time, we were not convinced that automated methods would appropriately distinguish between real astronomical sources and residuals of the central star's PSF subtraction, which can at times mimic star-like profiles.

3.5 Results

Other than the five companions reported in Golimowski et al. (2004a), which focused on individual discoveries, no further new companions were detected during this second phase of the search. We now report on the photometry, astrometry, and search sensitivities attained during the survey. While all numerical data are presented in this section, statistical interpretation of data concerning the M dwarfs is saved for Chapter 4.

3.5.1 Color−Magnitude Diagrams

Color−Magnitude Diagrams (CMDs), where the colors of an astronomical object in a given photometric system are plotted against its absolute magnitude so as to map out a color

sequence for a given observed sample, are the observational equivalent of the HR diagram . When the trigonometric parallax to all objects plotted in a CMD is known, the CMD has the advantage that it can be constructed from observations alone, without relying on theory. We constructed color-magnitude diagrams for the twenty-four different color-magnitude combinations from the observations through the four filters. Because the sample includes only four certain substellar objects (GJ 1001 B and C, GJ 229B, and 2MASSI J0559191-140448), synthetic photometry from the spectra of known L and T dwarfs was used to better determine the form of the substellar sequence in this color space. These values were obtained using flux-calibrated, near infrared spectra (Geballe et al. 2002; Knapp et al. 2004), weighted mean trigonometric parallaxes (Golimowski et al. 2004a, and references therein), and the NICMOS Exposure Time Calculator. Figure 3.5 shows four color-magnitude diagrams that are particularly well suited for mapping the stellar and substellar main sequence. Main sequence targets and the thirteen white dwarfs in the survey are labeled with large dots. These diagrams initially assume that any object in the field of view of a primary target is a companion and therefore shares the primary's trigonometric parallax. If the assumption is correct, the object will fall within the stellar or substellar sequence. Background objects, labeled with small dots, appear as having unrealistically faint absolute magnitudes and tend to cluster at the bottom of the diagrams. The synthetic photometry is denoted by spectral sub-type labels. Individual objects of interest are labeled with numbers and are listed in the caption of Figure 3.5.

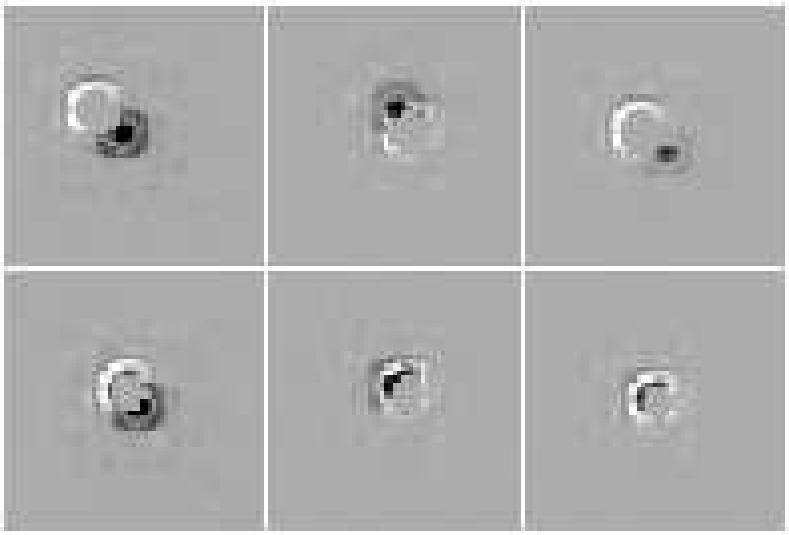

(a)

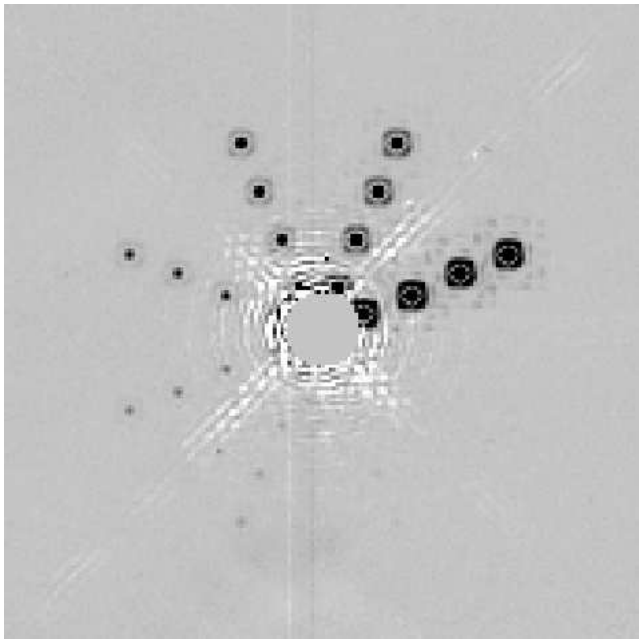

(b)

Figure 3.4 Examples of sensitivity simulations around GJ 213 (M4.0V, *F180M*=6.68). (a) To test sub-arcsecond separations, a mosaic of PSF insertions with several separations and magnitudes is created. In this figure the rows represent separations of 0.2″ (bottom), and 0.4″ (top). The columns represent apparent *F180M* magnitudes of 9, 10, and 11 from left to right. The artificial companions are visible at all three magnitudes for 0.4″ but only at the brightest magnitude for 0.2″. (b) PSF insertions are laid out in a radial pattern to test the sensitivity at separations of 1.0″ and greater. Apparent *F180M* magnitudes range from 12 to 19 in increments of 1, with the rays for 18 and 19 not detectable in this case. Separations are 1.0″, 2.0″, 3.0″, and 4.0″. In both simulations the residuals of the PSF subtraction are set to zero at a radius interior to the artificial companions to facilitate detection. A thorough inspection requires using surface and contour plots.

The trends in the *F110W−F180M* and the *F110W−F222W* colors (Figures 3.5(a) and 3.5(b)) clearly indicate that the onset of CH_4 absorption happens around the L6 spectral type, where the colors turn blue. Although any single diagram may show an overlap between the substellar sequence and the brighter background objects, the degeneracy is broken when we consider that L and T dwarfs follow different trends from the background sources in different color combinations. The most dramatic example of these shifts appears in Figures 3.5(c) and 3.5(d), where methane imaging causes a large shift from red to blue for the T dwarfs while the background sources show little change.

3.5.1.1 Benchmark Objects

GJ 1245ABC (labels 1, 2, and 4 in Figure 3.5) is an interesting system containing three low mass components. In particular, GJ 1245C (4) is one of the latest M dwarfs for which a dynamical mass is known. With a mass of $0.074\pm0.013 M_{\odot}$ (Henry et al. 1999), this object lies close to the theoretical hydrogen burning mass limit.

G 239-25B (label 3) was discovered during the first phase of this search, and the implications of the multiplicity of the G239-25 system are discussed in Golimowski et al. (2004a). Forveille et al. (2004) assign it a spectral type of L0±1 based on near infrared spectra. This spectral classification makes G 239-25B an important benchmark of the M/L transition at the bottom of the main sequence. Its proximity in color space to GJ 1245C re-enforces the importance of both objects as benchmarks.

GJ 1001BC (labels 5, 6, and 7) was resolved as a double L4.5 dwarf, and is discussed in detail in Golimowski et al. (2004a). The components of the system are nearly equal in

luminosity, and we plot them both individually (6 and 7) and combined (5) to illustrate how an equal flux binary appears in the sequence. When compared to the L/T sequence outlined by the synthetic photometry, both components of GJ 1001BC lie just before the strong shift towards the blue that happens as a result of the onset of CH_4 absorption. Their positions at this turning point are most easily seen in the *F110W−F222M* color (Figure 3.5(b)).

Finally, 2MASSI J0559191-140448 (T4.5, label 8) and GJ 229 B (T6, label 9) are the only T dwarfs imaged in the survey, and serve as confirmations that the sequence outlined by the synthetic photometry agrees with real photometry. Whereas GJ 229B is a companion to the M0.5V dwarf GJ 229A, 2MASSI J0559191-140448 is an isolated brown dwarf. Its positions in panels a and b of Figure 3.5 illustrate how a mid T dwarf can easily be mistaken for a white dwarf when more color combinations are not used to break the degeneracy.

3.5.1.2 Background Objects with Companion-Like Colors

Figure 3.5 shows that there are several sources having colors that mimic the colors of substellar companions in one or more panels. The ambiguity is often accentuated when analyzing data sets with simpler color combinations that were not designed a priori to discriminate substellar objects (e.g. 2MASS JHK_s). Interstellar reddening considerations are useful in identifying false companions. Because the distance horizon of our search is only ∼10 pc, any bona fide companions should not have appreciable reddening in the near infrared. Conversely, distant main sequence or giant stars may have significant reddening in the *F110W−F180M*, *F110W−F207M*, and *F110W−F222M* colors, which may place background objects in the color space occupied by L and T dwarfs. The degeneracy is broken when considering the

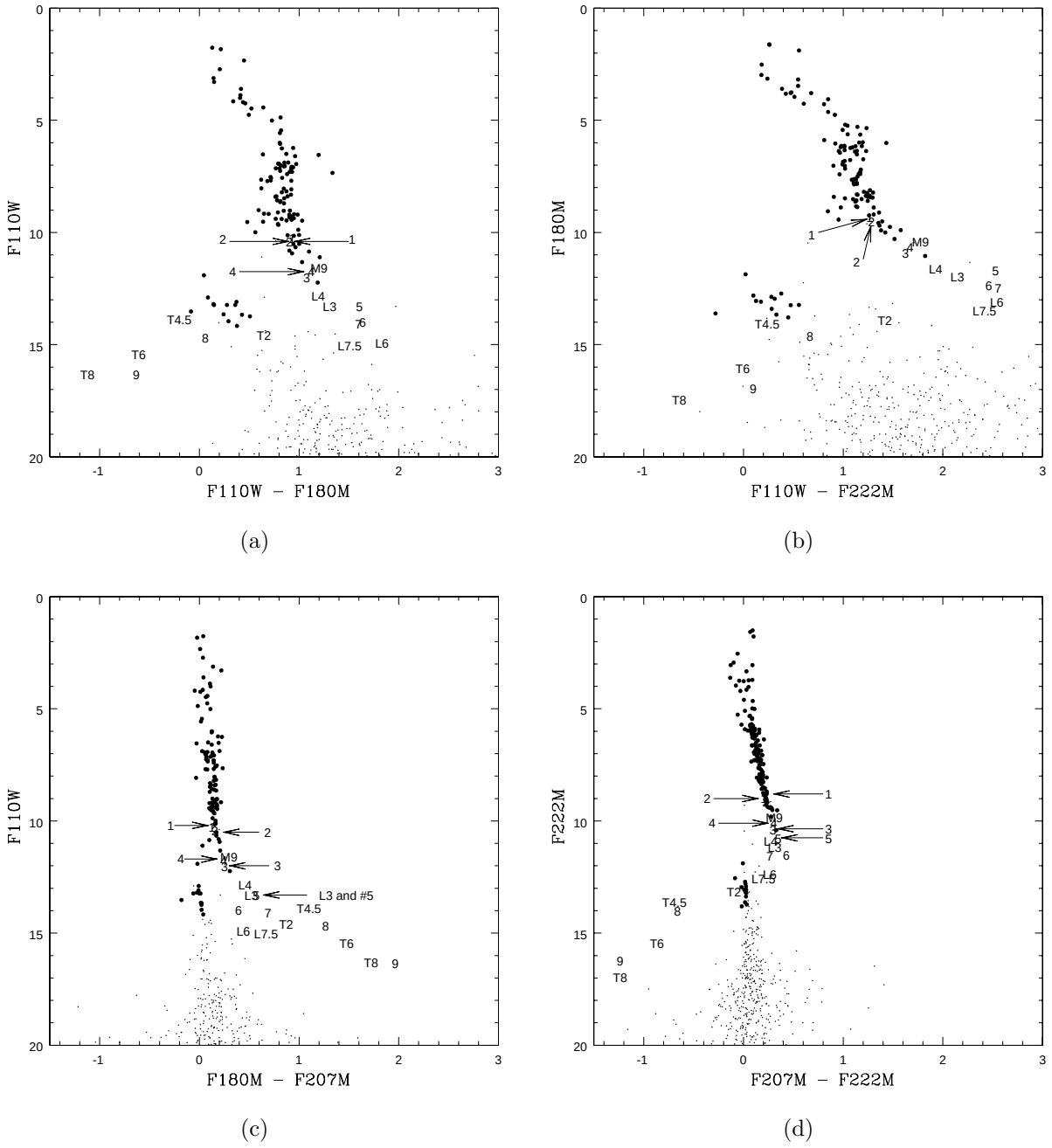

Figure 3.5 Selected color-magnitude diagrams designed to detect substellar companions. The large dots are the primary targets of the search, including 13 white dwarfs. The small dots are background objects. Synthetic photometry of L and T dwarfs, as well as one M9 dwarf, is plotted using a label for spectral type, with the precise dot position at the center of the label. In these diagrams, all objects within the field of view of a primary target are plotted assuming a common parallax (i.e. companionship). Only if the assumption is correct would the object fit in the stellar or substellar sequence. The benchmark objects discussed in §3.5.1.1 are labeled as follows: (1) GJ 1245A, (2) GJ 1245B, (3) G 239-25B, (4) GJ 1245C, (5) GJ 1001BC (combined), (6) GJ 1001B, (7) GJ 1001C, (8) 2MA 0559-1404, and (9) GJ 229B. Panels (a) and (b) illustrate the drastic color shift around spectral type L6 caused by the onset of CH_4 absorption. The reduced effect of interstellar reddening on background objects displayed in panels (c) and (d), as well as the large shift from red to blue for substellar objects, make these bands particularly useful for methane imaging.

F207M−F222M and especially the *F180M−F207M* colors, where the narrow spectral coverage reduces the reddening of distant main sequence sources (Figures 3.5(c) and 3.5(d)). Table 3.2 lists cases where the distinction between a background object and a putative companion was particularly subtle. The white dwarfs mimic late L and early T dwarfs in *F110W−F180M* and *F207M−F222M*, but the degeneracy is broken in *F180M−F207M*.

Table 3.2: Background Sources with Companion-Like Colors

Primary	Separation	P. A. (deg)	Mimics	Deciding Factor
GJ 633	8.5″	157.3	Late L in *F207M-F222M*	Too red to be late L in *F110W-F180M*
GJ 633	3.3″	268.6	Late L in *F207M-F222M*	Too red to be late L in *F110W-F180M*
GJ 1093	8.0″	250.6	Mid M in *F110W* colors	Background M1 or earlier in *F207M-F222M*
GJ 1224	12.6″	91.4	Mid L in *F110W-F222M*	Background early M in *F180M-F222M*
GJ 367	8.4″	3.3	Early L in *F180M-F207M*	Background main sequence in *F110W-F222M*
GJ 438	13.2″	254.0	Hot white dwarf	Too red to be hot WD in *F110W-F180M*

3.5.2 Astrometry of Known Binaries

High resolution images of nearby binary systems present opportunities to map relatively short period orbits and therefore determine dynamical masses. To that end, astrometry for select systems is reported in Table 3.3. In order to be listed in Table 3.3, both components of the system must have been imaged simultaneously in the same NIC2 field of view, and the centroids must be determined to a precision better than ±1 pixel. The values reported are the weighted averages of separations and position angles measured from the PSF centroids in all filters for which saturation[4] did not prevent reliable centroiding. In the simplest case of non-saturated and non-overlapping PSF cores, a centroiding error of ±0.1 pixel was adopted (Golimowski et al. 2004a). Twelve out of the 19 pairs listed in Table 3.3 meet these

[4]Saturated targets are indicated in the notes column of Table 3.4.

criteria. The other seven pairs are either very closely separated stars for which the PSF cores overlap significantly or have central pixel saturation. In either case, the centroiding was determined using PSF fits. With the exception of the M dwarfs, the majority of binaries in our survey had their PSF cores saturated beyond the point where it was possible to compute meaningful astrometry. The precise value of the NICMOS plate scale varied during HST cycle 7 (1997−1998) due to cryogen expansion that distorted the dewar housing the detectors. To calibrate the plate scales for these observations, the values tabulated by the Space Telescope Science Institute based on routine monitoring of crowded star fields were used. For separations, the errors listed in Table 3.3 take into account the four centroiding uncertainties (x_a, y_a, x_b, y_b) added in quadrature. For position angles, the errors take into account the propagated centroiding errors.

Table 3.3: Astrometry of Unsaturated Resolved Systems

Pair	ρ arcsec	σ_ρ arcsec	P.A. °E of N	$\sigma_{P.A.}$ °	Epoch	$\Delta F110W$[a]	$\Delta F180M$	$\Delta F207M$	$\Delta F222M$
GJ 1005AB	0.329	0.008	234.4	1.0	2002.7532	···	1.27	1.31	1.32
GJ 65AB	1.653	0.008	103.3	0.2	2002.8540	···	0.18	0.15	0.16
GJ 84AB[b]	0.443	0.006	103.4	1.0	2002.7506	4.59	4.01	4.18	3.82
GJ 105AC	3.220	0.036	293.5	0.4	1998.0225	5.96	5.87	5.45	5.40
LP 771-95AB	7.706	0.008	315.0	0.0	2003.4620	···	0.36	0.36	0.35
LP 771-95BC	1.344	0.008	138.1	0.2	2003.4620	···	0.56	0.54	0.50
GJ 169.1AB	9.201	0.008	63.7	0.0	2002.7693	···	5.89	5.98	6.07
GJ 229AB	7.627	0.031	164.1	0.1	1997.6202	9.63	11.44	9.44	10.75
GJ 257AB	0.560	0.008	280.4	0.6	1998.8271	···	0.03	0.00	0.00
GJ 1116AB	1.498	0.007	102.7	0.2	1998.8562	0.42	0.35	0.32	0.30
GJ 618AB	5.574	0.008	226.8	0.0	1998.7837	···	2.66	2.58	2.49
GJ 644A-BD	0.258	0.048	151.3	7.6	1998.7868	···	0.41	0.41	0.43
GJ 661AB	0.647	0.008	187.6	0.5	2002.6489	···	0.43	0.29	0.28
GJ 1230AC-B	5.117	0.008	6.1	0.0	2003.0605	···	1.91	1.88	1.85
GJ 747AB	0.234	0.048	87.4	8.4	2002.9441	···	0.02	0.05	0.03
GJ 1245AB	6.964	0.007	82.6	0.0	1998.7734	0.17	0.16	0.15	0.13
GJ 1245AC	0.594	0.007	269.6	0.5	1998.7734	1.49	1.29	1.18	1.08
GJ 860AB	3.184	0.008	99.5	0.1	1998.8590	···	1.01	0.97	0.94
GJ 896AB	5.351	0.008	87.9	0.0	2004.4956	···	1.54	1.48	1.43

[a]Missing values correspond to stars with central core saturation for which a PSF fit is not available.
[b]Values from Golimowski et al. (2004a), Table 4.

3.5.3 Results from the Sensitivity Search

Table 3.4, at the end of this chapter, lists the faintest detectable absolute magnitudes for putative companions at a range of angular separations from each target star in the survey. The distances and spectral types listed are based on the best trigonometric parallaxes and spectral type estimates available in the literature or unpublished trigonometric parallaxes recently measured or improved by our group. It is important to note that each line in Table 3.4 shows the results of one PSF insertion simulation, and does not necessarily correspond to a single star. As described in the notes column, a single PSF insertion simulation may have been done around the two components of a resolved system if their separation was small or if their contrast was large enough for the primary to dominate the field. Because of these situations, the number of entries in Table 3.4 is not meant to add up to the sample tallies in Table 3.1. The reader is referred to Table 3.1 for overall statistics of the sample and to Table 3.4 for data on individual targets.

All targets were inspected for real companions visually in all four bands over the entire field of view. Several factors must be considered when choosing the best filter for the PSF insertion simulations. Out of the four filters used in the search, the *F110W* and *F180M* filters are the most suitable for close separations ($\lesssim 0.4''$) due to their narrower PSFs when compared to the *F207M* and *F222M* filters. Whereas L dwarfs are brighter in *F180M* than in *F110W*, the T dwarfs are much fainter in *F180M* due to methane absorption. Although the *F110W* band produces the narrowest PSFs due to its shorter wavelength and is an

intrinsically bright band for T dwarfs, the sensitivities are reported in the *F180M* band for two reasons. First, the uniform exposure time scheme (§3.3) causes brighter targets to saturate out to several pixels in the *F110W* band even in 0.303 s, decreasing the ability to probe the smallest separations. Second, the width of the *F110W* PSF is comparable to the *NIC2* pixel scale, causing a sharp spike on the central pixel (Krist et al. 1998, Table 2). In low signal-to-noise situations it becomes difficult to distinguish the *F110W* PSF from bad pixels or other sharp artifacts introduced during the PSF subtraction process. As discussed in §4.1 our sensitivity limit falls mostly in the L dwarf regime for sub-arcsecond separations, and in the T dwarf regime for wider separations. Based on comparisons in particularly clear images, it is estimated that using *F110W* instead of *F180M* would increase the sensitivity by $\sim$1 magnitude, but would pose an unacceptable risk of false detections at close separations. We therefore uniformly report sensitivities for all separations in *F180M*, but emphasize that those values can be safely transformed to *F110W* limiting magnitudes for separation greater than $1.0''$ by adding 1.0 magnitude to the *F180M* limits in Table 3.4. Because late T dwarfs appear the faintest in *F180M*, a detection in that band also implies detection in the other three bands, therefore providing the color information needed to characterize the object. Listing our simulation results in the *F180M* band therefore maximizes the instrumental dynamic range of the images while still providing the sensitivity needed to characterize T dwarfs.

Table 3.4: Sensitivity to Companions

Name	Resolved PSFs in FOV	Spectral Type	Distance (pc)	Epoch	App. Mag. (*F180M*)	Absolute *F180M* Magnitude Limit 0.2″	0.4″	0.6″	0.8″	1.0″	2.0″	3.0″	4.0″	Notes
GJ 915	···	DA5	8.1	2003 Jun 3	12.53	11.9	12.4	14.4	14.4	14.9	15.4	15.4	15.4	a
GJ 1001A	A	M3.0V	13.0	1998 Aug 3	7.97	8.4	11.9	13.4	13.9	14.4	16.4	16.4	16.4	b,*g*
GJ 1	···	M1.5V	4.3	1998 Jan 10	4.64	8.0	11.0	12.5	13.0	14.5	16.5	17.5	18.5	···
GJ 1002	···	M5.0V	4.6	2002 Oct 27	7.79	12.4	13.4	14.9	15.9	16.4	18.4	19.4	19.4	···
GJ 1005AB	AB	M3.5VJ	5.9	2002 Oct 3	6.71	10.1	12.1	13.1	14.1	15.1	17.1	18.1	18.1	b,*d*,*f*
GJ 15A	A	M1.5V	3.5	2003 Jun 26	4.48	···	10.7	12.2	12.2	13.2	15.2	16.2	16.2	b,*d*,*i*
GJ 15B	B	M3.5V	3.5	1998 Aug 19	6.20	12.4	12.4	14.4	15.4	15.4	17.4	18.4	18.4	b
GJ 17	···	F9.5V	8.5	1997 Aug 29	2.81	···	8.1	9.1	10.1	10.6	13.1	14.1	15.1	i
GJ 19	···	G0.0V	7.4	1998 Feb 2	1.25	···	···	···	8.4	9.4	11.4	12.9	13.4	i
GJ 2012	···	DQ9	9.0	1997 Dec 31	13.58	15.8	16.8	16.8	16.8	17.8	17.8	17.8	17.8	a
GJ 33	···	K2.5V	7.4	1998 Oct 8	3.58	···	8.7	10.2	11.2	11.2	13.2	15.2	15.2	i
GJ 34A	A	G3V	5.9	2002 Sep 10	2.09	···	···	6.7	6.2	6.7	9.2	10.2	10.2	b,*d*,*i*
GJ 34B	A/B	K7.0V	5.9	1998 Aug 27	4.03	···	10.2	11.2	11.7	12.7	15.2	16.2	16.2	b
GJ 35	···	DZ7	4.3	1997 Oct 1	11.56	16.4	17.4	18.4	18.4	19.4	19.9	19.9	19.9	···
GJ 48	···	M2.5V	8.2	1998 Oct 16	5.70	10.1	10.6	11.6	13.1	13.6	15.6	17.1	17.1	···
GJ 53AB	A/B	K1.0VI	7.5	2002 Oct 11	3.60	···	7.6	8.6	10.6	11.6	13.6	14.6	15.6	b,*d*,*f*,*h*,*i*
GJ 54AB	AB	M3.0VJ	7.8	1998 Nov 9	5.80	9.3	10.3	11.8	12.3	13.3	15.3	17.3	17.3	b,*c*
GJ 54.1	···	M4.0V	3.7	2002 Sep 17	6.73	12.1	13.1	15.1	16.1	17.1	19.1	20.1	20.1	···
GJ 65A	A/B	M5.5V	2.6	2002 Nov 8	6.40	11.9	12.9	14.9	15.4	15.9	16.9	17.9	18.9	b,*h*
GJ 65B	A/B	M6.0V	2.6	2002 Nov 8	6.58	11.9	12.9	14.9	14.9	15.9	16.9	17.9	18.9	b,*h*
GJ 66A	A	K2.0V	7.6	2002 Sep 22	6.68	···	7.6	9.1	9.6	10.1	11.6	13.6	13.6	b,*d*,*i*
GJ 66B	A/B	K2.0V	7.6	2002 Nov 16	6.74	···	8.1	8.6	9.6	10.6	12.6	13.6	13.6	b,*d*,*e*,*i*
GJ 68	···	K1.0V	7.5	1997 Oct 20	3.32	···	7.9	9.9	10.9	11.9	13.9	14.9	15.9	···
LHS 145	···	DA7	9.7	2002 Oct 18	12.66	13.7	14.7	16.7	17.2	17.7	18.7	18.7	18.7	a
GJ 71	···	G8.5V	3.6	1997 Aug 14	1.59	···	···	10.8	11.3	11.8	13.8	15.8	16.8	···
GJ 75	···	G9.0V	10.0	1998 Aug 28	3.81	···	8.8	10.3	10.8	11.3	13.8	14.8	14.8	i
LHS 1302	···	M4.5V	9.9	2002 Oct 10	8.76	11.3	12.8	14.3	14.8	15.8	17.8	18.8	18.8	···
GJ 83.1	···	M4.0V	4.4	2002 Nov 24	6.90	11.7	12.7	14.7	15.2	16.2	17.7	18.7	18.7	···
LHS 1326	···	M5.5V	8.9	1997 Sep 17	9.26	12.0	14.5	15.5	16.0	16.5	17.5	18.5	18.5	e
GJ 84AB	A/B	M2.5VJ	9.1	2002 Oct 2	5.75	9.4	10.9	11.4	12.9	13.4	14.9	16.9	16.9	b,*f*
LHS 1339	···	M2.5V	9.2	2002 Oct 1	7.78	10.9	11.9	12.9	13.9	14.9	16.9	16.9	16.9	···
LHS 1375	···	M5.5V	8.5	1997 Oct 28	9.34	13.7	14.7	16.7	16.7	17.7	17.7	17.7	17.7	···
GJ 105AC	A/C	K3.0V	7.1	1998 Jan 9	9.19	0.9	13.9	15.9	16.9	17.9	18.9	20.9	21.9	b,*f*,*i*
APMPM J0237-5928	···	M4.5V	9.6	2002 Jul 24	8.68	11.8	12.8	13.8	14.8	15.8	17.8	17.8	17.8	···
LP 771-95A	A/B/C	M2.5V	6.9	2003 Jun 18	6.76	11.1	12.6	13.1	14.6	15.6	16.6	17.6	18.6	b
LP 771-95B	A/B/C	M3.5VJ	6.9	2003 Jun 18	7.12	10.9	11.9	13.9	14.9	15.9	16.9	17.9	···	b,*e*,*h*
LP 771-95C	A/B/C	M3.5VJ	6.9	2003 Jun 18	7.68	12.0	12.5	14.0	14.5	16.5	17.5	18.5	19.5	b,*e*,*h*
GJ 1057	···	M4.5V	8.5	1998 Jan 7	8.17	11.5	12.5	14.5	15.0	16.0	17.5	17.5	17.5	···
GJ 137	···	G5V	9.1	2002 Oct 5	3.04	···	7.2	8.2	9.2	10.2	12.2	13.2	14.2	d,*i*
GJ 139	···	G8.0V	6.0	1997 Oct 20	2.51	···	9.6	10.1	11.1	11.6	12.6	14.6	15.6	i
GJ 144	···	K2.0V	3.2	2002 Oct 18	1.88	···	···	10.5	11.0	11.0	12.5	14.5	14.5	c,*d*,*i*
GJ 1061	···	M5.0V	3.6	2002 Jul 29	6.97	12.1	13.1	14.6	15.1	16.1	18.1	19.1	19.1	···
GJ 1068	···	M4.0V	6.9	2002 Jul 22	8.21	11.8	13.8	14.8	14.8	15.8	17.8	17.8	17.8	d,*i*

Continued on next page

Name	Resolved PSFs in FOV	Spectral Type	Distance (pc)	Epoch	App. Mag. (*F180M*)	Absolute *F180M* Magnitude Limit 0.2″	0.4″	0.6″	0.8″	1.0″	2.0″	3.0″	4.0″	Notes
GJ 166A	A	K0.5V	4.9	2003 Feb 23	2.59	···	···	10.0	10.5	11.5	13.0	14.5	14.5	b,*d*,*i*
GJ 166B	B	DA4	4.9	2003 Apr 1	9.99	12.0	13.5	14.0	14.5	15.5	17.5	17.5	···	a,*b*,*d*,*e*
GJ 169.1A	A	M4.0V	5.5	2002 Oct 8	5.91	10.2	11.7	13.2	14.2	14.7	16.7	18.2	18.2	b
GJ 169.1B	A/B	DC5	5.5	2002 Aug 3	11.80	15.1	16.1	17.1	18.1	19.1	21.1	21.1	21.1	a,*b*,*e*
LHS 194	···	DQ7	9.5	1998 Apr 13	12.85	14.0	15.0	16.5	17.0	18.0	18.5	20.0	20.0	a
GJ 176	···	M2.0V	9.0	2003 Feb 17	5.68	9.9	10.9	12.4	13.4	13.9	15.9	16.9	16.9	···
GJ 178	···	F6V	8.0	1998 Feb 20	2.05	···	7.5	9.5	10.0	10.5	12.5	13.5	14.5	i
LHS 1731	···	M3.0V	9.2	2002 Sep 21	7.22	10.2	11.2	12.7	13.7	14.2	15.2	17.2	17.2	···
GJ 191	···	M2.0VI	3.9	1997 Oct 18	5.12	9.2	11.2	12.2	13.2	14.2	16.2	18.2	18.2	···
GJ 203	···	M3.0V	9.7	1997 Dec 22	7.80	8.9	11.9	13.9	14.4	15.9	16.9	18.9	18.9	···
GJ 213	···	M4.0V	5.8	1997 Aug 9	6.68	10.8	12.3	13.8	14.8	15.8	17.8	18.8	18.8	···
GJ 216B	B	K2.5V	8.9	2002 Oct 13	4.16	···	8.7	9.2	10.2	10.7	13.2	14.2	14.2	b,*d*,*i*
GJ 222AB	AB	G0.0VJ	8.6	1998 Aug 15	2.91	6.2	7.7	9.2	10.7	11.2	13.2	14.2	15.2	b,*c*,*i*
GJ 223.2	···	DZ9	6.4	1998 May 4	12.84	14.8	17.8	19.3	19.8	20.8	20.8	20.8	20.8	a
2MA 0559-1404	···	T4.5	10.2	2003 Jan 23	14.60	15.6	17.6	19.1	19.6	20.6	20.6	20.6	20.6	a,*g*
G 99-49	···	M3.5V	5.2	2003 Jan 8	6.33	10.7	12.2	12.7	14.2	15.2	16.7	17.7	18.7	···
LHS 1805	···	M3.5V	7.5	2003 Mar 8	6.91	10.5	12.5	13.5	14.0	15.0	16.5	18.5	18.5	···
LHS 1809	···	M5.0V	9.2	1998 Feb 12	8.73	11.9	12.4	14.9	15.9	16.4	17.9	18.9	18.9	···
GJ 226	···	M2.5V	9.3	1998 Feb 15	6.26	9.4	10.4	11.9	12.9	13.4	15.4	17.4	17.4	···
GJ 229A	A/B	M1.5V	5.7	1997 Aug 15	4.19	8.4	9.4	10.4	11.4	12.9	15.4	17.4	17.4	b
GJ 232	···	M4.0V	8.3	1997 Dec 20	8.19	11.6	13.6	14.6	15.6	16.1	18.6	18.6	18.6	···
L 032-009(A)	A	M2.5V	9.0	2003 May 7	5.72	9.4	10.4	11.9	12.9	13.4	15.9	16.9	16.9	b
L 032-008(B)	B	M3.0V	9.0	2002 Sep 23	6.49	9.7	10.7	12.7	13.7	14.2	16.7	17.7	17.7	b
GJ 244AB	A/B	A1.0V	2.6	2003 Mar 27	-1.39	···	···	···	···	6.0	8.5	9.5	9.5	b,*d*,*f*,*i*
GJ 250B	B	M2.0V	8.7	1998 Mar 24	5.89	8.2	10.2	12.2	13.2	14.2	16.2	17.2	17.2	b
GJ 257A	A/B	M3.0V	8.0	1998 Oct 30	7.15	10.5	10.5	12.5	13.5	14.5	15.5	17.5	17.5	b,*h*
GJ 257B	A/B	M3.0V	8.0	1998 Oct 30	7.18	10.5	11.5	12.5	13.5	14.5	15.5	17.5	17.5	b,*h*
GJ 1093	···	M5.0V	7.7	1997 Aug 29	8.56	12.1	13.1	15.1	16.1	16.6	18.1	18.1	18.1	···
LHS 224AB	A/B	M4.5VJ	9.2	2003 Mar 13	8.71	···	12.9	15.4	15.9	17.9	18.9	19.9	19.9	b,*c*
GJ 280A	A	F5.0IV-V	3.5	2003 Jan 11	-0.67	···	···	···	···	6.8	8.3	10.3	11.3	a,*b*,*d*,*f*,*i*
GJ 283A	A	DZQ6	9.1	2003 Mar 20	12.64	13.8	15.8	16.8	17.8	18.8	19.8	19.8	19.8	a,*b*
GJ 283B	B	M6.5V	9.1	2003 Mar 25	9.74	12.9	14.9	15.4	15.9	16.9	18.9	19.9	19.9	b
GJ 1103	···	M4.5V	8.7	2002 Sep 9	8.03	12.3	13.3	14.8	14.8	15.3	17.3	18.3	18.3	···
GJ 293	···	DQ9	7.9	2002 Aug 29	12.49	15.5	16.0	17.0	18.0	19.5	21.0	21.0	21.0	a
GJ 1105	···	M4.0V	8.2	2003 Mar 10	7.14	11.1	12.1	13.1	14.1	15.1	16.6	17.6	17.6	···
GJ 2066	···	M4.0V	6.8	1998 Sep 17	5.86	9.2	10.2	11.7	13.2	13.7	14.7	16.7	16.7	···
GJ 1111	···	M6.0V	3.6	2003 Mar 2	7.68	13.4	14.9	15.9	16.4	17.4	18.4	19.9	19.9	···
GJ 318	···	DA6	8.8	2003 Jul 4	11.60	13.9	14.9	15.9	16.9	18.4	21.9	20.9	20.9	a
GJ 1116A	A/B	M5.5VJ	5.2	1998 Nov 9	7.83	10.2	12.2	14.7	15.7	16.2	18.2	19.2	19.2	b,*h*
GJ 1116B	···	M5.5VJ	5.2	1998 Nov 9	8.17	10.6	12.6	13.1	14.6	16.1	17.6	18.6	18.6	b,*h*
LHS 2090	···	M6.0V	6.3	2003 Jan 25	8.77	12.3	13.8	15.8	17.3	17.8	19.8	20.8	20.8	···
GJ 338A	A	M0.0V	6.1	2002 Nov 27	4.04	8.6	10.6	11.1	11.6	12.6	14.1	16.1	16.1	b,*d*,*i*
GJ 341	···	M0.0V	10.4	1997 Oct 15	5.73	7.6	9.6	11.6	12.6	13.1	14.6	16.6	16.6	g
GJ 357	···	M2.0V	9.0	2003 Feb 13	6.72	10.9	12.9	13.4	14.4	14.9	16.9	17.9	17.9	···
GJ 1128	···	M4.0V	6.5	1998 Nov 1	7.31	11.7	12.7	14.2	14.7	16.2	17.2	19.2	19.2	···
GJ 367	···	M2.0V	9.7	1997 Sep 17	5.99	8.5	11.0	12.0	13.0	13.5	16.0	17.0	17.0	···

Continued on next page

Name	Resolved PSFs in FOV	Spectral Type	Distance (pc)	Epoch	App. Mag. (*F180M*)	Absolute *F180M* Magnitude Limit 0.2″	0.4″	0.6″	0.8″	1.0″	2.0″	3.0″	4.0″	Notes
GJ 370	···	K6V	11.1	1997 Aug 12	4.86	8.6	9.6	10.6	11.6	12.1	14.6	15.6	16.6	g
LHS 2206	···	M4.0V	9.2	2003 Feb 19	8.66	10.8	12.3	13.8	15.8	16.3	18.8	19.8	19.8	···
GJ 380	···	K7.0V	4.8	2003 Feb 19	3.30	6.6	8.1	9.6	11.1	12.1	14.6	15.6	15.6	d,*i*
GJ 388	···	M2.5V	4.8	1998 Mar 26	4.81	8.9	11.4	12.4	13.4	13.9	16.4	17.4	17.4	···
GJ 393	···	M2.0V	7.1	2003 Jun 16	5.46	9.7	11.2	12.7	13.2	13.7	16.2	17.2	17.2	···
LHS 288	···	M5.5V	4.7	1997 Jul 31	6.14	9.2	11.7	13.7	14.2	15.2	16.7	17.7	17.7	···
LHS 292	···	M6.5V	4.5	2004 Jun 2	8.26	11.2	13.2	14.7	15.7	16.7	19.2	20.7	20.7	a,*d*
GJ 1138AB	A/B	M4.5VJ	9.7	2003 May 10	8.04	10.1	12.1	14.1	15.1	15.1	16.1	17.1	17.1	b,*c*,*d*
GJ 402	···	M4.0V	6.8	1998 Mar 15	6.67	10.5	12.0	13.5	14.0	15.0	16.5	17.5	17.5	···
GJ 406	···	M5.5V	2.3	2003 Feb 27	6.41	14.0	14.5	16.0	16.5	17.5	19.5	20.5	20.5	···
GJ 408	···	M2.5V	6.7	2003 Feb 6	5.60	10.0	11.0	12.5	13.5	14.5	15.5	17.5	17.5	···
GJ 411	···	M2.0V	2.5	2003 Jun 22	3.72	10.0	11.0	13.0	13.5	14.5	16.0	17.0	18.0	d,*i*
GJ 412A	A	M1.0V	4.8	2003 Jun 14	5.00	10.6	11.1	12.6	13.6	14.6	15.6	17.6	17.6	b,*d*,*i*
GJ 412B	B	M5.5V	4.8	2003 May 5	8.23	11.8	14.3	15.8	16.8	17.3	18.8	19.8	19.8	b
GJ 432A	A	K0.0V	9.5	2003 Mar 2	4.14	···	9.1	10.1	10.6	12.1	13.1	14.1	14.1	b,*d*,*i*
GJ 432B	B	DC	9.5	2004 Jun 29	13.67	15.1	15.6	17.1	17.1	17.6	17.6	17.6	17.6	a,*b*,*h*
GJ 433	···	M2.0V	8.9	2003 Feb 3	5.76	8.5	10.5	12.0	13.0	14.0	15.0	16.0	16.0	···
GJ 434	···	G8.0V	9.6	1997 Dec 13	3.64	4.6	7.6	10.1	10.6	11.6	13.1	14.1	15.1	···
GJ 438	···	M1.0V	10.9	2002 Sep 3	6.58	8.8	10.3	11.8	12.3	13.3	14.8	15.8	15.8	d,*g*,*i*
GJ 440	···	DQ6	4.6	1997 Jul 29	11.20	16.7	17.7	18.7	18.7	18.7	19.7	19.7	19.7	e
GJ 442A	A	G2.0V	9.2	1998 Aug 16	3.30	5.7	8.2	9.2	10.2	11.7	12.7	14.2	15.2	b
GJ 442B	B	M4.0V:	9.2	2002 Aug 31	8.24	9.7	11.7	13.7	14.2	15.2	17.2	17.2	17.2	b
GJ 445	···	M3.5V	5.3	2003 Mar 28	6.24	9.9	11.9	12.9	13.9	14.9	16.4	18.4	18.4	···
GJ 447	···	M4.0V	3.3	1997 Jul 13	5.93	10.9	12.9	14.4	15.4	16.9	18.4	19.4	19.4	···
GJ 1151	···	M4.5V	8.1	1997 Jul 15	7.93	10.4	13.4	14.4	15.4	16.4	17.4	17.4	17.4	···
GJ 450	···	M1.5V	8.6	2003 Apr 2	5.74	8.8	9.8	11.3	12.3	13.3	15.3	16.3	16.3	···
GJ 451	···	K1.0VI	9.0	2003 Mar 5	4.50	7.7	9.2	10.7	11.2	12.2	14.2	15.2	15.2	d,*i*
GJ 1154	···	M4.5V	8.3	1998 Mar 15	7.84	9.9	12.4	13.9	15.4	16.4	17.4	18.4	18.4	···
GJ 475	···	G0.0V	8.4	1997 Aug 6	2.80	4.4	6.4	8.9	9.4	11.4	12.4	14.4	15.4	···
GJ 479	···	M2.5V	9.6	2003 Jul 3	6.30	9.1	11.1	12.1	12.1	14.1	16.1	17.1	17.1	···
LHS 337	···	M4.0V	6.3	1998 Sep 3	7.70	10.5	12.5	14.0	15.0	16.5	17.0	18.0	18.0	···
GJ 480.1	···	M3.0V	7.9	2003 Jan 7	7.68	9.5	12.5	14.0	15.0	16.0	16.5	16.5	17.5	···
GJ 486	···	M4.0V	8.3	2003 May 16	6.66	9.4	11.4	12.4	12.9	14.4	15.4	17.4	17.4	···
GJ 493.1	···	M4.5V	8.1	1997 Aug 14	7.97	11.0	13.5	14.5	15.0	16.5	17.5	17.5	17.5	···
GJ 494	···	M0.0V	11.4	1997 Aug 13	5.74	8.2	10.7	11.7	12.2	13.7	14.7	15.7	16.7	g
GJ 506	···	G7.0V	8.5	2003 Jul 1	2.97	···	7.3	8.3	9.3	10.3	12.3	13.3	14.3	d,*i*
GJ 518	···	DZ9	8.2	1998 Jan 3	12.81	14.9	15.4	16.9	17.4	17.4	17.9	···	···	a,*e*
LHS 2784	···	M3.5V	9.2	2002 Dec 5	7.29	9.2	11.2	13.2	14.2	15.7	16.7	18.2	18.2	···
GJ 551	C	M5.0V	1.3	2003 Apr 6	4.84	10.4	12.9	14.4	15.4	16.4	17.4	19.4	19.4	b,*d*,*i*
LHS 2930	···	M6.5V	9.6	1997 Oct 18	10.21	12.1	15.1	16.1	16.6	17.1	17.6	17.6	17.6	e
GJ 555	···	M4.0V	6.2	1998 Mar 20	6.19	10.5	11.5	13.0	13.5	15.0	16.0	18.0	18.0	···
GJ 559A	A	G2.0V	1.3	1998 Oct 22	-1.89	···	···	···	7.9	8.9	9.9	12.4	12.4	a,*b*,*d*,*i*
GJ 559B	B	K0V	1.3	1998 Oct 19	···	···	···	···	8.4	9.9	11.4	13.4	13.4	a,*b*,*i*
G 239-25AB	A/B	M3VJ	9.8	1998 Nov 7	6.73	9.0	11.0	12.0	13.5	14.0	16.0	17.0	17.0	b,*f*,*g*
GJ 566A	A/B	G7.0V	6.7	1998 Sep 14	2.94	···	···	8.8	10.8	12.8	13.8	14.8	14.8	b,*h*,*i*
GJ 566B	A/B	K4V	6.7	1998 Sep 14	···	···	6.8	8.8	8.8	10.3	11.8	···	···	a,*b*,*e*,*h*,*i*

Continued on next page

Name	Resolved PSFs in FOV	Spectral Type	Distance (pc)	Epoch	App. Mag. (*F180M*)	Absolute *F180M* Magnitude Limit 0.2″	0.4″	0.6″	0.8″	1.0″	2.0″	3.0″	4.0″	Notes
TVLM 513-46546	···	M9.0V	10.5	2002 Sep 8	11.16	11.4	13.4	14.9	15.4	16.4	17.4	17.9	17.9	a,*e*,*g*
GJ 581	···	M3.0V	6.3	1998 May 6	6.07	9.5	11.5	13.0	14.0	15.5	17.0	18.0	18.0	···
GJ 588	···	M2.5V	5.9	1997 Sep 18	4.95	7.6	10.6	12.1	13.1	14.6	16.1	17.1	17.1	···
GJ 609	···	M3.5V	9.9	1997 Dec 31	7.62	10.5	13.0	13.5	14.5	15.0	17.0	17.5	17.5	···
GJ 618B	A/B	M4.5V	8.3	1998 Oct 14	8.83	9.9	11.4	12.4	12.9	13.9	16.4	16.4	16.4	b,*e*
GJ 623AB	AB	M2.5VJ	8.0	1998 Sep 11	6.16	···	10.5	11.5	13.0	13.5	15.5	16.5	16.5	b,*c*
GJ 625	···	M1.5V	6.5	2002 Sep 10	5.94	7.9	10.9	11.9	12.9	13.9	15.9	16.9	17.9	···
GJ 628	···	M3.5V	4.2	1997 Aug 12	5.37	9.8	10.8	12.8	14.3	14.8	16.8	17.8	17.8	···
GJ 631	···	K0.0V	9.7	1998 Jul 13	3.69	7.1	9.1	10.1	11.1	11.6	13.1	14.1	15.1	···
GJ 633	···	M2.5V	21.9	1997 Sep 6	8.33	10.3	11.3	12.8	13.3	14.8	15.3	15.3	15.3	g
GJ 638	···	K7.0V	9.8	2002 Aug 28	4.88	7.0	9.0	10.0	10.5	11.5	14.0	15.0	16.0	d
GJ 643	···	M3.0V	6.4	2002 Oct 15	7.03	11.5	12.5	14.0	15.0	16.0	18.0	19.0	19.0	···
GJ 644ABD	A/BD	M2.5VJ	6.4	1998 Oct 15	4.78	···	8.0	10.0	10.5	11.5	13.0	15.0	16.0	b,*c*,*d*
GJ 644C	C	M7.0V	6.4	2003 Jun 8	9.20	12.0	14.0	16.0	16.5	17.0	18.0	18.0	18.0	b,*d*
GJ 1207	···	M3.5V	8.6	1997 Sep 16	7.29	10.3	12.3	13.8	14.3	15.8	17.3	17.3	17.3	···
GJ 649	···	M0.5V	10.2	1997 Sep 23	5.69	7.9	9.9	10.9	12.9	14.4	15.9	16.9	16.9	g
LHS 3262	···	M5.0V	9.4	1997 Aug 17	8.07	10.1	13.1	14.6	15.1	16.1	17.1	17.6	17.6	···
G 203-47AB	AB	M3.5VJ	7.4	2002 Nov 8	6.76	10.1	12.1	13.1	14.1	14.6	16.6	17.6	17.6	b,*c*,*d*
GJ 661AB	A/B	M3.0VJ	6.4	2002 Aug 26	5.07	7.5	9.5	11.0	13.0	13.5	16.0	17.5	18.0	b,*d*,*f*,*h*
GJ 664	···	K5.0V	5.9	2002 Oct 22	···	···	···	···	10.6	11.1	12.6	14.1	15.1	15.1	d
GJ 666B	A/B	K7.0V	8.7	1998 Oct 26	4.95	8.3	9.8	11.3	12.3	13.3	15.3	16.3	16.3	b
GJ 667A	A/B	K4.0VJ	7.2	2003 Feb 1	3.23	6.7	7.7	8.7	9.7	10.7	12.7	14.7	15.7	b,*d*,*h*,*i*
GJ 667B	A/B	K4.0VJ	7.2	2003 Feb 1	3.23	6.7	8.7	9.7	9.7	11.7	13.7	15.7	15.7	b,*d*,*h*,*i*
GJ 673	···	K7.0V	7.7	1997 Oct 27	4.20	6.6	8.6	10.6	11.6	13.1	14.6	15.6	16.6	···
GJ 674	···	M2.5V	4.5	1997 Sep 7	5.02	9.7	10.7	12.7	13.7	14.7	16.7	17.7	17.7	···
GJ 678.1	···	M0.5V	9.9	2002 Aug 22	5.65	7.0	10.0	11.5	12.0	13.0	15.0	16.0	16.0	d
GJ 682	···	M4.0V	5.0	1998 Oct 30	5.79	8.5	11.5	13.5	14.0	15.0	16.5	17.5	17.5	···
GJ 687	···	M3.0V	4.5	1998 Feb 5	4.61	8.7	10.2	12.7	13.2	13.7	15.7	17.7	17.7	···
GJ 686	···	M0.5V	8.0	1997 Aug 1	5.69	8.5	10.5	12.5	14.0	14.5	15.5	16.0	16.5	···
GJ 694	···	M3.0V	9.5	1998 Jul 24	6.10	9.1	10.1	11.6	13.1	14.1	16.1	17.1	17.1	···
GJ 2130BC	···	M2.0V	14.1	1998 Sep 17	6.75	8.7	10.2	11.2	12.2	13.2	16.2	16.2	16.2	b,*c*,*g*
GJ 1221	···	DXP9	6.0	1997 Aug 15	12.48	16.1	17.1	18.1	19.1	19.1	19.1	19.1	19.1	···
GJ 699	···	M3.5V	1.8	1997 Sep 21	4.82	10.7	12.7	14.7	15.7	17.2	17.7	19.7	19.7	···
GJ 701	···	M1.0V	7.7	1997 Aug 14	5.45	8.5	10.5	12.5	13.0	14.0	14.5	15.5	15.5	···
GJ 702A	A/B	K0.0V	5.1	2002 Sep 18	1.88	···	···	8.5	9.5	10.5	12.5	14.5	14.5	b,*d*,*i*
GJ 702B	A/B	K5.0V	5.1	2002 Sep 18	1.88	···	6.5	8.5	10.5	12.5	13.5	14.5	14.5	b,*d*,*e*,*i*
GJ 1224	···	M4.0V	7.5	1997 Sep 19	7.98	11.6	12.6	14.1	14.6	16.6	17.6	18.6	18.6	···
LHS 3376	···	M4.5V	7.2	2002 Aug 20	8.26	12.2	13.7	14.2	14.7	16.2	17.2	17.7	17.7	···
GJ 713AB	AB	F7VJ	8.1	2003 Feb 28	2.37	···	···	7.5	8.5	9.5	11.5	13.5	13.5	b,*c*,*d*,*i*
GJ 1227	···	M4.5V	8.2	1997 Jul 30	7.93	12.4	13.4	14.4	15.4	15.9	17.4	17.4	17.4	···
GJ 721	···	A0.0V	7.7	2002 Dec 12	-0.03	···	···	···	4.1	5.6	8.6	9.6	9.6	a,*d*,*i*
GJ 1230AC	AC/B	M4.0VJ	8.2	2003 Jan 23	6.91	8.4	9.9	12.4	12.9	13.4	16.4	17.4	17.4	b,*c*,*d*
GJ 1230B	AC/B	M5.0V	8.2	2003 Jan 23	8.03	11.4	13.4	14.4	15.4	16.4	17.4	17.4	17.4	b,*d*,*e*
GJ 725A	A	M3.0V	3.5	1998 Jul 21	4.59	9.3	10.3	12.3	13.3	15.3	16.3	17.3	17.3	b
GJ 725B	B	M3.5V	3.5	1998 Oct 13	5.15	8.3	11.3	13.3	14.3	15.3	17.3	18.3	18.3	b
GJ 745A	A	K7.0V	8.6	1998 Aug 25	6.68	9.8	11.3	12.3	13.3	14.3	15.3	17.3	17.3	b

Continued on next page

Name	Resolved PSFs in FOV	Spectral Type	Distance (pc)	Epoch	App. Mag. (*F180M*)	Absolute *F180M* Magnitude Limit 0.2″	0.4″	0.6″	0.8″	1.0″	2.0″	3.0″	4.0″	Notes
GJ 745B	B	M1.0V	8.6	2002 Oct 7	6.75	9.3	10.3	12.3	13.3	14.3	15.3	17.3	17.3	b,*d*,*e*
GJ 747AB	AB	M3.5VJ	8.1	2002 Dec 11	6.66	···	···	10.4	11.4	12.4	14.4	15.4	17.4	a,*b*,*c*,*d*
GJ 752A	A	M2.5V	5.8	1998 Nov 10	4.73	8.7	10.2	11.7	12.2	13.2	15.2	16.2	17.2	b
GJ 752B	B	M8.0V	5.8	2002 Aug 6	9.18	12.2	14.2	15.2	16.2	17.2	19.2	19.2	19.2	b
GJ 1235	···	M4.0V	9.9	1997 Aug 16	8.14	11.0	13.0	14.0	15.5	16.0	17.0	18.0	18.0	···
GJ 764	···	G9.0V	5.7	2003 Jan 1	3.04	···	8.2	9.2	10.2	11.7	13.2	14.2	15.2	i
GJ 768	···	A7.0V	5.1	1997 Oct 13	0.18	···	···	8.5	9.5	10.5	12.5	13.0	13.5	i
GJ 1245AC	A/B/C	M5.5VJ	4.5	1998 Oct 10	7.32	11.7	12.7	14.2	15.2	16.2	17.7	18.7	18.7	b,*f*,*h*
GJ 1245B	A/B/C	M6.0V	4.5	2003 Feb 14	7.67	11.2	12.7	13.7	14.7	15.7	17.7	18.7	18.7	b
GJ 780	···	G8.0IV	6.1	1997 Aug 25	1.92	···	7.1	8.6	10.1	11.1	13.1	14.1	14.1	i
GJ 783A	A/B	K2.5V	6.0	2003 Mar 21	3.00	···	8.1	9.1	9.6	10.6	13.1	14.1	14.1	b,*d*,*i*
GJ 783B	A/B	M2.5V	6.0	2003 Mar 21	···	9.1	11.1	12.1	13.1	14.1	16.1	17.1	17.1	b,*e*
GJ 784	···	M0.0V	6.2	1997 Oct 14	4.39	7.0	10.0	11.5	12.0	13.0	15.0	16.0	16.0	···
GJ 785	···	K2.0V	8.9	1997 Oct 19	3.73	···	8.3	9.3	10.3	11.3	13.3	14.3	14.3	i
GJ 1253	···	M5.0V	9.5	1998 Jan 7	8.27	10.1	12.1	13.6	15.1	16.1	17.1	18.1	18.1	···
GJ 791.2AB	AB	M4.5VJ	8.8	2002 Oct 28	7.67	10.3	12.3	13.3	14.3	15.3	17.3	18.3	18.3	b,*c*,*d*
GJ 793	···	M3.0V	8.0	1997 Aug 9	6.03	8.5	11.0	12.5	13.5	15.5	16.5	17.5	17.5	···
GJ 809	···	M0.0V	7.0	2003 Jul 2	4.92	7.8	9.8	10.8	11.8	12.8	14.8	15.8	16.8	d,*i*
GJ 820A	A	K5.0V	3.5	2002 Dec 3	2.54	···	···	9.3	10.3	11.3	13.3	14.3	15.3	b,*d*,*i*
GJ 820B	B	K7.0V	3.5	2002 Oct 16	2.89	7.3	8.3	9.3	11.3	12.3	14.3	15.3	15.3	b,*d*,*i*
GJ 827	···	F9.0V	9.2	1997 Aug 30	2.96	6.2	7.2	9.2	10.2	11.2	13.2	14.2	14.2	i
GJ 829AB	A/B	M3.0VJ	6.7	2002 Nov 17	5.74	9.4	10.9	11.9	12.9	13.9	15.9	16.9	16.9	b,*c*,*d*
GJ 831AB	A/B	M4.0VJ	7.9	2002 Oct 11	6.69	8.5	10.5	12.5	13.5	14.5	16.5	17.5	17.5	b,*c*
GJ 832	···	M1.5V	4.9	1997 Jul 28	4.60	8.5	10.5	11.5	12.5	14.5	15.5	16.5	16.5	···
G 188-38	···	M3.5V	8.9	1997 Oct 11	6.96	8.7	10.2	12.2	13.2	14.2	15.2	16.2	16.2	···
GJ 846	···	M3.5V	10.2	1997 Nov 17	5.36	8.0	9.0	11.0	12.0	13.0	14.0	15.0	16.0	g
LHS 3746	···	M3.5V	7.4	2002 Nov 18	6.79	9.6	10.6	11.6	13.6	14.6	16.6	17.6	17.6	···
GJ 845A	A	K4.0V	3.6	1997 Aug 4	2.17	···	···	10.2	11.2	12.2	14.2	16.2	16.2	b,*i*
GJ 849	···	M3.0V	8.9	1997 Nov 15	5.69	9.2	10.2	11.2	12.2	13.2	15.2	17.2	17.2	···
LHS 3799	···	M4.5V	7.4	1997 Oct 29	7.47	10.1	12.6	14.1	14.6	15.6	16.6	17.6	17.6	···
GJ 860A	A/B	M3.0V	4.0	1998 Nov 10	5.04	10.0	11.0	13.0	14.0	15.0	17.0	18.0	18.0	b,*d*
GJ 860B	A/B	M4.0V	4.0	1998 Nov 10	5.04	12.0	13.0	14.0	14.5	15.0	17.0	18.0	18.0	b,*d*,*e*
GJ 867AC	AC	M2.0VJ	8.6	2002 Nov 18	5.11	8.8	10.3	11.3	12.3	13.3	15.3	16.3	16.3	b,*c*,*d*,*i*
GJ 867B	B	M3.5V	8.6	1998 Aug 14	6.66	8.8	10.3	12.3	12.8	14.3	16.3	17.3	17.3	b
GJ 873	···	M3.5V	5.0	2002 Dec 24	5.55	8.5	10.5	12.5	13.5	14.5	16.5	17.5	18.5	···
GJ 876	···	M3.5V	4.6	1997 Dec 5	5.16	8.7	10.7	12.7	13.7	14.7	15.7	17.7	18.7	···
GJ 1276	···	DZ9+	8.5	1997 Sep 21	13.56	15.3	16.3	17.3	17.3	17.3	18.3	18.3	18.3	a
GJ 877	···	M2.5V	8.6	1997 Aug 29	5.94	8.3	10.3	11.3	12.3	13.3	16.3	17.3	17.3	···
GJ 880	···	M1.5V	6.8	2002 Oct 15	4.80	8.3	9.8	10.8	11.8	12.8	14.8	15.8	16.8	d,*i*
GJ 881	A	A4.0V	7.6	1998 Aug 6	0.94	···	···	5.6	6.6	7.6	8.6	10.6	11.6	a,*b*,*d*,*i*
GJ 884	···	K7.0V	8.2	1997 Dec 28	4.44	7.4	9.4	10.4	11.4	12.4	13.4	15.4	15.4	···
GJ 887	···	M1.0V	3.2	1997 Sep 11	3.45	7.4	9.9	11.4	12.9	14.4	15.4	17.4	17.4	···
GJ 892	···	K3.0V	6.5	1997 Sep 19	3.17	···	8.4	9.9	10.9	11.9	12.9	14.9	14.9	i
GJ 896A	A/B	M3.5V	6.2	2004 Jun 30	5.57	7.0	8.5	10.0	11.0	12.0	14.0	15.0	16.0	a,*b*
GJ 896B	A/B	M4.5V	6.2	2004 Jun 30	6.55	8.0	10.0	12.0	12.0	13.0	14.0	15.0	16.0	a,*b*

Continued on next page

Name	Resolved PSFs in FOV	Spectral Type	Distance (pc)	Epoch	App. Mag. (*F180M*)	Absolute *F180M* Magnitude Limit 0.2″	0.4″	0.6″	0.8″	1.0″	2.0″	3.0″	4.0″	Notes
GJ 1286	···	M5.0V	7.2	1997 Sep 18	8.42	13.7	14.7	15.7	16.2	16.7	18.7	18.7	18.7	···
GJ 902	···	K3V	11.4	1997 Oct 19	4.56	7.7	8.7	10.7	11.7	11.7	13.7	14.7	15.7	[g]
GJ 905	···	M5.5V	3.1	2003 Jan 12	6.25	11.5	13.5	14.0	14.5	15.5	17.5	18.5	19.5	···
GJ 1289	···	M3.5V	8.1	1997 Sep 10	7.39	10.5	12.5	13.5	14.5	15.5	17.5	18.5	18.5	···
GJ 908	···	M1.0V	5.9	1997 Sep 9	5.13	9.6	10.6	12.1	13.1	14.1	16.1	17.1	17.1	···

[a]No PSF subtraction
[b]Known multiple system, excluding planets. J in spectral type label means joint spectral type.
[c]Sensitivity measured around unresolved or very close binary
[d]2MASS H magnitude for primary
[e]Off-center by more than 5″
[f]Sensitivity measured around brighter component only
[g]Beyond 10 pc
[h]Sensitivity measurements exclude 30° between components.
[i]Saturated core

CHAPTER 4

M Dwarf Multiplicity and its Implications

This chapter is based on §§5.4 and higher of "The Solar Neighborhood *XXVIII*: The Multiplicity Fraction of Nearby Stars from 5 to 70 AU and the Brown Dwarf Desert Around M Dwarfs", by Dieterich et al. (2012).

Of the 188 star systems imaged within 10 pc in the NICMOS survey, 126 systems have M dwarfs as the primary (or single) component[1] (Table 3.1). We now apply the sensitivity limits listed in Table 3.4 to derive the multiplicity fraction for M dwarfs under several scenarios.

4.1 Establishing Search Completeness for M Dwarfs

Figures 4.1 (a) and (b) show the ranges in sensitivities obtained for M dwarfs at each of the eight angular separations probed by the PSF insertion simulations. In Figure 4.1(b), the known distance to each target was used to convert contrasts into absolute magnitudes, and relate these absolute magnitudes to the spectral types of putative companions. Because sensitivity is a complex function of contrast, instrumental background, apparent magnitude, and the quality of the PSF subtraction, there is a significant spread about the mean values quoted in Figure 4.1. Overall, the search would detect companions with $\Delta F180M$=2.5 to 10.2 magnitudes at separations of 0.2″ to 4.0″, respectively.

[1]GJ 169.1AB is an M4.0V/white dwarf binary. Although the brighter M4.0V component is generally considered to be the primary component, the current situation does not reflect the components' masses or spectral types at the time of stellar formation and main sequence evolution, when the current white dwarf was much more massive and luminous than the M dwarf. We therefore do not consider GJ 169.1AB to be a system with an M dwarf primary.

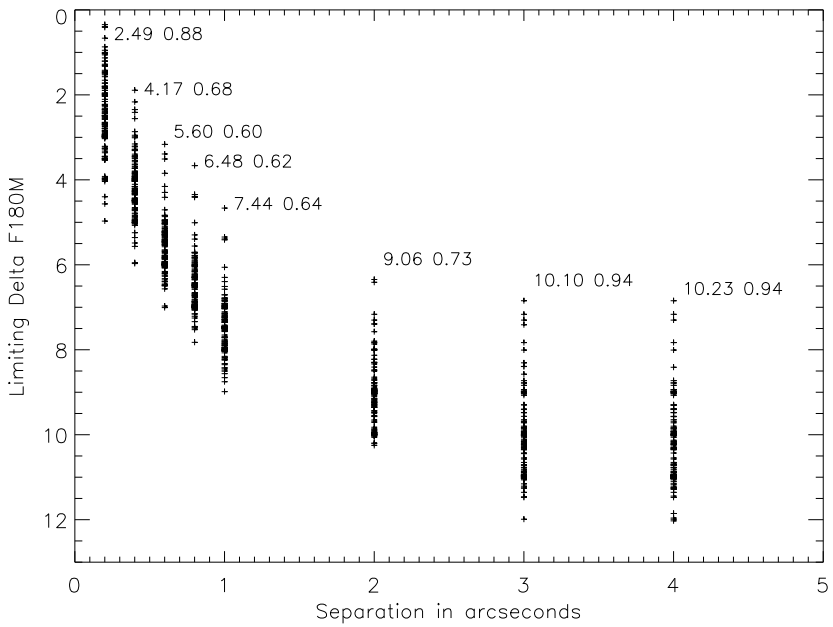

(a)

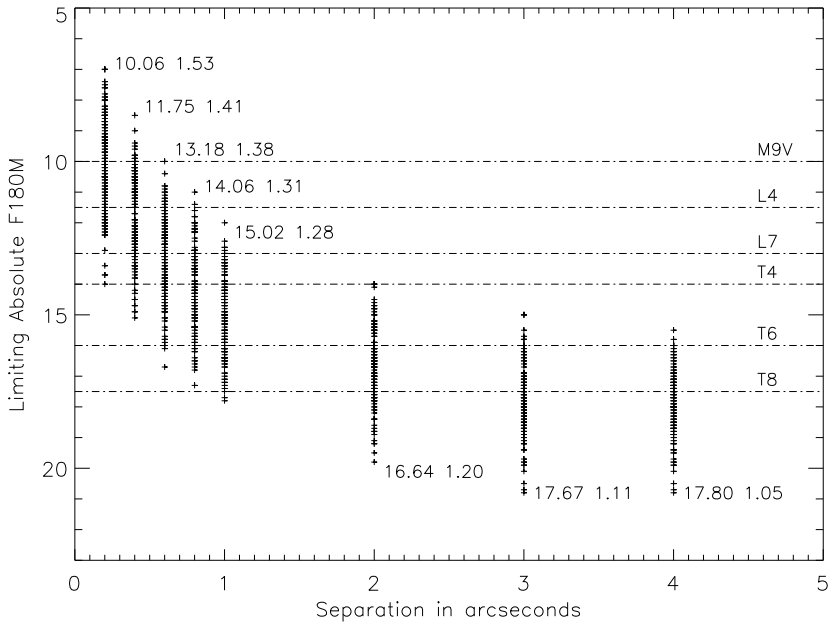

(b)

Figure 4.1 Search sensitivities for the eight angular separations tested by PSF insertion simulations. In both panels, the two numbers next to each cluster of points are the mean and standard deviation for that separation, respectively. (a) The ability to detect a companion is primarily determined by the angular separation and the components' Δm. This instrumental representation has a lower standard deviation, but does not directly indicate the characteristics of the putative companions. (b) The limiting absolute magnitudes from Table 3.4 yield a range of possible companion types detectable at each angular separation. The even vertical spacing in (b) is a consequence of the lower precision of the absolute magnitudes in Table 3.4 when compared to the observed photometry for each science target used to calculate Δ magnitudes in (a). The absolute *F180M* magnitude for select spectral subtypes is taken from the synthetic photometry displayed in Figure 3.5.

In order to transform the observational sensitivities (Figure 4.1(a)) to astrophysical parameters, we substitute physical separations in AU in place of angular separations and apply the statistical relation between physical separation and semi-major axis for a sample of binaries with random inclinations and eccentricities,$< a >= 1.26 < \rho >$ (Fischer & Marcy 1992), obtaining Figure 4.2. The large plus signs in Figure 4.2 indicate the 90% detection limits for semi-major axes ranging from 0 to 40 AU, binned in 2 AU increments. A flat contrast curve is assumed for sensitivities beyond 40 AU. Because of the large factor in distance covered by this volume-limited search, the 90% detection limits in physical separation are effectively established by the most distant stars in the sample. It is possible to boost sensitivity at closer physical separations by establishing a closer distance horizon for the search, at the expense of overall sample size. We examined the effect of using a closer distance horizon for calculating sensitivity limits, and came to the conclusion that it is more important to maintain a robust sample, especially because more sensitive but much smaller studies have already been done (e.g., Close et al. 2003).

It is also important to consider the effect that the small field of view of *NIC2* ($19.5'' \times 19.5''$) has on sample completeness at large physical separations. Figure 4.3 is a histogram displaying the fraction of M dwarfs, including resolved system secondaries, sampled within 10 pc (N=141) as a function of outer search radius, binned in 10 AU increments. While all M dwarfs were probed to semi-major axes as close as 5 AU[2], only the farthest 12 targets were

[2]As noted in Table 3.4, GJ 15A, LHS 224AB, GJ 623AB, and GJ 644ABD are M dwarfs for which core saturation prevented the establishment of a sensitivity limit at $0.2''$. A single M dwarf system, GJ 747AB, saturated out to $0.4''$. All of these cases correspond to statistically corrected semi-major axes smaller than 5 AU.

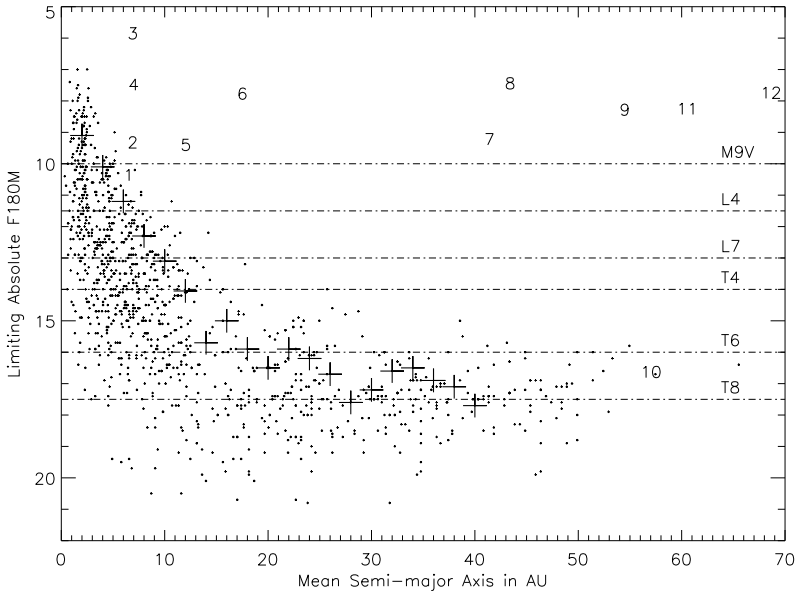

(a)

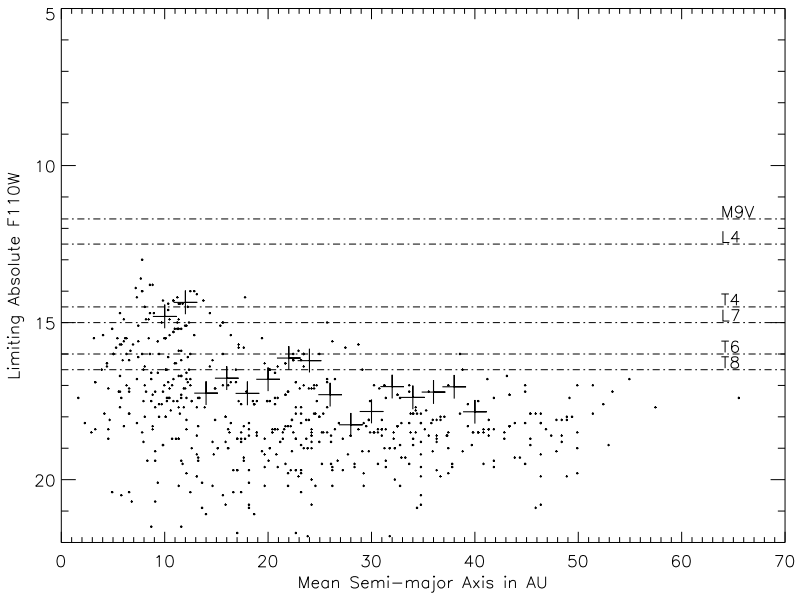

(b)

Figure 4.2 (a) Search sensitivity displayed as a function of absolute *F180M* magnitude and mean semi-major axis, assuming $< a >= 1.26 < \rho >$ (Fischer & Marcy 1992). Each dot represents the sensitivity derived from a PSF insertion around an M dwarf (Table 3.4). The range of limiting absolute magnitudes is significantly wider at close separations because all targets were probed at close physical separations, whereas only targets close to the distance limit of 10 pc could be probed at wide physical separations given NIC2's small field of view. Contrast is also more strongly dependent on overall brightness at close angular separations. The large plusses represent the absolute magnitude limits where 90% of companions can be detected at a given physical separation. The numbers indicate the positions of the companions listed in Table 4.1: (1) GJ 84B, (2) GJ 65B, (3) GJ 661B, (4) GJ 257B, (5) GJ 1116B, (6) GJ 860B, (7) GJ 1245B, (8) GJ 896B, (9) GJ 1230B, (10) GJ 229B, (11) GJ 618B, and (12) LP 771-95B. The large blank space in the center and right-hand-side of the diagram is a clear representation of the "brown dwarf desert". (b) Same as (a), but using absolute *F110W*, and omitting separations $\leq 1.0''$. While the sensitivity to T dwarfs is increased in (b), the sensitivity to L dwarfs is decreased and close separations cannot be probed. See §3.5.3 for discussion.

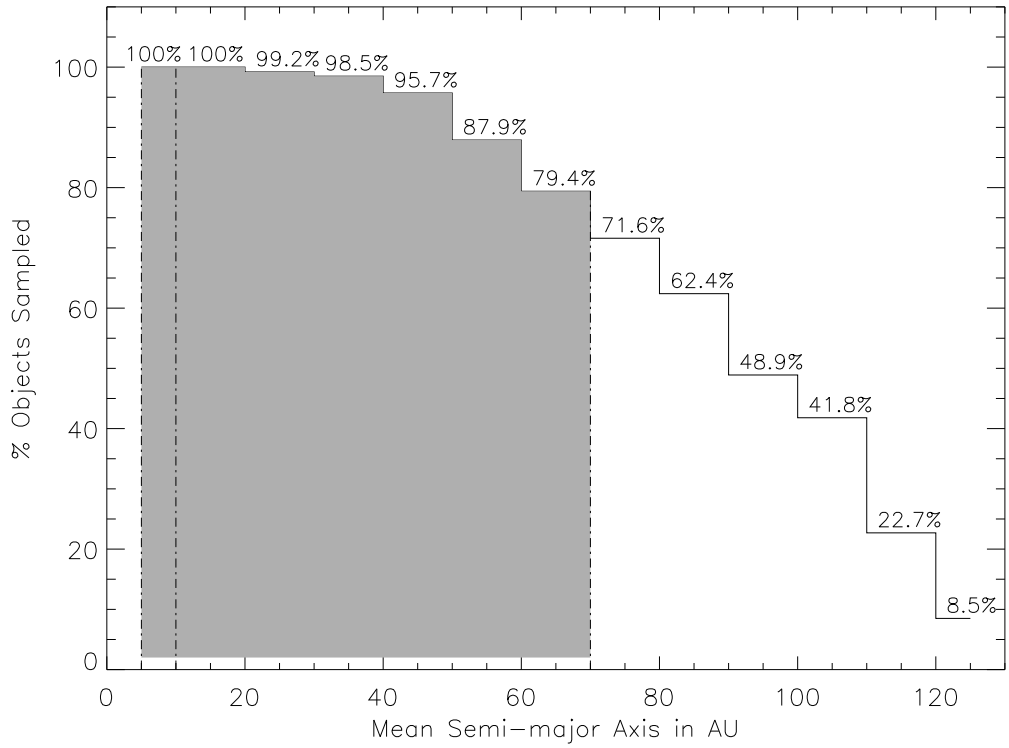

Figure 4.3 Statistical semi-major axis distribution for companion search around all 141 M dwarf components within 10 pc. The shaded area indicates the separation ranges we consider when calculating the multiplicity fraction, with the dashed lines indicating the inner radius limits for M and L dwarfs (5 AU), and for the T dwarfs (10 AU) and the outer radius for both (70 AU). Search completeness diminishes with increasing separation because NIC2's field of view limits our search radius to $\sim 9''$.

probed to semi-major axes greater than 120 AU. In order to retain the statistical significance of the sample, only physical separations corresponding to mean semi-major axes between 5 and 70 AU (100% to 79.4% complete) were considered, and the number of companions found in the bins from 40 to 70 AU was divided by that bin's completeness fraction.

4.2 The M Dwarf Multiplicity Fraction

Table 4.1 lists companions to M dwarfs in the sample within the completeness range of 5 to 70 AU that were re-detected in the search or are new companions discovered during this

search and published in Golimowski et al. (2004a). Combining these known binaries to the null detections and sensitivity limits presented in Figures 4.1−4.3, we now present formal multiplicity fractions for three distinct combinations of companion types and ranges in semi-major axes. These results are summarized in Table 4.2. In each case, the 1σ confidence intervals were calculated using the binomial distribution approach outlined by Burgasser et al. (2003b). This approach is preferable whenever the probability distribution is non-Gaussian due to a small sample. In each of the three different scenarios discussed below the multiplicity fraction is low enough that even with the sample of 126 systems, the probability distribution is not symmetric about the central peak value because proximity to the limiting case of a multiplicity fraction of zero causes a sharper drop-off towards the lower limit of the probability distribution (Figure 4.4). Given a multiplicity fraction ϵ_m, the probability distribution of finding n binaries in a sample of N systems is governed by

$$P(n) = \frac{N!}{n!(N-n)!}\epsilon_m^n(1-\epsilon_m)^{N-n}.$$

This relationship can be inverted to solve for the probability distribution of a given multiplicity fraction given the observational results N and n, yielding

$$P'(\epsilon_m) = (N+1)P(n),$$

which can then be integrated numerically to find the lower and upper limits of ϵ_m corresponding to 68% (1σ for a Gaussian distribution) of the area under the probability distribution

curve, as shown by the shaded areas in Figure 4.4.

Table 4.1: Recovered M Dwarf Multiple Systems

A Component[a]	Spectral Type	M_H[b]	Mass[c] $M_\odot$	B Component	Spectral Type	M_H[b]	Mass $M_\odot$	Angular Separation	Inferred Semi-major Axis (AU)[f]
GJ 229A	M1.5V	5.41	0.59	GJ 229B	T6.0	16.81	0.05:[d]	7.62″	55.2
GJ 84A	M2.5V	5.95	0.52	GJ 84B	M7.0V	10.54	0.084[e]	0.44″	5.2
GJ 661A	M3.0V	6.03	0.51	GJ 661B	M3.0V	6.03	0.51	0.70″	5.6
GJ 896A	M3.5V	6.60	0.39	GJ 896B	M4.5V	7.62	0.22	5.35″	42.1
GJ 618A	M2.5V	6.62	0.38	GJ 618B	M4.5V	8.43	0.15	5.62″	58.7
GJ 860A	M3.0V	7.02	0.31	GJ 860B	M4.0V	7.95	0.18	3.19″	16.2
GJ 1230A	M4.0V	7.34	0.26	GJ 1230B	M5.0V	8.46	0.15	5.11″	53.2
LP 771-95A	M2.5V	7.56	0.23	LP 771-95B	M3.5V	7.92	0.18	7.74″	67.8
GJ 257A	M3.0V	7.63	0.22	GJ 257B	M3.0V	7.66	0.21	0.57″	5.7
GJ 1245A	M5.5V	9.05	0.12	GJ 1245B	M6.0V	9.40	0.10	7.01″	40.1
GJ 1116A	M5.5V	9.24	0.11	GJ 1116B	M6.0V	9.58	0.10	1.51″	9.9
GJ 65A	M5.5V	9.32	0.11	GJ 65B	M6.0V	9.50	0.10	1.66″	5.6

4.2.1 The M Dwarf Multiplicity Fraction for M0V to M9V Companions at Separations of 5 to 70 AU

At an inner search radius of 5 AU, the search is 90% sensitive to $M_{F180M} \lesssim 11.2$, corresponding to early L spectral types (Figure 4.2(a)). Eleven of the 12 known companions listed in Table 4.1 are M dwarfs meeting this sensitivity criterion. Five of these companions lie between 40 and 70 AU, where the completeness of the search is reduced due to the limited field of view. Placing these five systems into the separation bins shown in Figure 4.3 yields 2 systems in the 40−50 AU bin, 2 systems in the 50−60 AU bin, and one additional system in the 60−70 AU bin. Dividing these numbers by the fractional completeness of these bins (0.957, 0.879, and 0.794) and summing the results yields 5.62. We then transform the

[a] Ordered by decreasing mass, as shown in Figure 4.5.
[b] H band photometry from 2MASS. Close binaries were deconvolved adopting $\Delta H = \Delta F180M$.
[c] Based on the Mass-Luminosity Relation of Henry & McCarthy (1993).
[d] Estimate based on Allard et al. (1996).
[e] Golimowski et al. (2004a)
[f] Statistically corrected for projection effects (Fischer & Marcy 1992).

multiplicity obtained at 90% confidence level to a true volume limited multiplicity fraction by dividing 11.62 (the sum of 5.62 and the remaining companions from 5−40 AU) by 0.9, obtaining 12.91. Rounding this number up to 13, we see that we would likely have recovered 2 additional real companions with separations ranging from 5 to 70 AU. Applying the binomial distribution, we conclude that the multiplicity fraction for M dwarf companions orbiting M dwarf primaries at semi-major axes from 5 to 70 AU is $\epsilon_m = 10.3^{+3.4}_{-2.1}\%$ (Figure 4.4(a)).

4.2.2 The M Dwarf Multiplicity Fraction for L0 to L9 Companions at Separations of 5 to 70 AU

Although the search did not detect any L dwarf companions within 10 pc and in the separation regime of 5 to 70 AU,[3] it is possible to assign a multiplicity fraction based on completeness arguments. Figure 4.2(a) shows that at 5 AU, the detection rate for L dwarfs is only ∼50%. It is not possible to obtain a truly volume limited multiplicity fraction in this separation range. We therefore constrain the sample to include only the 51 systems for which the detection of an L9 companion at 5 AU is possible. Applying the binomial distribution, we obtain a multiplicity fraction of of $\epsilon_m = 0.0^{+3.5}_{-0.0}\%$ (Figure 4.4(b)). An alternative approach is to maintain the volume limited nature of the sample by increasing the inner limit of the separation range. From Figure 4.2a, the inner radius at which >90% of the systems were probed is 12 AU. We therefore calculate a volume limited multiplicity fraction for L0 to L9 companions to M dwarfs of $\epsilon_m = 0.0^{+1.4}_{-0.0}\%$ valid at separations ranging from 12 to 70 AU.

[3]GJ 1001 B and C are beyond 10 pc (Henry et al. 2006).

4.2.3 The M Dwarf Multiplicity Fraction for L0 to T9 Companions at Separations of 10 to 70 AU

The sensitivity to T dwarfs at close separations is diminished due to their intrinsic faintness. We therefore restrict the inner search radius to 10 AU, where the search was 90% sensitive to L dwarfs and ∼50% sensitive to late T dwarfs. At separations beyond 12 AU, Figure 4.2(b) indicates considerable scatter in the 90% sensitivity limits. Based on the trend on Figure 4.2b, we adopt a 90% sensitivity limit of M_{F110W}= 17.5, corresponding to spectral type ∼T9. One T6 dwarf, the class prototype GJ 229B (§2.1), was detected at an inferred semi-major axis of 55.3 AU. Following the same approach used for the L dwarfs, we calculate the multiplicity fraction for a sub-sample as well as for the volume limited sample. There were 43 systems for which a late T dwarf detection at 10 AU was possible. This sub-sample yields a multiplicity fraction of $\epsilon_m = 2.3^{+5.0}_{-0.7}\%$ The complete sample is sensitive to late T dwarfs at separations ≥ 14 AU. We therefore calculate a volume limited multiplicity fraction of $\epsilon_m = 0.8^{+1.8}_{-0.2}\%$ valid at separations ranging from 14 to 70 AU.

The multiplicity fractions derived above for the various separation and contrast regimes are summarized in Table 4.2. Figure 4.4 illustrates the probability densities derived from binomial statistics for three of the configurations listed in Table 4.2.

Table 4.2: M Dwarf Multiplicity Fractions

Companion Range Spectral Type	Search Radius AU	Systems Probed	Detections	Hidden	Mult. Fraction %	Volume Limited?
M0V - M9V	5 - 70	126	11	2	$10.3^{+3.4}_{-2.1}$	Yes
L0 - L9	5 - 70	51	0	0	$0.0^{+3.5}_{-0.0}$	No
L0 - L9	12 - 70	126	0	0	$0.0^{+1.4}_{-0.0}$	Yes
L0 - T9	10 - 70	43	1	0	$2.3^{+5.0}_{-0.7}$	No
L0 - T9	14 - 70	126	1	0	$0.8^{+1.8}_{-0.2}$	Yes

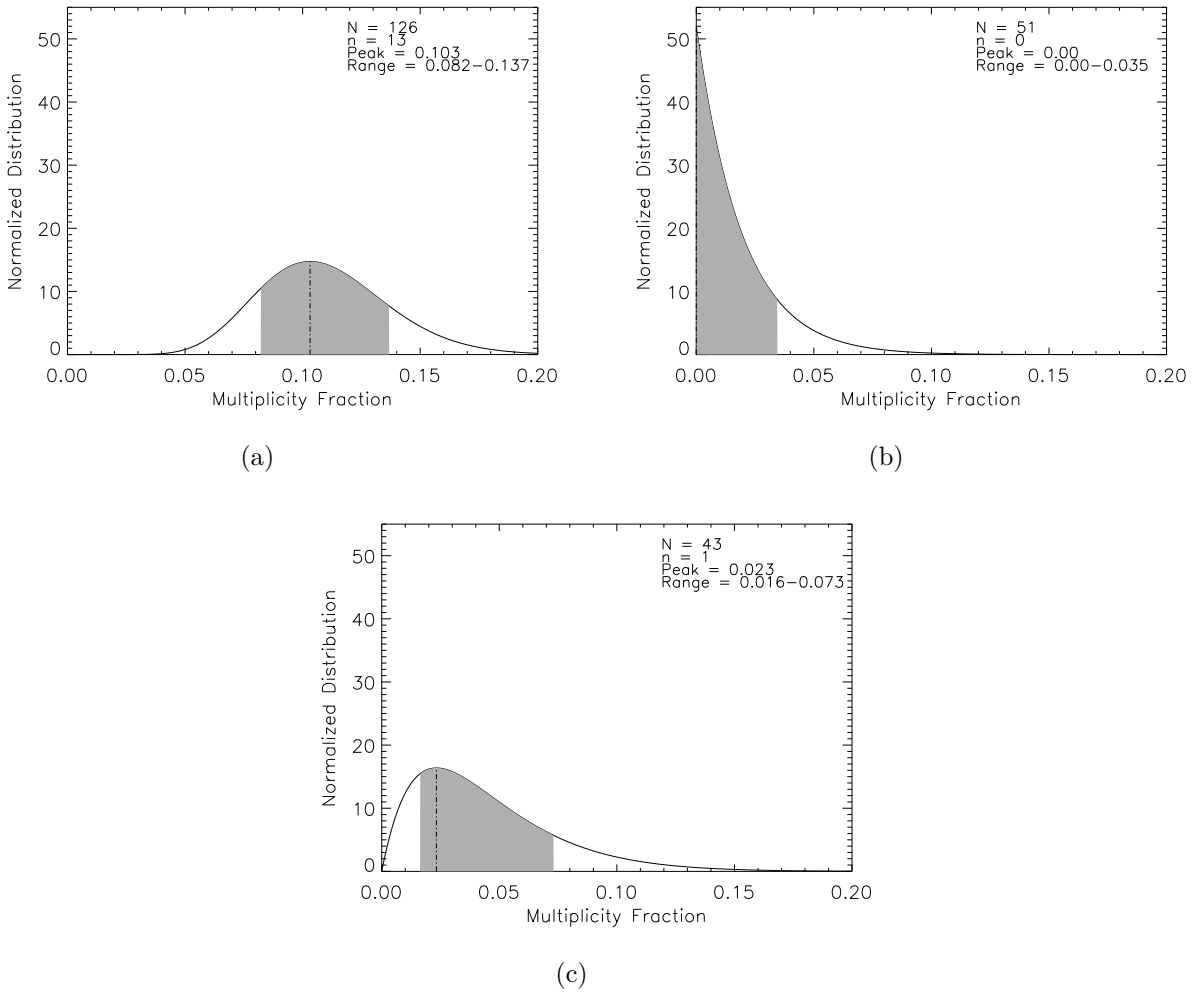

Figure 4.4 Probability density distributions for select multiplicity fractions listed in Table 4.2, calculated using the binomial distribution. The shaded areas correspond to 68% of the area under the curve, equivalent to the 1σ confidence range. The individual plots correspond to: (a) M dwarf companions, (b) L dwarf companions (not volume limited), and (c) L and T dwarf companions (not volume limited).

4.3 Sensitivity to Companion Masses

Estimating masses for field brown dwarfs is a difficult problem. Whereas the masses of main sequence stars can be estimated from mass-luminosity relations (Henry & McCarthy 1993;

Henry et al. 1999; Delfosse et al. 2000), brown dwarfs are constantly cooling, and therefore have a mass-luminosity-age relation. Such a relation has not yet been established empirically (§2.7). Currently, the best way of estimating brown dwarf masses is by correlating spectral types to effective temperatures, and then checking the effective temperature against evolutionary model predictions, assuming a certain age for the brown dwarf in question. This approach is heavily model dependent, and the end result of such calculation can at best serve as a guideline for the mass range for a particular object. With this caveat in mind, we now apply this approach to the limiting spectral types listed in Table 4.2.

Assuming a mean age of 3 Gyr for the nearby L dwarf field population (Seifahrt et al. 2010), the effective temperatures for brown dwarfs of spectral types L3, L5, L8, T5, and T7 are estimated to be roughly 2000K, 1750K, 1500K, 1200K, and 900K, respectively (Golimowski et al. 2004b; Cushing et al. 2008). Adopting the evolutionary models of Chabrier et al. (2000), one can estimate approximate masses of 0.073 $M_{\odot}$, 0.070 $M_{\odot}$, 0.057 $M_{\odot}$, 0.052 $M_{\odot}$, and 0.040 $M_{\odot}$ for spectral types L3, L5, L8, T5, and T7 (Table 4.3). The last number has considerable uncertainty due to the need to extrapolate the Chabrier models at low temperatures. We therefore adopt $0.040 M_{\odot}$ at 3 Gyr as a guideline for the minimum mass detectable by the search. It is important to note that the scatter in age in the nearby field population is likely to cause a large dispersion in the masses of detectable objects. Unless there are further data indicative of the age of an individual brown dwarf, the mean value adopted here should be used with extreme caution.

Table 4.3: Masses ($M_\odot$) Based on Models of Chabrier et al. (2000).

Sp. Type	L3	L5	L8	T5	T7
T_{eff}[a]	2000	1750	1500	1200	900:
1 Gyr	0.070	0.060	0.050	0.050	0.030:
3 Gyr	0.073	0.070	0.057	0.052	0.040:
5 Gyr	0.075	0.072	0.065	0.065	0.050:

4.4 A Current Map of the Brown Dwarf Desert

The idea of the brown dwarf desert continues to evolve. The term was originally used to describe the fact that radial velocity surveys of solar analogs detect an abundance of extra-solar planets but rarely detect brown dwarfs, even though a brown dwarf's higher mass makes its detection easier. In their seminal work, Marcy & Butler (2000) found that <1% of main sequence Sun-like stars harbor brown dwarfs. Several other studies have since then obtained similar results for different ranges in separation, primary mass, and system age. Oppenheimer et al. (2001) conducted the first successful search for brown dwarf companions, discovering the T dwarf prototype GJ 229B. Their infrared coronagraphic search of stars within 8 pc detected a single substellar object, from which they cautiously imply a stellar/substellar multiplicity fraction of ∼1%. McCarthy & Zuckerman (2004) used Keck coronagraphy to search 102 nearby field GKM stars at separations from 75 to 1200 AU. They found one brown dwarf companion, and report a binary fraction of 1±1%[4]. Their result agrees well within statistical uncertainties to the results of this search (Table 4.2),

[a]Golimowski et al. (2004b)

[4]Using the binomial distribution treatment employed in the NICMOS search, 1 detection out of 102 observations is equivalent to a multiplicity fraction of $1^{+3}_{-0.2}$%.

suggesting a wide desert with no significant change in the substellar companion fraction from 10 to 1200 AU. Luhman et al. (2005) used HST's Wide Field Planetary Camera 2 (WFPC2) to survey 150 members of the young cluster IC 348 ($\sim$2 Myr) at separations of 120$-$1600 AU. Of these stars, 85 were in the mass range 0.08$-$0.5$M_{\odot}$, approximately corresponding to the mass range for main sequence M dwarfs (Henry & McCarthy 1993). They found one possible substellar companion to a low mass star, but note that it is not possible to ascertain companionship due to the wide separation of this system ($\sim$1400 AU). Based on this finding, Luhman et al. derive an upper limit of 4% for the substellar companion fraction of low mass stars. This result is again in very good agreement with the results reported here, suggesting that there is little evolution in the multiplicity fraction of low mass stars after the first few million years, and again suggesting no significant change in the substellar companion fraction beyond 10 AU. Regarding single objects, Luhman et al. find that 14 out of 150 objects are likely substellar based on evolutionary models (Chabrier et al. 2000). They note that the fact that they detect ten times more isolated stars than isolated brown dwarfs in IC 348 indicates that the brown dwarf desert may not be limited to the formation of companions, but may also extend to the formation of single objects (§4.6.2). Metchev & Hillenbrand (2009) used adaptive optics on Keck and Palomar to survey 266 Sun-like (F5$-$K5) stars, and infer a brown dwarf companion frequency of $3.2^{+3.1}_{-2.7}$%[5] for separations of 28 to 1590 AU. Finally, direct imaging searches for planetary companions would be capable of detecting brighter brown dwarfs. Masciadri et al. (2005) used VLT/NACO to search 30 young (<200 Myr) GKM stars and found no brown dwarf or planetary companions at separations larger

[5] 2σ limits.

than 36 AU. In a similar fashion, Biller et al. (2007) used VLT and MMT to search 45 young GKM field stars at separations of 20−40 AU, and also found no brown dwarfs. Due to smaller sample sizes, the last two studies do not add significant constraints to the brown dwarf desert, but their null detections are certainly in agreement with constraints set by the larger studies.

The sum of these studies, along with the results of the HST/NICMOS search, indicate a consistent image of a brown dwarf desert that is mostly invariant with respect to the mass of the primary star, and which is valid for a wide range of separations ranging from 5 AU to 1600 AU. Whether the search is sensitive to substellar companions to Sun-like stars at intermediate to large separations (Metchev & Hillenbrand 2009), substellar companions to low mass stars at intermediate separations (this study), or a mixture of young stars with masses ranging from solar down to the M dwarf regime (Masciadri et al. 2005; Biller et al. 2007) the detection rate is always consistent with a stellar-substellar binary fraction on the order of a few percent.

4.5 Is the Desert Real?

The multiplicity fraction of Sun-like stars is ∼50% (Duquennoy & Mayor 1991; Raghavan et al. 2010). The multiplicity rate for stellar companions to M dwarfs at all separations is ∼30% (Henry & McCarthy 1990; Henry 1991; Fischer & Marcy 1992). Based on the results of this survey (Table 4.2) and the companion searches discussed in §4.4, it is clear that stellar companions outnumber brown dwarf companions by a factor $\gtrsim$10. Does this paucity of brown

dwarfs, however, constitute a "real desert"? A few studies (e.g., Metchev & Hillenbrand 2009; Grether & Lineweaver 2006) have suggested that the dearth of brown dwarf companions is a natural consequence of a well behaved, Salpeter-like (Salpeter 1955) universal CMF that tends to lower multiplicities at lower mass ratios, and that a real brown dwarf desert would only exist if the observed number of brown dwarf companions is significantly lower than what a universal CMF would predict. In particular, Grether & Lineweaver note that the overlap of the planetary CMF and the stellar CMF reaches a minimum at $\sim$0.03 $M_{\odot}$, causing the observed paucity of brown dwarf companions. In this search, we test the hypothesis of a universal CMF by focusing primarily on low mass stars. As shown in Table 4.1, the twelve M dwarf binaries detected between 5 and 70 AU have primary masses ranging from $\sim$0.6 to $\sim$0.1 $M_{\odot}$. Figure 4.5 is a plot of the masses of the primary and the secondary components of this sample. Figure 4.5 shows that the mass ratios of detectable low mass binaries tend to increase (i.e., approach equal mass components) as masses approach the hydrogen burning limit, thus excluding the formation of brown dwarf secondaries. The completeness analysis (§4.1) demonstrates that this trend is not an observational selection effect. Indeed, detecting lower mass companions is easier for intrinsically fainter primary stars, so the selection effect works against the trend noted in Figure 4.5. Reconciling these observations with the idea of a universal CMF would require this function to be rather restricted in the sense that it would not be a function of mass ratio, or would only be valid for Sun-like stars. For any reasonably broad definition, it is reasonable to conclude that deviations from a universal CMF do exist in the brown dwarf regime. The brown dwarf desert is therefore

a reality whether one defines it in terms of total numbers or in terms of a deviation from a trend.

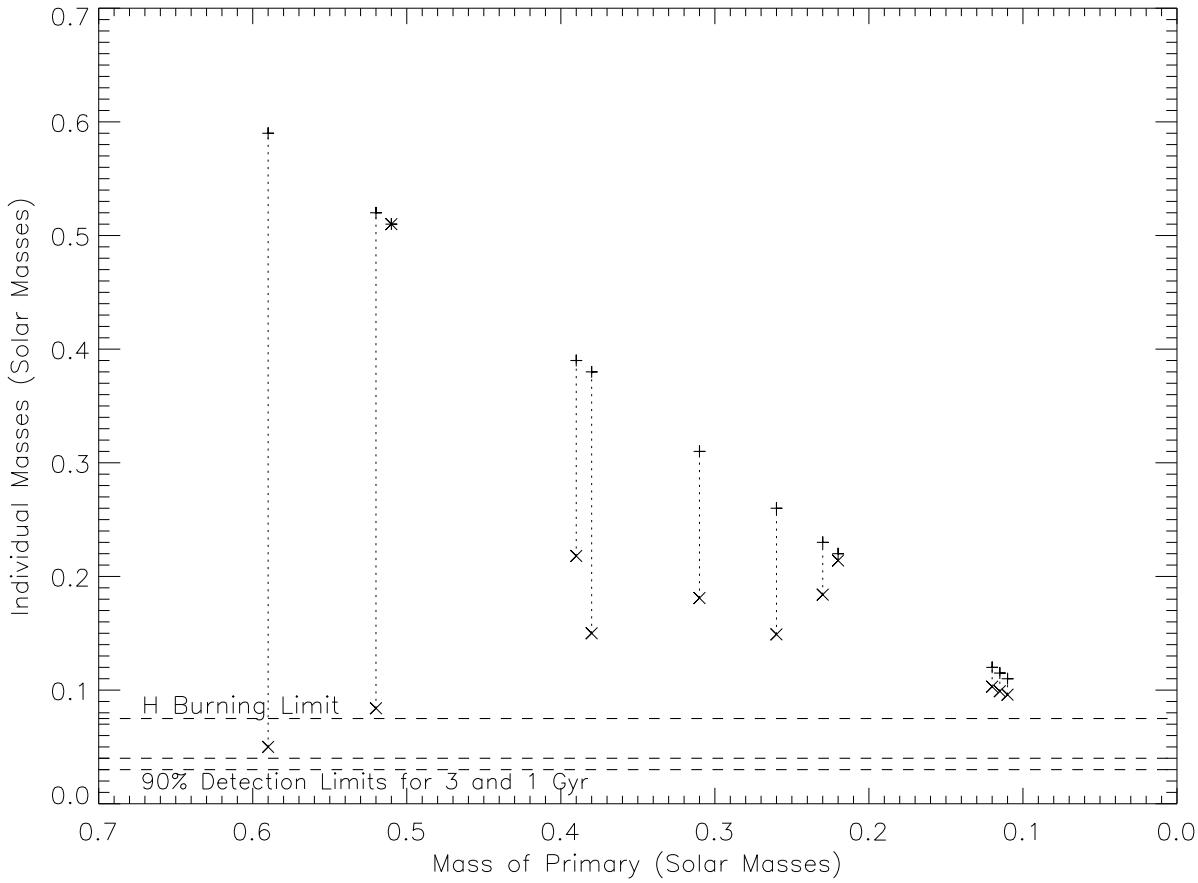

Figure 4.5 Mass distribution for the binaries in Table 4.1. The horizontal dashed lines denote the hydrogen burning limit (0.075 $M_{\odot}$) and the 90% detection limits for this search assuming brown dwarf ages of 1 Gyr and 3 Gyr (Table 4.3). As the masses of the primary components approach the hydrogen burning limit, the mass ratios tend to unity, thus implying that brown dwarfs rarely form as secondaries. From left to right, the binaries are ordered as they appear in Table 4.1.

4.6 The CMF, the IMF, and the Big Picture

VLM binaries have a strong tendency towards high (i.e., unity) mass ratios (e.g., Burgasser et al. 2007). The effect has been demonstrated to be an intrinsic characteristic of VLM stars and

brown dwarfs through Bayesian analysis (Allen 2007). The results of this survey (Figure 4.5) show that mass ratios tend to increase as stellar masses approach the hydrogen burning limit, with the strong onset of nearly equal mass duplicity happening somewhere between 0.2 and 0.1 $M_{\odot}$. Other studies have also suggested that the basic population properties of IMF, CMF, and the binary separation distribution all appear to change significantly at a mass of $\sim$0.1 $M_{\odot}$, slightly above the hydrogen burning limit. Close et al. (2003) conducted an adaptive optics search of 39 VLM objects with spectral types ranging from M8.0V to L0.5, and found a mass distribution similar to the one shown in Figure 4.5 (see their Table 3). They also probed smaller separations than our formal limit of 5 AU, and found that whereas higher mass stars have a separation distribution peaked at 30 AU (Duquennoy & Mayor 1991), VLM binaries have a separation distribution peaked at 4 AU. Also, Bayesian analysis of several studies (Allen 2007) demonstrates that VLM and brown dwarf binaries with separations $>$ 20 AU are extremely rare. We note that Close et al. probed significantly smaller separations than we did, but did not establish formal detection limits. Kraus et al. (2005) conducted a search for VLM binaries in the Upper Scorpius OB association, and also found results consistent with a discontinuity in the separation distribution at a mass of 0.1$M_{\odot}$.

4.6.1 Isolated Objects

In an analysis of data from several open cluster studies, Thies & Kroupa (2007) demonstrate that the observed mass distribution is incompatible with the existence of an IMF that is monotonic about the hydrogen burning limit. They note that because stellar formation and stellar ignition are in principle unrelated processes governed by different areas of physics,

there is no reason to expect that the IMF discontinuity would be caused by the onset of hydrogen burning. They therefore allow for an arbitrary overlap of the stellar and brown dwarf components of the IMF, thus allowing for a smooth turnover. In light of the companion mass distribution for low mass stars (Figure 4.5), new developments in the hydrodynamical simulations of star cluster formation (Bate 2009, 2011), and new observations of young stellar clusters (Kraus et al. 2008, 2011; Evans et al. 2012), we re-examine the nature of the IMF discontinuity at masses close to the hydrogen burning limit.

The details of the mass function for older field objects close to the hydrogen burning limit are difficult to quantify. The difficulty is mostly due to the lack of a robust volume limited census of L and T dwarfs based on trigonometric parallaxes or reliable distance estimates (errors <20%). For the M dwarfs, the situation is more clear. Recent results from the RECONS 10 pc census indicate a *minimum* M dwarf space density of 0.057 pc^{-3} (Henry et al. 2006)[6]. Cruz et al. (2007) find a space density of 4.9×10^{-3} pc^{-3} for M dwarfs later than M7V and a lower limit of 3.8×10^{-3} pc^{-3} for L dwarfs (§2.7, Figure 2.2). Assuming that field age ($\sim$1$-$5 Gyr) brown dwarfs with masses slightly below the hydrogen burning limit (0.075$-$0.055 $M_\odot$ are predominately mid to late L dwarfs (§4.3, Table 4.3), and that stars of spectral type M7V or later have masses $\lesssim$0.1 $M_\odot$ (Henry et al. 1999; Delfosse et al. 2000), the ratio of objects with masses above 0.1 M to $\sim$20% below the HBMM is 6.9. The shape of the M dwarf distribution in the RECONS 10 pc census corresponds broadly to the

[6]0.059 pc^{-3} for epoch 2012.0. See www.recons.org for the latest numbers and analysis. Comparison of the 10 pc sample with the 5 pc sample indicates that the 10 pc M dwarf sample is $\sim$70% complete. We note, however, that an analysis of the RECONS sensitivity limits indicates that the assumption of a representative M dwarf sample within 5 pc may be significantly biased by statistics of small numbers.

distribution of the NICMOS sample, (Figure 3.1), with the drop-off happening at around spectral type M6V, corresponding to $\sim$0.1 $M_{\odot}$. Even if the actual density for L dwarfs is a few times greater than the lower limit of Cruz et al. (2007), there is still a significant difference in the number of stars versus brown dwarfs. This analysis is in agreement with the recent WISE results, which estimate that the lower limit of the star to brown dwarf ratio in the solar neighborhood is six to one, and that in the final WISE count stars will still greatly outnumber brown dwarfs (Kirkpatrick et al. 2012).

4.6.2 Testing Formation Scenarios

What do these apparent discontinuities in the IMF and the CMF tell us about the validity of several proposed scenarios of VLM star and brown dwarf formation? We review the principal formation scenarios following the discussion in the review article of Luhman (2012), and then evaluate how well each of these scenarios explains the general properties of the IMF and the CMF noted above.

Core Fragmentation. In this scenario, collapsing gas in a molecular cloud forms denser cores that then fragment into multiple cores of different masses. Subsequent accretion is dominated by the more massive cores and the less massive cores eventually form brown dwarfs (Bonnell et al. 2008).

Core Ejection. Some protostellar objects are ejected from a star forming region via dynamical interactions with other objects or due to the natural velocity dispersion within a cluster. The ejection stops the accretion process (Reipurth & Clarke 2001).

Photoionization. Radiation from a nearby hot O or B star dissipates the inter-stellar medium in the vicinity of a low mass accreting core, thus halting the accretion process (Hester et al. 1996; Whitworth & Zinnecker 2004).

Disk Instability. In a manner similar to planet formation, localized instabilities in an accretion disk around a star cause some gas to collapse and form a proto-stellar core (e.g., Thies et al. 2010; Stamatellos et al. 2011)

In addition to these four processes, Bate (2011) notes that hydrodynamic cloud collapse simulations (Bate 2009, 2011) are in good agreement with the stellar IMF and stellar CMF, but overproduce the number of brown dwarfs unless radiative feedback is incorporated into the model (Bate 2011). The last model produces a cluster of stars and brown dwarfs whose statistical properties are very similar to those of observed young clusters, suggesting that radiative feedback is indeed an important mechanism in brown dwarf formation. A significant problem with this idea is the lack of a clear mechanism through which feedback is ignited only in stellar objects. At ages of a few Myr, the vast majority of an object's luminosity comes from the release of internal gravitational energy, so the onset of hydrogen burning would have a negligible effect on overall luminosity (Chabrier & Baraffe 1997). Also, while studies such as those by Jayawardhana et al. (2003), Bouy et al. (2008), and Comerón et al. (2010) show that there is some evidence for late accretion that is still happening at the time of hydrogen ignition around 3−5 Myr (Chabrier & Baraffe 1997), the bulk of accretion happens in the first million years, where stellar and substellar objects are virtually indistinguishable.

The relevant population properties for VLM stars and brown dwarfs described in §§4.6,

4.6.1, and Chapter 2 can be summarized as follows:

1. Stars significantly outnumber brown dwarfs.

2. There is evidence for a discontinuity in the IMF, CMF and other companion properties at masses close to the HBMM.

3. Stellar/substellar binaries are rare regardless of the characteristics of the more massive component.

4. Substellar binaries tend to have high mass ratios.

5. Wide separation substellar binaries are rare.

Core fragmentation has the potential of producing objects over a wide range of masses, both stellar and substellar. If accretion continues after the initial fragmentation and is then halted by radiative feedback, as proposed by Bate (2011), it could explain why there exist more stars than brown dwarfs. However, core fragmentation offers limited insights into the binary properties, with no apparent mechanism for favoring high mass ratio binaries and preventing the creation of stellar/substellar pairs. Disk instability is generally thought to produce lower mass companions in the planetary mass range. Because the matter available in an accretion disk is roughly proportional to the mass of the accreting star, brown dwarf formation through disk instability would imply that high mass stars are more likely to have brown dwarf companions. This assertion is refuted by the invariability of the brown dwarf desert argued in §4.4. Core ejection and photoionization are both mechanisms where brown dwarf formation is influenced primarily by environmental factors. This consideration

would explain why high mass ratio binaries are more common amongst brown dwarfs, as the mechanism halting accretion would have the same effect on both components of the binary. The potential for dynamical disruption during core ejection would also explain why close separation binaries with higher binding energies are more common. However, the ideas of core fragmentation and core ejection have problems of their own. There is no evidence for the spatial segregation of brown dwarfs that would happen as a consequence of core ejection. Luhman (2012) also note that the mass function of brown dwarfs in young clusters does not appear to be altered by the presence of hot O stars, thus providing evidence against the photoionization scenario.

The above discussion shows that while the binary properties of VLM stars and brown dwarfs may be explained by formation through core ejection or photoionization, a look at the broader implications of the proposed mechanisms of VLM star and brown dwarf formation still leads to largely inconclusive results. The results discussed in this chapter place constraints in the theory in the sense that any viable candidate theory of star and brown dwarf formation must now explain the existence of a brown dwarf desert that exists even at relatively high mass ratios in the case of M star primaries. However, substantial questions regarding formation still exist, and the available data are still not sufficient to clearly differentiate amongst the proposed models for brown dwarf and VLM star formation.

CHAPTER 5

The HLIMIT Survey − Overview and Observations

This chapter as well as Chapter 6 are based on "The Solar Neighborhood *XXXII*: The Hydrogen Burning Limit" (Dieterich et al. 2014).

5.1 Introduction

The first comprehensive stellar structure and evolution models for the low mass end of the main sequence were published in the late 20^{th} century (e.g., Burrows et al. 1993; Baraffe et al. 1995, §2.3). While the predictions of these models are widely accepted today, they remain largely unconstrained by observations. The problem is particularly noteworthy when it comes to the issue of distinguishing the smallest stars from the substellar brown dwarfs. While the internal physics of stars and brown dwarfs is different, their atmospheric properties overlap in the late M and early L spectral types, thus making them difficult to distinguish based on photometric and spectroscopic features alone. One test used to identify substellar objects − the lithium test (Rebolo et al. 1992)− relies on the fact that lithium undergoes nuclear burning at temperatures slightly lower than hydrogen, and therefore should be totally consumed in fully convective hydrogen burning objects at time scales much less than their evolutionary time scales. Detection of the LiI λ6708 line would therefore signal the substellar nature of an object. This is a powerful test, but it fails us when we most need it. While evolutionary models predict the minimal stellar mass to be anywhere from $0.07M_{\odot}$ to $0.08M_{\odot}$ (§6.7.3), the lithium test only works for masses $\lesssim 0.06M_{\odot}$ due to the lower mass at which core temperatures are sufficient to fuse lithium. Other tests are discussed in 5.1.1.

The models for low mass stars and brown dwarfs in current usage (Burrows et al. 1993, 1997; Baraffe et al. 1998; Chabrier et al. 2000; Baraffe et al. 2003) predict the end of the stellar main sequence at temperatures ranging from 1550−1750K, corresponding roughly to spectral type L4. These models have achieved varying degrees of success, but as we discuss in §6.7.3, are mutually inconsistent when it comes to determining the properties of the smallest possible star. The inconsistency is not surprising given that none of these decade-old evolutionary models incorporates the state-of-the-art in atmospheric models, nor do they account for the recent 22% downward revision in solar abundances (Caffau et al. 2011), which are in agreement with the results of solar astero-seismology[1].

Over the last ten years, few changes were made to evolutionary models for VLM stars and brown dwarfs in large part because the models provide predictions that are not directly observable. Whereas an atmospheric model can be fully tested against an observed spectrum, testing an evolutionary model requires accurate knowledge of mass, age, and metallicity as well as an accurate atmospheric model that serves as a boundary condition.

The problem of understanding the stellar/substellar boundary can essentially be formulated by posing two questions. The first one is: *"What do objects close to either side of the stellar/substellar boundary look like to an observer?"* The second question is: *"What are the masses and other structural parameters of objects on either side of the stellar/substellar boundary?"* While it is the second question that usually gets the most attention, we note that any attempt to determine masses at the stellar/substellar boundary assumes an inher-

[1]A review of the history of revisions to solar abundances, including issues related to solar astero-seismology, is given in Allard et al. (2013).

ently model dependent (and therefore possibly flawed) answer to the first question. What is needed is an observational test that relies as little on evolutionary models as possible. Prior to describing the methods used to attack the problem in this study, we describe several possible ways of addressing the first question with minimal reliance on modeling, and highlight each test's strengths and weaknesses.

5.1.1 Possible Tests for Detecting the Stellar/Substellar Boundary

Lithium. The Lithium test is the only practical test in current usage for detecting an object's stellar or substellar nature. As already stated, it relies on the fact that most brown dwarfs do not reach core temperatures high enough to burn lithium. The fully convective nature of VLM stars and brown dwarfs assures that any lithium in the photosphere is depleted at time scales much shorter than the evolutionary time scale. The test has the advantage of being easy to apply to individual objects through spectroscopic detection of the LiI λ6708 line. It has the major disadvantage that it does not work for brown dwarfs more massive than $\sim$0.06 $M_{\odot}$, which are capable of burning lithium. It is therefore not suitable for pinpointing the stellar/substellar boundary, which presumably lies between 0.07 and 0.08 $M_{\odot}$. The Li test also does not work well for young objects with ages $\lesssim$ 50 Myr because the LiI λ6708 line is gravity sensitive and becomes weaker at the lower gravities of younger objects (Kirkpatrick et al. 2006, 2008). It is also true that depending on the object's mass it may take up to several Myr for the supply of primordial Li to be depleted through nuclear burning; however, for brown dwarfs this time scale is shorter than the time scale for Li detectability due to surface gravity.

Dynamical Masses of Stellar/Substellar Binaries. Short period binaries offer the most powerful and accurate empirical way of measuring mass. This test relies on detecting a nearly equal mass binary in which the components lie on opposite sides of the stellar/substellar boundary. If the binary is old enough (few Gyr), then the substellar component will have cooled as a brown dwarf, and the small difference in mass between the pair will correspond to a large difference in luminosity. This test is simple in principle, but it presents several observational challenges. Due to the natural dispersion in the HBMM caused by different metallicities within the nearby stellar population, several binaries would need to be observed. The constraints on the HBMM would only be as good as the mass difference between the binary components, and finding a pair in which the components are indeed very close to the HBMM and yet on opposite sides of the boundary may prove difficult. Finally, it would be necessary to know the mass ratio of the binary pair. Determining the mass ratio can only be done through precise radial velocity measurements or in the case of astrometric binaries, in which the motion of the components is measured relative to the background of distant stars.

Breakdown of the Mass−Luminosity Relation. The MLR for stars is a mostly monotonic function where luminosity decreases as a function of decreasing mass. Assuming a large enough sample of VLM star and brown dwarf binaries with dynamical mass measurements, it is in principle possible to note where a monotonic function ends and where the Mass-Luminosity-Age Relation (MLAR) for brown dwarfs causes a broad distribution of masses to have the same luminosity. The problem with this method is that as of now

we simply do not have a large enough sample of binaries on which to carry it out. One would also need a manner to distinguish young brown dwarfs of late M and early L spectral type that overlap the latest main sequence stars. If luminosity and effective temperature are known, this distinction could be done on the basis of radius (§5.6).

Gap in the Luminosity Function. Because high mass brown dwarfs are constantly cooling, their luminosity is comparable to that of VLM stars for only a small fraction of their lives, whereas VLM stars retain their main sequence luminosity for a time longer than the current age of the Universe. The transient nature of high mass brown dwarfs then causes a dearth of objects at luminosities immediately fainter than the minimum stellar luminosity. The result is apparent in the theoretical LFs of Burgasser (2004) and Allen et al. (2005), where the relative paucity of early to mid L dwarfs is attributed to the onset of the brown dwarf cooling curve. From the predictions of those works, it is not clear if the gap would be well-defined enough to allow for a clear determination of the end of the main sequence. Rigorous application of this test requires a volume complete sample, but it has the advantage of not needing dynamical masses. This topic is further explored in §6.7.1.

The Radius Test. Because brown dwarfs are supported by electron degeneracy pressure, their *Radius-Mass Relation* (RMR) is different than that of stars. Whereas stars decrease in radius with decreasing mass, brown dwarfs show a slight increase in radius as mass decreases. As described in Chabrier & Baraffe (2000), the radius of field age brown dwarfs of all masses can be approximated by

$$R = R_0 m^{-1/8}$$

where all quantities are entered in solar units and $R_0 \sim 0.06 R_\odot$ for field aged objects. The resulting relation has a minimum radius for masses just below the HBMM (Chabrier et al. 2009; Burrows et al. 2011). The method has the advantage that while the exact value for the minimum radius is model dependent, the existence of a local minimum in the radius trend for the most massive brown dwarfs is a matter of basic physics and is universally accepted. The radius of an individual brown dwarf also decreases as the object ages, with the minimum value not attained until the brown dwarf is several billion years old and has entered the T dwarf luminosity regime. The result of the mass and age trends in brown dwarf radii means that any brown dwarf that still shines with luminosity comparable to that of VLM stars in the Galactic disk population will have a radius larger than that of the smallest stars. For a large enough sample of objects spanning the stellar/substellar boundary, the end of the stellar main sequence should be followed by a discontinuity in the luminosity-radius trend as older stars are followed by younger and less massive brown dwarfs. After the discontinuity, the slope of the relation should also change from positive to negative because less luminous objects tend to be less massive objects if one assumes a small age dispersion.

The radius test is the primary method used in this study to determine the properties of the stellar/substellar boundary. Determining an object's radius requires good knowledge of its Spectral Energy Distribution (SED), a trigonometric parallax, and an atmospheric model that is reliable enough to yield the object's effective temperature based on the morphology of its SED. In the remainder of this chapter we discuss the observations and analysis techniques used to obtain reliable measures of luminosity, temperature, and radius for a large sample

of objects. The analysis of the resulting radius trends is done in Chapter 6.

Table 5.3 at the end of this chapter lists the observed sample as well as all observed properties. Table 6.3 in Chapter 6 lists the derived properties. Both tables use the same scheme in listing an ID number for each object. These ID numbers are used as reference in several figures. Dieterich et al. (2014) contains a machine-readable table that has all columns of Tables 5.3 and 6.3 as well as 2MASS and WISE photometry.

5.2 The Observed Sample

The goal of the target selection was to obtain an observing list that samples the color continuum between spectral types M6V to L4, corresponding to $V - K$ ranging from 6.2 to 11.8, for the nearby Galactic disk population. Targets with known spectral types were selected from the literature, with at least eight targets in each spectral subclass, for a total of 82 targets. Because the differences between stellar and substellar objects become more pronounced at ages > 1 Gyr, we avoided objects with known youth signatures. All targets have original distance estimates within 25 pc, and are located south of declination $+30°$. This declination requirement makes all targets observable from CTIO. Of these 82 targets, 26 have previously established trigonometric parallaxes. The remaining 56 were placed on the CTIOPI parallax observing list. In this study we report new trigonometric parallaxes for 37 targets and new VRI photometry for all 63 targets that either have trigonometric parallaxes from the literature or have new trigonometric parallaxes reported here. Parallax observations for 19 targets are still ongoing and will be described in a future publication.

Figure 5.1 is a histogram showing the spectral type distribution of the observed sample for this study. There are more M dwarfs than L dwarfs in Figure 5.1 because more M dwarfs had trigonometric parallaxes from the literature. Once parallax observations for the 19 ongoing targets are finished the spectral type distribution will become nearly even.

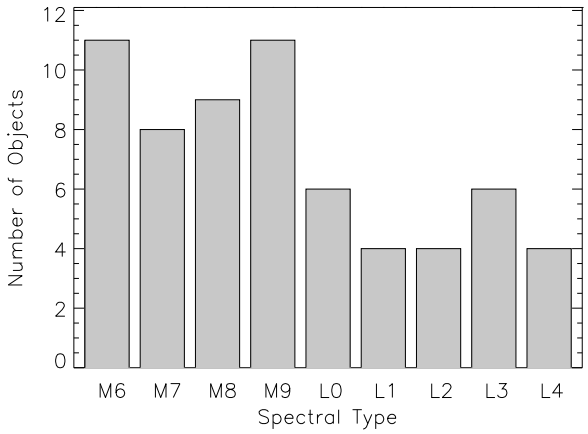

Figure 5.1 Spectral type distribution for the observed sample. M dwarfs are more heavily sampled because most M dwarfs already had trigonometric parallaxes at the beginning of the study. Several L dwarf parallax measurements are still in progress.

5.3 Photometric Observations

VLM stars and brown dwarfs have traditionally been studied in the near infrared where they emit most of their flux. However, as discussed in detail in §5.5, optical photometry is essential for determining the effective temperatures and the bolometric fluxes of these very red objects. We obtained VRI photometry for all targets in the sample using the CTIO 0.9m telescope for the brighter targets and the *SOAR Optical Imager* (SOI) camera on the Southern Astrophysics Research (*SOAR*) 4.1m telescope for fainter targets. SOAR observations were conducted between September 2009 and December 2010 during six observing

runs comprising NOAO programs 2009B-0425, 2010A-0185, and 2010B-0176. A total of 17 nights on SOAR were used for optical photometry. Table 5.3 indicates which telescope was used for each target. The division between the 0.9m telescope and SOAR fell roughly along the M/L divide. To ensure consistency, 28 targets were observed on both telescopes.

Essentially the same observing procedure was used for both photometry programs. After determining that a night was likely to be entirely cloudless in the late afternoon, three or four photometric standard fields were chosen and an observing schedule was constructed so that each field was observed at three different airmasses, typically around 2.0, 1.5, and the lowest possible airmass given the standard field's declination. We used the photometric standards compiled by Arlo Landolt (Landolt 1992, 2007, 2009) as well as standards from Bessel (1990) and Graham (1982). In each night, at least two standards were red standards with $V - I > 3.0$. Details of the transformation equations used to derive the nightly photometric solution from the observation of photometric standards are given in Jao et al. (2005).

When calibrating photometry, it is advisable that the range of colors of the photometric standards should be greater than the range of colors of the science targets. In other words, it is desirable to have photometric standards that are redder than the reddest science target and bluer than the bluest science target. The red end of this requirement creates problems for observing our sample because a list of red enough standards has not been compiled yet. The closest match are the unpublished RECONS very red standards used for photometry of late M dwarfs in the CTIOPI program. The standards were selected on the basis of their astrometric observations showing very little variability ($\lesssim$0.005 mag) over a period of several

years when compared to the field of background stars (§6.5). Currently these standard stars are GJ 1061 ($V - I = 3.63$), LHS 1723 ($V - I = 3.02$), GJ 406 ($V - I = 4.12$), GJ 644C ($V - I = 4.61$), SCR 1845-6357AB ($V - I = 4.94$), and GJ 876 ($V - I = 2.78$). When observing photometry, we picked the reddest possible star from this list depending on the time of the year. Even with these new standards, there is still a significant difference between the reddest standard and the $V - I \sim 6$ typical of an L4 dwarf. To test what effect the lack of redder standards had on the photometry of L dwarfs, we observed several objects more than once (Table 5.3) using different sets of standards of varying deficiency in their redness. The result was that these different epochs using different standards agreed to within the typical errors of our photometry. We therefore conclude that, while not optimal, observing L dwarfs with standards no redder than $V - K \sim 3$ produces acceptable results. We note that the photometric solution derived from the photometric standards is essentially a measurement of atmospheric extinction as a function of wavelength, and not as a function of color. In other words, the CCD detector cannot tell the difference between a photon that passes through the blue end of a given filter's range and a photon that passes through the red end of the same filter. In the same way, two photons of a particular wavelength obviously produce the same instrumental signature even if one comes from a very red object and the other comes from a very blue object. What does change is the degree of atmospheric extinction within different ends of the wavelength range of a given filter, and observing standards of colors similar to the science targets is meant to correct for that difference; one would like the shape of the SED of the standard and the science target to be similar *within the wavelength range*

of the filter in question. In this sense, it seems that the combination of SED slope within the wavelength range of the optical filters and the differential atmospheric extinction within those ranges were not sufficiently different from the $V - K \sim 3$ standards to the $V - I \sim 6$ science targets to cause appreciable problems.

After flat fielding, bias subtraction, and mosaic integration in the case of SOAR/SOI images, we performed aperture photometry using the *IRAF apphot* package. Landolt standards are reduced using an aperture $7''$ in radius. Ideally, we would perform aperture photometry on our targets using the same size aperture ($7''$) as Landolt used to compile the standards we are using, but the faintness of our targets required us to use a smaller aperture for two reasons. First, the depth of our exposures (as faint as $V \sim 24$ at SOAR and $V \sim 21$ at the CTIO 0.9m, see §6.1) means that the science target is often not more than $7''$ apart from another resolved source. Second, the signal-to-noise error associated with a photometric observation is a combination of the Poisson error and the sky subtraction error. The latter's contribution is proportional to the area of the photometric aperture and is particularly problematic in deep exposures where the sky annulus may contain diffuse background sources. It therefore makes sense to use a smaller aperture and apply an aperture correction based on the curve of growth of bright stars in the same exposure. We used a $3''$ aperture with an aperture correction to $7''$. The uncertainty associated with this aperture correction depends strongly on the seeing, but is typically on the order of 1% to 3%. The final photometric error is the sum in quadrature of the signal-to-noise error, the error due to the aperture correction, and the error from the nightly photometric solution, which is typically on the order of 1% to 2%.

Each photometric night had at least two targets in overlap with another night in order to check the validity of the the night's photometric solution. Optical variability is discussed in §6.5, where it is shown that the variability is usually less than the formal uncertainty in the photometry, thus justifying the use of only one epoch of photometry in cases where it was not possible to obtain a second epoch due to time constraints on SOAR.

Several different *UBVRI* photometric systems are in current usage. While the photometry taken on the CTIO 0.9m telescope used filters in the Johnson-Kron-Cousins system, data taken on SOAR used Bessell filters. Descriptions of both systems, as well as conversion relations, are given in Bessell (1995). The V filter is photometrically identical between both systems. The R and I filters have color dependent differences that reach a few percent in the color regime explored by Bessell (1995), which considered stars as red as $(V-R)=1.8$ and $(V-I)=4.0$. The targets in this study are significantly redder, with $(V-I)$ as red as 5.7. In §6.1 we derive new relations relevant to the very red regime considered in this study. The values listed in Table 5.3 are on the system used on each telescope.

5.4 Astrometric Observations

The *Cerro Tololo Inter-American Observatory Parallax Investigation* (CTIOPI); (Jao et al. 2005; Henry et al. 2006) is a large and versatile astrometric monitoring program targeting diverse types of stellar and substellar objects in the solar neighborhood. Observations are taken using the CTIO 0.9m telescope and its sole instrument, a 2048×2048 Tektronix imaging CCD detector with a plate scale of $0.401''$ pixel^{-1}. We use the central quarter of the CCD

chip, yielding a $6.8' \times 6.8'$ field of view. Details of the observing procedures and data reduction pipeline are given in Jao et al. (2005). A brief description of the aspects most relevant for the observation of very red and faint targets is given here.

Each target was typically observed for five "evening" epochs (i.e., before the midpoint of a given night) and five "morning" epochs over the course of at least two years. Observations were typically taken in sets of three consecutive 600 s exposures always within ± 60 minutes of target transiting the meridian, and in most cases within ± 30 minutes of meridian transit. This restriction in hour angle means that the target is always observed very close to its lowest possible airmass, which minimizes the effects of differential atmospheric refraction. All but one target were observed in the I band, where their optical spectrum is the brightest and also where atmospheric refraction is minimized. The sole exception is GJ 1001 A-BC, for which the parallax of the A component was measured in the R band to avoid saturation on the CCD. The long exposures caused the fields to be rich with background stars, which greatly facilitated the selection of parallax reference stars. In most cases we were able to setup the parallax field with the ideal configuration of $\sim$10 reference stars symmetrically distributed around the science target. Care was taken to position the reference fields using the same pixel coordinates for all epochs. Our experience shows that this consistency of positioning the reference fields helps reduce the final parallax error faster, but is not absolutely required. There have been instances when a mis-aligned epoch was added to the parallax reduction, and having an additional epoch, although not perfectly positioned, still reduced the parallax error. Such instances were considered on an individual basis.

VRI photometry (§5.3) of the reference field was used to transform the relative parallaxes into absolute parallaxes using photometric distance relations. This transformation accounts for the fact that the parallax reference stars are not located at infinite distances and therefore have a finite, albeit much smaller, parallax. Any original reference star later found to be closer than 100 pc was discarded. The *VRI* photometry of the reference field and the science star was also used to correct for small shifts in the apparent positions of the stars due to atmospheric differential color refraction.

5.5 Methodology for Calculating Effective Temperature

The following two sections describe the methodology for determining effective temperature and luminosity using computer procedures written in IDL. All IDL codes are included in the appendix of this dissertation.

Determining the effective temperatures ($T_{\rm eff}$)[2] of M and L dwarfs has traditionally been difficult due to the complex nature of radiative transfer in cool stellar atmospheres. The task is particularly challenging in the L dwarf regime, where inter-phase chemistry between solid grains and the same substances in the gas phase becomes relevant. Significant progress has occurred recently with the publication of the *BT-Settl* family of model atmospheres (Allard et al. 2012, 2013). The *BT-Settl* models are the first to include a comprehensive cloud model based on non-equilibrium chemistry between grains and the gas phase and the

[2]The *effective temperature* ($T_{\rm eff}$) of a surface is *defined* as the temperature at which a perfect blackbody would emit the same flux (energy per time per area) as the surface in question according to the Stephan-Boltzmann law: $F = \sigma_{SB} T^4$. This quantity often differs from the stellar atmosphere's actual temperature, which is a function of optical depth as well as other factors.

rate of gravitational settling of solid grains. They have also been computed using the latest revised solar metallicities (Caffau et al. 2011). The authors (e.g., Allard et al. 2012) have demonstrated unprecedented agreement between observed M and L spectra and the *BT-Settl* model atmospheres.

We determined $T_{\rm eff}$ for each object in our sample by comparing observed photometric colors to synthetic colors derived from the *BT-Settl* model grid using custom made IDL procedures [3]. Our procedure exploits the fact that synthetic colors can be computed from synthetic spectra and those colors can then be directly compared to observed colors. How well the synthetic colors match the observed colors is then a measure of how well the input properties of a given synthetic spectrum ($T_{\rm eff}$, log g, and $[M/H]$) match the real properties of the object in question. The best matching $T_{\rm eff}$ can then be found by interpolating $T_{\rm eff}$ as a function of the residuals of the color comparison (observed color − synthetic color) to the point of zero residual. The technique can be applied independently to each available photometric color, and the standard deviation of the resulting ensemble of $T_{\rm eff}$ values is the measure of the uncertainty in $T_{\rm eff}$.

In our implementation of this technique, we combined our *VRI* photometry (Bessel system) with *2MASS JHK*$_s$ (Skrutskie et al. 2006) and *WISE W1*, *W2*, and *W3* photometry (Wright et al. 2010) to derive a total of 36 different colors for each object covering the spectral range from $\sim$0.4μm to $\sim$16.7μm[4]. We then calculated the same 36 colors for each

[3] A thorough review of photometric quantities, terminology, and procedures for deriving synthetic colors is given in the appendix of Bessell & Murphy (2012).

[4] We did not use the *WISE W4* band centered at $\sim$22μm because it produces mostly null detections and upper limits for late M and L dwarfs.

spectrum in the *BT-Settl* model grid using the photometric properties for each band listed in Table 5.1.

Table 5.1: Photometric Properties of Individual Bands

Band	Blue Limit [a] μm	Red Limit [a] μm	Effective Isophotal λ μm	Mag. Zero Point $photon\ s^{-1}\ cm^{-2}$	Reference
V	0.485	0.635	0.545	1.0146×10^{11}	Bessell & Murphy (2012)
R	0.554	0.806	0.643	7.1558×10^{10}	Bessell & Murphy (2012)
I	0.710	0.898	0.794	4.7172×10^{10}	Bessell & Murphy (2012)
J	1.102	1.352	1.235	1.9548×10^{10}	Cohen et al. (2003)
H	1.494	1.804	1.662	9.4186×10^{9}	Cohen et al. (2003)
K_s	1.977	2.327	2.159	4.6692×10^{9}	Cohen et al. (2003)
W1	2.792	3.823	3.353	1.4000×10^{9}	Jarrett et al. (2011)
W2	4.037	5.270	4.603	5.6557×10^{8}	Jarrett et al. (2011)
W3	7.540	16.749	11.560	3.8273×10^{7}	Jarrett et al. (2011)

For each color, we then tabulated the residuals of (observed color − synthetic color) as a function of the synthetic spectrum's temperature. The residuals are negative if the synthetic spectrum's temperature is too cold, approach zero for spectra with the right temperature, and are positive for models hotter than the science object. For each color, we then interpolated the residuals as a function of temperature to the point of zero residual. The temperature value of this point was taken as the object's effective temperature according to the color in question. We then repeated the procedure for all 36 color combinations, thus providing 36 independent determinations of $T_{\rm eff}$. The adopted $T_{\rm eff}$ for each object is the mean of the $T_{\rm eff}$ values from each color. The uncertainty in $T_{\rm eff}$ is the standard deviation of the values used to compute the mean. After performing this procedure we noted that the majority of colors produced $T_{\rm eff}$ results that converged in a Gaussian fashion about a central value, while other colors produced outliers that were a few hundred Kelvin away from the Gaussian peak.

[a] 10% transmission normalized to band's peak transmission

Further inspection showed that colors for which the bluest band was an optical band (*VRI*) were producing the convergent results while colors in which both bands were infrared bands tended to produce erratic values with no apparent systemic trend. We therefore performed the calculations a second time using only the colors that had the *VRI* bands as the bluest band and excluding $I - J$, which also did not converge well, for a total of twenty colors. Occasionally, a color combination still produced an outlier at $T_{\rm eff} >> 2\sigma$ from the adopted value. These outliers were excluded as well; however, the majority of objects had their effective temperatures computed using all twenty colors. The fact that none of the colors composed of infrared bands alone had good convergence emphasizes the need to include optical photometry when studying VLM stars and brown dwarfs. Most likely, the reason for the non-convergence of colors that do not involve an optical band is due to the smaller effect that temperature has on the relative flux between two bands when both bands are close to the SED's peak flux. Examination of color-magnitude diagrams with the $I - J$ color also showed a degenerate sequence where the same colors corresponds to a wide range of absolute magnitudes.

Figure 5.2 shows the graphical output of the procedure for determining $T_{\rm eff}$ for the case of DENIS J0751-2530 (L2.5, ID #21). The families of vertically oriented small dots represent the residuals for the color matches between the synthetic spectra and the actual observed colors. Each vertical grouping of small dots corresponds to a synthetic spectrum with $T_{\rm eff}$ given in the horizontal axis and contains one dot for each color comparison. As temperature approaches the actual effective temperature of DENIS J0751-2530 the residuals become

smaller and less dispersed. If the models were a perfect representation of the SED of DENIS J0751-2530 all colors would converge to a single point when interpolated to zero residual. Because the models and the procedure are not perfect, each color interpolates to a different temperature at the point of zero color residual. The mean and the standard deviation of the $T_{\rm eff}$ spread from interpolating the several colors to the point of zero residual is taken as the effective temperature and its uncertainty. The short vertical lines represent the mean value before (dashed lines) and after (dot-dashed lines) the exclusion of $R - J$. The long dashed lines represent the 1σ uncertainty.

The model grid we used was a 3-dimensional grid with a $T_{\rm eff}$ range from 1300K to 4500K in steps of 100K, log g range from 3.0 to 5.5 in steps of 0.5 dex, and metallicity, $[M/H]$, range of -2.0 to 0.5 in steps of 0.5 dex. The procedure was repeated for each different combination of log g and $[M/H]$. The final adopted $T_{\rm eff}$ was the one from the combination of gravity and metallicity that yielded the lowest $T_{\rm eff}$ dispersion amongst the colors. As expected for VLM stars and brown dwarfs in the solar neighborhood, the vast majority of objects had their best fit effective temperatures at log $g = 5.0$ and $[M/H] = 0.0$. The color$-T_{\rm eff}$ interpolations often did not converge for grid points where log g or $[M/H]$ was more than 1.0 dex away from the final adopted value.

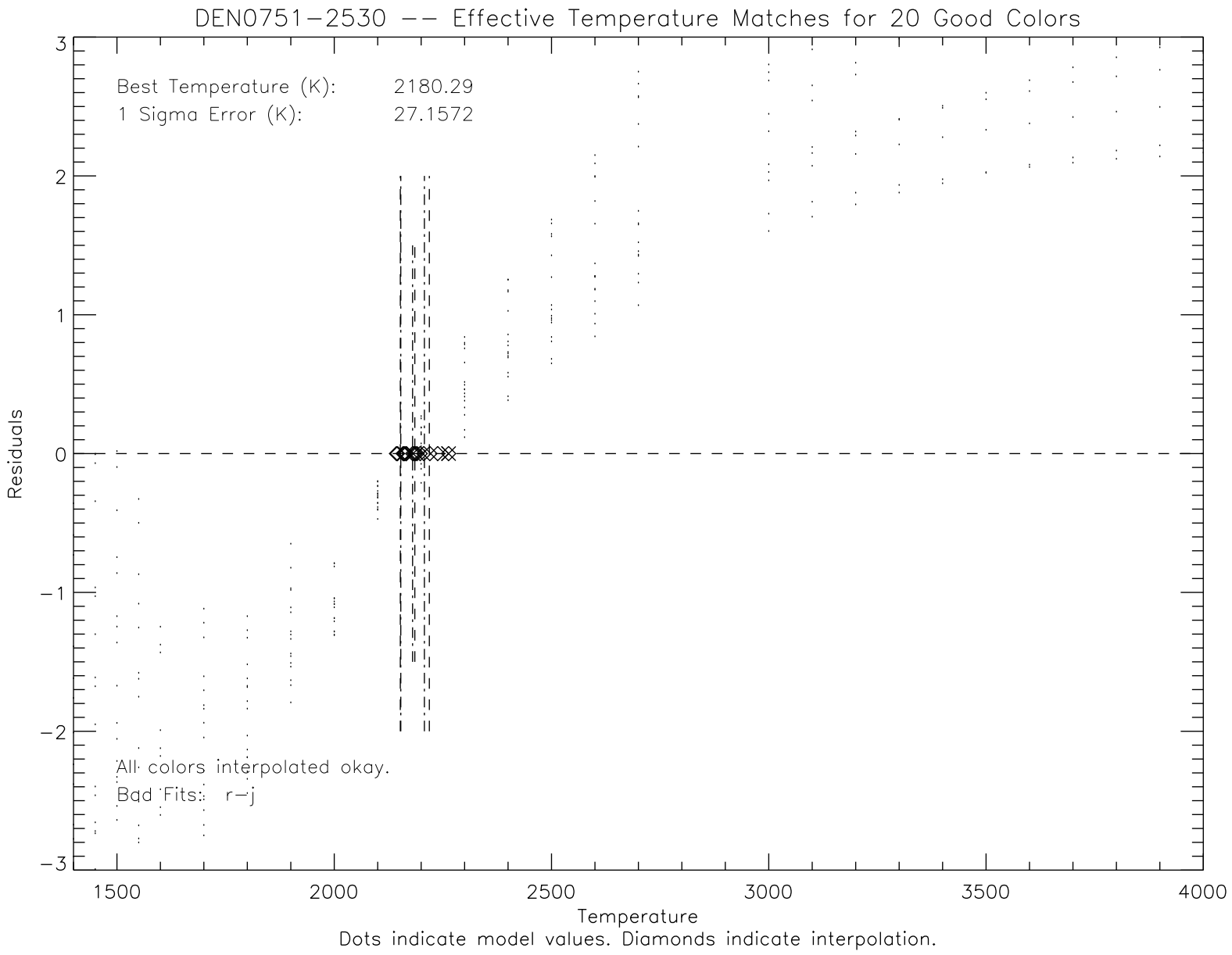

Figure 5.2 Effective temperature calculation for the L2.5 dwarf DENIS J0751-2530. The small dots represent the residuals of the color comparisons based on synthetic spectra at different temperatures. Interpolation to the points of zero residual yield the effective temperature. The long vertical lines denote the 1σ dispersion before and after the exclusion of outliers. See text for discussion.

5.6 Methodology for Calculating Luminosity and Radius

The IDL procedure for determining effective temperatures also indicates which model spectrum in the *BT-Settl* grid provides the overall best fit to the observed photometry. We used the indicated best fit spectrum as a template for an object's SED in order to calculate an object's luminosity. Because the model spectra are spaced in a discrete grid, and because no model spectrum can be expected to provide a perfect match to observations, significant differences may still remain between the best fit synthetic spectrum and the real SED. We devised an iterative procedure that applies small modifications to the chosen SED template in order to provide a better match to the photometry. We first calculated synthetic photometry from the SED template for all nine bands listed in Table 5.1 using a procedure identical to the one used for calculating synthetic colors for the purpose of $T_{\rm eff}$ determination. We then did a band by band comparison of the synthetic photometry to the observed photometry and computed a corrective flux factor by dividing the flux corresponding to the observed photometry by the synthetic flux. Next, we paired the corrective flux factors to the corresponding isophotal effective wavelength for each band and fit those values to a 9^{th} order polynomial using the IDL function *poly_fit*, thus creating a continuous corrective function with the same wavelength coverage as the SED template. While it may seem unusual to fit nine bands of photometry to a 9^{th} order polynomial, we note that the purpose of the fit is not to follow the general trend in the data, but rather to provide corrections to each individual band while still preserving the continuity of the SED. It therefore makes sense to use a function with the same order as the number of data points. To facilitate computations, *poly_fit* was run on a

logarithmic wavelength scale that was then transformed back to a linear scale. The original SED template was then multiplied by the corrective function and the process was iterated until residuals for all bands fell below 2%. Because the *W3* band is much broader than the other bands, two additional points were used to compute the corrective function at the blue and red ends of the band as well as at the isophotal wavelength. Figure 5.3 describes the process graphically. The first iteration typically produced mean color shifts of 0.1 to 0.25 magnitudes, depending on how well the real SED of a given object matched the closest point in the spectral template grid.

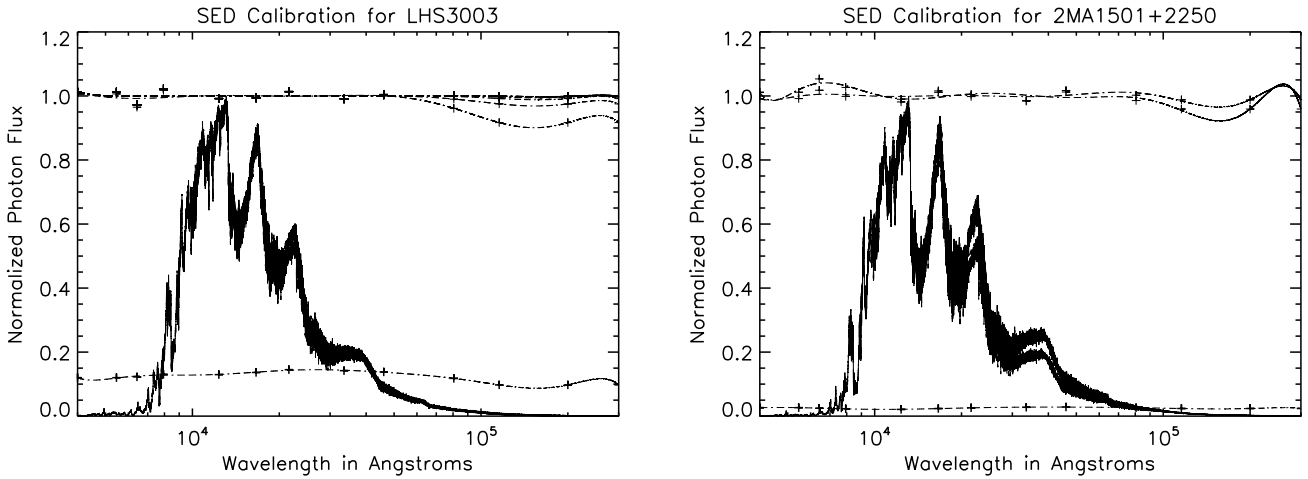

(a) (b)

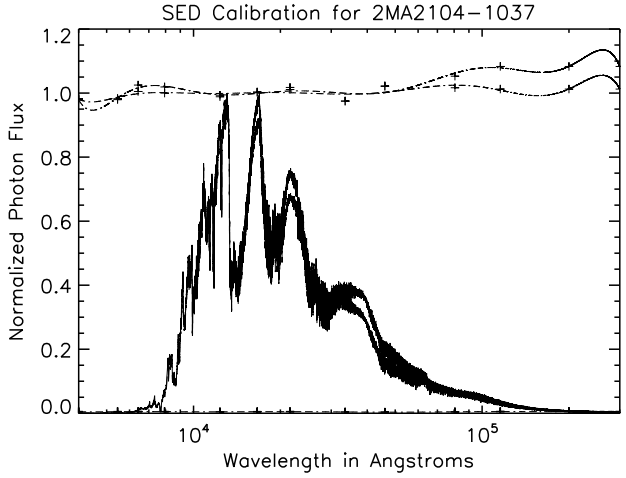

(c)

Figure 5.3 SED calibrations for (a) LHS 3003 (M7V), (b) 2MASS J1501+2250 (M9V) and (c) 2MASS J2104-1037 (L3). The corrective polynomial functions are shown by dashed lines and are fits to the corrective factors shown by plus signs. In the first two cases the polynomial generated in the first iteration stands out at the bottom of the graph due to the flux mismatch caused by the distance difference between the object's real distance and the distance at which the SED template was calculated. The first iteration is too close to the wavelength axis to be noticeable in (c). The following iterations then produce corrective functions that differ only slightly from a flat 1.0 function and perform a "fine tuning" of the modifications caused by the first iteration. Both the original SED template and the final fit are plotted normalized to 1 at their maximum values. In the cases of 2MASS J1501+2250 and 2MASS J2104-1037 the end result is an SED slightly redder than the template. The template used for LHS 3003 was a very good fit and the resulting SED almost entirely overlaps the initial template. Table 5.2 lists the cumulative correction factors applied to each band for the three objects in this figure.

Table 5.2: Corrective Factors for SEDs in Figure 5.3[a]

Object	Iterations	*V*	*R*	*I*	*J*	*H*	K_s	*W1*	*W2*	*W3*
LHS 3003	22	0.865	0.917	0.927	0.952	1.000	1.044	1.042	1.002	0.711
2MASS J1501+2250	3	1.144	1.037	0.986	0.911	1.000	1.113	1.203	1.201	1.032
2MASS J2104-1037	3	1.031	1.066	1.028	0.931	1.000	1.033	0.842	0.724	1.075

The *BT-Settl* models are published with flux units as they appear at the stellar surface. These are very high fluxes when compared to observed fluxes on Earth. To facilitate computations the model spectra were first normalized to a value that is comparable in magnitude to the observed photometric fluxes that are used to calibrate the spectrum. Given the range of magnitudes of the observed objects, we found that normalizing the model spectra so that their bolometric flux is 10^{-10}erg s^{-1} cm^{-2} works well. The first iteration corrected for the bulk of the flux mismatch between the real target and this arbitrary normalization, thus causing a much larger correction than the subsequent iterations. The number of iterations necessary for conversion varied greatly, ranging anywhere from three to twenty or more. Table 5.2 shows the overall corrective factor for each band for the three examples shown in Figure 5.3, as well as the number of iterations that were necessary. The flux factors in Table 5.2 were normalized to 1.000 at the *H* band for ease of comparison. To check that the corrective polynomial approach was producing consistent results, we computed the luminosities for the objects listed in Table 5.2 using 9^{th} order polynomials as well as 8^{th} order polynomials. The results of dividing the luminosity obtained using the 8^{th} order polynomials by that obtained using 9^{th} order polynomials were 1.00052, 1.00077, and 0.99451 respectively for LHS

[a]All values are normalized to 1.000 in the *H* band.

3003, 2MASS J1501+2250, and 2MASS J2104-1037. The uncertainties associated with the adopted 9^{th} order solution are 3.08%, 1.91%, and 6.97% respectively for LHS 3003, 2MASS J1501+2250, and 2MASS J2104-1037. This test shows that so long as the polynomials used are of high enough order, varying the order of the corrective polynomial causes changes to the resulting luminosities that are well within the formal uncertainties.

The uncertainty in the final flux under the SED was calculated as follows and combined the uncertainty associated with the photometry used to calibrate the SED to the uncertainty generated by the SED calibrating procedure. The SED was divided into nine wavelength ranges corresponding to each of the nine photometric bands. After the iterative process was complete, the flux under eache SED region was multiplied by the fractional uncertainty of the photometry in the corresponding band. The results of this calculation were then summed so that the uncertainty contributed by the photometric uncertainty in each band was proportional to the fractional flux covered by that band. To account for the uncertainty in the SED calibrating procedure, the flux corresponding to each band was multiplied by the factional residual of the final SED fit to that band. This fractional residual is the difference between the observed photometry and the synthetic photometry from the final SED fit. Because we required the polynomial corrective process to iterate until this number fell below 2% for all bands, the uncertainty associated with the fitting process is never more than 2% of the total flux of the SED. The uncertainties due to photometry and due to the residuals in the SED fit were then summed in quadrature to provide the final uncertainty. Due to the fact that most of the SED's flux is in the near infrared for the objects in question, the

photometric uncertainty was dominated by the 2MASS uncertainties in J, H, and K_s. The fit uncertainty's final contribution was often small compared to the photometric uncertainty because the worst fits (i.e., the 2% maximum limit) tended to occur either in the optical bands or in the WISE bands, were the fractional flux is small. Because of that, the final uncertainty was still dominated by the 2MASS photometric uncertainty and was on the order of 3−4%.

Finally, the total flux was divided by the fraction of a blackbody's total flux covered by the SED template given the effective temperature of the object in question. This correction accounted for the finite wavelength range of the SED and was typically on the order of 1.5%.

Once the effective temperatures and the bolometric luminosity were determined by the procedures described above, determining the radii of stars or brown dwarfs with a known trigonometric parallax followed easily from the Stephan-Boltzmann law:

$$L = 4\pi R^2 \sigma_{SB} T_{\rm eff}^4$$

where L is the object's luminosity, R is its radius, $\sigma_{SB} = 5.6704 \times 10^{-5}$ erg cm^{-2} s^{-1} K^{-4} is the Stephan-Boltzmann constant, and $T_{\rm eff}$ is the effective temperature.

In order to check the accuracy of the procedures for determining effective temperatures and luminosities, the methodology was applied to seven early to mid M dwarfs that have direct model-independent radius measurements obtained using Georgia State University's *CHARA* Array Long Baseline Optical Interferometer (Boyajian et al. 2012). Figure 5.4 shows the comparison. The mean absolute residual is 3.4% and in all cases the radius we

derive agrees to the interferometric radii within the formal 1σ uncertainties calculated by our methodology. While it is currently difficult to directly measure the angular diameters of late M and L dwarfs using interferometry, the good agreement we obtain when comparing the results of the SED fitting procedure to direct radius measurements for hotter M dwarfs serves as a check on the technique. While direct radius measurements exist for several eclipsing binaries, the individual components of these systems lack the photometric coverage needed for applying our method and therefore cannot be used as checks. In Figure 5.5 we compare our effective temperatures used to derive the radii of Figure 5.4 to effective temperatures obtained by Boyajian et al. (2012). This comparison serves mostly as a check on the methodology of Boyajian et al. (2012) for obtaining effective temperatures, as their effective temperatures are computed from model atmospheres based on the radii measured with interferometry. Because our method uses effective temperatures to compute radii, the radius check of Figure 5.4 is an implicit check of our effective temperatures.

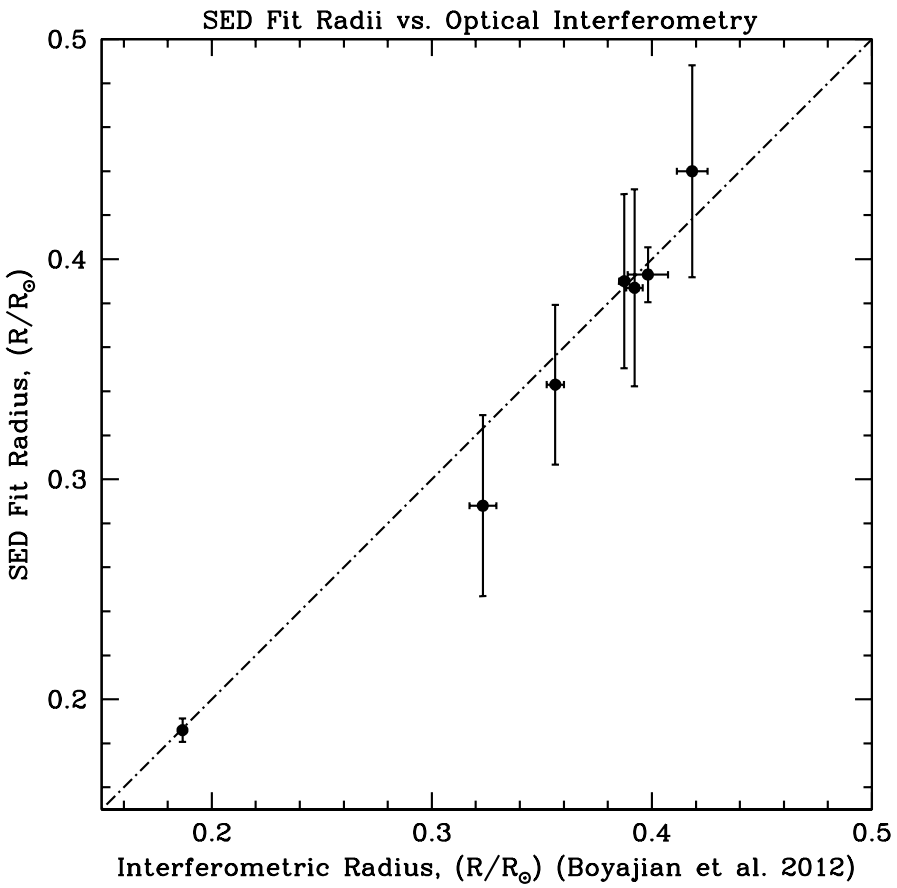

Figure 5.4 Comparison of M dwarf radii obtained via the SED fitting technique to values based on direct angular diameter measurements obtained with Georgia State University's *CHARA* Array Optical Interferometer (Boyajian et al. 2012). From smallest to largest, the points correspond to: Barnard's Star (M4.0V), GJ 725B (M3.5V), GJ 725A (M3.0V), GJ 15A (M1.5V), GJ 411 (M2.0V), GJ 412A (M1.0V), and GJ 687 (M3.0V). The percent residuals in the sense (SED fit − CHARA) are: -0.3%, -10.9%, -3.6%, 0.8%, -1.3%, -1.3%, and 5.3%, respectively. The mean absolute residual is 3.4%. In all cases the radius we derive agrees to the interferometric radii within the formal 1σ uncertainties calculated by our methodology.

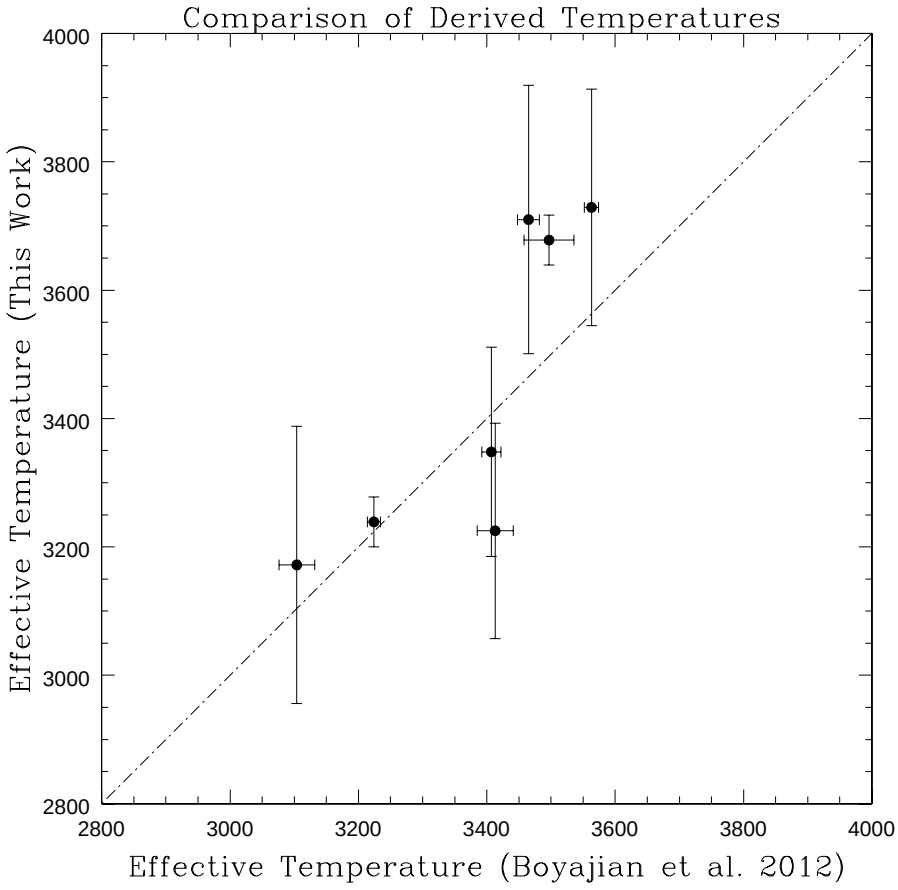

Figure 5.5 Comparison of the derived effective temperatures for the M dwarfs used for radius comparison between interferometry (Boyajian et al. 2012) and this work. In both cases, the effective temperature is derived from atmospheric models. Whereas our work uses a calculated effective temperature to derive radius, Boyajian et al. (2012) use a directly observed radius to derive effective temperature. The radius check of 5.4 can therefore also be seen as a check on our effective temperatures.

Table 5.3: Observed Properties

ID	R. A. 2000	Dec 2000	Name	Spct Type	ref.[a,b]	μ $''$/yr	P.A. deg	Parallax mas	ref.[b]	Distance pc	V_{tan} Km/s	V	R	I	Tel.[c]	VRI Epochs	Notes
1	00:04:34.9	−40:44:06	GJ 1001BC	L4.5	14	1.643	156.0	77.02±2.07	1	$13.15^{+0.36}_{-0.34}$	102.4	22.77±.025	19.24±.045	16.76±.012	S	2	d,e,f
2	00:21:05.8	−42:44:49	LEHPM1-0494B	M9.5	9	0.253	089.1	39.77±2.10	1	$25.14^{+1.40}_{-1.26}$	30.1	21.61±.085	19.08±.010	16.69±.001	S	2	d,e
3	00:21:10.7	−42:45:40	LEHPM1-0494A	M6.0	24	0.253	086.5	37.20±1.99	1	$26.88^{+1.51}_{-1.36}$	32.2	17.28±.045	15.67±.005	13.84±.005	S	2	d,e
4	00:24:24.6	−01:58:20	BRI B0021-0214	M9.5	20	0.155	328.8	86.60±4.00	3	$11.54^{+0.55}_{-0.50}$	8.4	20.01±.051	17.45±.016	15.00±.025	S	1	···
5	00:36:16.0	+18:21:10	2MASS J0036+1821	L3.5	10	0.907	082.4	114.20±0.80	11	$8.75^{+0.06}_{-0.06}$	37.6	21.43±.024	18.32±.016	15.92±.022	S	1	···
6	00:52:54.7	−27:06:00	RG 0050-2722	M9.0	18	0.098	026.0	41.00±4.00	4	$24.39^{+2.63}_{-2.16}$	11.3	21.54±.051	19.14±.017	16.57±.026	S	1	···
7	01:02:51.2	−37:37:44	LHS 132	M8.0	22	1.479	079.8	81.95±2.73	17	$12.20^{+0.42}_{-0.39}$	85.5	18.53±.021	16.30±.008	13.88±.012	C	3	···
8	02:48:41.0	−16:51:22	LP 771-021	M8.0	15	0.274	175.7	61.60±5.40	5	$16.23^{+1.55}_{-1.30}$	21.0	19.97±.050	17.70±.015	15.27±.015	S	2	···
9	02:53:00.5	+16:52:58	SO0253+1652	M6.5	21	5.050	137.9	259.41±0.89	21,30	$3.85^{+0.01}_{-0.01}$	92.2	15.14±.006	13.03±.004	10.65±.003	C	3	···
10	03:06:11.5	−36:47:53	DENIS J0306-3647	M8.5	18	0.690	196.0	76.46±1.42	1	$13.07^{+0.24}_{-0.23}$	42.7	19.38±.002	16.98±.023	14.49±.009	C	2	···
11	03:39:35.2	−35:25:44	LP 944-020	M9.0	7	0.408	048.5	155.89±1.03	1	$6.41^{+0.04}_{-0.04}$	12.4	18.70±.026	16.39±.007	14.01±.011	C	3	···
12	03:51:00.0	−00:52:45	LHS 1604	M7.5	15	0.526	176.0	68.10±1.80	4	$14.68^{+0.39}_{-0.37}$	36.6	18.11±.053	16.08±.020	13.80±.017	C	2	d
13	04:28:50.9	−22:53:22	2MASS J0428-2253	L0.5	16	0.189	038.1	38.48±1.85	1	$25.98^{+1.31}_{-1.19}$	23.2	21.68±.050	19.18±.025	16.79±.017	S	2	···
14	04:35:16.1	−16:06:57	LP 775-031	M7.0	25	0.356	028.0	95.35±1.06	1	$10.48^{+0.11}_{-0.11}$	17.6	17.67±.005	15.49±.029	13.08±.030	C	2	···
15	04:51:00.9	−34:02:15	2MASS J0451-3402	L0.5	15	0.158	036.5	47.46±1.51	1	$21.07^{+0.69}_{-0.64}$	15.7	22.11±.052	19.38±.015	16.84±.024	S	1	d
16	05:00:21.0	+03:30:50	2MASS J0500+0330	L4.0	29	0.350	177.9	73.85±1.98	1	$13.54^{+0.37}_{-0.35}$	22.4	23.01±.037	19.77±.026	17.32±.032	S	1	···
17	05:23:38.2	−14:03:02	2MASS J0523-1403	L2.5	15	0.195	032.5	80.95±1.76	1	$12.35^{+0.27}_{-0.26}$	11.4	21.05±.112	18.71±.021	16.52±.012	C	2	d
18	06:52:19.7	−25:34:50	DENIS J0652-2534	L0.0	28	0.250	289.3	63.76±0.94	1	$15.68^{+0.23}_{-0.22}$	18.5	20.77±.050	18.38±.005	15.85±.016	S	2	···
19	07:07:53.3	−49:00:50	ESO 207-61	M8.0	31	0.405	005.0	60.93±3.02	4	$16.41^{+0.85}_{-0.77}$	31.5	21.09±.035	18.74±.023	16.19±.032	S	1	···
20	07:46:42.5	+20:00:32	2MASS J0746+2000AB	L0.0J	33	0.377	261.9	81.84±0.30	11,34,35	$12.21^{+0.04}_{-0.04}$	21.8	20.05±.038	17.42±.037	14.90±.038	S	1	f
21	07:51:16.4	−25:30:43	DENIS J0751-2530	L2.5	28	0.889	279.2	59.15±0.84	1	$16.90^{+0.24}_{-0.23}$	71.2	21.66±.045	18.86±.020	16.39±.005	S	2	···
22	08:12:31.7	−24:44:42	DENIS J0812-2444	L1.5	28	0.196	135.5	45.47±0.96	1	$21.99^{+0.47}_{-0.45}$	20.4	21.89±.053	19.45±.016	17.05±.025	S	1	···
23	08:28:34.1	−13:09:19	SSSPM J0829-1309	L1.0	28	0.578	273.0	87.96±0.78	1	$11.36^{+0.10}_{-0.09}$	31.1	21.19±.023	18.41±.025	16.01±.026	S	1	d
24	08:29:49.3	+26:46:33	GJ 1111	M6.5	31	1.290	242.2	275.80±3.00	4	$3.62^{+0.03}_{-0.03}$	22.1	14.94±.033	12.88±.005	10.58±.018	C	2	···
25	08:40:29.7	+18:24:09	GJ 316.1	M6.0	32	0.908	240.0	71.10±1.00	4	$14.06^{+0.20}_{-0.19}$	60.5	17.67±.042	15.72±.017	13.44±.006	C	2	···
26	08:47:28.7	−15:32:37	2MASS J0847-1532	L2.0	15	0.240	146.1	58.96±0.99	1	$16.96^{+0.28}_{-0.28}$	19.2	21.93±.068	19.16±.028	16.86±.024	C	2	···
27	08:53:36.0	−03:29:28	LHS 2065	M9.0	31	0.550	249.4	117.98±0.76	1	$8.47^{+0.05}_{-0.05}$	22.0	18.94±.032	16.74±.015	14.44±.029	C	3	···
28	09:00:23.6	+21:50:04	LHS 2090	M6.0	21	0.774	221.2	156.87±2.67	21	$6.37^{+0.11}_{-0.10}$	23.3	16.11±.032	14.12±.020	11.84±.010	C	3	···
29	09:49:22.2	+08:06:45	LHS 2195	M8.0	6	0.887	177.4	60.32±1.67	1	$16.57^{+0.47}_{-0.44}$	69.7	19.76±.152	17.66±.035	15.20±.036	C	1	···
30	10:48:12.8	−11:20:11	LHS 292	M6.0	31	1.645	158.0	220.30±3.60	4	$4.53^{+0.07}_{-0.07}$	35.3	15.78±.057	13.63±.002	11.25±.025	C	3	···
31	10:49:03.4	+05:02:23	LHS 2314	M6.0	2	0.624	217.0	41.10±2.30	4	$24.33^{+1.44}_{-1.28}$	71.9	19.14±.033	17.13±.033	14.91±.025	C	2	···
32	10:56:29.2	+07:00:53	GJ 406	M6.0	31	4.696	235.0	419.10±2.10	4	$2.38^{+0.01}_{-0.01}$	53.1	13.58±.008	11.64±.028	9.44±.014	C	2	···
33	10:58:47.9	−15:48:17	DENIS J1058-1548	L3.0	12	0.290	288.1	57.70±1.00	11,34,35	$17.33^{+0.30}_{-0.29}$	23.8	23.01±.005	20.01±.045	17.66±.027	S	2	···
34	11:06:18.9	+04:28:32	LHS 2351	M7.0	···	0.460	129.1	48.1±3.1	5	$20.79^{+1.43}_{-1.25}$	45.3	19.49±.049	17.27±.017	14.87±.017	C	2	···
35	11:21:49.0	−13:13:08	LHS 2397aAB	M8.5J	8	0.507	264.7	65.83±2.02	1	$15.19^{+0.48}_{-0.45}$	36.5	19.43±.036	17.33±.048	14.84±.040	S	1	d,f
36	11:26:39.9	−50:03:55	2MASS J1126-5003	L4.5	27	1.646	286.2	59.38±1.64	1	$16.84^{+0.47}_{-0.45}$	131.3	23.75±.010	20.11±.020	17.51±.005	S	2	···
37	11:53:52.7	+06:59:56	LHS 2471	M6.5	···	0.955	160.0	70.30±2.60	4	$14.22^{+0.54}_{-0.50}$	64.3	18.10±.009	16.02±.035	13.77±.005	C	2	···
38	11:55:42.9	−22:24:58	LP 851-346	M7.5	18	0.409	244.0	89.54±1.77	1	$11.16^{+0.22}_{-0.21}$	21.6	18.18±.027	15.97±.030	13.50±.031	C	2	···
39	12:24:52.2	−12:38:36	BRI B1222-1222	M9.0	31	0.322	234.4	58.60±3.80	5	$17.06^{+1.18}_{-1.03}$	26.0	20.41±.039	17.99±.036	15.54±.038	S	1	···
40	12:50:52.2	−21:21:09	LEHPM2-0174	M6.5	···	0.566	125.8	57.77±1.72	1	$17.31^{+0.53}_{-0.50}$	46.4	18.36±.063	16.15±.005	13.78±.027	C	2	···
41	13:05:40.2	−25:41:06	Kelu-1AB	L2.0J	19	0.285	272.2	52.00±1.54	11	$19.23^{+0.58}_{-0.55}$	25.9	22.03±.060	19.14±.050	16.80±.001	S	2	d,f
42	13:09:21.9	−23:30:33	CE 303	M7.0	13	0.381	176.0	69.33±1.33	1	$14.42^{+0.28}_{-0.27}$	26.0	19.37±.026	17.00±.013	14.58±.008	C	2	···
43	14:25:27.9	−36:50:22	DENIS J1425-3650	L3.0	29	0.544	211.6	86.45±0.83	1	$11.56^{+0.11}_{-0.11}$	29.8	22.81±.060	19.67±.041	17.35±.034	S	1	···
44	14:39:28.4	+19:29:15	2MASS J1439+1929	L1.0	11	1.295	288.3	69.60±0.50	11	$14.36^{+0.10}_{-0.10}$	88.1	···	18.45±.056	15.97±.052	S	1	g
45	14:40:22.9	+13:39:23	2MASS J1440+1339	M8.0	25	0.331	204.7	45.00±1.11	1	$22.22^{+0.56}_{-0.53}$	34.8	18.95±.026	17.04±.080	14.81±.010	C	2	···

Continued on next page

ID	R. A. 2000	Dec 2000	Name	Spct Type	ref.[a,b]	μ $''$/yr	P.A. deg	Parallax mas	ref.[b]	Distance pc	V_{tan} Km/s	V	R	I	Tel.[c]	VRI Epochs	Notes
46	14:54:07.9	−66:04:47	DENIS J1454-6604	L3.5	28	0.565	125.1	84.88±1.71	1	$11.78^{+0.24}_{-0.23}$	31.5	···	19.22±.034	16.89±.022	C	1	g
47	14:56:38.5	−28:09:51	LHS 3003	M7.0	17	0.965	210.0	152.49±2.02	4	$6.55^{+0.08}_{-0.08}$	29.9	16.95±.014	14.90±.006	12.53±.008	C	2	···
48	15:01:07.9	+22:50:02	2MASS J1501+2250	M9.0	31	0.074	211.7	94.40±0.60	11	$10.59^{+0.06}_{-0.06}$	3.7	19.63±.021	17.39±.006	15.02±.018	C	2	···
49	15:39:41.9	−05:20:43	DENIS J1539-0520	L3.5	25	0.602	079.9	61.25±1.26	1	$16.32^{+0.34}_{-0.32}$	46.5	···	19.69±.035	17.56±.046	C	1	g
50	15:52:44.4	−26:23:07	LHS 5303	M6.0	18	0.495	155.1	94.63±0.70	1	$10.56^{+0.07}_{-0.07}$	24.7	16.53±.039	14.66±.021	12.49±.007	C	2	···
51	15:55:15.7	−09:56:05	2MASS J1555-0956	L1.0	13	1.217	129.9	74.53±1.21	1	$13.41^{+0.22}_{-0.21}$	77.4	21.04±.150	18.28±.019	15.82±.019	C	1	···
52	16:07:31.3	−04:42:06	SIPS J1607-0442	M8.0	13	0.415	180.2	63.90±1.47	1	$15.64^{+0.36}_{-0.35}$	30.7	19.49±.024	17.19±.014	14.78±.014	C	1	···
53	16:32:58.8	−06:31:45	SIPS J1632-0631	M7.0	13	0.342	176.3	53.31±1.48	1	$18.75^{+0.53}_{-0.50}$	30.4	20.23±.042	18.01±.014	15.58±.005	C	2	···
54	16:45:22.1	−13:19:51	2MASS J1645-1319	L1.5	13	0.874	203.8	90.12±0.82	1	$11.09^{+0.10}_{-0.10}$	45.9	20.96±.045	17.99±.001	15.65±.014	S	2	···
55	16:55:35.3	−08:23:40	GJ 644C	M7.0	17	1.202	223.4	154.96±0.52	26	$6.45^{+0.02}_{-0.02}$	36.7	16.85±.059	14.64±.015	12.25±.015	C	3	e
56	17:05:48.3	−05:16:46	2MASS J1705-0516AB	L0.5	23	0.165	132.5	55.07±1.76	1	$18.15^{+0.59}_{-0.56}$	14.2	21.67±.032	19.04±.009	16.67±.006	C	1	d,f
57	19:16:57.6	+05:09:02	GJ 752B	M8.0	31	1.434	203.8	171.20±0.50	26	$5.84^{+0.01}_{-0.01}$	39.7	17.68±.029	15.21±.032	12.76±.026	S	1	e
58	20:45:02.3	−63:32:05	SIPS J2045-6332	M9.0	25	0.218	158.0	41.72±1.50	1	$23.96^{+0.89}_{-0.83}$	24.7	21.14±.155	18.49±.036	16.04±.008	C	2	d
59	21:04:14.9	−10:37:37	2MASS J2104-1037	L3.0	15	0.662	116.0	53.00±1.71	1	$18.86^{+0.62}_{-0.58}$	59.2	22.37±.023	19.46±.023	17.18±.021	S	1	···
60	22:24:43.8	−01:58:52	2MASS J2224-0158	L4.5	11	0.984	152.3	86.70±0.69	11	$11.53^{+0.09}_{-0.09}$	53.7	23.82±.039	20.26±.028	17.77±.022	S	1	···
61	23:06:58.7	−50:08:58	SSSPM J2307-5009	M9.0	20	0.458	082.7	46.59±1.57	1	$21.46^{+0.74}_{-0.69}$	46.5	21.36±.050	18.90±.005	16.46±.019	S	2	···
62	23:54:09.3	−33:16:25	LHS 4039C	M9.0	29	0.505	218.3	44.38±2.09	1	$22.53^{+1.11}_{-1.01}$	53.9	20.96±.015	18.45±.001	15.98±.001	S	2	d,e
63	23:56:10.8	−34:26:04	SSSPM J2356-3426	M9.0	20	0.312	167.1	52.37±1.71	1	$19.09^{+0.64}_{-0.60}$	28.2	20.81±.055	18.34±.001	15.89±.001	S	2	···

[a]Unfortunately many papers do not cite references for spectral types. We have made an effort to track down primary sources. The references listed here are either primary sources or, if a primary source could not be found, secondary sources that discuss spectral typing. In a few cases several papers list the same spectral type with no reference and do not discuss the spectral type. In these cases this column was left blank.

[b]References: (1) This work; (2) Reid et al. (1995); (3) Tinney et al. (1995); (4) van Altena et al. (1995); (5) Tinney (1996); (6) Gizis & Reid (1997); (7) Kirkpatrick et al. (1997); (8) Martín et al. (1999); (9) Basri et al. (2000); (10) Gizis et al. (2000); (11) Dahn et al. (2002); (12) Geballe et al. (2002); (13) Gizis et al. (2002); (14) Leggett et al. (2002); (15) Cruz et al. (2003); (16) Kendall et al. (2003); (17) Costa et al. (2005); (18) Crifo et al. (2005); (19) Liu & Leggett (2005a); (20) Lodieu et al. (2005); (21) Henry et al. (2006); (22) Reylé et al. (2006); (23) Reid et al. (2006); (24) Caballero (2007); (25) Schmidt et al. (2007); (26) van Leeuwen (2007); (27) Looper et al. (2008); (28) Phan-Bao et al. (2008); (29) Reid et al. (2008); (30) Gatewood & Coban (2009); (31) Jenkins et al. (2009); (32) Shkolnik et al. (2009); (33) Konopacky et al. (2010); (34) Dupuy & Liu (2012); (35) Faherty et al. (2012)

[c]S - *SOAR*; C - *CTIO* 0.9m

[d]See notes in §6.8.

[e]Member of resolved multiple system. Parallaxes for 1, 55, and 57 are for brighter components.

[f]Unresolved multiple

[g]No V photometry is available. SED fit and $T_{\rm eff}$ excludes V.

CHAPTER 6

Results from the HLIMIT Survey

This chapter is based on §§ 6 and higher of "The Solar Neighborhood *XXXII*: The Hydrogen Burning Limit" (Dieterich et al. 2014).

6.1 Photometric Results

Table 5.3 lists the *VRI* photometry, the telescope in which the photometry was taken, and the number of epochs for which each target was observed. For the 28 targets observed on both telescopes, Table 5.3 lists the set of observations with the smallest error or the most epochs, with the number of epochs taking priority in selecting which data set to adopt. The electronic version of Table 1 of Dieterich et al. (2013) lists both sets of photometry for these objects, along with 2MASS J, H, and K_s and WISE $W1$, $W2$, and $W3$ photometry for all objects. We achieved sensitivities of $V = 23.75 \pm 0.01$ on SOAR with 90 minute exposures under dark skies and good seeing. The time demands of the CTIOPI program at the 0.9m telescope forced us to limit exposures to 20 minutes for the majority of targets. Under dark skies and good seeing (i.e., $\lesssim 1.0''$) 20 minute integrations yielded results as faint as $V = 19.50 \pm 0.05$. In exceptional cases when we took longer integrations we were able to achieve $V = 21.93 \pm 0.07$ in 90 minutes under extraordinary conditions. The majority of the measurements had errors < 0.05 magnitudes (i.e., 5%); however, for the fainter 0.9m observations the errors are as large as 0.15 magnitudes. It was our original intention to observe all targets for at least two epochs, but this was not possible for some targets due to time constraints on SOAR. As discussed in §6.5, the optical variability for the sample

is comparable to the photometric error, meaning that single epoch photometry should be generally consistent with the values we would obtain by averaging more observations.

Table 5.3 shows the photometry in the photometric system used by the telescope in which the measurements were taken − Johnson-Kron-Cousins for the CTIO 0.9m telescope and Bessell for SOAR. Rather than extrapolating the relations of Bessell (1995), we used the 28 objects observed on both telescopes to derive new relations between the colors $(V - R_B)$ and $(V - R_C)$ as well as $(V - I_B)$ and $(V - I_C)$ and show the results in Figure 6.1. Given the photometric uncertainties of the V and R observations (typically $\lesssim$5%, Table 5.3), we find no systematic deviation between the two $(V - R)$ colors. We therefore adopt $R_B = R_C$ for the purpose of this study. We do detect a trend in the $(V - I)$ colors, as shown in Figure 6.1b. Based on the data shown in Figure 6.1, we derive the transformation

$$(V - I_B) = -0.0364(V - I_C)^2 + 1.4722(V - I_C) - 1.3563.$$

We emphasize that the relations we derive here are based on a small sample and serve the purposes of our study only. They should not be used as general relations analogous to those of Bessell (1995). In particular, the difference in the I band is likely dominated by the different detector efficiencies between the CTIO 0.9m and the SOAR/SOI CCDs in the far red. The I photometry listed in Table 5.3 is in the photometric system of the telescope that took the adopted observations.

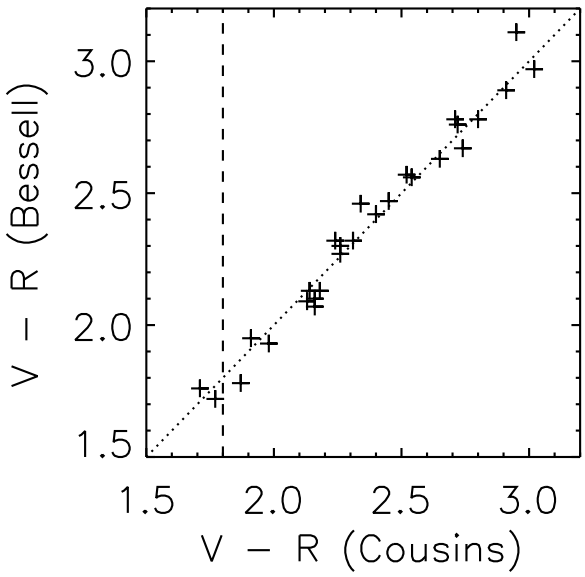

(a)

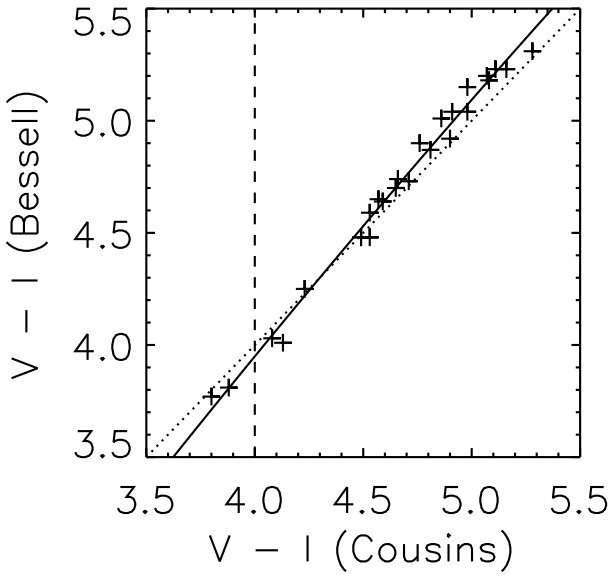

(b)

Figure 6.1 Comparison of photometry for 28 objects observed on both the CTIO 0.9m telescope (Kron-Cousins filters) and the SOI instrument on the SOAR 4.1m telescope (Bessell filters). The dotted line indicates a 1 to 1 relation. The V band is photometrically identical on both systems. Panel "a" shows that there is no systematic difference between R_C and R_B. Panel "b" shows the trend for the I band. The solid line represents the polynomial fit $(V-I_B) = -0.0364(V-I_C)^2+1.4722(V-I_C)-1.3563$. Most of the difference in the I band is likely due to different sensitivities between the two detectors in the far red. The dashed vertical lines indicate the red limit of the Bessell (1995) color relations for the two filter systems.

6.2 New Trigonometric Parallaxes

As reported in Table 6.1, the new trigonometric parallax measurements have a mean uncertainty of 1.43 mas, corresponding to a distance error of ∼1% at 10 pc and ∼3.5% at the original distance horizon of 25 pc. When comparing these results to other samples observed by CTIOPI we found that nearby late M and early L targets tend to be ideal targets for optical parallax investigations on one meter class telescopes. Although the intrinsic faintness of the targets made them a challenge in nights with poor seeing or a bright moon, the parallax solution converged with fewer epochs and had smaller errors than what we experience for brighter samples. We suspect that several factors contribute to this good outcome. First, the long exposures average out short atmospheric anomalies that may cause asymmetric Point Spread Functions (PSFs). The resulting symmetric PSF profiles facilitate centroiding. Second, the long exposures generate images rich in background stars that are likely more distant than reference stars available in shorter exposures. Because exposure times for brighter targets are often limited by the time it takes for the science target to saturate the detector, these faint and distant reference stars are not available for brighter parallax targets. Third, as already mentioned, the use of the *I* band minimizes atmospheric refraction when compared to other optical bands.

From a mathematical point of view, solving a trigonometric parallax consists of fitting the measured apparent displacements of the science target to an ellipse whose eccentricity and orientation is pre-determined by the target's position on the celestial sphere.

Table 6.1: New Trigonometric Parallaxes, Proper Motions, and Optical Variability

ID	Name	R. A.	Decl.	Filt.	N_{sea}[a]	N_{frm}[b]	Coverage	Years	N_{ref}[c]	π(rel)	π(corr)	π(abs)	μ	P.A.	V_{tan}	Var.[d]
		2000.0	2000.0							mas	mas	mas	mas yr^{-1}	deg E. of N.	Km s^{-1}	milli-mag
1	GJ 1001BC	00:04:34.9	-40:44:06	*R*	10s	112	1999.64-2011.74	12.10	6	75.99±2.06	1.03±0.16	77.02±2.07	1643.6±0.6	156.0±.04	102.4	···
2	LEHPM1-0494B	00:21:05.8	-42:44:49	*I*	5s	24	2008.86-2012.83	3.97	9	39.22±2.10	0.55±0.08	39.77±2.10	252.9±1.6	089.1±.53	30.1	15.4
3	LEHPM1-0494A	00:21:10.7	-42:45:40	*I*	5s	24	2008.86-2012.83	3.97	9	36.65±1.99	0.55±0.08	37.20±1.99	252.8±1.5	086.5±.53	32.2	6.5
10	DENIS J0306-3647	03:06:11.5	-36:47:53	*I*	4s	39	2009.75-2012.94	3.19	8	75.79±1.42	0.67±0.08	76.46±1.42	690.0±1.1	196.0±.16	42.7	8.4
11	LP 944-020	03:39:35.2	-35:25:44	*I*	8s	59	2003.95-2012.94	8.99	10	154.53±1.03	1.36±0.10	155.89±1.03	408.3±0.3	048.5±.07	12.4	8.8
13	2MASS J0428-2253	04:28:50.9	-22:53:22	*I*	4s	22	2010.01-2012.94	2.92	9	38.04±1.85	0.44±0.04	38.48±1.85	189.3±1.9	038.1±1.11	23.2	18.0
14	LP 775-031	04:35:16.1	-16:06:57	*I*	7c	74	2003.95-2012.88	8.94	8	94.53±1.05	0.82±0.13	95.35±1.06	356.0±0.4	028.0±.11	17.6	8.1
15	2MASS J0451-3402	04:51:00.9	-34:02:15	*I*	5s	22	2008.86-2013.12	4.26	8	46.43±1.43	1.03±0.47	47.46±1.51	157.6±1.0	036.5±.75	15.7	50.6
16	2MASS J0500+0330	05:00:21.0	+03:30:50	*I*	4c	23	2009.75-2012.89	3.15	13	73.38±1.98	0.47±0.12	73.85±1.98	350.2±1.7	177.9±.41	22.4	14.8
17	2MASS J0523-1403	05:23:38.2	-14:03:02	*I*	3c	24	2010.98-2013.12	2.14	9	80.35±1.76	0.60±0.10	80.95±1.76	194.5±1.6	032.5±.94	11.4	11.7
18	DENIS J0652-2534	06:52:19.7	-25:34:50	*I*	4c	36	2010.02-2013.12	3.10	12	63.24±0.94	0.52±0.04	63.76±0.94	249.6±0.7	289.3±.31	18.5	10.5
21	DENIS J0751-2530	07:51:16.4	-25:30:43	*I*	4c	35	2010.15-2013.12	2.97	10	58.65±0.84	0.50±0.02	59.15±0.84	889.1±0.8	279.2±.09	71.2	15.3
22	DENIS J0812-2444	08:12:31.7	-24:44:42	*I*	4s	28	2010.02-2013.25	3.24	14	44.79±0.96	0.68±0.03	45.47±0.96	196.4±0.7	135.5±.41	20.4	19.9
23	SSSPM J0829-1309	08:28:34.1	-13:09:19	*I*	4c	24	2009.94-2013.26	3.32	10	87.24±0.76	0.72±0.16	87.96±0.78	577.3±0.7	273.0±.10	31.1	9.2
26	2MASS J0847-1532	08:47:28.7	-15:32:37	*I*	5s	35	2009.32-2013.27	3.95	12	58.34±0.99	0.62±0.09	58.96±0.99	239.5±0.7	146.1±.34	19.2	9.9
27	LHS 2065	08:53:36.0	-03:29:28	*I*	10s	101	2003.95-2013.26	9.31	6	117.19±0.76	0.79±0.03	117.98±0.76	550.3±0.2	249.4±.04	22.0	12.1
29	LHS 2195	09:49:22.2	+08:06:45	*I*	4s	36	2010.01-2013.10	3.09	9	59.55±1.66	0.77±0.15	60.32±1.67	886.7±1.2	177.4±.12	69.7	11.1
35	LHS 2397aAB	11:21:49.0	-13:13:08	*I*	7c	68	2005.09-2013.26	8.16	9	65.28±2.02	0.55±0.07	65.83±2.02	506.9±0.6	264.7±.11	36.5	22.1
36	2MASS J1126-5003	11:26:39.9	-50:03:55	*I*	5s	20	2009.19-2013.25	4.07	13	58.82±1.64	0.56±0.12	59.38±1.64	1645.7±1.0	286.2±.06	131.3	25.3
38	LP 851-346	11:55:42.9	-22:24:58	*I*	7s	56	2007.18-2013.28	6.10	9	88.92±1.77	0.62±0.06	89.54±1.77	408.6±0.9	244.0±.23	21.6	10.4
40	LEHPM2-0174	12:50:52.2	-21:21:09	*I*	8s	45	2005.14-2013.38	8.25	9	57.33±1.72	0.44±0.03	57.77±1.72	565.7±0.6	125.8±.15	46.4	7.8
42	CE 303	13:09:21.9	-23:30:33	*I*	4s	47	2010.16-2013.27	3.11	11	68.41±1.32	0.92±0.14	69.33±1.33	380.5±1.1	176.0±.26	26.0	10.2
43	DENIS J1425-3650	14:25:27.9	-36:50:22	*I*	5s	33	2009.31-2013.28	3.96	13	85.80±0.79	0.65±0.24	86.45±0.83	543.7±0.8	211.6±.17	29.8	15.1
45	2MASS J1440+1339	14:40:22.9	+13:39:23	*I*	5s	34	2009.25-2013.26	4.01	8	44.13±1.11	0.87±0.07	45.00±1.11	331.1±0.9	204.7±.28	34.8	6.9
46	DENIS J1454-6604[e]	14:54:07.9	-66:04:47	*I*	5s	22	2009.32-2013.26	3.94	11	84.21±1.70	0.67±0.17	84.88±1.71	564.8±1.3	125.1±.25	31.5	19.9
49	DENIS J1539-0520[e]	15:39:41.9	-05:20:43	*I*	5c	29	2009.25-2013.25	4.00	11	60.51±1.26	0.74±0.08	61.25±1.26	602.3±1.1	79.9±.17	46.5	17.0
50	LHS 5303	15:52:44.4	-26:23:07	*I*	9s	85	2004.57-2012.59	8.02	10	94.10±0.70	0.53±0.07	94.63±0.70	495.4±0.2	155.1±.05	24.7	10.7
51	2MASS J1555-0956	15:55:15.7	-09:56:05	*I*	4c	25	2010.19-2013.28	3.08	10	73.94±1.21	0.59±0.05	74.53±1.21	1217.0±1.3	129.9±.12	77.4	9.9
52	SIPS J1607-0442	16:07:31.3	-04:42:06	*I*	4c	32	2010.39-2013.26	2.87	8	62.79±1.47	1.11±0.06	63.90±1.47	414.6±1.2	180.2±.26	30.7	12.2
53	SIPS J1632-0631	16:32:58.8	-06:31:45	*I*	3c	40	2010.19-2012.58	2.39	11	52.31±1.47	1.00±0.14	53.31±1.48	342.2±1.9	176.3±.45	30.4	17.9
54	2MASS J1645-1319	16:45:22.1	-13:19:51	*I*	5c	48	2009.32-2013.27	3.95	15	89.19±0.81	0.93±0.10	90.12±0.82	873.8±0.6	203.8±.08	45.9	11.6
56	2MASS J1705-0516AB	17:05:48.3	-05:16:46	*I*	5s	18	2009.32-2013.25	3.93	10	53.34±1.74	1.73±0.26	55.07±1.76	164.7±1.1	132.5±.79	14.2	40.9
58	SIPS J2045-6332	20:45:02.3	-63:32:05	*I*	4c	45	2010.59-2013.54	2.95	11	40.65±1.50	1.07±0.07	41.72±1.50	220.4±1.2	158.0±.88	24.7	38.9
59	2MASS J2104-1037	21:04:14.9	-10:37:37	*I*	4c	22	2009.56-2012.58	3.02	12	52.23±1.70	0.77±0.15	53.00±1.71	661.9±1.3	116.0±.22	59.2	12.5
61	SSSPM J2307-5009	23:06:58.7	-50:08:58	*I*	4c	41	2009.55-2012.81	3.26	9	46.21±1.57	0.38±0.06	46.59±1.57	457.8±1.6	82.7±.32	46.5	11.5
62	LHS 4039C	23:54:09.3	-33:16:25	*I*	4c	58	2003.51-2007.74	4.23	5	41.91±2.08	2.47±0.15	44.38±2.09	505.5±1.8	218.3±.40	53.9	20.0
63	SSSPM J2356-3426	23:56:10.8	-34:26:04	*I*	3c	28	2009.56-2011.77	2.21	9	51.80±1.71	0.57±0.07	52.37±1.71	312.5±2.1	167.1±.67	28.2	10.2

[a]Number of seasons observed, where 2−3 months of observations count as one season, for seasons having more than three images taken. The letter "c" indicates a continuous set of observations where multiple nights of data were taken in each season, whereas an "s" indicates scattered observations when one or more seasons have only a single night of observations. Generally "c" observations are better.

[b]Total number of images used in reduction. Images are typically taken in sets of three consecutive observations.

[c]Number of reference stars used to reduce the parallax.

[d]Photometric variability of the science target.

[e]No V photometry. Correction for differential color refraction based on estimated V from color-magnitude relations.

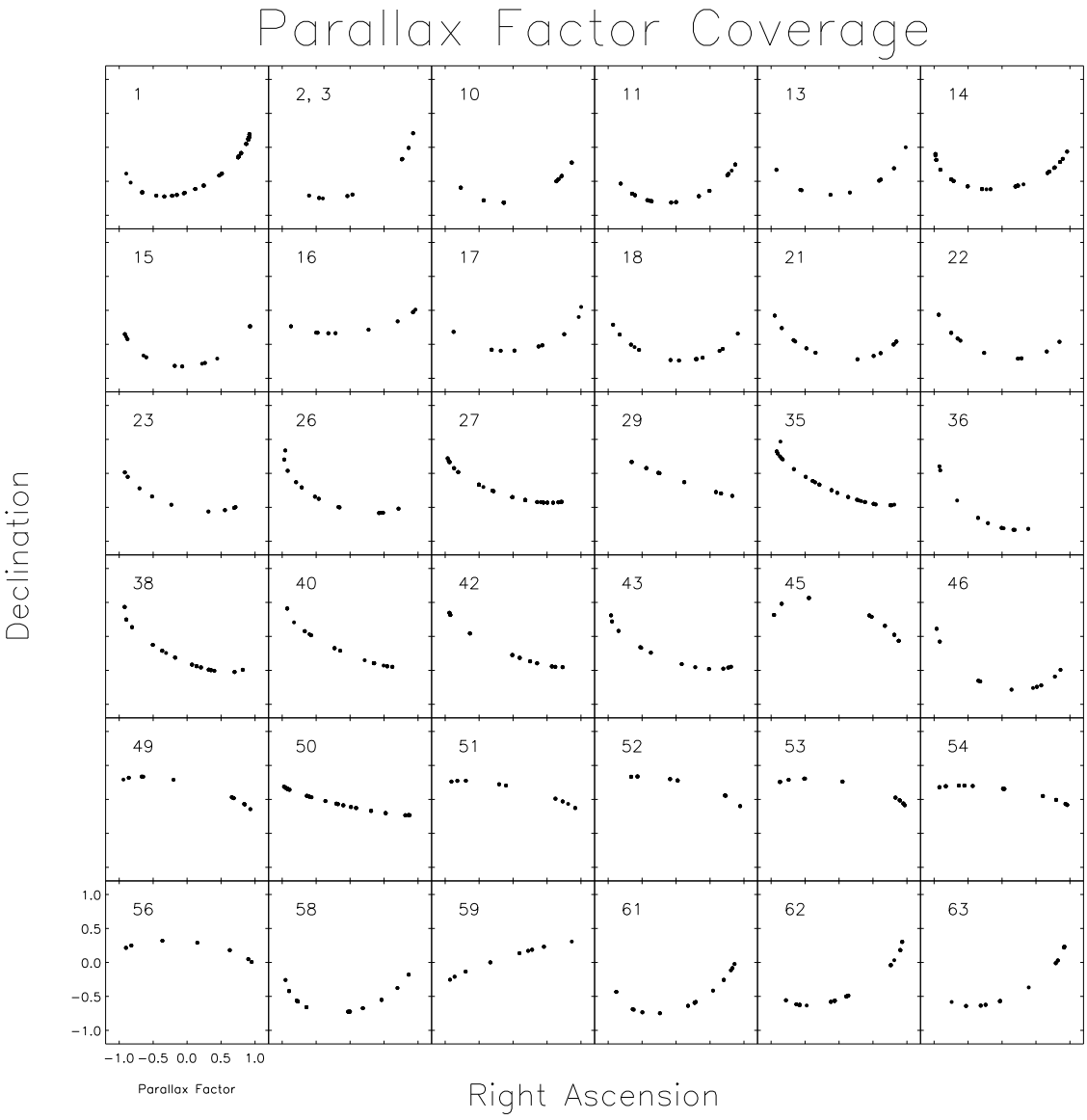

Figure 6.2 Parallax ellipses for the 37 parallaxes reported in this study (objects 2 and 3 comprise a wide binary and parallaxes are derived for both components using the same images). The black dots sample the ellipse that each object appears to trace on the sky as a result of Earth's annual motion. The eccentricity of the ellipse is a function of the target's location in the celestial sphere, with objects close to the ecliptic plane producing the most eccentric ellipses. Low parallax factor observations provide significant constraints when the ellipse is not markedly eccentric.

At the same time, we must also fit the constant linear component of motion due to the object's proper motion. The size of the ellipse's major and minor axes provide a measure of the object's distance. Figure 6.2 shows the parallax ellipses for the observations. In these plots a parallax factor of 1 or -1 indicates the target's maximum apparent displacement from its mean position in the right ascension axis. Because we restricted the hour angle of the observations to ±30 minutes (§5.4), high parallax factor observations occurred during evening and morning twilight. As is clear from Figure 6.2, these twilight observations are essential for determining the parallax ellipse's major axis. The extent to which observations with lower parallax factors constrained the final parallax solution depended greatly on the parallax ellipse's eccentricity. An object with coordinates close to the ecliptic pole produces a parallax ellipse that is nearly circular, and in that case low parallax factor observations can still provide significant constraints to the parallax solution (e.g., object # 1). The opposite occurs with the high eccentricity parallax ellipses for objects lying close to the ecliptic plane, where low parallax factor observations contribute little towards the final solution (e.g., object # 29).

Regardless of the target's position on the celestial sphere, we found out that attempting to fit a parallax ellipse to more than ∼4 epochs but fewer than ∼7 epochs will often produce an erroneous answer whose formal uncertainty is also unrealistically small. True convergence of a parallax result was best determined by assuring that the following conditions were met: (1) adding new epochs caused changes that were small compared to the formal uncertainty; (2) high parallax factors observations were taken during both evening twilight and morning

twilight; and (3) the parallax ellipses shown in Figure 6.2 appeared to be sufficiently sampled so that the points trace out a unique ellipse.

Nine of the 37 targets listed in Table 6.1 have previously published trigonometric parallaxes. These targets are listed in Table 6.2 with our new trigonometric parallax and the previous value. In five cases trigonometric parallaxes were not yet published at the beginning of this study in 2009 (Andrei et al. 2011; Dupuy & Liu 2012; Faherty et al. 2012). LHS 4039C (Subasavage et al. 2009) is a member of a resolved triple system; we re-reduced our data set with LHS 4039C as the science target (see §6.8). Finally, we note that LP944-020 (Tinney 1996) is no longer a member of the 5 pc sample and 2MASS J1645-1319 is no longer a member of the 10 pc sample (Henry et al. 2006).

Table 6.2: Targets with Previously Published Parallaxes

ID	Name	New π_{abs} (mas)	New distance (pc)	Previous π_{abs} (mas)	Previous distance (pc)	Reference
1	GJ 1001 BC	77.02±2.07	$12.98^{+0.36}_{-0.34}$	76.86±3.97	$13.01^{+0.71}_{-0.63}$	Henry et al. (2006)
11	LP 944-020	155.89±1.03	$6.41^{+0.04}_{-0.04}$	201.40±4.20	$4.96^{+0.11}_{-0.10}$	Tinney (1996)
26	2MASS J0847-1532	58.96±0.99	$16.96^{+0.28}_{-0.28}$	76.5±3.5	$13.07^{+0.63}_{-0.57}$	Faherty et al. (2012)
27	LHS 2065	117.98±0.76	$8.47^{+0.05}_{-0.05}$	117.30±1.50	$8.52^{+0.11}_{-0.11}$	van Altena et al. (1995)
35	LHS2397Aab	65.83±2.02	$15.19^{+0.48}_{-0.45}$	73.0±2.1	$13.78^{+0.41}_{-0.38}$	Dupuy & Liu (2012)
49	DENIS J1539-0520	61.25±1.26	$16.32^{+0.34}_{-0.32}$	64.5±3.4	$15.50^{+0.86}_{-0.78}$	Andrei et al. (2011)
54	2MASS J1645-1319	90.12±0.82	$11.09^{+0.10}_{-0.10}$	109.9±6.1	$9.01^{+0.53}_{-0.48}$	Faherty et al. (2012)
56	2MASS J1705-0516AB	55.07±1.76	$18.15^{+0.59}_{-0.56}$	45.0±12.0	$22.22^{+8.08}_{-4.68}$	Andrei et al. (2011)
62	LHS 4039C	44.38±2.09	$22.53^{+1.11}_{-1.01}$	44.24±1.78	$22.60^{+0.95}_{-0.87}$	Subasavage et al. (2009)

Table 9 of Dupuy & Liu (2012) lists all known ultra-cool dwarfs with trigonometric parallaxes at the time of that publication. In that list, 156 objects have spectral types matching the spectral type range of our study, M6V to L4. In addition, out of the seventy trigonometric parallaxes reported by Faherty et al. (2012), 24 are first parallaxes for objects in the M6V

to L4 spectral type range. The 28 objects for which we publish first parallaxes in this paper therefore represent a 15.5% increase in the number of objects with trigonometric parallaxes in the M6V to L4 spectral type range, for a total of 208 objects.

6.3 Effective Temperatures and Luminosities

Table 6.3 lists the derived properties of effective temperature, luminosity, and radius for the entire sample. All resulting quantities are synthesized and summarized graphically in Figure 6.3, a *bona fide Hertzsprung-Russell* (HR) diagram for the end of the stellar main sequence. Figure 6.3 is followed by versions that use the ID number from Table 6.3 and spectral types as plotting symbols.

Table 6.3: Derived Properties

ID	R. A. 2000.0	Dec. 2000.0	Name	Spct. Type	$T_{\rm eff}$ K	Luminosity $log(L/L_{\odot})$	Radius $R_{\odot}$	Notes
1	00:04:34.9	−40:44:06	GJ 1001BC	L4.5	1725±21	-4.049±.048	0.105±.005	d,e,f
2	00:21:05.8	−42:44:49	LEHPM1-0494B	M9.5	2305±57	-3.506±.046	0.110±.008	d,e
3	00:21:10.7	−42:45:40	LEHPM1-0494A	M6.0	2918±21	-2.818±.046	0.152±.008	d,e
4	00:24:24.6	−01:58:20	BRI B0021-0214	M9.5	2315±54	-3.505±.042	0.109±.007	···
5	00:36:16.0	+18:21:10	2MASS J0036+1821	L3.5	1796±33	-3.950±.011	0.109±.004	···
6	00:52:54.7	−27:06:00	RG 0050-2722	M9.0	2402±34	-3.599±.078	0.091±.008	···
7	01:02:51.2	−37:37:44	LHS 132	M8.0	2513±29	-3.194±.030	0.133±.005	···
8	02:48:41.0	−16:51:22	LP 771-021	M8.0	2512±19	-3.507±.076	0.093±.008	···
9	02:53:00.5	+16:52:58	SO0253+1652	M6.5	2656±37	-3.137±.013	0.127±.004	···
10	03:06:11.5	−36:47:53	DENIS J0306-3647	M8.5	2502±40	-3.366±.017	0.110±.004	···
11	03:39:35.2	−35:25:44	LP 944-020	M9.0	2312±71	-3.579±.010	0.101±.006	···
12	03:51:00.0	−00:52:45	LHS 1604	M7.5	···	···	···	d
13	04:28:50.9	−22:53:22	2MASS J0428-2253	L0.5	2212±57	-3.441±.042	0.129±.009	···
14	04:35:16.1	−16:06:57	LP 775-031	M7.0	2532±25	-3.033±.012	0.157±.003	···
15	04:51:00.9	−34:02:15	2MASS J0451-3402	L0.5	2146±41	-3.676±.029	0.104±.005	d
16	05:00:21.0	+03:30:50	2MASS J0500+0330	L4.0	1783±19	-4.010±.024	0.103±.003	···
17	05:23:38.2	−14:03:02	2MASS J0523-1403	L2.5	2074±27	-3.898±.021	0.086±.003	d
18	06:52:19.7	−25:34:50	DENIS J0652-2534	L0.0	2313±56	-3.600±.015	0.098±.005	···
19	07:07:53.3	−49:00:50	ESO 207-61	M8.0	2403±31	-3.625±.039	0.088±.004	···

Continued on next page

ID	R. A. 2000.0	Dec. 2000.0	Name	Spct. Type	$T_{\rm eff}$ K	Luminosity $log(L/L_{\odot})$	Radius $R_{\odot}$	Notes
20	07:46:42.5	+20:00:32	2MASS J0746+2000AB	L0.0J	2310±51	-3.413±.009	0.122±.005	f
21	07:51:16.4	−25:30:43	DENIS J0751-2530	L2.5	2186±32	-3.732±.013	0.094±.003	···
22	08:12:31.7	−24:44:42	DENIS J0812-2444	L1.5	2295±47	-3.696±.021	0.089±.004	···
23	08:28:34.1	−13:09:19	SSSPM J0829-1309	L1.0	2117±37	-3.845±.011	0.088±.003	d
24	08:29:49.3	+26:46:33	GJ 1111	M6.5	2690±27	-3.107±.022	0.128±.004	···
25	08:40:29.7	+18:24:09	GJ 316.1	M6.0	2683±30	-3.039±.013	0.139±.003	···
26	08:47:28.7	−15:32:37	2MASS J0847-1532	L2.0	1922±66	-3.798±.017	0.113±.008	···
27	08:53:36.0	−03:29:28	LHS 2065	M9.0	2324±27	-3.516±.010	0.107±.002	···
28	09:00:23.6	+21:50:04	LHS 2090	M6.0	2680±24	-3.084±.016	0.132±.003	···
29	09:49:22.2	+08:06:45	LHS 2195	M8.0	2481±36	-3.399±.025	0.107±.004	···
30	10:48:12.8	−11:20:11	LHS 292	M6.0	2588±32	-3.166±.016	0.129±.004	···
31	10:49:03.4	+05:02:23	LHS 2314	M6.0	2691±13	-3.169±.049	0.119±.006	···
32	10:56:29.2	+07:00:53	GJ 406	M6.0	2700±56	-3.036±.044	0.138±.009	···
33	10:58:47.9	−15:48:17	DENIS J1058-1548	L3.0	1804±13	-3.997±.019	0.102±.002	···
34	11:06:18.9	+04:28:32	LHS 2351	M7.0	2619±27	-3.218±.056	0.119±.008	···
35	11:21:49.0	−13:13:08	LHS 2397aAB	M8.5J	2376±25	-3.291±.028	0.133±.005	d,f
36	11:26:39.9	−50:03:55	2MASS J1126-5003	L4.5	1797±49	-4.035±.025	0.098±.006	···
37	11:53:52.7	+06:59:56	LHS 2471	M6.5	2611±22	-3.113±.032	0.135±.005	···
38	11:55:42.9	−22:24:58	LP 851-346	M7.5	2595±28	-3.194±.018	0.125±.003	···
39	12:24:52.2	−12:38:36	BRI B1222-1222	M9.0	2398±38	-3.454±.057	0.108±.007	···
40	12:50:52.2	−21:21:09	LEHPM2-0174	M6.5	2598±25	-2.909±.026	0.173±.006	···
41	13:05:40.2	−25:41:06	Kelu-1AB	L2.0J	2026±45	-3.616±.033	0.126±.007	d,f
42	13:09:21.9	−23:30:33	CE 303	M7.0	2508±35	-3.309±.018	0.117±.004	···
43	14:25:27.9	−36:50:22	DENIS J1425-3650	L3.0	1752±69	-4.029±.009	0.104±.008	···
44	14:39:28.4	+19:29:15	2MASS J1439+1929	L1.0	2186±100	-3.703±.010	0.098±.009	g
45	14:40:22.9	+13:39:23	2MASS J1440+1339	M8.0	2624±22	-3.163±.022	0.126±.003	···
46	14:54:07.9	−66:04:47	DENIS J1454-6604	L3.5	1788±100	-3.931±.019	0.112±.012	g
47	14:56:38.5	−28:09:51	LHS 3003	M7.0	2581±17	-3.266±.013	0.116±.002	···
48	15:01:07.9	+22:50:02	2MASS J1501+2250	M9.0	2398±36	-3.602±.009	0.091±.002	···
49	15:39:41.9	−05:20:43	DENIS J1539-0520	L3.5	1835±100	-4.006±.019	0.098±.010	g
50	15:52:44.4	−26:23:07	LHS 5303	M6.0	2718±12	-2.972±.008	0.147±.001	···
51	15:55:15.7	−09:56:05	2MASS J1555-0956	L1.0	2194±27	-3.712±.015	0.096±.002	···
52	16:07:31.3	−04:42:06	SIPS J1607-0442	M8.0	2466±30	-3.271±.021	0.126±.004	···
53	16:32:58.8	−06:31:45	SIPS J1632-0631	M7.0	2485±26	-3.459±.025	0.100±.003	···
54	16:45:22.1	−13:19:51	2MASS J1645-1319	L1.5	1925±66	-3.793±.011	0.113±.008	···
55	16:55:35.3	−08:23:40	GJ 644C	M7.0	2611±43	-3.214±.007	0.120±.004	e
56	17:05:48.3	−05:16:46	2MASS J1705-0516AB	L0.5	2207±62	-3.695±.029	0.097±.006	d,f
57	19:16:57.6	+05:09:02	GJ 752B	M8.0	2478±29	-3.340±.009	0.115±.003	e
58	20:45:02.3	−63:32:05	SIPS J2045-6332	M9.0	2179±111	-3.129±.032	0.190±.020	d
59	21:04:14.9	−10:37:37	2MASS J2104-1037	L3.0	1851±53	-3.812±.030	0.120±.008	···
60	22:24:43.8	−01:58:52	2MASS J2224-0158	L4.5	1567±88	-4.185±.013	0.109±.012	···
61	23:06:58.7	−50:08:58	SSSPM J2307-5009	M9.0	2347±48	-3.593±.030	0.096±.005	···

Continued on next page

ID	R. A. 2000.0	Dec. 2000.0	Name	Spct. Type	$T_{\rm eff}$ K	Luminosity $log(L/L_{\odot})$	Radius $R_{\odot}$	Notes
62	23:54:09.3	−33:16:25	LHS 4039C	M9.0	2412±40	-3.423±.041	0.111±.006	d,e
63	23:56:10.8	−34:26:04	SSSPM J2356-3426	M9.0	2438±42	-3.542±.029	0.094±.004	···

[d]See notes in §6.8.

[e]Member of resolved multiple system. Parallaxes for 1, 55, and 57 are for brighter components.

[f]Unresolved multiple

[g]No V photometry is available. SED fit and $T_{\rm eff}$ excludes V.

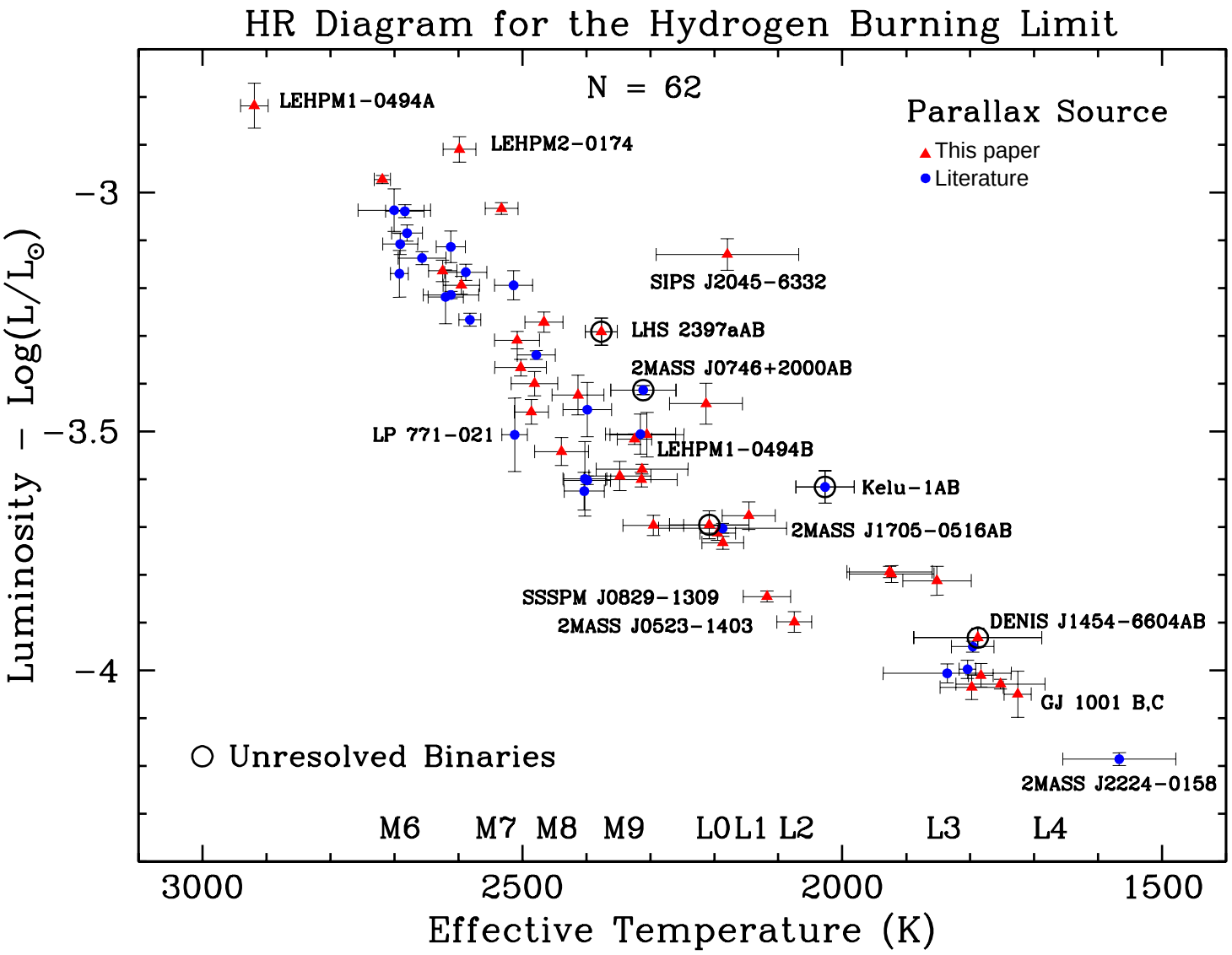

Figure 6.3 HR Diagram for objects with spectral types ranging from M6V to L4.5. Several representative objects are named. Known binaries with joint photometry are enclosed in open circles. A few known binaries are clearly over-luminous, denoting their low luminosity ratios. The L4.5 binary GJ 1001BC was deconvolved based on the nearly identical luminosity of both components (Golimowski et al. 2004a). As we discuss in §6.7, the L2.5 dwarf 2MASS J0523-1403 lies at a pronounced minimum in the radius-luminosity relation and its location likely constitutes the end of the stellar main sequence. Versions of this diagram that use the ID labels in Tables 5.3 and and spectral type labels for plotting symbols follow on the next two pages.

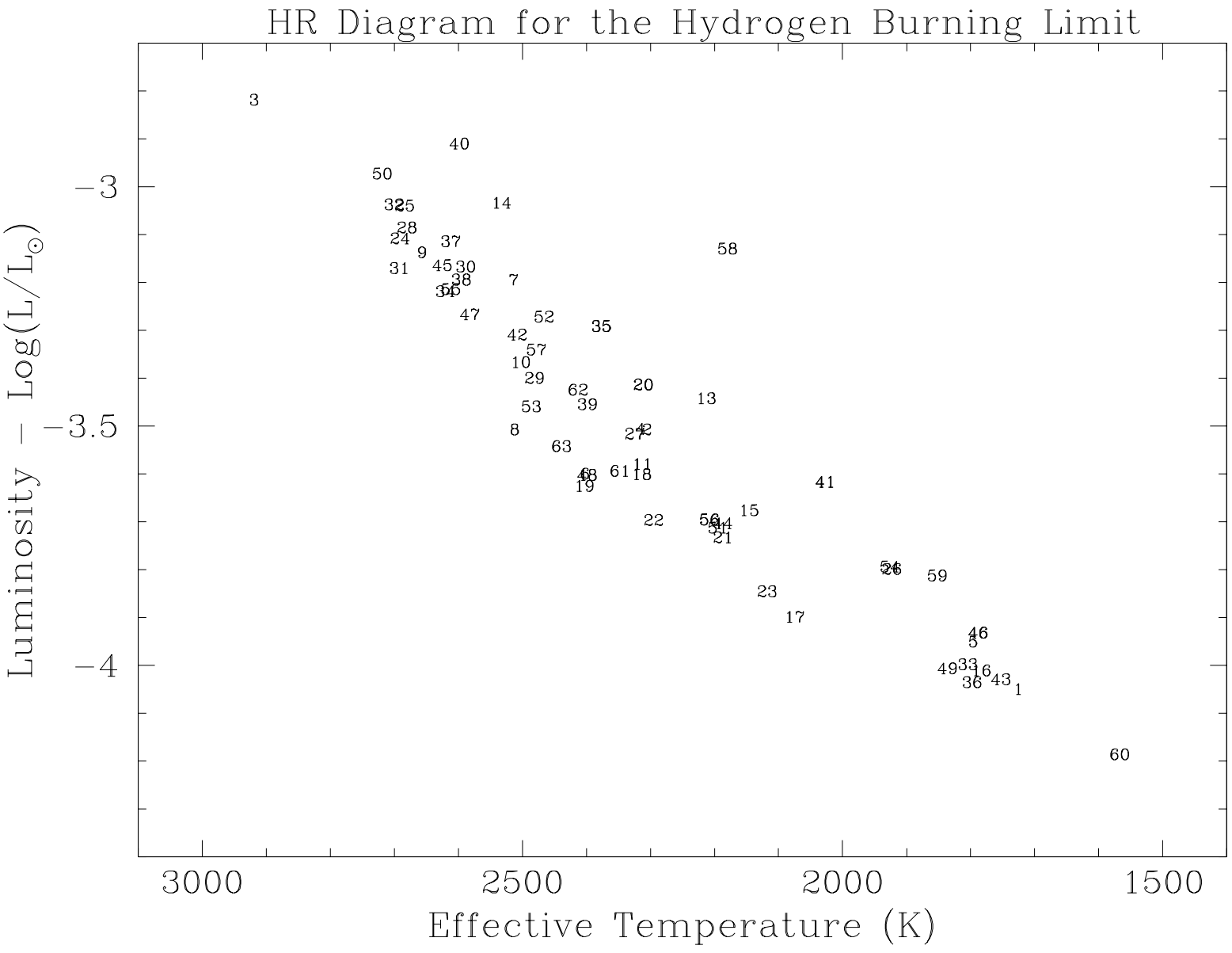

Figure 6.4 Same as Figure 6.3 but using ID numbers from Tables 5.3 and 6.3 as plot labels.

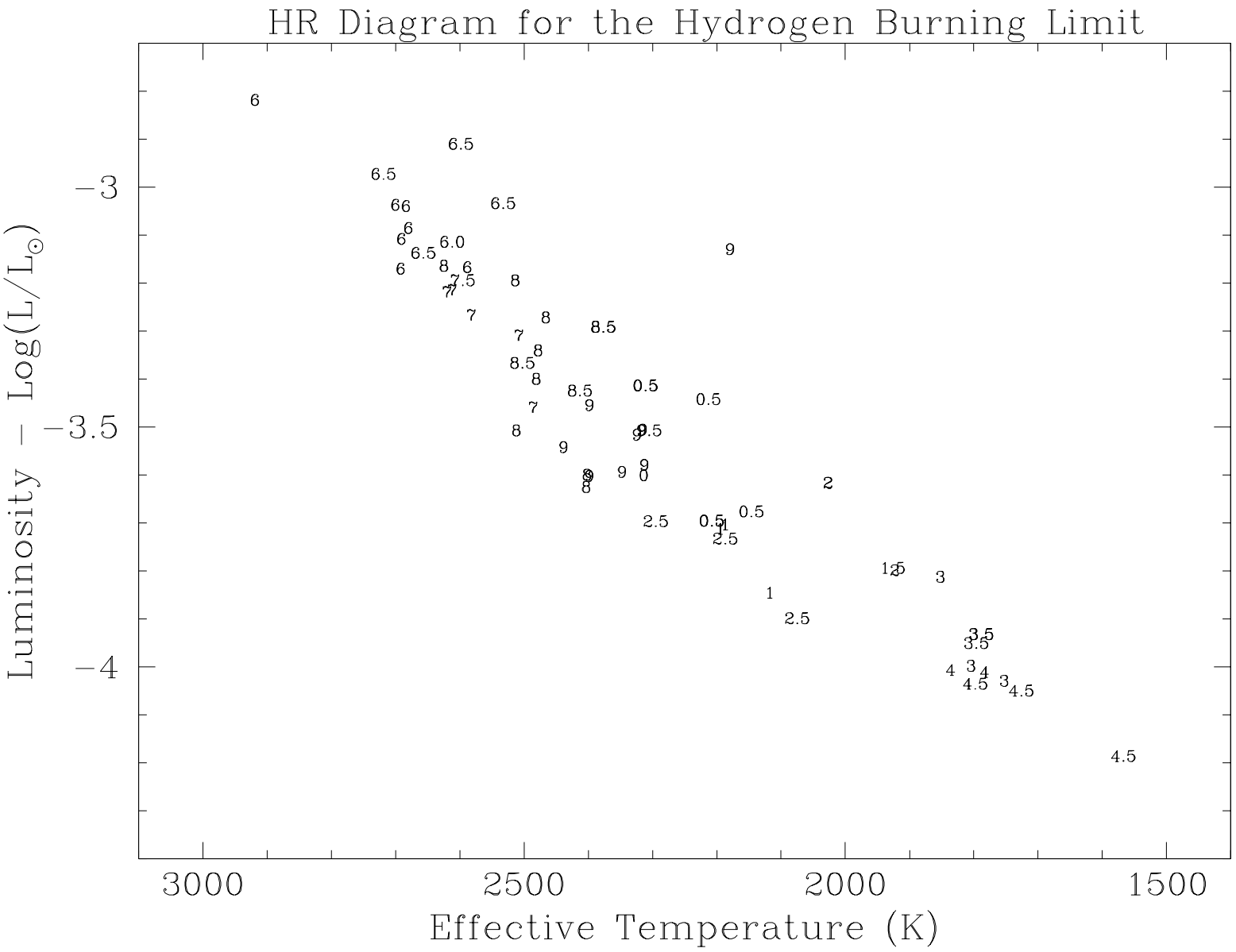

Figure 6.5 Same as Figure 6.3 but using spectral types as plot labels. Numbers 6−9.5 correspond subtypes of M dwarfs and 0−4.5 correspond subtypes of L dwarfs.

While the agreement with interferometric measurements shown in Figure 5.4 lends confidence that the overall methodology is right, the effective temperatures derived based on nine bands of photometry are still essentially model-dependent. The uncertainties in temperatures listed in Table 6.3 and shown by the error bars in Figure 6.3 can therefore be interpreted as measures of how accurate the model atmospheres are in a given temperature range. Inspection of Figure 6.3 shows that the models work very well for temperatures above 2600 K, with uncertainties generally smaller than 30 K. The uncertainties then progressively increase as the temperature lowers and can be greater than 100 K for objects cooler than 2000 K. The turning point at 2,600 K has been explained by the model authors (Allard et al. 2012) as a consequence of solid grain formation starting at that temperature, thus making the atmosphere significantly more complex.

The year 2012 brought about crucial advances in our ability to determine effective temperatures for cool stellar (and substellar) atmospheres. First, the publication of the WISE All Sky Catalog[1] provided uniform photometric coverage in the mid-infrared for known cool stars and brown dwarfs. Second, as already discussed, the publication of the *BT-Settl* model atmospheres with revised solar metallicities has provided opportunities to match observational data to fundamental atmospheric parameters with unprecedented accuracy (§5.6). Despite these recent advances, it is still useful to compare the results obtained here with earlier pioneering work in the field of effective temperature determination for cool atmospheres. Golimowski et al. (2004b) computed effective temperatures for 42 M, L, and T, dwarfs based on observations in the L' (3.4−4.1 μm) and M' (4.6−4.8 μm) bands. They

[1]http://wise2.ipac.caltech.edu/docs/release/allsky/

first used photometry to calculate bolometric fluxes based on observed spectra, and then used evolutionary models (Burrows et al. 1997) to determine a range of effective temperatures based on bolometric luminosities and radii with the assumption of an age range of 0.1 to 10 Gyr as well as a unique value for 3 Gyr. Cushing et al. (2008) determined the effective temperatures of nine L and T dwarfs by fitting observed flux-calibrated spectra in the wavelength range 0.6−14.5 μm to their own model atmospheres. Their technique, like ours, has the advantage of relying solely on atmospheric models as opposed to the significantly more uncertain evolutionary models, as discussed in detail in §6.7.3. Finally, Rajpurohit et al. (2013) have recently compared optical spectra (0.52−1.0 μm) for 152 M dwarfs to the same *BT-Settl* models we use in this study. Twenty-five of their M dwarfs have spectral types of M6V or later.

Table 6.4 compares the results presented here to overlapping objects in these three studies. While it is difficult to generalize from the small overlap amongst the different samples, there is a tendency for our results to be ∼100K cooler than the others. The cause of this discrepancy is not clear. In the case of Golimowski et al. (2004b) the most likely explanation is that their assumed mean age of 3 Gyr may not be representative of our sample. An age mismatch combined with the significant uncertainty in the evolutionary models could easily account for this temperature difference. Out of the five objects in common between this study and Rajpurohit et al. (2013), the effective temperature for one object agrees well while three objects have mismatches of ∼100K, and another has a significantly larger mismatch. While we do not know what is causing the different values, we note that the comparison

of radii derived with our methodology with empirically measured radii (Figure 5.4) makes systematic error in our measurements an unlikely explanation. A temperature difference of ∼100K would produce a systematic radius difference of 5% to 10% in the temperature range under consideration, and yet our derived radii have a mean absolute residual of only 3.4% in a random scatter. We must, however, note that because the stars used in the comparison in Figure 5.4, the comparison does not exclude the possibility of a systemic effect at lower temperatures in the *BT-Settl* models. Because Rajpurohit et al. (2013) base their calculations on optical spectra alone, we speculate that the discrepancy may be due to the stronger effects of metallicity in altering the optical colors of late M dwarfs. Changes in metallicity in the optical part of the spectrum often mimic changes in temperature, and it may be very hard to distinguish the two effects without resorting to infrared data, where the effects of metallicity are less pronounced.

Table 6.4: Comparison of Effective Temperatures from Different Studies

ID	Name	Spectral Type	This Work	G2004[a] Range	G2004[a] 3 Gyr	C2008[a]	R2013[a]
30	LHS 292	M6.0V	2588±32	2475−2750	2725	···	2700
32	GJ 406	M6.0V	2700±56	2650−2900	2900	···	···
40	LEHPM2-0174	M6.5V	2598±25	···	···	···	2700
47	LHS 3003	M7.0V	2581±17	2350−2650	2600	···	···
38	LP 851-346	M7.5V	2595±28	···	···	···	2600
7	LHS 132	M8.0V	2513±29	···	···	···	2600
27	LHS 2065	M9.0V	2324±27	2150−2425	2400	···	···
58	SIPS J2045-6332	M9.0V	2179±111	···	···	···	2500
4	BRI B0021-0214	M9.5V	2315±54	2150−2475	2425	···	···
20	2MASS J0746+2000AB	L0.0J	2310±51	1900−2225	2200	···	···
44	2MASS J1439+1929	L1.0	2186±100	1950−2275	2250	···	···
41	Kelu-1AB	L2.0J	2026±45	2100−2350	2300	···	···
33	DENIS J1058-1548	L3.0	1804±13	1600−1950	1900	···	···
5	2MASS J0036+1821	L3.5	1796±33	1650−1975	1900	1700	···
1	GJ 1001 BC	L4.5	1725±21	1750−1975	1850	···	···
60	2MASS J2224-0158	L4.5	1567±88	1475−1800	1750	1700	···

[a]G2004 Golimowski et al. (2004b); C2008 Cushing et al. (2008); R2013 Rajpurohit et al. (2013)

In addition to comparisons to other studies with objects in common to ours, we compare the general trends of the HR diagram (Figure 6.3) with the values derived by Konopacky et al. (2010). That study used Keck AO resolved near infrared photometry of M and L binaries as well as HST resolved optical photometry to derive effective temperatures and luminosities. Twenty-two of their targets fall in the temperature range of our study, but because theirs was a high resolution AO study there are no targets in common. Figure 6.6 shows their results over-plotted on our HR diagram. The large uncertainties in Konopacky et al. (2010) make their data difficult to interpret, and are probably a result of the lack of mid infrared photometry in their methodology. There is good agreement between their results and ours at cooler temperatures, but the two trends steadily diverge for temperatures above $\sim$2000 K, with Konopacky et al. (2010) predicting temperatures as much as 500 K cooler for a given luminosity. The discrepancy is probably a result of atmospheric modeling. While the *BT-Settl* models used in our study predict the rate of atmospheric dust formation and sedimentation for a wide range of temperatures, the "DUSTY" models (Allard et al. 2001) used by Konopacky et al. (2010) assume the extreme case where grains do not settle below the photosphere, thus providing a strong source of opacity. The "DUSTY" models replicate the conditions of L dwarf atmospheres well but gradually become inadequate at hotter temperatures where grain formation is less relevant (Allard et al. 2013). The additional source of opacity then causes the M dwarfs to appear cooler and larger than they really are.

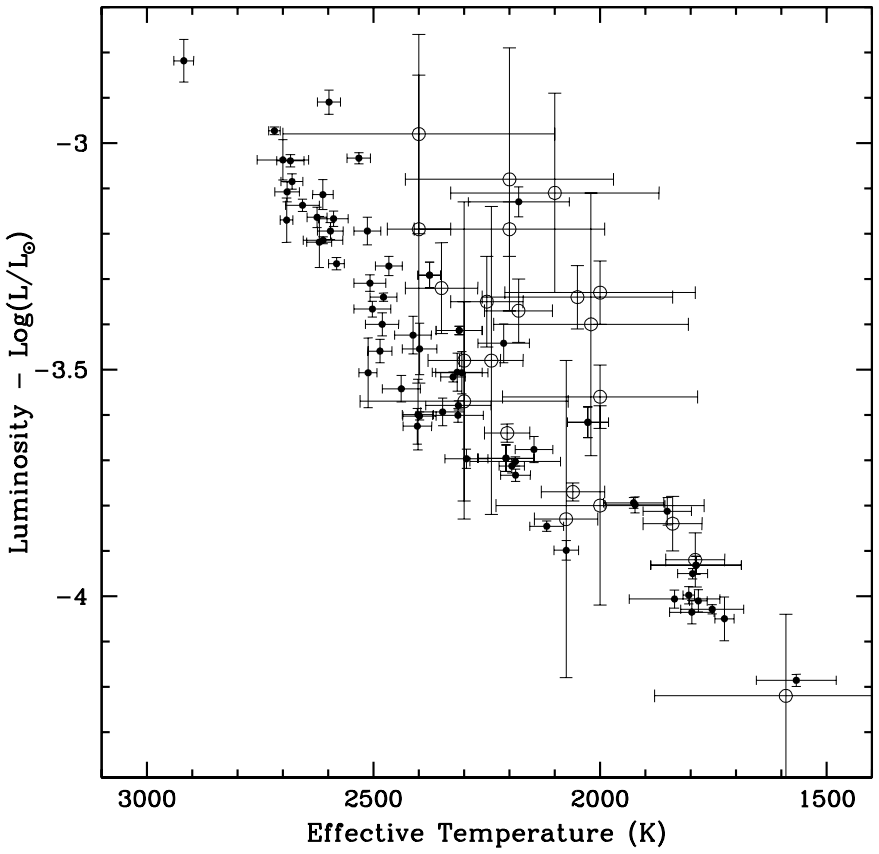

Figure 6.6 HR diagram of Figure 6.3 with data from Konopacky et al. (2010) over-plotted with open circles. The data agree well at low temperatures, but steadily diverge at higher temperatures. Both data sets have the minimum radius at ∼2075K.

6.3.1 χ^2 *Tests for Temperature Fits*

In §5.6 and Figure 5.4 we demonstrated that our methodology for determining effective temperatures, luminosities, and radii is in good agreement with interferometric radius measurements for early and mid M dwarfs. Unfortunately no directly measured radii are available for objects in the temperature range of this study so that a similar direct comparison can be made. The lack of a direct test on radii for the late M and early L dwarf range leaves open the possibility that perhaps the *BT-Settl* models work fine at higher temperatures, but

have systematic errors at lower temperatures. In particular, the possibility that the gap at $T \sim 2000$ K and subsequent reversal of the radius trend seen in Figures 6.12 and 6.15 is due to some sort of problem in model fitting must be investigated.

As an additional check on our results, we performed a χ^2 goodness of fit test that compares the observed photometric colors to synthetic colors to all models in our *BT-Settl* model grid (§5.5). Two caveats must be kept in mind in evaluating the results of the χ^2 test. First, whereas the methodology developed in §5.5 is optimized to interpolate results in between the steps of the discrete *BT-Settl* model grid, a χ^2 test evaluates the goodness of fit to the model spectra in grid increments and not in between them. The goodness of fit is therefore also a function of how close the observed colors happen to be to the colors of a particular model in the grid (as opposed to in between two grid elements). One must therefore expect that a wide range of minimal χ^2 values can indicate an adequate fit. Figure 6.7 shows the minimum χ^2 values for the objects in the observed sample plotted as a function of the objects' interpolated temperature. We see that most objects have a minimum reduced χ^2 value that falls on the range of zero to 0.2, and that there appears to be a well-defined upper boundary to this range. This effect is likely the result of the discrete nature of the *BT-Settl* grid. The resulting temperature for a particular object that has a minimum reduced χ^2 in the upper part of this range should therefore be treated with the same degree of confidence as the temperature for an object with a lower χ^2 value; the higher χ^2 value is likely the result of the object's colors being in between those of two grid elements, and could be brought down by a shift in the grid steps. In this sense, the methodology of §5.5 is superior to a simple χ^2

minimization approach because the 20 independent color comparisons draw information from several grid elements and the method uses interpolation to find the best fit. Second, we must keep in mind that a given effective temperature may appear several times in the *BT-Settl* grid because the grid is three-dimensional, with gravity and metallicity also playing a role. Because shifts in both gravity and metallicity can mimic the effect of a shift in temperature, multiple models with different combinations of gravity, metallicity, and temperature may have very similar χ^2 values. This degeneracy was broken in our adopted methodology §5.5 by testing several combinations of gravity and metallicity and determining which one was best at having most colors indicate a small temperature range. Because a χ^2 minimization procedure offers a single value (the χ^2 for a particular model) as opposed to the 20 values (one for each color) offered by our technique, it is more difficult to discard outliers and determine to which temperature the independent color tests are converging using the χ^2 methodology.

Despite these caveats, the χ^2 tests are nevertheless useful in assessing the temperature fits. Figure 6.7 shows the fits for the entire sample as a function of the objects' temperature. We see a slight increase in the minimum χ^2 values as the temperature decreases. The slight elevation is to be expected given the more uncertain optical photometry for cooler objects and the more complex nature of their atmospheres. Figure 6.7 shows four outliers with higher χ^2 values at temperatures below 2000 K. The two highly elevated values correspond to 2MASS J1126-5003 (ID# 36) and 2MASS J2224-0158 (ID# 60), from left to right. The minimum in the χ^2 trends for these two objects was not as sharp as those for the rest of the sample, and the results for those objects should be assigned a lesser degree of confidence. The

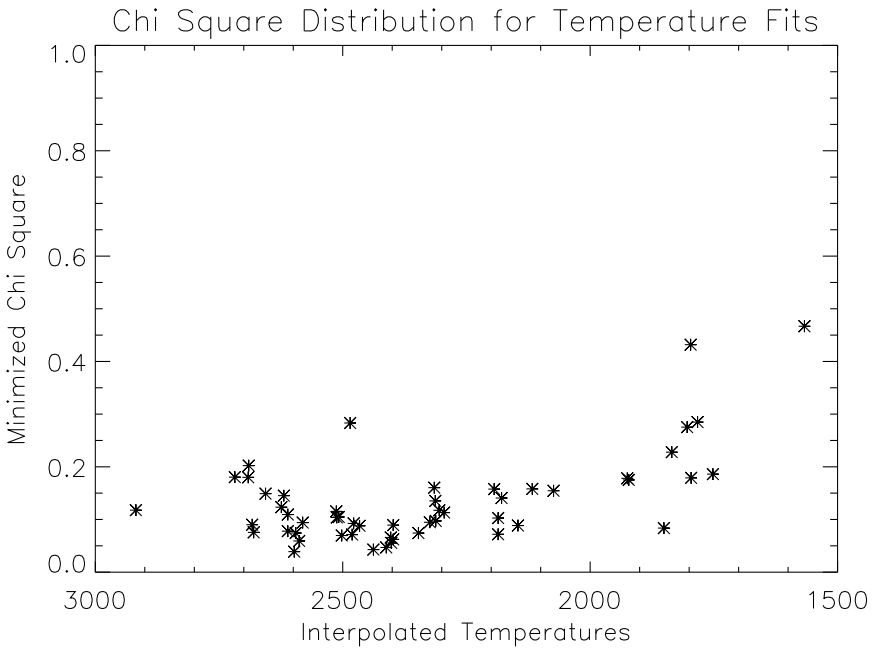

Figure 6.7 Minimum χ^2 for objects in the observed sample. Known unresolved binaries have been excluded. The horizontal axis denotes the interpolated effective temperature adopted for each object. The wide range of χ^2 values between zero and 0.2 is likely due to grid discreteness and differences in χ^2 values within that range should not be interpreted as differences in the goodness of the interpolated fit. The plot suggests that the dispersion of χ^2 values is somewhat higher at temperatures cooler than 2000 K. From left to right, the two very elevated values in the cool side of the plot correspond to 2MASS J1126-5003 (ID# 36) and 2MASS J2224-0158 (ID# 60). The minimum in the minimization trends (Figure 6.8) for these objects was marginal and the data should be treated with caution. The two slightly elevated objects are DENIS J1058-1548 (ID# 33) and 2MASS J0500+0330 (ID# 16), from left to right. Both of these objects had good minimization trends.

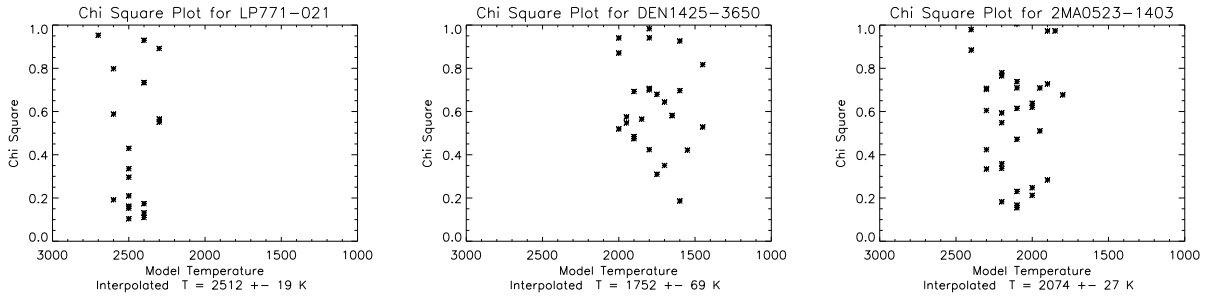

Figure 6.8 χ^2 plots for three representative objects. In all cases, there is a clear range of minimum χ^2 values that indicate that models around that temperature range are significantly better fits than at higher or lower temperatures. Because of grid discreteness and grid degeneracy in metallicity and gravity, it is often not possible to determine which single model is the best fit for most colors under consideration. Therefore, it is possible that the model with the lowest χ^2 value has a temperature slightly different from the interpolated temperature.

two slightly elevated cool objects are DENIS J1058-1548 (ID# 33) and 2MASS J0500+0330 (ID# 16), from left to right. Both of these objects had good minimization trends, suggesting that their slight elevation is not representative of a bad fit.

The χ^2 tests are a confirmation of the trend indicated by the error bars in Figure 6.15, where the error bars indicate that the dispersion amongst the effective temperatures determined by different colors is generally no higher at cooler temperatures. Both tests show that the morphology of the synthetic spectra are equally good representations of Nature at cool temperatures as they are at higher temperatures. There remains the possibility that somehow the models are assigning an inaccurate effective temperature to a morphologically correct spectrum, however given the strong dependence of spectral morphology on effective temperature, this hypothesis is most unlikely − a spectrum that adequately represents Nature most likely has an accurate effective temperature as a parameter. Figure 6.8 shows the range of χ^2 values that results from comparing the colors of three objects to models of several different temperatures. In all three cases the χ^2 trend has a pronounced minimum region that corresponds to the best effective temperature range. While the caveats about grid discreteness and degeneracy due to gravity and metallicity must be kept in mind and prevent us from picking the best temperature match amongst the spectra with the few lowest χ^2 values, it is still apparent that the convergence about a temperature range is strong. In other words, a few models clearly represent Nature much better than the other ones. From that, we can conclude that the range of temperatures indicated by the minimum χ^2 range is likely in agreement with the real temperature of the object in question.

6.4 Color-Magnitude Relations

Color-absolute magnitude relations are often the first tools used in estimating the distance to a star or brown dwarf. Determining useful relations using only near infrared colors is challenging for late M and L dwarfs due to the degenerate nature of the near infrared color-magnitude sequence. One possible solution is the use of spectral type-magnitude relations (e.g., Cruz et al. 2003); however, such relations require accurate knowledge of spectral types in a consistent system and are subject to the uncertainties inherent to any discrete classification system. Here we present new color-magnitude relations based on the optical photometry, 2MASS photometry, and trigonometric parallaxes reported in Table 5.3. Table 6.5 presents third order polynomial fits for all color-magnitude combinations of the filters *VRIJHK*$_s$ except for those with the color $R-I$, which becomes degenerate (i.e., nearly vertical) for $R-I>2.5$. As an example, the first line of Table 6.5 should be written algebraically as

$$M_V = 0.21509(V-R)^3 - 2.81698(V-R)^2 + 14.16273(V-R) - 1.45226\ (\pm 0.53)$$

$$1.61 \leq (V-R) \leq 3.64$$

The relations are an extension of those published in Henry et al. (2004) into the very red optical regime. They are also complementary to the *izJ* relations of Schmidt et al. (2010). Figure 6.9 shows the color-absolute magnitude diagrams and polynomial fits for M_v *vs.* $(V-K_s)$ and M_{Ks} *vs.* $(R-K_s)$. Known binaries as well as objects that are otherwise elevated in the color-magnitude diagrams were excluded when computing the polynomial fits. The

1σ uncertainties vary widely by color, and are as small as 0.24 magnitudes for colors that combine the V filter with the JHK_s filters.

Table 6.5: Coefficients for Color-Magnitude Polynomial Fits

abs. mag.	color	3^{rd} order	2^{nd} order	1^{st} order	constant	range	σ
M_V	$V-R$	0.21509	−2.81698	14.16273	−1.45226	1.61−3.64	0.53
M_V	$V-I$	−0.48431	7.02913	−30.24232	55.89960	3.44−6.24	0.64
M_V	$V-J$	−0.05553	1.34699	−8.78095	32.19850	5.28−9.75	0.30
M_V	$V-H$	−0.03062	0.79529	−5.04776	23.53283	5.91−11.00	0.24
M_V	$V-K$	−0.02006	0.54283	−3.22970	19.05263	6.23−11.80	0.25
M_V	$R-J$	0.38685	−4.78978	21.67522	−19.02625	3.67−6.19	0.39
M_V	$R-H$	−0.03466	0.96656	−4.96743	21.51357	4.30−7.44	0.37
M_V	$R-K$	−0.06296	1.36944	−7.28721	25.94882	5.30−8.24	0.40
M_V	$I-J$	1.18205	−9.28970	27.59574	−11.71022	1.84−3.70	0.42
M_V	$I-H$	0.24541	−2.81568	13.65365	−4.94381	2.47−4.95	0.48
M_V	$I-K$	0.09183	−1.32390	8.75709	−0.69280	2.79−5.75	0.51
M_V	$J-H$	5.05439	−19.22739	30.20127	5.70728	0.51−1.25	1.11
M_V	$J-K$	4.35996	−22.11834	40.93688	−5.24138	0.80−2.05	0.92
M_V	$H-K$	23.11303	−54.44877	51.74136	4.69129	0.29−0.80	0.84
M_R	$V-R$	0.21509	−2.81698	13.16273	−1.45226	1.61−3.64	0.53
M_R	$V-I$	−0.39598	5.59585	−23.46994	44.27366	3.44−6.24	0.60
M_R	$V-J$	−0.06508	1.48971	−9.70545	32.85954	5.28−9.75	0.33
M_R	$V-H$	−0.03213	0.78557	−4.94969	21.92657	5.91−11.00	0.28
M_R	$V-K$	−0.01882	0.47360	−2.65145	16.13934	6.23−11.80	0.27
M_R	$R-J$	0.10246	−0.87144	3.43087	7.64284	3.67−6.19	0.31
M_R	$R-H$	−0.09460	1.86774	−9.85431	28.99232	4.30−7.44	0.26
M_R	$R-K$	−0.08589	1.71800	−9.39445	28.84437	5.30−8.24	0.28
M_R	$I-J$	0.56097	−4.48907	14.76241	−2.05088	1.84−3.70	0.30
M_R	$I-H$	0.16178	−1.99780	10.43314	−2.43140	2.47−4.95	0.32
M_R	$I-K$	0.05698	−0.92853	6.77139	0.79636	2.79−5.75	0.35
M_R	$J-H$	6.18765	−22.77418	31.75342	3.61753	0.51−1.25	0.84
M_R	$J-K$	3.81245	−19.70377	36.29580	−4.63378	0.80−2.05	0.69
M_R	$H-K$	26.23045	−59.75888	51.53576	3.25785	0.29−0.80	0.65
M_I	$V-R$	−0.30086	1.51360	1.22679	6.92302	1.61−3.64	0.55
M_I	$V-I$	−0.48431	7.02913	−31.24230	55.89957	3.44−6.24	0.64
M_I	$V-J$	−0.08775	2.06323	−14.53807	43.98302	5.28−9.75	0.37
M_I	$V-H$	−0.05264	1.35632	−10.21586	35.60933	5.91−11.00	0.32
M_I	$V-K$	−0.03540	0.96451	−7.46468	29.33155	6.23−11.80	0.30
M_I	$R-J$	0.05949	−0.06127	−1.61308	15.59044	3.67−6.19	0.37
M_I	$R-H$	−0.15245	3.02932	−17.57707	43.57051	4.30−7.44	0.29

Continued on next page

abs. mag.	color	3^{rd} order	2^{nd} order	1^{st} order	constant	range	σ
M_I	$R-K$	−0.13466	2.76845	−16.87739	44.05227	5.30−8.24	0.29
M_I	$I-J$	0.34947	−2.28896	7.32700	3.70661	1.84−3.70	0.26
M_I	$I-H$	−0.05625	0.65099	−0.12146	8.93958	2.47−4.95	0.27
M_I	$I-K$	−0.07979	0.96350	−1.79721	11.08030	2.79−5.75	0.30
M_I	$J-H$	1.00902	−9.06504	20.09129	4.41802	0.51−1.25	0.76
M_I	$J-K$	2.30591	−13.03453	26.79644	−2.67247	0.80−2.05	0.62
M_I	$H-K$	6.36493	−24.92761	31.89872	4.41508	0.29−0.80	0.60
M_J	$V-R$	−0.33337	2.21935	−2.66206	9.68513	1.61−3.64	0.39
M_J	$V-I$	−0.36037	5.32260	−24.29187	45.23880	3.44−6.24	0.45
M_J	$V-J$	−0.05553	1.34699	−9.78094	32.19847	5.28−9.75	0.30
M_J	$V-H$	−0.03301	0.88633	−6.95483	26.83274	5.91−11.00	0.26
M_J	$V-K$	−0.02220	0.63644	−5.19321	22.87309	6.23−11.80	0.25
M_J	$R-J$	0.10247	−0.87144	2.43089	7.64280	3.67−6.19	0.31
M_J	$R-H$	−0.07510	1.64461	−10.09617	28.93402	4.30−7.44	0.25
M_J	$R-K$	−0.07709	1.67484	−10.64410	31.00300	5.30−8.24	0.26
M_J	$I-J$	0.34947	−2.28897	6.32701	3.70660	1.84−3.70	0.26
M_J	$I-H$	−0.01826	0.36899	−0.39111	8.86504	2.47−4.95	0.25
M_J	$I-K$	−0.05043	0.71480	−1.94540	10.88528	2.79−5.75	0.26
M_J	$J-H$	−1.75450	1.46627	6.33858	6.88885	0.51−1.25	0.52
M_J	$J-K$	0.89335	−5.42563	12.79557	2.55729	0.80−2.05	0.44
M_J	$H-K$	−0.71691	−5.04246	13.53644	6.37982	0.29−0.80	0.44
M_H	$V-R$	−0.14308	0.68377	1.11084	6.14662	1.61−3.64	0.33
M_H	$V-I$	−0.27640	4.04822	−18.12088	34.99090	3.44−6.24	0.38
M_H	$V-J$	−0.04698	1.11998	−7.94481	26.92333	5.28−9.75	0.25
M_H	$V-H$	−0.03062	0.79529	−6.04775	23.53280	5.91−11.00	0.24
M_H	$V-K$	−0.02177	0.59741	−4.70539	20.62932	6.23−11.80	0.24
M_H	$R-J$	0.05414	−0.30135	0.23514	9.78688	3.67−6.19	0.27
M_H	$R-H$	−0.09460	1.86773	−10.85430	28.99230	4.30−7.44	0.26
M_H	$R-K$	−0.08348	1.70954	−10.45700	29.39801	5.30−8.24	0.27
M_H	$I-J$	0.19024	−1.18253	3.72420	5.16641	1.84−3.70	0.24
M_H	$I-H$	−0.05625	0.65099	−1.12146	8.93959	2.47−4.95	0.27
M_H	$I-K$	−0.06209	0.76792	−1.96050	10.17762	2.79−5.75	0.28
M_H	$J-H$	−1.75451	1.46627	5.33858	6.88885	0.51−1.25	0.52
M_H	$J-K$	1.03555	−6.09029	13.19045	2.07593	0.80−2.05	0.45
M_H	$H-K$	0.29861	−8.11097	14.59934	5.74926	0.29−0.80	0.43
M_K	$V-R$	−0.00121	−0.37537	3.46600	4.16422	1.61−3.64	0.31
M_K	$V-I$	−0.20466	3.00271	−13.26362	27.36341	3.44−6.24	0.34
M_K	$V-J$	−0.03630	0.86706	−6.07434	22.17402	5.28−9.75	0.24
M_K	$V-H$	−0.02655	0.68316	−5.12699	20.83821	5.91−11.00	0.24
M_K	$V-K$	−0.02006	0.54283	−4.22970	19.05261	6.23−11.80	0.25
M_K	$R-J$	0.04475	−0.23500	0.13773	9.38717	3.67−6.19	0.26
M_K	$R-H$	−0.10097	1.92794	−11.03651	28.84667	4.30−7.44	0.27
M_K	$R-K$	−0.08589	1.71800	−10.39445	28.84436	5.30−8.24	0.28

Continued on next page

abs. mag.	color	3^{rd} order	2^{nd} order	1^{st} order	constant	range	σ
M_K	$I-J$	0.14572	−0.88536	2.93380	5.59314	1.84−3.70	0.25
M_K	$I-H$	−0.09030	0.98749	−2.35957	10.16948	2.47−4.95	0.28
M_K	$I-K$	−0.07979	0.96350	−2.79722	11.08030	2.79−5.75	0.30
M_K	$J-H$	−1.86948	1.75166	4.48358	6.92764	0.51−1.25	0.49
M_K	$J-K$	−1.86948	1.75166	4.48358	6.92764	0.51−1.25	0.49
M_K	$H-K$	0.29864	−8.11102	13.59936	5.74925	0.29−0.80	0.43

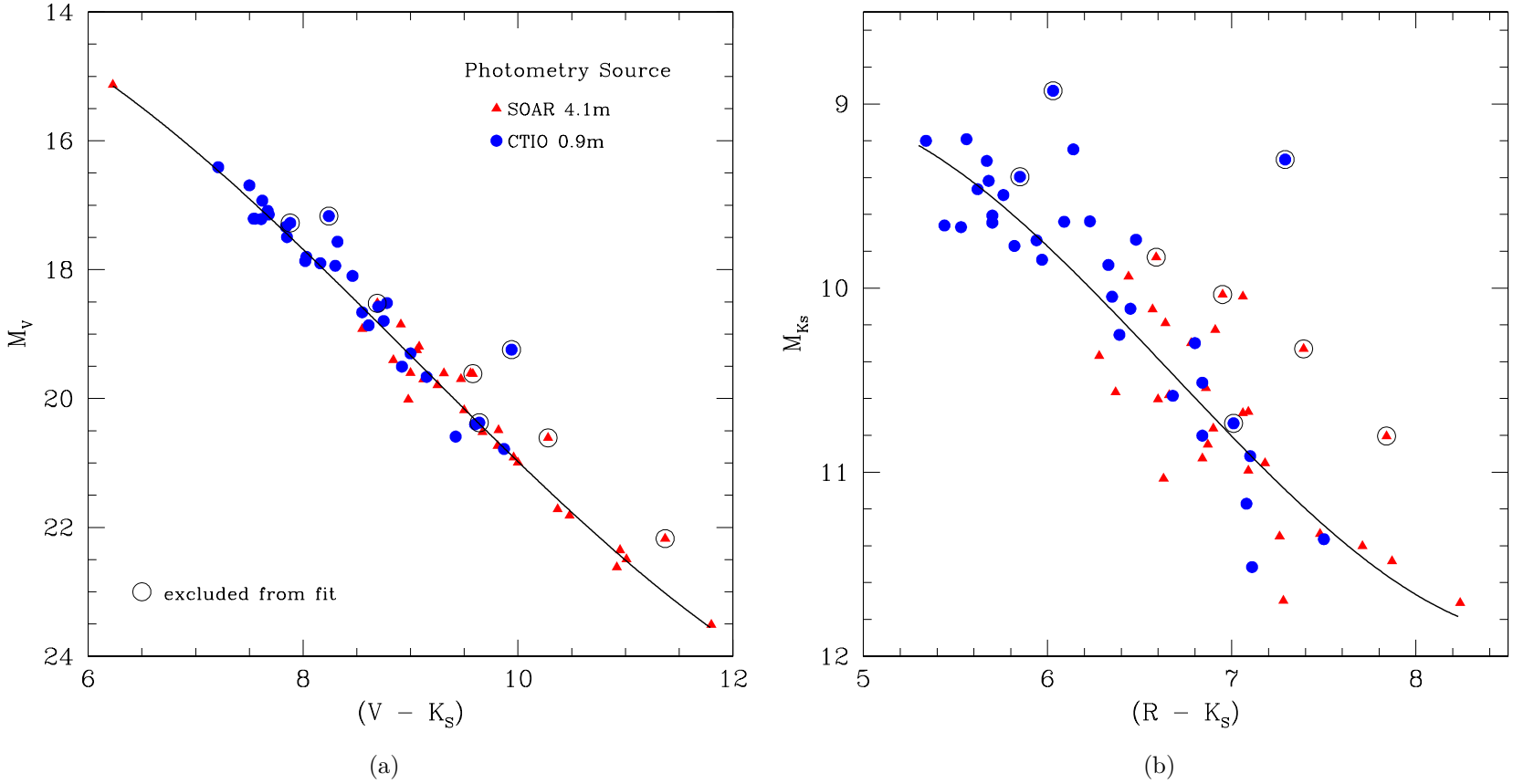

Figure 6.9 Example color-absolute magnitude diagrams over-plotted with third order polynomial fits. The $M_v \times$ (V−K) relation shown in (a) has a particularly low uncertainty ($\sigma = 0.25$ mag) due to the steep decrease in V band flux in the late M and L dwarf sequence. The $M_k \times$ (R−K) relation shown in (b) has a slightly higher uncertainty ($\sigma = 0.28$ mag) but is more practical from an observational point of view due to the difficulty in obtaining V band photometry for L dwarfs. Binary or otherwise elevated objects were excluded from the polynomial fits and are shown enclosed with open circles. Figure (b) uses the same labeling scheme as Figure (a).

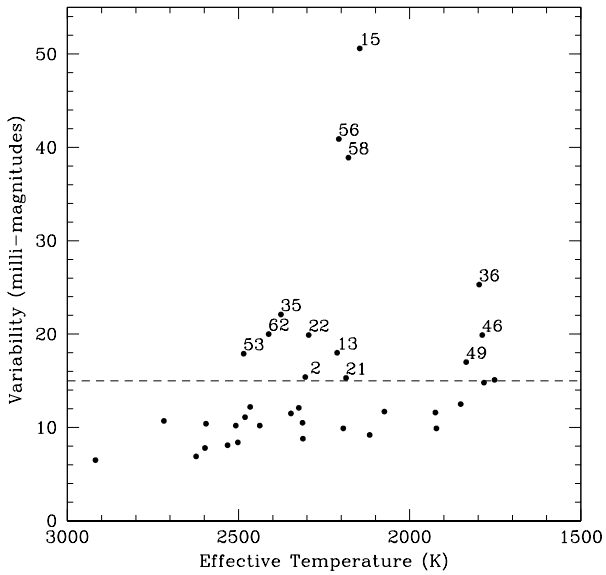

Figure 6.10 *I* band photometric variability derived from trigonometric parallax observations. The linear increase in minimum variability with decreasing temperature is most likely not real and caused by lower signal-to-noise for fainter targets. To account for this trend we established the threshold for deeming a target variable at 15 milli-magnitudes, indicated by the dashed line. Thirteen out of a sample of 36 targets are above the threshold and are labeled wit the ID number used in Table 6.1. See §6.8 for a discussion of the three most variable targets.

6.5 Optical Variability

Photometric variability in very low mass stars and brown dwarfs has lately become an active area of research because variability can serve as a probe of many aspects of an object's atmosphere (e.g, Heinze et al. 2013). The leading candidate mechanisms thought to cause photometric variability are non-uniform cloud coverage in L and early T dwarfs (e.g., Radigan et al. 2012; Apai et al. 2013), optical emission due to magnetic activity, and the existence of cooler star spots due to localized magnetic activity. The period of variability is often thought to correspond to the object's period of rotation. Harding et al. (2011) have suggested that the link between optical variability and radio variability in two L dwarfs is

indicative of auroral emission analogous to that seen in Jupiter. Khandrika et al. (2013) report an overall variability fraction of $36^{+7}_{-6}\%$ for objects with spectral types ranging from L0 to L5 based on their own observations as well as six previous studies (Bailer-Jones & Mundt 2001; Gelino et al. 2002; Koen 2003; Enoch et al. 2003; Koen et al. 2004; Koen 2005). The threshold for variability of these studies ranged from 10 to 36 milli-magnitudes and were conducted using various photometric bands.

We have measured I band photometric variability as part of our parallax observations. Differential photometry of the parallax target is measured with respect to the astrometric reference stars. Any reference star found to be variable to more than 50 milli-magnitudes is discarded and the remaining stars are used to determine the baseline variability for the field. Details of the procedure are discussed in Jao et al. (2011). Figure 6.10 shows the 1σ variability for 36 parallax targets[2]. Because the parallax targets were mostly fainter than the reference stars, photometric signal-to-noise of the target objects is the limiting factor for sensitivity to variability. This limit becomes more pronounced for cooler and fainter stars, thus creating the upward linear trend for the least variable objects in Figure 6.10. Because of this trend, we have conservatively set the threshold for deeming a target variable at 15 milli-magnitudes, as indicated by the dashed line in Figure 6.10. We detect 13 variable objects out of 36, corresponding to an overall variability of $36^{+9}_{-7}\%$ where the uncertainties are calculated using binomial statistics[3]. While this result is in excellent agreement to that

[2]GJ 1001BC is photometrically contaminated by the much brighter A component, and was therefore excluded from the variability study.

[3]A review of binomial statistics as applied to stellar populations can be found in the appendix of Burgasser et al. (2003b)

of Khandrika et al. (2013) (36^{+7}_{-6}%), we note that our sample includes spectral types M6V to L4, while theirs ranges from L0 to L5. Targets found to be significantly variable are labeled in Figure 6.10 with their ID numbers. The objects 2MASS J0451-3402 (L0.5, ID# 15), 2MASS J1705-0516AB (L0.5 joint type, ID# 56), and SIPS J2045-6332 (M9.0V, ID# 58) stand out as being much more variable than the rest of the sample. We defer discussion of these objects until §6.8.

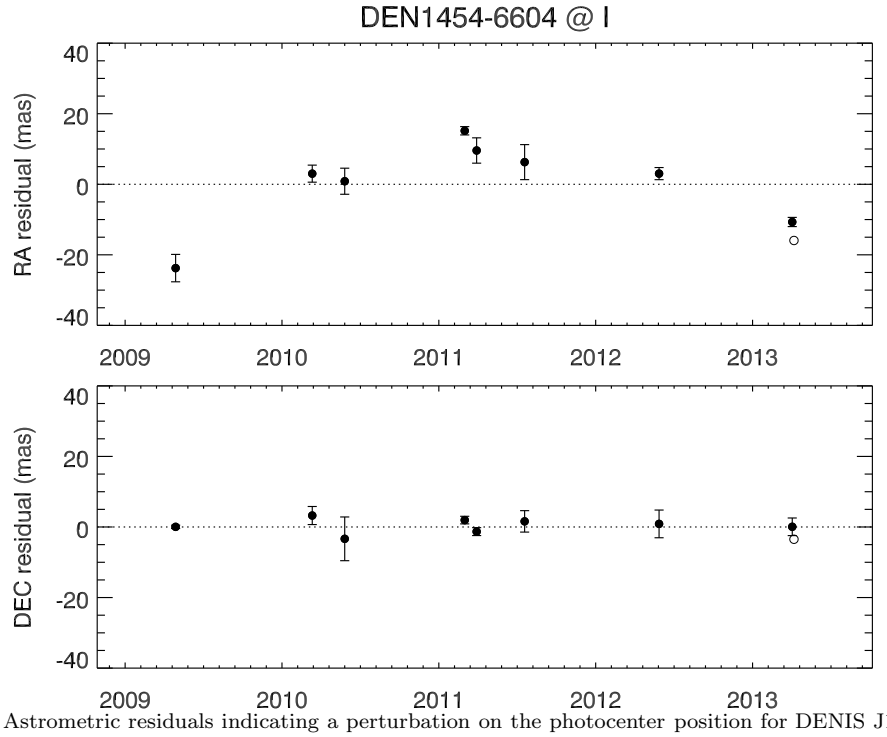

Figure 6.11 Astrometric residuals indicating a perturbation on the photocenter position for DENIS J1454-6604 with data taken in the I band. The dots correspond to the positions of the system's photocenter once proper motion and parallax reflex motion are removed. Each solid dot is the nightly average of typically three consecutive observations. The open dot represents a night with a single observation. The lack of a discernible perturbation in the declination axis indicates that the system is viewed nearly edge-on and that its orbital orientation is primarily East−West.

6.6 DENIS J1454-6604AB – A New Astrometric Binary

DENIS J1454-6604AB is an L3.5 dwarf first identified by Phan-Bao et al. (2008). We report a trigonometric parallax of 84.88±1.71 mas, corresponding to a distance of $11.78^{+0.24}_{-0.23}$ pc.

Figure 6.11 shows the residuals to the trigonometric parallax solution, denoting the motion of the object's photocenter once the parallax reflex motion and the proper motion have been subtracted. The sinusoidal trend in the RA axis is strong indication of an unseen companion that is causing the system's photocenter to move with respect to the reference stars. The absence of a discernible trend in the declination axis indicates that the system must be nearly edge-on and its orbit has an orientation that is predominantly East-West. At this stage it is not possible to determine the system's period or component masses. While it may appear in Figure 6.11 that the system has completed nearly half an orbital cycle in the $\sim$4 years that we have been monitoring it, unconstrained eccentricity means that the system may take any amount of time to complete the remainder of its orbit.

Once the full orbit of a photocentric astrometric system is mapped, determining the mass and luminosity ratio of the system is a degenerate problem. The same perturbation can be produced by either a system where the companion has a much lower mass and luminosity than the primary or by a system where the components have *nearly* the same mass and luminosity. We note that a system where the two components are *exactly* equal would be symmetric about the barycenter and would therefore produce no perturbation at all (§7.2). The fact that the system appears elevated in the HR diagram (Figure 6.3) is an indication that the secondary component is contributing considerable light and that therefore the nearly equal mass scenario is more likely. As described in Dieterich et al. (2011), a single high resolution image where both components are resolved is enough to determine the flux ratio of the components and therefore determine individual dynamical masses once the full

photocentric orbit has been mapped.

We will closely monitor this system with the goal of reporting the component masses once orbital mapping is complete.

6.7 The End of the Stellar Main Sequence

One of the most remarkable facts about VLM stars is that a small change in mass or metallicity can bring about profound changes to the basic physics of the object's interior, if the change in mass or metallicity pushes the object into the realm of the brown dwarfs, i.e., on the other side of the hydrogen burning minimum mass limit. If the object is unable to reach thermodynamic equilibrium through sustained nuclear fusion, the object's collapse will be halted by non-thermal electron degeneracy pressure. The macroscopic properties of (*sub*)stellar matter are then ruled by different physics and obey a different equation of state (e.g., Saumon et al. 1995). Once electron degeneracy sets in at the core, the greater gravitational force of a more massive object will cause a larger fraction of the brown dwarf to become degenerate, causing it to have a smaller radius. The mass-radius relation therefore has a pronounced local minimum near the critical mass attained by the most massive brown dwarfs (Chabrier et al. 2009; Burrows et al. 2011). Identifying the stellar/substellar boundary by locating the minimum radius in the stellar/substellar sequence has an advantage over other search methods (§5.1.1): while the *values* associated with the locus of minimum radius depend on the unconstrained details of evolutionary models (§6.7.3), its *existence* is a matter of basic physics and is therefore largely model independent.

In Figures 6.12 and 6.15 we re-arrange the HR diagram of Figure 6.3 to make radius an explicit function of luminosity (Figure 6.12) and effective temperature (Figure 6.15). Both Figures are followed by versions that use object ID numbers and spectral types as labels. We do not plot the data for LEHPM2-0174 and SIPS J2045-6332, which have abnormally elevated radii and would have made the figures difficult to read. These two objects are presumably young and are discussed individually in §6.8. After excluding the objects marked as known binaries and a few other elevated objects that we suspect are binary or young objects, both diagrams show the inversion of the radius trend near the location of the L2.5 dwarf 2MASS J0523-1403. Figures 6.12 and 6.15 can be compared to Figures 3, 4, and 5 of Burrows et al. (2011) and Figures 1 and 2 of Chabrier et al. (2009) for insight into how the data fit the predicted local minimum in the radius trends. While these works examine radius as a theoretical function of mass at given isochrones, there is a remarkable similarity between the overall shape of the theoretical mass-radius trend and the luminosity-radius and temperature-radius trends we detect empirically. The real data are likely best represented by a combination of isochrones that is biased towards the ages at which high mass substellar objects shine as early L dwarfs (See §6.7.1 and Figures 6.21−6.24). While Figure 1 of Chabrier et al. (2009) indicates radii as small as $\sim 0.075 R_{\odot}$ for the 10 Gyr isochrone, we should not expect to see radii this small in this study because substellar objects with that age are no longer in the luminosity range we observed (M6V to L4, §5.2). The same argument is valid for the figures in Burrows et al. (2011). Indeed, because luminosity and temperature are primarily functions of mass for stars and primarily functions of mass and

age for brown dwarfs, the plots in Figures 6.12 and 6.15 essentially replicate the morphology of the mass-radius relation with added dispersion caused by the observed sample's finite ranges of metallicity and age.

2MASS J0523-1403 has $T_{\rm eff} = 2,074 \pm 27K$, $\log(L/L_{\odot}) = -3.898 \pm 0.021$, $(R/R_{\odot}) = 0.086 \pm 0.0031$, and $V - K = 9.42$. While we cannot exclude the possibility of finding a stellar object with smaller radius, it is unlikely that such an object would be far from the immediate vicinity of 2MASS J0523-1403 in these diagrams[4]. If cooler and smaller radii stars exist, they should be more abundant than the brown dwarfs forming the upward radius trend at temperatures cooler than 1900 K in Figure 6.15 because such stars would spend the vast majority of their lives on the main sequence, where their positions in the diagrams would be almost constant, whereas brown dwarfs would constantly cool and fade, thus moving to the right in the plots. We detect no such objects. We note that while the brown dwarfs cooler than 1900 K in Figure 6.15 are brighter than any putative lower radius star of the same temperature, the difference would amount to only $\sim$0.3 magnitudes, which is not enough to generate a selection effect in our sample definition.

[4]See Table 6.6 for model predictions regarding the radius of the smallest possible star.

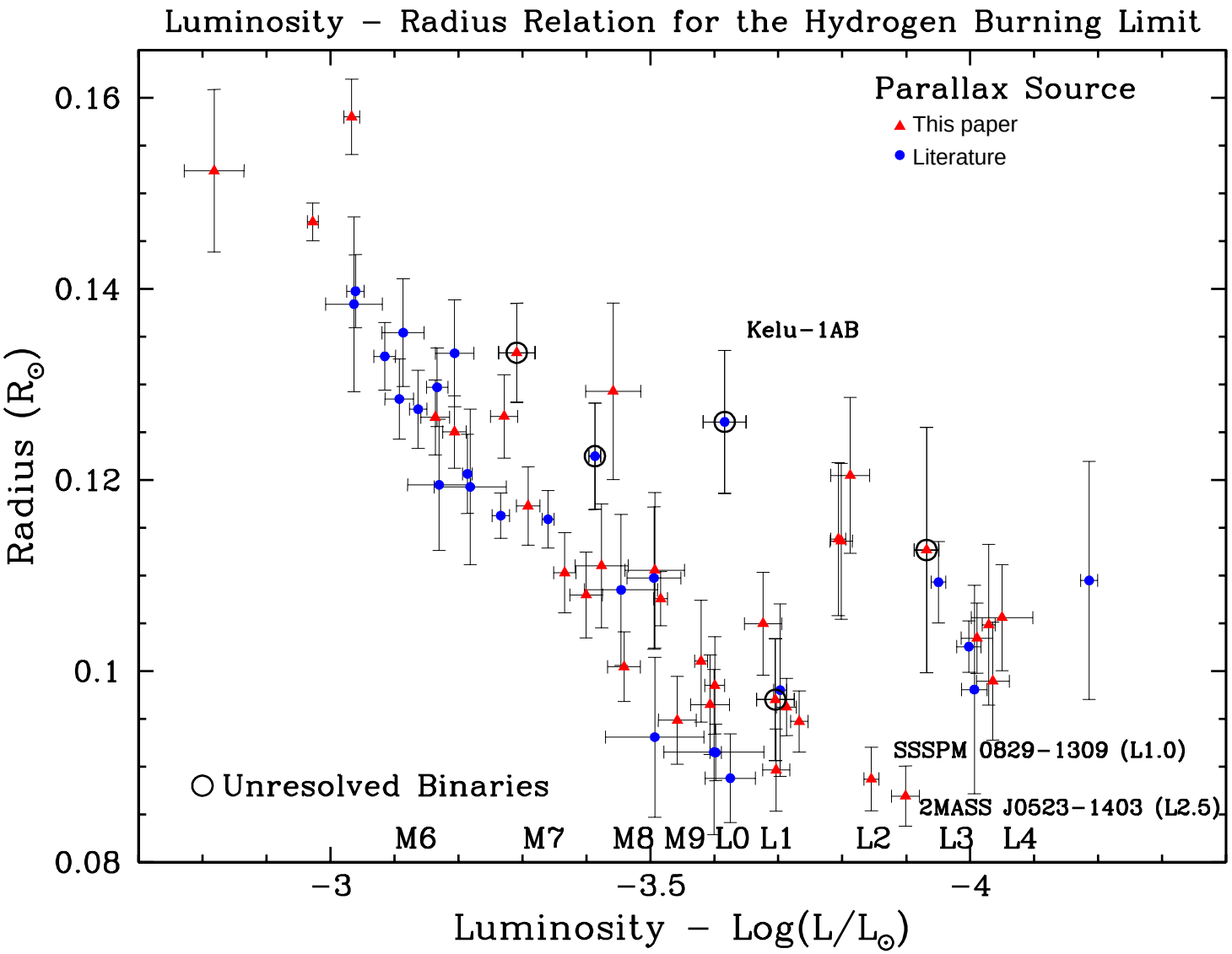

Figure 6.12 Luminosity–Radius diagram for the observed sample. The targets are the same as in Figure 6.3 except for LEHPM2-0174 and SIPS J2045-6332, which were excluded for scaling purposes due to their large radii and are discussed in §6.8. This diagram provides the same fundamental information as an HR diagram, but makes radius easier to visualize. Once known and suspected binaries are excluded, the radius trend has an inversion about 2MASS J0523-1403 (L2.5), indicating the onset of core electron degeneracy for cooler objects. The location and relevance of Kelu-1AB is discussed in §6.8.

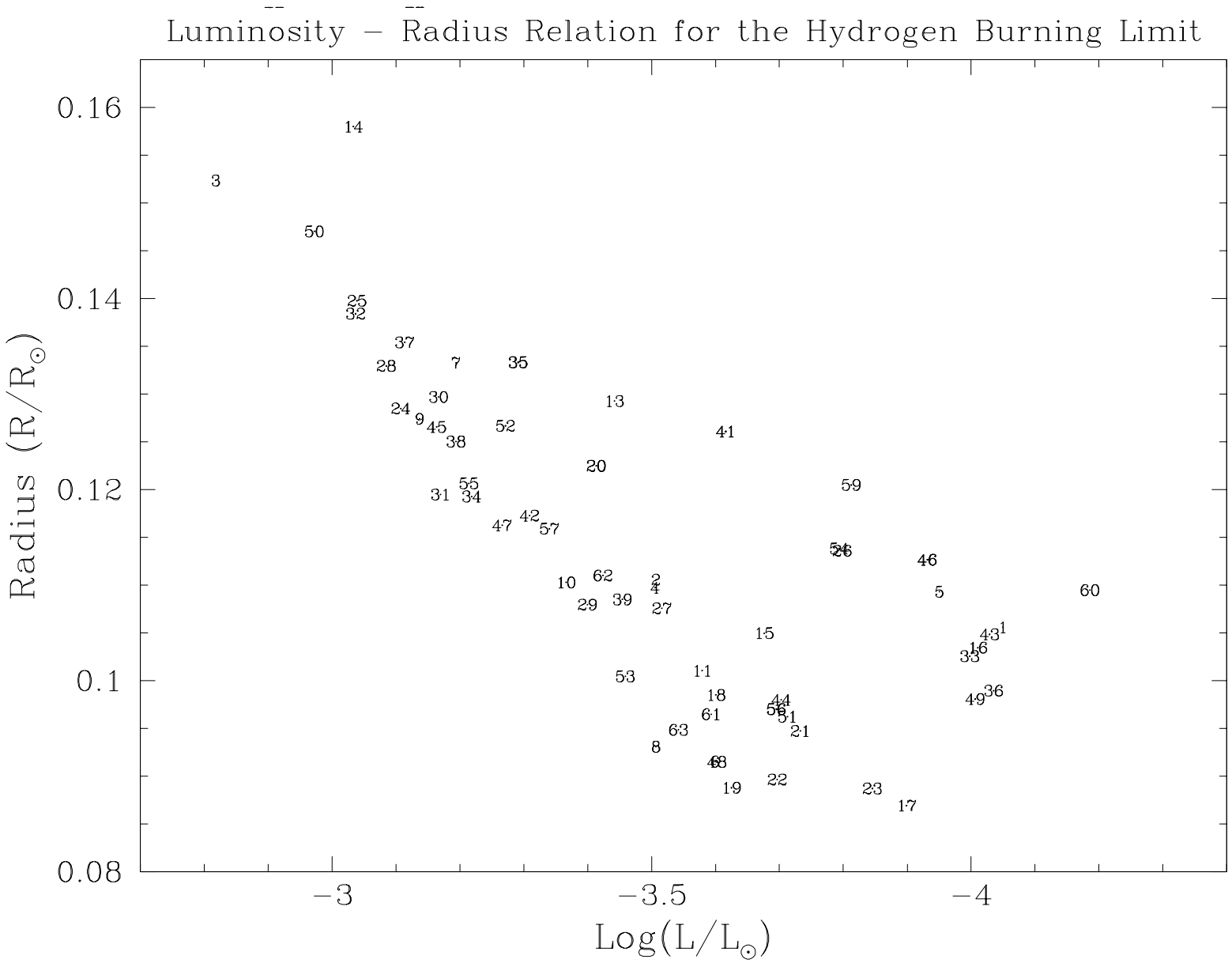

Figure 6.13 Same as Figure 6.12, but plotted with the ID numbers used in Tables 5.3 and 6.3.

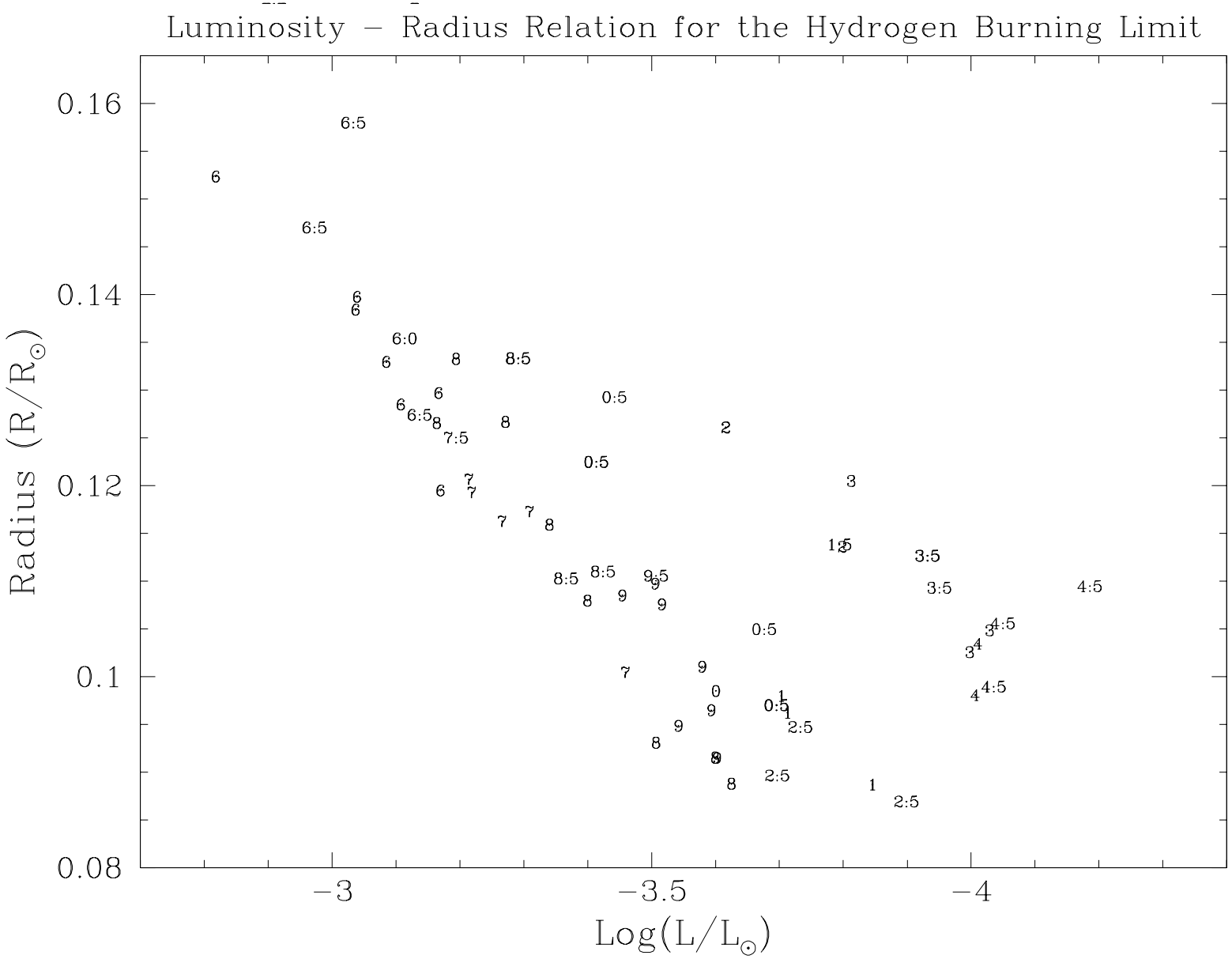

Figure 6.14 Same as Figure 6.12, but plotted with spectral types. Numbers 6−9.5 represent M subtypes. Numbers 0−4.5 represent L subtypes.

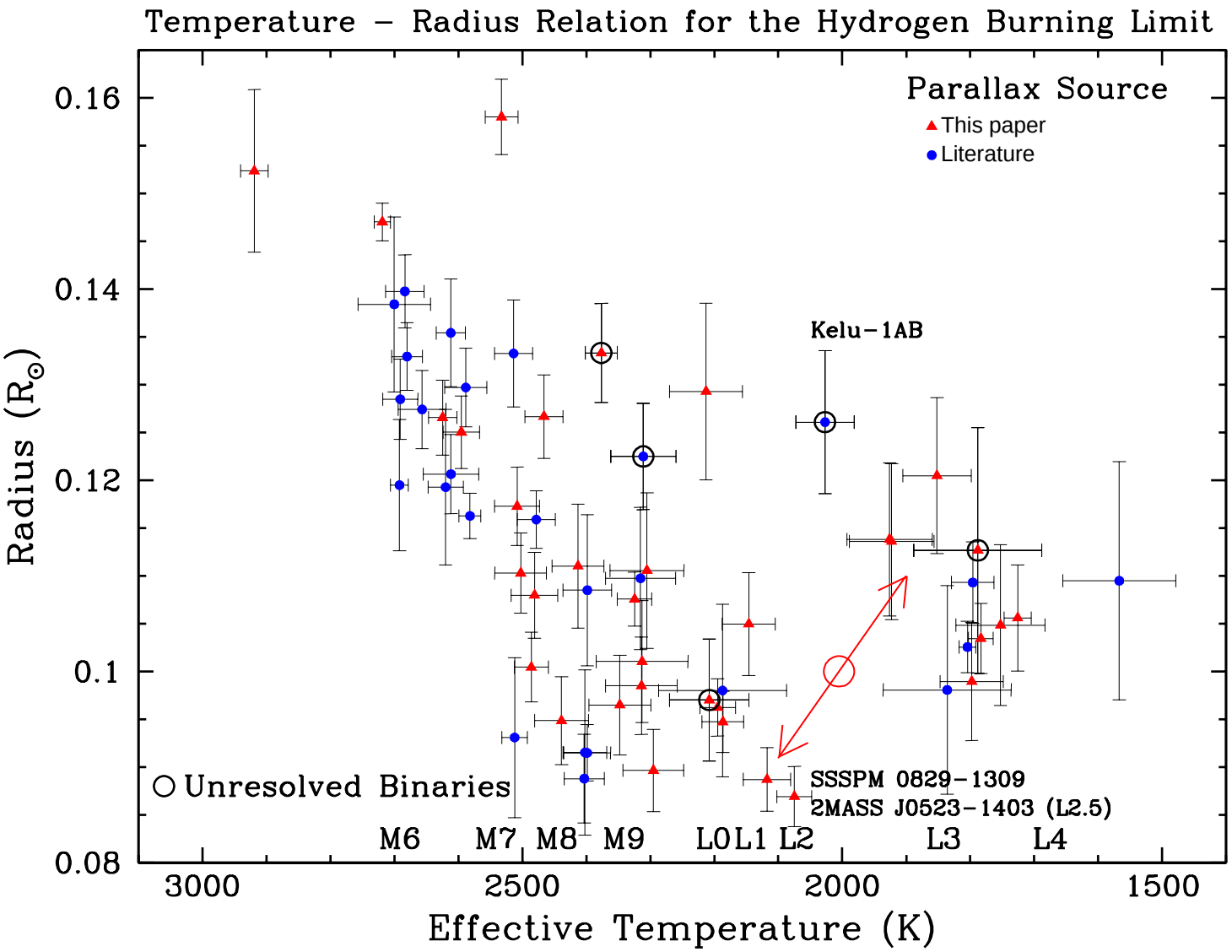

Figure 6.15 Temperature−Radius diagram for the observed sample. The targets are the same as in Figure 6.3 except for LEHPM2-0174 and SIPS J2045-6332, which were excluded for scaling purposes due to their large radii and are discussed in §6.8. This diagram provides the same fundamental information as an HR diagram, but makes radius easier to visualize. Once known and suspected binaries are excluded, the radius trend has an inversion about 2MASS J0523-1403 (L2.5), indicating the onset of core electron degeneracy for cooler objects. The location and relevance of Kelu-1AB is discussed in §6.8. The red double-headed arrow indicates the effect of varying the temperature by 100K at 2000K (5%) at a radius of 0.10 $R_{\odot}$. For most targets the uncertainty in radius is dominated by the uncertainty in effective temperature, meaning that an object's position would vary along the diagonal line of a rectangle formed by the error bars of temperature and radius.

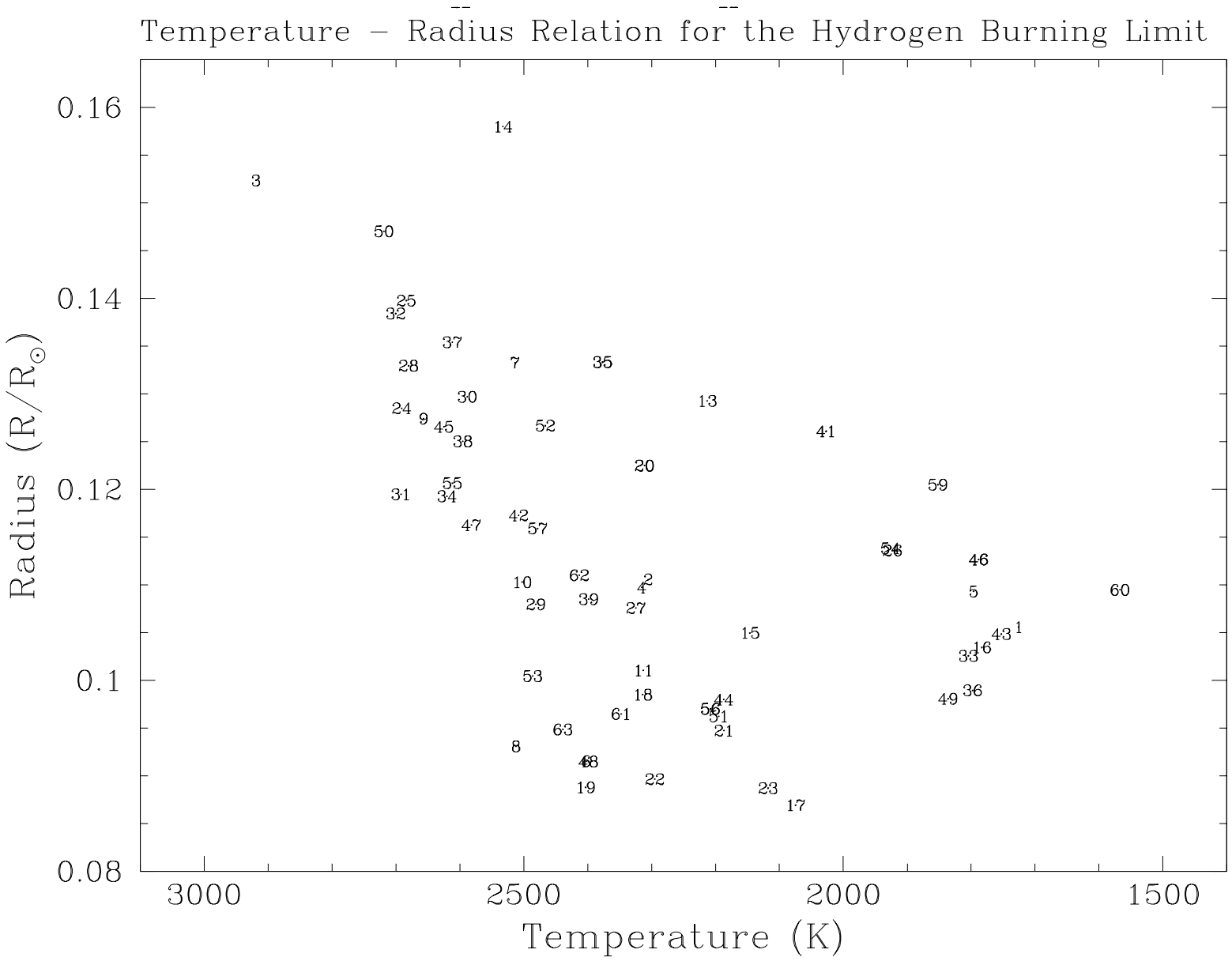

Figure 6.16 Same as Figure 6.15, but plotted with the ID numbers used in Tables 5.3 and 6.3.

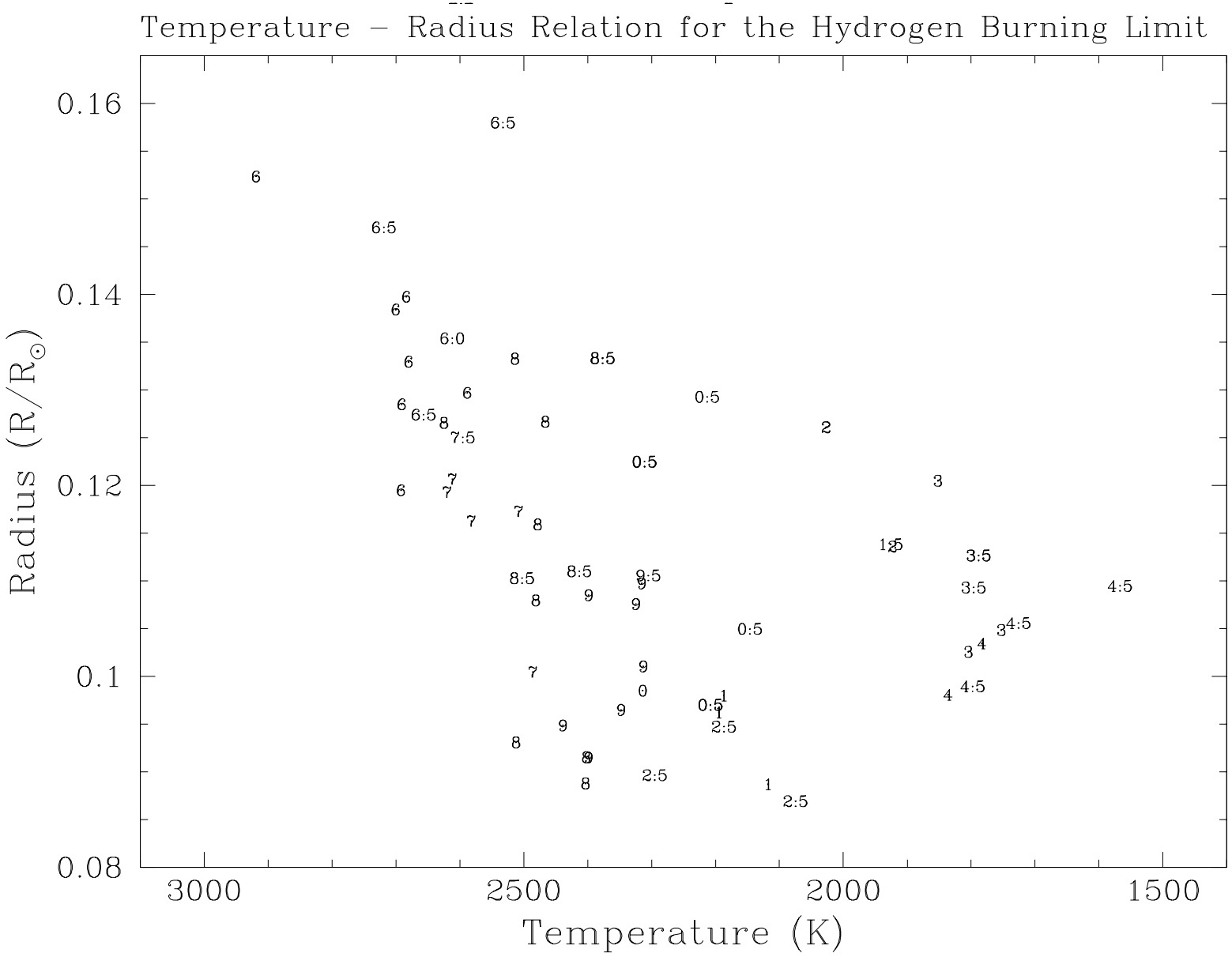

Figure 6.17 Same as Figure 6.15, but plotted with spectral types. Numbers 6−9.5 represent M subtypes. Numbers 0−4.5 represent L subtypes.

6.7.1 A Discontinuity at the End of the Main Sequence

Figures 6.12 and 6.15 show a relative paucity of objects forming a gap at temperatures (luminosities) immediately cooler (fainter) than 2MASS J0523-1403. This gap is then followed by a densely populated region where the radii are larger in both diagrams. Although we cannot at this point exclude the hypothesis that this gap is due to statistics of small numbers, we note that the existence of such a gap is consistent with the onset of the brown dwarf cooling curve. The stellar sequence to the left-hand-side of 2MASS J0523-1403 is well populated because VLM stars have extremely long main sequence lives, therefore holding their positions in the diagrams. The space immediately to the right-hand-side of 2MASS J0523-1403 is sparsely populated because objects in that region must be in a very narrow mass and age range. They must be very high mass brown dwarfs that stay in that high luminosity (temperature) region for a relatively brief period of time before they fade and cool. The population density increases again to the right of this gap because that region can be occupied by brown dwarfs with several combinations of age and mass.

The space density as functions of luminosity and effective temperature inferred from Figures 6.12 and 6.15 can be compared to theoretical mass and luminosity functions, while keeping in mind the important caveat that our observed sample is not volume complete (§5.2). The mass functions of Burgasser (2004) and Allen et al. (2005) both predict a shallow local minimum in the space distribution of dwarfs at temperatures $\sim$2000 K. In particular, Figure 6 of Burgasser (2004) predicts a relatively sharp drop in space density at 2000 K, in a manner similar to our results. However, the subsequent increase in space density at

cooler temperatures is predicted to be gradual in both Burgasser (2004) and Allen et al. (2005) (Figure 2). Neither mass function predicts the sudden increase in space density we see at ∼1800 K in Figure 6.15. This last point is particularly noteworthy because the sample selection criteria for this study (§5.2) aims to evenly sample the spectral type sequence. Our selection effect works *against* the detection of any variation in space density as a function of mass and luminosity, and yet we still detect a sharper gap between ∼2000 K and ∼1800 K than what is expected from the mass functions. Burgasser (2004) also predicts a population with significant stellar content down to temperatures of ∼1900 K, whereas the temperature-radius and luminosity-radius trends indicate that the coolest stellar object in our sample is 2MASS J0523-1403, with $T_{\rm eff} = 2074 \pm 27$ K. In summary, one may say that the current mass functions are useful in replicating the overall morphology of the observed distribution, but do not fully explain the detailed structure we notice at the end of the stellar main sequence. Only observing a truly volume-complete sample will yield definite answers about population properties such as the mass function.

The discontinuity is even more pronounced in terms of radius: whereas radius decreases steadily with decreasing temperature until the sequence reaches 2MASS J0523−1403 ($R = 0.086 R_{\odot}$), it then not only starts increasing, but jumps abruptly to a group of objects with $R \sim 0.1 R_{\odot}$. The discontinuity in radius is also visible as an offset in the HR diagram (Figure 6.3). This discontinuity is further evidence of the end of the stellar main sequence and has a simple explanation: whereas stars achieve their minimum radius at the zero age main sequence, brown dwarfs continue to contract slightly as they cool (Burrows et al. 1997;

Baraffe et al. 1998; Chabrier et al. 2000; Baraffe et al. 2003). Substellar objects with radii falling in the discontinuity should therefore be high mass brown dwarfs that fall outside the luminosity range of our sample (M6V to L4, §5.2). We note that this sudden increase in radius is a different effect than the previously mentioned sudden decreases in luminosity and temperature. The fact that these discontinuities occur at the same location and can be explained by consequences of the stellar/substellar boundary provides strong evidence that we have indeed detected the boundary.

The above argument for the causes of the discontinuity also lend credence to the idea that 2MASS J0523-1403 is a star despite the fact that it has the smallest radius in the sample. We note that 2MASS J0523-1403 and the L1.0 dwarf SSSPM J0829-1309 located immediately to its left fit nicely within the linear stellar sequences in Figures 6.3, 6.12, and 6.15. As already discussed, we would also expect stars to be more prevalent than brown dwarfs around the locus of minimum radius due to the limited amount of time during which a massive brown dwarf would occupy that parameter space. Most importantly, there is a difference between the *local* minimum in the radius trends and the *absolute* minimum. While theory predicts that the object with the smallest radius should be the most massive *brown dwarf* (Burrows et al. 2011), such an object would not attain its minimum radius until it cools down and enters the T and Y dwarf regime, and therefore drifts beyond the luminosity range of this study.

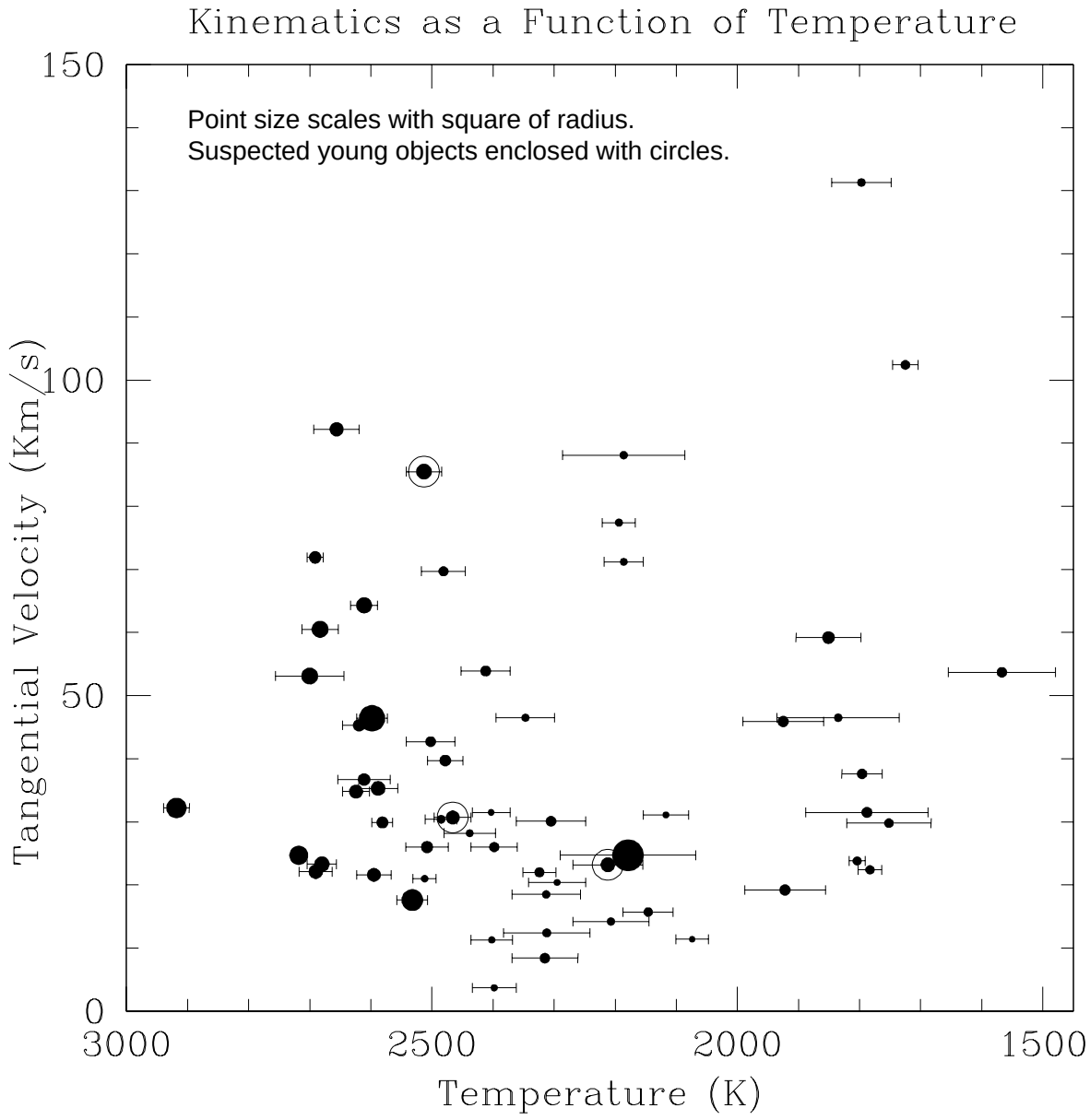

Figure 6.18 Temperature−Tangential Velocity Relation for the observed sample. The radius of the symbols scales with the square of the object's radius. Three suspected young objects are over-plotted with open circles. Known unresolved binaries have been excluded. No definitive signs of distinct kinematic groups are apparent. In particular, objects cooler than 2000 K, which are elevated in Figure 6.15 do not seem to be a very young population.

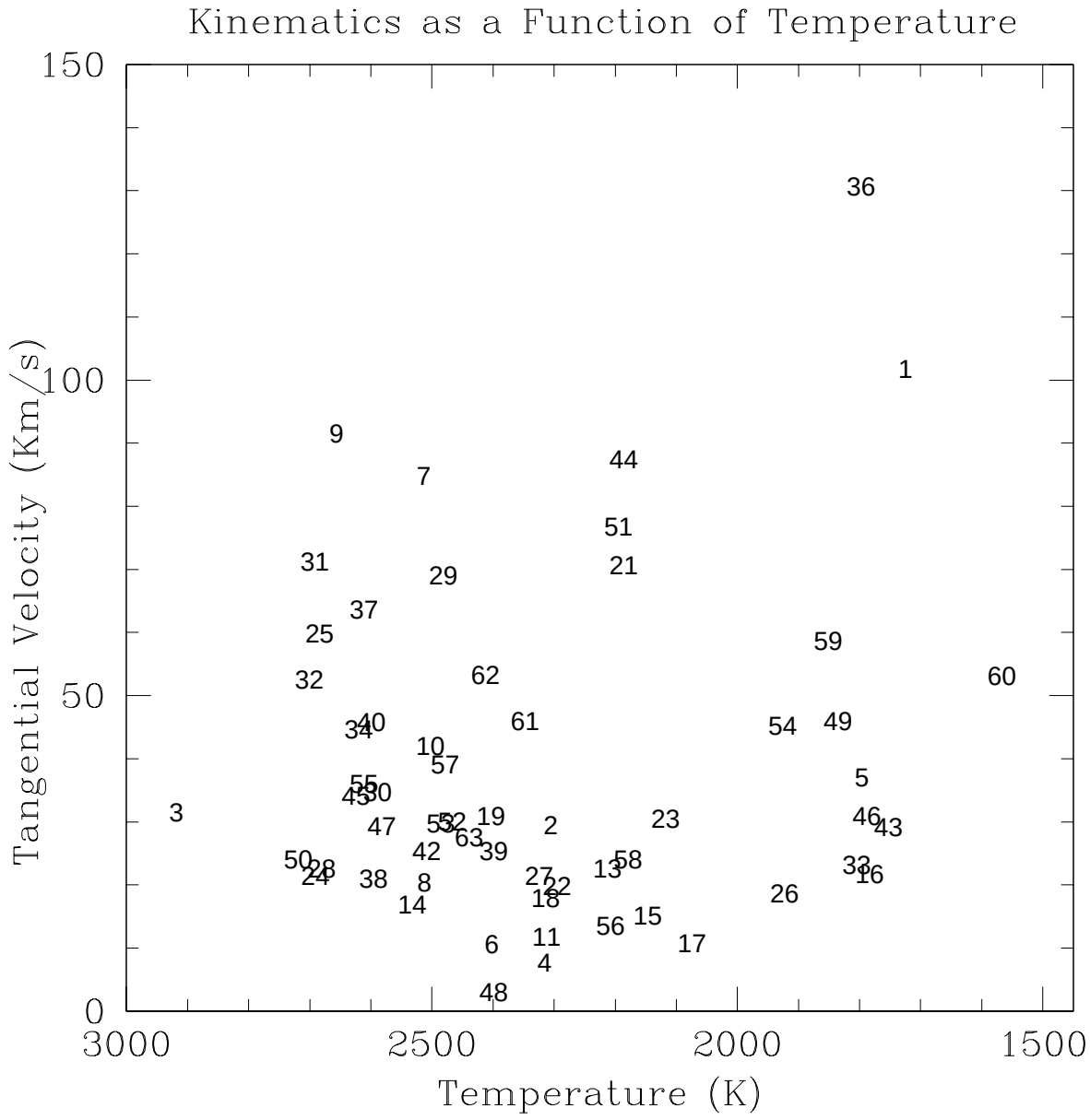

Figure 6.19 Same as Figure 6.18, plotted with ID numbers.

6.7.2 Kinematic Analysis

The space velocities of a stellar population can be statistically associated with stellar age (§2.4). The basic idea behind the concept is that stars are born from molecular clouds that

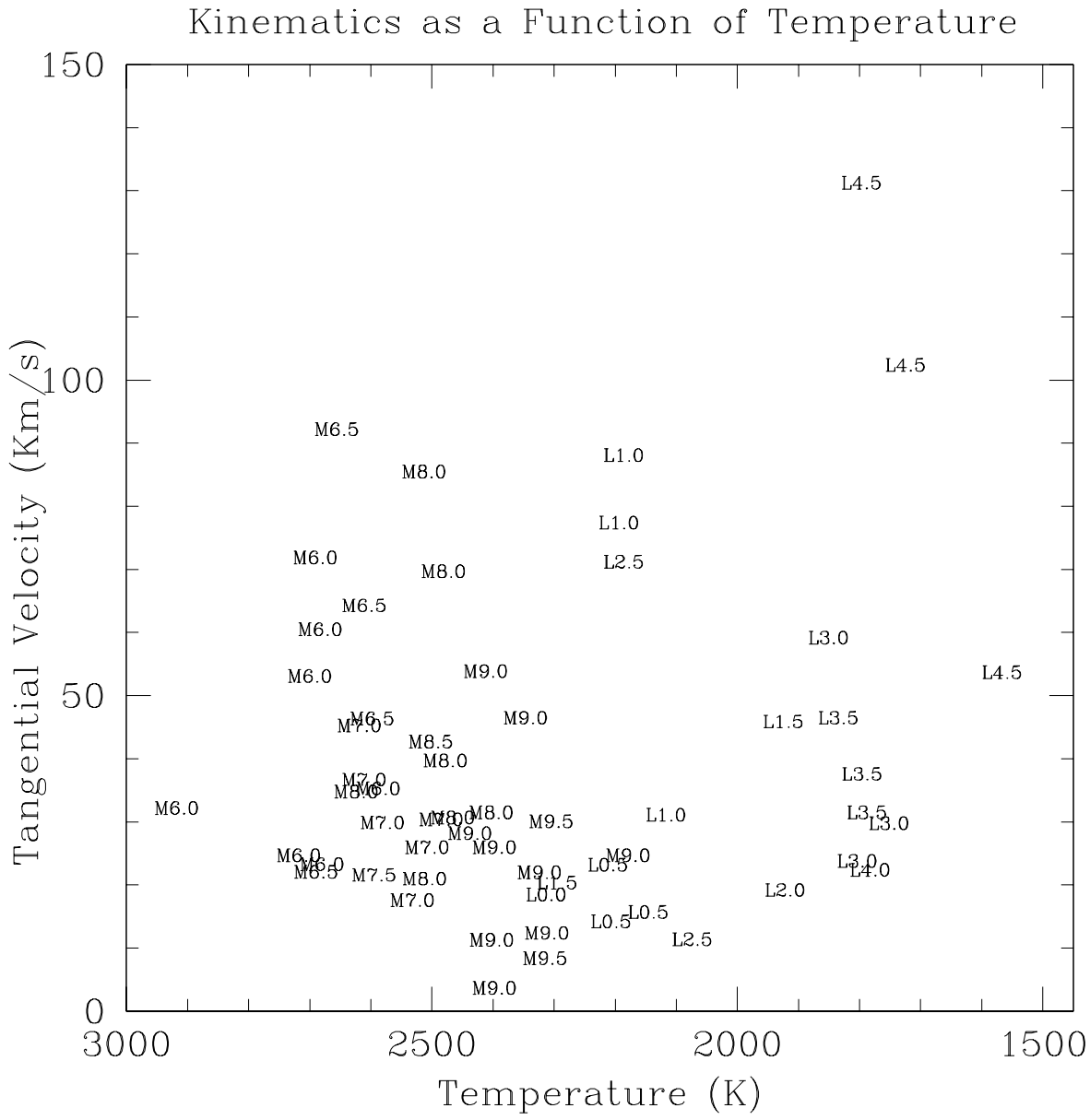

Figure 6.20 Same as Figure 6.18, plotted with spectral types.

are concentrated in the Galaxy's thin disk, a low kinetic energy region, and gradually pick up speed as they undergo dynamical interactions with older stars. The test is particularly useful in the first several Myr of a star's life, when youth and low kinematic velocities are

more strongly correlated. While a complete determination of an object's Galactic motion requires knowledge of its radial velocity from spectroscopic observations, proper motions and trigonometric parallaxes are enough to establish the two components of tangential velocity.

In Figure 6.18 we plot the tangential velocities for the observed sample as a function of effective temperature. The lack of definitive trends in Figure 6.18 excludes the possibility that objects cooler than 2000K form a distinct very young population and that their youth (larger radii) are causing them to appear elevated in the temperature-radius diagram (Figure 6.15). If any trend can be discerned in Figure 6.18, it is that the cooler objects appear to have somewhat *higher* kinematics than the late Ms. The higher tangential velocities noted for the cooler objects could be a selection effect, as high proper motion objects tend to be disproportionally targeted for inclusion in nearby parallax searches. However, the same selection effect applies to the sample of smallest stars as well. The cause of the apparent minimum in the tangential velocity trend around $T \sim 2300$ K (∼M9V) is not clear, and could also be due to a selection effect.

6.7.3 Comparison of the HR Diagram to Evolutionary Models

We now compare our results to the predictions of the four most prevalent evolutionary models encompassing the stellar/substellar boundary (Burrows et al. 1993, 1997; Baraffe et al. 1998; Chabrier et al. 2000; Baraffe et al. 2003)[5]. All of these models are the combination of an interior structure model and an atmospheric model used as a boundary condition. Atmospheric models have become highly sophisticated and achieved a great degree of success over

[5]While Burrows et al. (1997) is well known for presenting a unified theory of brown dwarf and giant planet evolution, data in that paper concerning the hydrogen burning limit are from Burrows et al. (1993).

the last several years. On the other hand, the evolutionary models discussed here are at least a decade old, and none of them currently incorporates the state-of-the-art in atmospheric models. The discrepancy is due in part to the lack of observational constraints for evolutionary models. While an atmospheric model may be fully tested against an observed spectrum, testing an evolutionary model requires accurate knowledge of age and mass. The available evolutionary models are also hindered by the fact that none of them incorporate the latest revised solar abundances that are used to translate observed metallicity diagnostic features into the number densities for different species used by the models. The current accepted values for solar abundances (Caffau et al. 2011) constitutes a reduction of 22% when compared to the original values used by the evolutionary models discussed here (e.g. Grevesse et al. 1993). We therefore cannot expect any of the models we consider here to be strictly correct, but comparing their predictions to our results is nevertheless a useful endeavor.

Figures 6.21 through 6.24 show several evolutionary tracks from these models over-plotted on the luminosity-radius and temperature-radius diagrams. Table 6.6 lists the properties predicted for the HBMM tracks for the four models. We also include the zero metallicity model of Burrows et al. (1993), which is listed to illustrate the effect of a reduction in metallicity. All models except for the unrealistic zero metallicity model predict the hydrogen burning limit at significantly cooler temperatures and lower luminosities than our values. The evolutionary tracks of Chabrier et al. (2000) and Baraffe et al. (2003) have reasonable agreement with the observations for $\log(L/L_{\odot}) \gtrsim -3.5$, where objects are solidly in the stellar domain. Chabrier et al. (2000) has also achieved some success in reproducing the

radii of brown dwarfs with $\log(L/L_{\odot}) \sim -4.0$, but cannot account for the small radius of 2MASS J0523-1403 and several other stellar objects. And while Burrows et al. (1993, 1997) seems to accurately predict the radius of the smallest stars, the model radii are too small everywhere else in the sequence. In sum, we see that at the level of accuracy needed to predict the entirety of our observations these models are for the most part mutually exclusive.

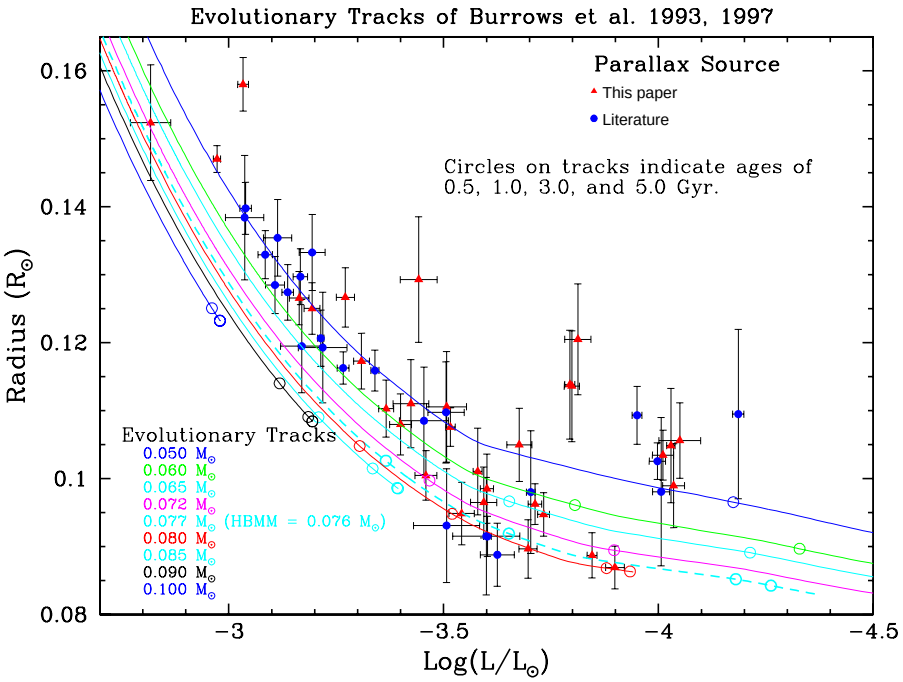

(a)

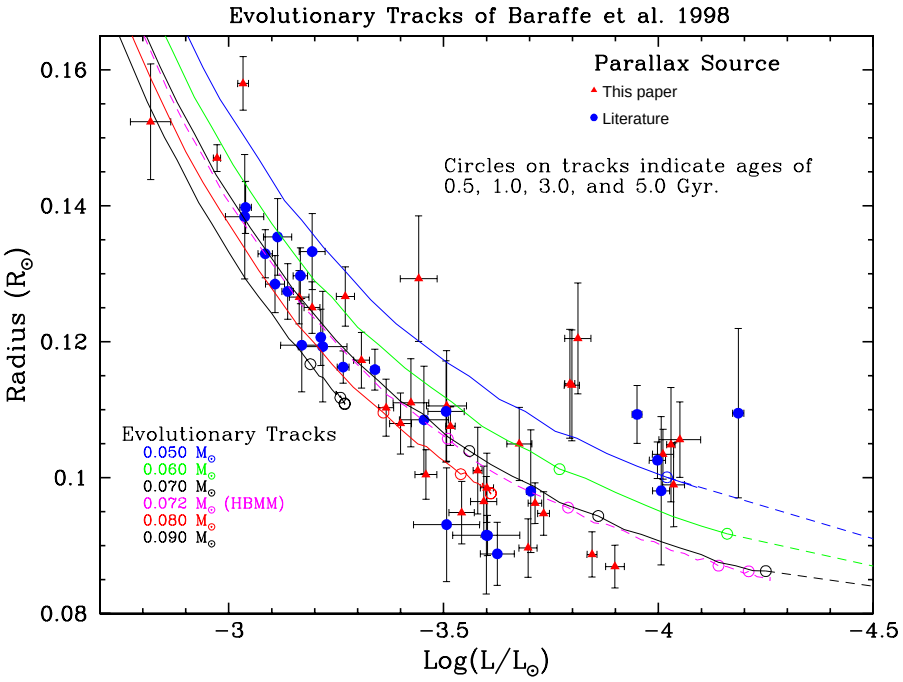

(b)

Figure 6.21 Evolutionary tracks for the models of (a) Burrows et al. (1997, 1993) and (b) Baraffe et al. (1998) over-plotted on the luminosity-radius diagram. Dashed lines indicate the continuation of substellar evolutionary tracks where no data are available. The open circles on the evolutionary tracks represent ages of 0.5, 1.0, 3.0, and 5.0 Gyr from left to right, with the circles for older ages not in plotting range in some of the substellar tracks. The circles for older ages overlap each other in the stellar tracks because there is little evolution at those ages. The track corresponding to the hydrogen burning minimum mass is plotted with a dashed line and has its properties summarized in Table 6.6.

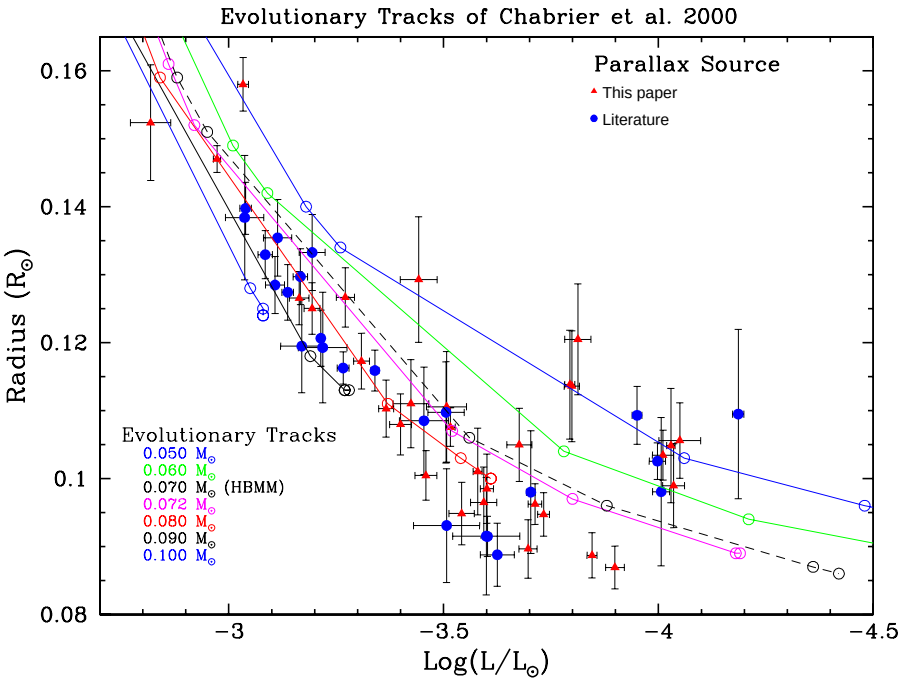

(a)

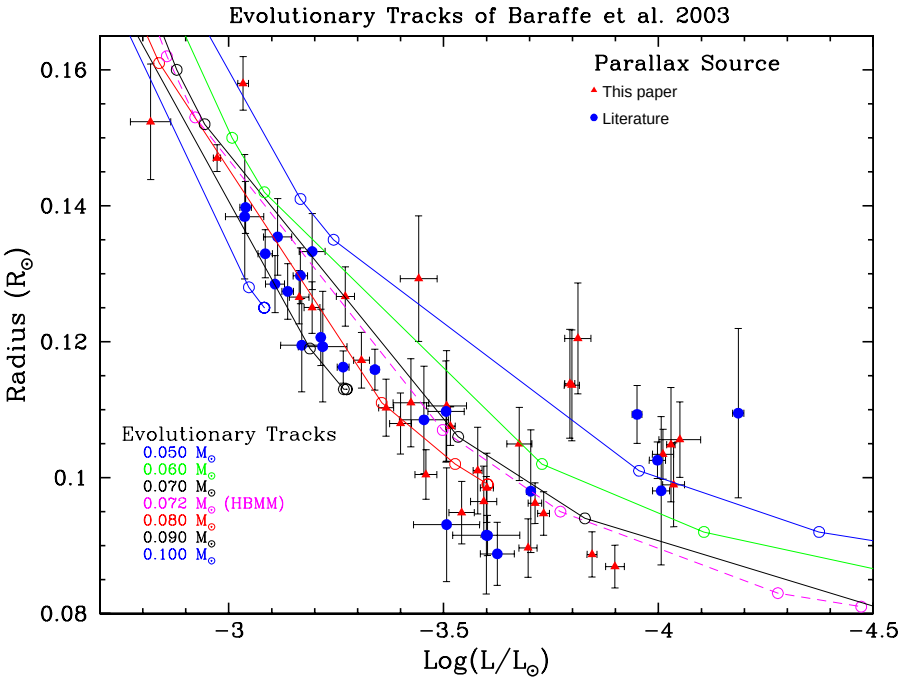

(b)

Figure 6.22 Evolutionary tracks for the models of (a) Chabrier et al. (2000) and (b) Baraffe et al. (2003) over-plotted on the luminosity-radius diagram. Open dots represent ages of 0.05, 0.10, 0.12, 0.50, 1.00, and 10.0 Gyr, except for the 0.10 $M_{\odot}$ track, which starts at 0.10 Gyr. The circles for older ages are not in the plotting range in some of the substellar tracks. The circles for older ages overlap each other in the stellar tracks because there is little evolution at those ages. The track corresponding to the hydrogen burning minimum mass is plotted with a dashed line and has its properties summarized in Table 6.6. The models were computed only at the values where open dot are plotted, with lines connecting the open dots for visualization purposes only.

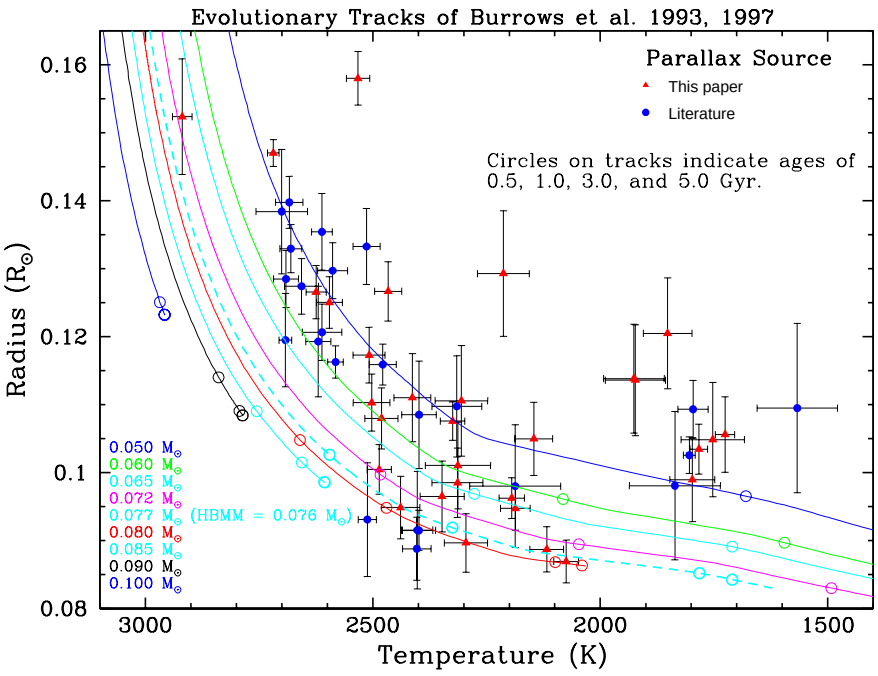

(a)

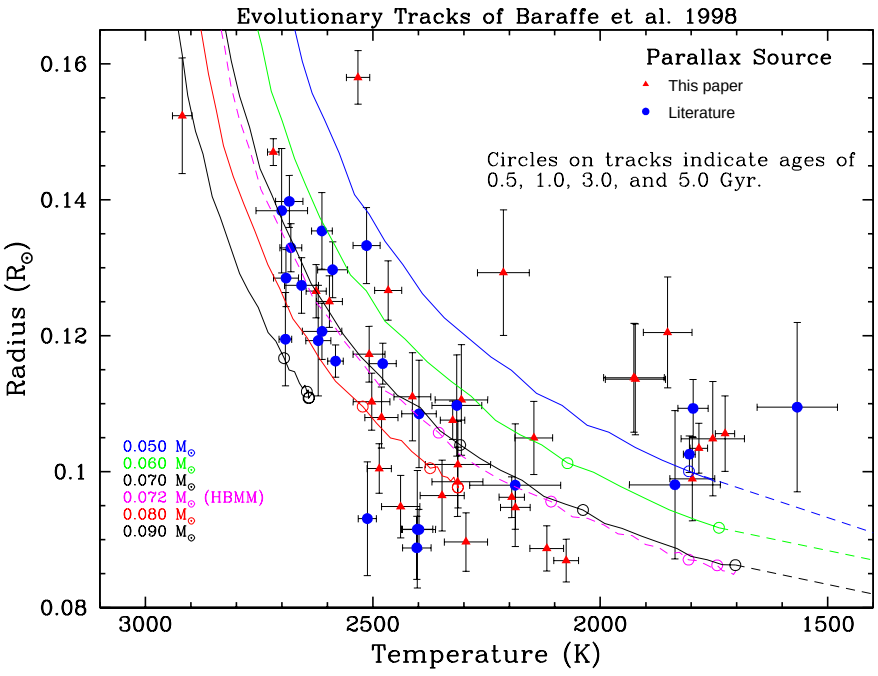

(b)

Figure 6.23 Evolutionary tracks for the models of (a) Burrows et al. (1997, 1993) and (b) Baraffe et al. (1998) over-plotted on the temperature-radius diagram. Dashed lines indicate the continuation of substellar evolutionary tracks where no data are available. The open circles on the evolutionary tracks represent ages of 0.5, 1.0, 3.0, and 5.0 Gyr from left to right, with the circles for older ages not in the plotting range in some of the substellar tracks. The circles for older ages overlap each other in the stellar tracks because there is little evolution at those ages. The track corresponding to the hydrogen burning minimum mass is plotted with a dashed line and has its properties summarized in Table 6.6.

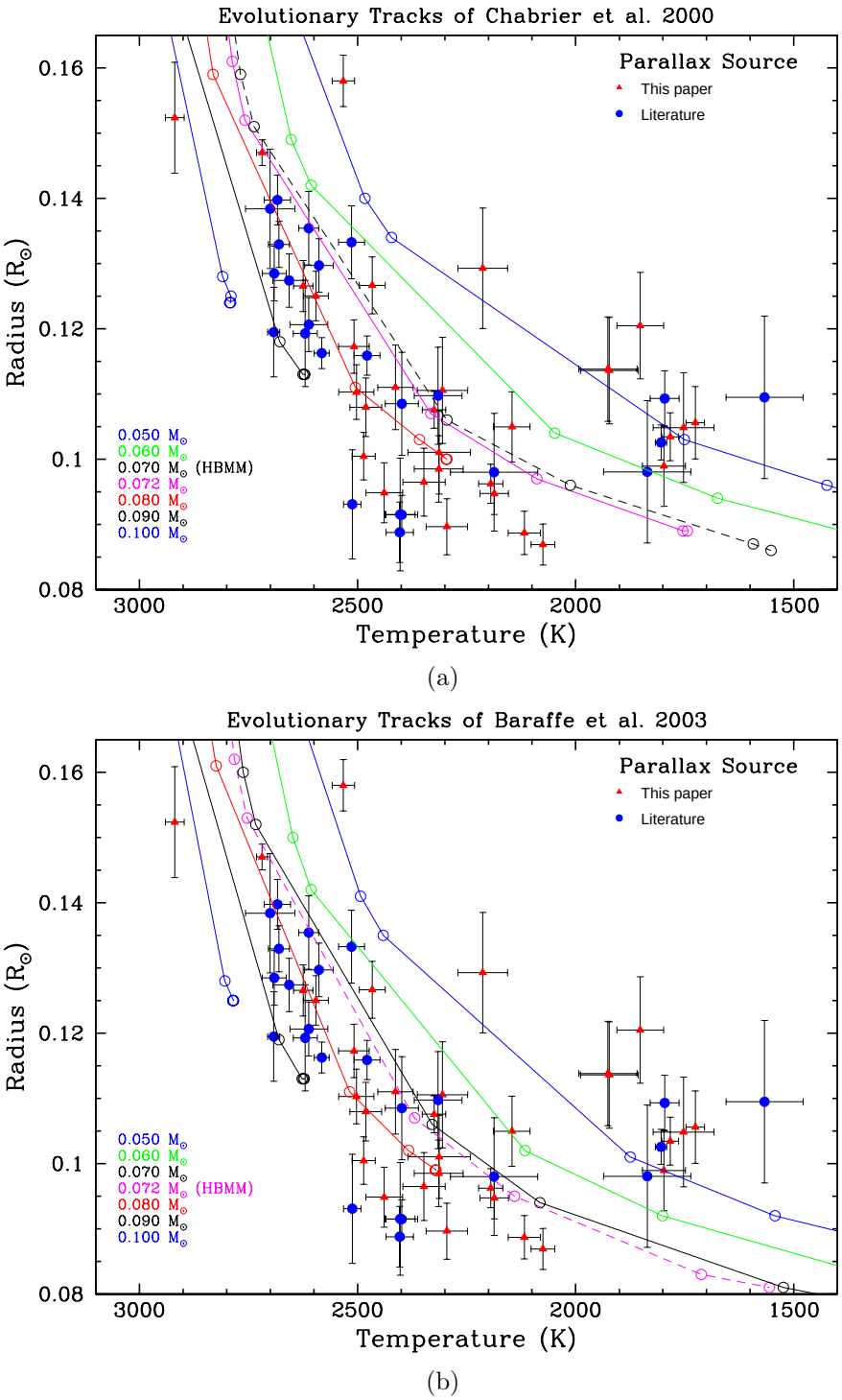

Figure 6.24 Evolutionary tracks for the models of (a) Chabrier et al. (2000) and (b) Baraffe et al. (2003) over-plotted on the temperature-radius diagram. Open dots represent ages of 0.05, 0.10, 0.12, 0.50, 1.00, and 10.0 Gyr, except for the 0.10 $M_{\odot}$ track, which starts at 0.10 Gyr. The circles for older ages are not in the plotting range in some of the substellar tracks. The circles for older ages overlap each other in the stellar tracks because there is little evolution at those ages. The track corresponding to the hydrogen burning minimum mass is plotted with a dashed line and has its properties summarized on Table 6.6. The models were computed only at the values where open dot are plotted, with lines connecting the open dots for visualization purposes only.

Table 6.6: Properties of Evolutionary Models

Model	H Burning min. Mass ($M_\odot$)	H Burning min. $T_{\rm eff}$ (K)	H Burning min. $Log(L/L_\odot)$	Metallicity[a] $Z/Z_\odot$	min. Stellar Radius ($R/R_\odot$)	Atmospheric Properties
Burrows et al. (1993, 1997)	0.0767	1747	-4.21	1.28	0.085	gray with grains
Burrows et al. (1993)	0.094	3630	-2.90	0.00	0.090	metal free
Baraffe et al. (1998)	$\sim$0.072	1700	-4.26	1.28	0.085	non-gray without grains
Chabrier et al. (2000)	$\sim$0.070	1550	-4.42	1.28	0.086	"DUSTY" grains do not settle
Baraffe et al. (2003)	$\sim$0.072	1560	-4.47	1.28	0.081	"COND" clear & metal depleted
Our Results	...	$\sim$2075	~ -3.9	...	$\sim$0.086	...

[a]Models with $Z/Z = 1.28$ were originally meant as solar metallicity models. The new value takes into account the revised solar metallicities of Caffau et al. (2011).

While the differences between our results and model predictions (Table 6.6) may at first seem large, they must be examined in the context of the recently revised solar abundances that are 22% lower than the metallicities used to compute the models (Caffau et al. 2011). Lowering the metal content of a (sub)stellar object has the effect of decreasing opacities both in the atmosphere and in the interior. The net effect is a facilitation of radiative transfer from the object's core to space and thus a decrease in the temperature gradient between the core and the atmosphere. Because in the low metallicity scenario energy escapes the stellar core more easily, maintaining the minimal core temperature necessary for sustained hydrogen burning requires a higher rate of energy generation. As shown by the $Z/Z_{\odot} = 0$ model of Table 6.6, the minimum stellar mass, minimum effective temperature, and minimum luminosity all increase as a result of a decrease in metallicity. The effect of metallicity on the minimum luminosity is particularly strong. When compared to the Burrows $Z/Z_{\odot} = 1.28$ model, the $Z/Z_{\odot} = 0.00$ model produces a minimum luminosity that is greater by a factor of 20.4. Our results suggest a minimum luminosity that is greater than that predicted by the $Z/Z_{\odot} = 1.28$ models by a factor ranging from $\sim$2.0 to $\sim$3.2, depending upon the model chosen. From Figure 4 of Burrows et al. (2011), a lower metallicity would also cause a more pronounced local minimum in the radius trends we detect in Figures 6.12 and 6.15.

It is interesting to note that if we accept the masses of the several evolutionary tracks shown in Figures 6.21 through 6.24, then three out of the four models (Burrows et al. 1997; Baraffe et al. 1998, 2003) show a jump from stellar masses at $\log(L/L_{\odot}) \sim 3.9$ ($T_{\rm eff} \sim 2075$ K) to masses $\lesssim 0.050\ M_{\odot}$ for cooler objects. The Chabrier et al. (2000) models show a slightly

smaller jump to masses $\lesssim 0.060 M_{\odot}$. This interpretation is difficult to reconcile with the idea of a continuous mass function for substellar objects. Because more massive objects cool more slowly, we would expect to see more brown dwarfs in the mass range of $\sim$0.070$-$0.050 $M_{\odot}$ than less massive objects occupying the same temperature range. As an example, the mass function of Allen et al. (2005) predicts the mean mass of spectral type L5 to be 0.067 $M_{\odot}$, and yet comparing our results to evolutionary models shows masses $\lesssim 0.050 M_{\odot}$ in the L3 temperature range. A discontinuous mass function that produces objects of stellar mass and then jumps to such low masses without producing the intermediate mass objects is not likely. Observations and theory could be reconciled by either increasing the masses associated with the evolutionary tracks or decreasing the radii predicted by our SED fitting technique (§5.6). We note however that a systematic over-prediction of radius values by our fitting technique would likely manifest itself in a manner independent of spectral type, and would therefore also be noticeable in the stellar part of Figures 6.21 through 6.24 and in our comparison to interferometric radii (Figure 5.4). There remains the possibility that the *BT-Settl* models work fine down to temperatures of $\sim$2100K, but are under-predicting temperatures (and therefore over-predicting radius) for cooler objects. While this possibility cannot be entire excluded, we would expect the uncertainties in temperature to be significantly larger for the cooler objects in comparison to the hotter objects if the models were not working well for cooler temperatures.

Finally, we note that while our observations do not address the minimum mass for hydrogen burning, higher values for mass should also be expected as a result of the downward

revision in solar abundances. Independent confirmation of this effect through a dynamical mass study would further enhance the body of evidence we have presented for the end of the stellar main sequence at values close to those of 2MASS J0523-1402 (L2.5): $T_{\rm eff} \sim 2075K$, $\log(L/L_{\odot}) \sim -3.9$, $(R/R_{\odot}) \sim 0.086$, and $V - K = 9.42$.

6.7.4 Comparison of Radii With Other Studies

Unfortunately, there are only a few other observational studies that directly measure or calculate radii for objects in the temperature range considered here. These objects are too faint to be observed by the *Kepler* mission except as companions to more massive stars. Their faintness also means that they are likely to remain outside the domain of long baseline optical interferometry for the foreseeable future. There are nevertheless several examples of VLM eclipsing binary companions where the primary star in the system is an early M dwarf or a solar analogue (e.g., Burrows et al. 2011, and references therein). Such systems are valuable for comparisons regarding mass and radius, but lack the photometric coverage needed to calibrate the SED and derive the luminosity in a manner analogous to this work. We note that the only known eclipsing system where both members are brown dwarfs (Stassun et al. 2006) is a member of the Orion star forming region, and is therefore only a few million years old. Stassun et al. (2006) measure radii of 0.669±0.034 $R_{\odot}$ and 0.511±0.026 $R_{\odot}$ for the two components. At such a young age and such large radii, this system is a valuable probe of early substellar evolution, but should not be compared to the much older objects we discuss in this study.

There have been two recent studies that derive the stellar parameters needed for placing

objects in the HR diagram. As already mentioned, Konopacky et al. (2010) derived effective temperatures that agree with our values for early L dwarfs but steadily diverge as the temperature increases (§6.3, Figure 6.6), and their errors are ∼200K. Although their data are limited at temperatures cooler than ∼2000K for the determination of a robust radius trend, they also have a local minimum in radius at $T_{\rm eff}$ = 2075 K, for 2MASS J2140+16B, consistent with our results. More recently, Sorahana et al. (2013) derived radii for several L and T dwarfs based on *AKARI* near infrared spectra. They report a sharp radius minimum of 0.064 $R_\odot$ at 1800K. Figure 6.25 shows their results over-plotted in our temperature-radius plot. While the results are interesting, we note that they derived the effective temperature and did SED fits based on near infrared spectra only and thus were not able to take advantage of the strong dependence of optical colors on temperature (§5.5). Their effective temperatures agree to other studies for most objects but are higher by as much as a few hundred K when compared to Golimowski et al. (2004b) and Cushing et al. (2008) for objects corresponding to the sharp drop in radius, indicating that the small radii may be compensating by an over-estimation of temperature.

6.8 Notes on Individual Objects

GJ 1001BC (L4.5 ID# 1) is a binary L dwarf with nearly equal luminosity components (Golimowski et al. 2004a). Golimowski et al. (2006, 2007) report a preliminary total system dynamical mass of $0.10 M_\odot$ based on orbital mapping using HST and VLT. The conservative assumption of a mass ratio ≥3:2 based on nearly equal luminosity would make individual

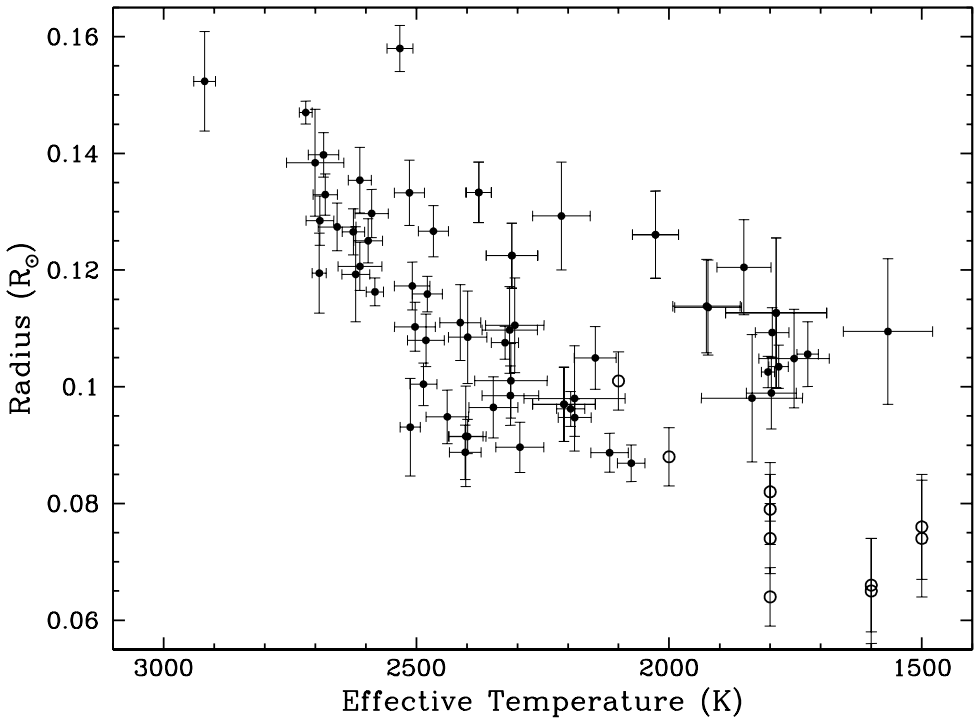

Figure 6.25 Data from Sorahana et al. (2013) (open circles) over-plotted on our temperature-radius diagram. Their radius minimum at 1800K is probably a result of their unrealistically high temperatures for these objects.

masses range between $0.04M_{\odot}$ and $0.06M_{\odot}$, thus placing both objects in the brown dwarf regime. We derive $T_{\rm eff} = 1725 \pm 21$ and $\log(L/L_{\odot}) = -4.049 \pm 0.48$ for each component, assuming the two objects are identical. These numbers are generally above the hydrogen burning limit numbers predicted by models but below our numbers (Table 6.6). This inconsistency is further evidence that the hydrogen burning limit must happen at higher luminosities and temperatures than what is predicted by the currently accepted models.

LEHPM1-0494 A (M6.0V ID# 3) and **B (M9.5V ID# 2)** are reported by Caballero (2007) to be a wide common proper motion binary with separation of 78″. We report trigonometric parallaxes for both components based on individual reductions of the same

field of view, and derive distances of $26.88^{+1.51}_{-1.36}$ pc for the A component and $25.14^{+1.40}_{-1.26}$ pc for the B component for a projected separation of ∼2100 AU. These trigonometric distances are in good agreement with Caballero's distance estimate of 23±2 pc and support his claim of a physical association between these two objects.

LHS 1604 (M7.5V ID# 12) was first reported by Cruz et al. (2007) as being over-luminous by ∼0.6 magnitudes in J. They suggested that the near-infrared photometry is consistent with an unresolved M7.5V/M9.0V binary. LHS 1604 is the only star in our sample for which we were not able to calculate $T_{\rm eff}$ or perform an SED fit using the procedures outlined in §§5.5 and 5.6 − the fits diverged due to a large infrared excess. We observed LHS 1604 using high resolution laser guide star adaptive optics on Gemini North and preliminary results do not show a resolved companion. We defer a thorough analysis of this target to a future publication where we discuss our high resolution observations and use them to place limits on the properties of the putative companion (Dieterich et al. in preparation). We are also monitoring LHS 1604 for astrometric perturbations but it is too early to notice any trends.

2MASS J0451-3402 (L0.5 ID# 15) has the highest photometric variability in our sample. It was first noted as a photometrically variable target by Koen (2004), who reported a sinusoidal trend with a period of 3.454 days and mean amplitude of ∼1% (10 milli-magnitudes), though varying to as high as 4% (40 milli-magnitudes). While our observations do not have the cadence necessary to obtain phase information, the variability of 51 milli-magnitudes in the I band we detect is in agreement, if not somewhat higher, with

that of Koen (2004). It is interesting to note the spike in variability around $T_{\rm eff} \sim 2100$ K in Figure 6.10. Further investigation is needed to determine whether this trend has a physical cause associated with that temperature range or whether this is a coincidence.

2MASS J0523-1403 (L2.5 ID# 17) is discussed throughout this chapter as the object closest to the local minimum in the luminosity-radius and temperature-radius trends (Figures 6.12 and 6.15). As we discussed in §6.7, there is strong evidence indicating that the end of the stellar main sequence must lie in its proximity in parameter space. The target has been described as having variable radio and Hα emission (Berger 2002; Antonova et al. 2007; Berger et al. 2010). Despite the common association between Hα emission and youth, we note that it is difficult to conceive of a target with such a small radius ($R/R_{\odot} = 0.086 \pm .0031$) as being young. As discussed in §6.5, radio emission is often used as a probe of magnetic fields, and may be accompanied by optical variability if they result in auroral phenomena. We detect no significant I band variability for 2MASS J0523-1403 (upper limit $\sim$11.7 milli-magnitudes), meaning that either the star was in a mostly quiescent state during the $\sim$3 years for which we monitored the target (2010.98$-$2013.12) or that the link between radio emission and I band variability is not universal.

SSSPM J0829-1309 (L1.0 ID# 23) is an object very similar to 2MASS J0523-1403 but slightly more luminous. The two objects have 1σ uncertainties that overlap in radius and $T_{\rm eff}$, but not luminosity. As shown in Figure 11, the location of SSSPM J0829-1309 is crucial for establishing 2MASS J0523-1403 as being close to the minimum of the radius trends. Taken together, 2MASS J0523-1403 and SSSPM J0829-1309 show that the radius

trends in Figures 6.12 and 6.15 are real and therefore the conclusions we draw in this paper are not the result of one isolated odd object (i.e., 2MASS J0523-1403).

LHS 2397aAB (M8.5V (joint) ID# 35) is an M8.0V/L7.5[6] binary (Freed et al. 2003). Dupuy et al. (2009) report a total system dynamical mass of $0.146^{+0.015}_{-0.013}$ $M_{\odot}$. Konopacky et al. (2010) derive individual dynamical masses of 0.09±0.06 $M_{\odot}$ for the primary and 0.06±0.05 $M_{\odot}$ for the secondary. The system is therefore an important probe of the hydrogen burning mass limit because two coeval components presumably with the same metallicity lie on opposite sides of the stellar/substellar boundary. We are mapping the astrometric orbit for this system in a manner similar to that discussed in §6.6 for DENIS J1454-6604AB and will publish refined individual dynamical masses as soon as orbital mapping is complete.

LEHPM2-0174 (M6.5V ID# 40) appears over-luminous in Figure 6.3. It is most likely an unresolved multiple, a young object, or both. We note that we could not determine a reliable source for the spectral type of this object, thus leaving open the possibility that it has been miss-characterized as an M6.5V. LEHPM2-0174 is excluded from Figures 6.12 and 6.15 because scaling the figure to fit its radius ($0.173R_{\odot}$) would make the figure difficult to read.

Kelu-1AB (L2.0 (joint) ID# 41) is a well known L2/L4 binary (Liu & Leggett 2005b). That study notes that the presence of LiI λ6708 makes both components substellar with masses $\lesssim 0.06$ $M_{\odot}$ according to the lithium test of Rebolo et al. (1992), although they note that the LiI λ6708 detection is tenuous. Deconvolution of this system would

[6]infrared spectral type for secondary

provide important information about the hydrogen burning limit due to its location in the temperature-radius trend (Figure 6.15). If we assume that the system is an equal luminosity binary, then the deconvolved radii of the components are $\sim$0.089 $M_{\odot}$. That number would further constrain the position of 2MASS J0523-1309 as being in the minimum of the radius trend. However, because the components of Kelu1-AB do *not* have equal luminosities, we can expect the A component to be a more massive brown dwarf or a stellar component with mass just above the hydrogen burning limit. In either case, the A component would have a smaller radius than the B component. Determining the precise radius, $T_{\rm eff}$ and luminosity of the A component is crucial for determining the exact location of the point of minimal radius in Figure 6.15.

2MASS J1705-0516AB (L0.5 (joint) ID# 56) was first reported as an M9V/L3 binary by Reid et al. (2006). The system's position in the midst of the main sequence in the HR diagram (Figure 6.3) shows that the system is dominated by the A component in luminosity. Our parallax observations detect a clear astrometric perturbation. We are working on mapping the system's orbit and will soon be able to publish dynamical masses for the individual components. Like LHS 2397aAB, this system will serve as a crucial benchmark system with components likely residing on either side of the stellar/substellar boundary. As indicated in Figure 6.10, this target has one of the largest optical variabilities in the sample, at 41 milli-magnitudes in I. We defer a more thorough discussion of 2MASS J1705-0516AB to a future paper (Dieterich et al. in preparation).

SIPS J2045-6332 (M9.0V ID# 58) is an extremely over-luminous object (Figure

6.3). We note that unresolved equal luminosity duplicity alone cannot explain the over-luminosity. The object is also highly variable at 39 milli-magnitudes in I, as shown in Figure 9. The variability suggests that youth may play a role in explaining the over-luminosity of SIPS J2045-6332.

LHS 4039C (M9.0V ID# 62) is a member of a triple system with an M4V−M9V binary with separation 6″ and a DA white dwarf 103″ away (Scholz et al. 2004; Subasavage et al. 2009). Subasavage et al. (2009) reported the trigonometric parallax for the white dwarf component as 42.82±2.40 mas. In this paper we have reduced the same data using LHS 4039C as the science target and measure a parallax of 44.38±2.09, thus supporting the physical association of the system. The intriguing combination of a white dwarf and a VLM star in the same system allows us to constrain the properties of LHS 4039C based on the better understood models of white dwarf evolution. Based on the white dwarf cooling time of 0.81±0.05 Gyr (Subasavage et al. 2009) and the progenitor age of 4.4±3.7 Gyr (Iben & Laughlin 1989) assuming a progenitor mass of $1.17\pm0.26 M_{\odot}$ (Williams et al. 2009), we infer a total system age of 5.2±3.7 Gyr. Assuming the system to be coeval, LHS4039C is then a main sequence star with no remaining traces of youth. Its locus on the HR diagram is therefore an indication of where the VLM stellar main sequence lies.

CHAPTER 7

The Gemini Adaptive Optics High Resolution Imaging Survey

This chapter presents a pilot study to obtain resolved images of close separation ($< 1''$) binaries that have the potential to eventually yield dynamical masses, and provide other insights into the nature of VLM stars and brown dwarfs. The target list for this project consists of objects for which an astrometric perturbation was previously detected through CTIOPI, or previously resolved binaries for which establishing ΔJHK_s magnitudes would allow for a further characterization of the components (Table 7.1). Due to the need to map the entire photocentric orbits of targets with astrometric perturbations before establishing dynamical masses, the project was conceived from the beginning as a long term project that draws on the results of previous efforts and will also contribute to the future results of other projects. In this dissertation we focus on describing the techniques used for high resolution observations and listing our detections. A thorough analysis and characterization of the resolved components is reserved for a future paper.

7.1 Introduction

Mass is the most fundamental parameter governing the structure and evolution of any stellar or substellar object. It is therefore desirable to directly measure the masses of as many objects as possible when characterizing a particular population. A model independent measurement of mass can be obtained by analyzing the motions of binary stars, where orbital parameters

can be related to mass by Kepler's third law:

$$(m_1 + m_2) = \frac{a^3}{p^2} \ ,$$

where m_1 and m_2 are the masses of the two components of the binary, a is the semi-major axis of the *relative* orbit of the secondary star around the primary star, and p is the orbital period. If the masses are entered in units of solar masses ($M_\odot$), and a is entered in AU, then p is in units of Earth years. Further, if each individual component can be established with respect to the system's barycenter, then

$$a = a_1 + a_2$$

where a_1 and a_2 are the semi-major axes of the orbits of the primary and secondary component, respectively, and

$$m_1 a_1 = m_2 a_2 \ .$$

The last equation can then be solved simultaneously with Kepler's third law to yield the masses of individual components.

For VLM stars and brown dwarfs, orbits with time scales suitable for dynamical mass determination ($\lesssim$ 10 yrs) have semi-major axes in the order of a few AU, which translates to angular separations $\lesssim 0.2''$ for the solar neighborhood (distance within $\sim$20 pc). This separation regime is well suited for investigation with adaptive optics (AO) systems on 8 meter class telescopes, which can typically obtain diffraction-limited images in the near

infrared, with angular resolutions as good as $\sim 0.065''$. AO imaging also has the advantage of providing photometric information if the object is resolved through several different filters, and can be used for astrometry if the image quality and separations allow for centroiding of the individual components of a binary. AO imaging is also a particularly powerful technique when it is used to resolve the components of astrometric binaries in which the orbit of the system's photocenter has been established with respect to the background of distant "fixed" stars. In that case, a single resolved AO observation is all that is necessary for obtaining the system's mass ratio, and therefore obtaining the masses of the individual components.

We have performed an AO campaign using the *Near Infra-Red Imager* (NIRI) instrument coupled with the *ALTtitude conjugate Adaptive optics for the InfraRed* (ALTAIR) AO module on the Gemini North telescope in order to resolve systems for which astrometric perturbations were detected through CTIOPI, as well as previously known binary systems that lacked resolved near infrared photometry. In total, 37 targets were imaged. We were able to obtain resolved images for 19 targets while 12 targets yielded null detection. Images for the remaining six targets have not yet been analyzed. Out of the 19 resolved targets, five had their multiplicity confirmed for the first time through this study. The remaining 14 had previously been confirmed as binaries through observations with HST's *Fine Guidance Sensors* (FGS) or infrared speckle imaging (Henry & McCarthy 1993; Henry et al. 1999). We provide an overview of astrometric binaries in §7.2 to motivate the observations, describe the Gemini AO observations in §§7.3 and 7.4, discuss preliminary results in §7.5. We discuss what is left to do and the future of this project in §7.6.

7.2 Astrometric Binaries – an Overview

The process of measuring a trigonometric parallax is in essence the measurement of the science star's minute motion with respect to a background field of distant "fixed" stars (§§5.4, 6.2). The resulting motion is a combination of the heliocentric tangential motion of the science target arising from Galactic kinematics (the proper motion), the reflex motion arising from Earth annual heliocentric motion (the trigonometric parallax itself), and any remaining motion arising from the orbital motion of the science target if it is a multiple system. The latter is observed in the form of an astrometric perturbation to the residuals of the science target's photocentric displacement with respect to the background stars once the proper motion and the trigonometric parallax have been calculated and subtracted. If sufficient epochs have been observed, the astrometric perturbation traces out the relative orbit of the system's photocenter with respect to the fixed barycenter. Figure 7.1 shows two examples of what astrometric residuals look like after the parallax motion and the proper motion have been subtracted. The first case shows the astrometric residuals for LP 944-020 for which residuals in both coordinate axes are small and do not form any pattern. The second case shows the residuals for GJ 1215ABC, where a large and clear sinusoidal perturbation indicative of orbital motion is present in both axes.

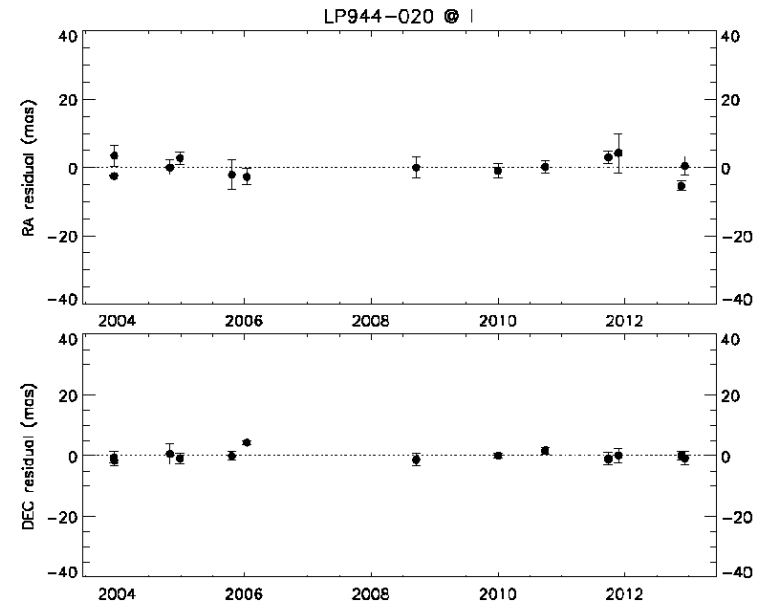

(a)

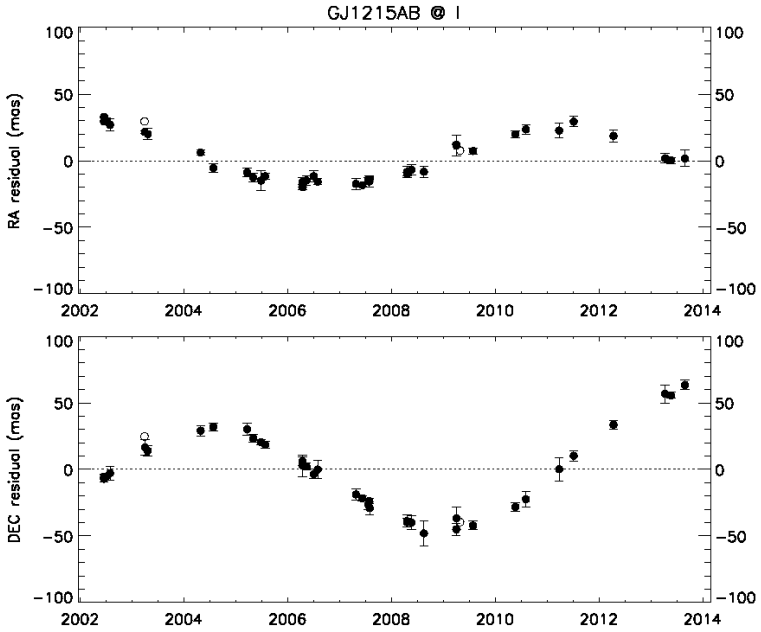

(b)

Figure 7.1 Astrometric residuals for (a) LP 944-020, and (b) GJ 1215ABC. Note the different plotting scales for the two objects in the vertical axes. The residuals represent the motion of the target's photocenter with respect to the background of distant stars after the components of motion due to the proper motion and the trigonometric parallax have been subtracted. Panel (a) shows small residuals randomly distributed about zero in both coordinate axes, and is typical of a good parallax solution. Panel (b) shows a clear sinusoidal perturbation indicative of the orbital motion of an unresolved multiple system's photocenter about the system's barycenter. Each data point and its error bars represents the mean and standard deviation of the typically five consecutive observations taken in a single night. If enough observations are taken, the astrometric perturbations can be used to map out the photocenter's orbit, as is the case with GJ 1215ABC.

7.2.1 From Photocentric Orbits to Component Masses

In order to understand how the observed photocentric orbit arises from a physical binary configuration it is useful to first consider the extreme cases of binaries with large differences in luminosities as well as equal luminosity binaries. Consider first a system in which the two components have a small mass ratio (i.e., one component is much more massive than the other) and that the secondary's contribution to the overall luminosity is also negligible. The system's photocenter is therefore effectively at the same location as the primary component, which contributes almost all the light in the band through which observations were taken. Both components orbit the system's barycenter, which is very close to the location of the primary component. The resulting motion of the photocenter then maps out the small orbital motion of the primary component. Consider also the case of a binary system where the components have equal mass and equal luminosity. In that case the system's barycenter is located exactly half way between the two components, and the components' motions are equal and opposite to each other. In this case both components have large displacements about the system's barycenter, but because the light distribution is always symmetric about the barycenter, the system's photocenter does not move, and no astrometric perturbation is detected.

Now consider the case where the components' luminosities are slightly different. The system's photocenter is then slightly offset from the barycenter toward the direction of the more luminous component, and a small astrometric perturbation is detected. Because unresolved observations give us no information about the components' luminosity ratio or physical sep-

aration, obtaining the mass ratio from a photocentric orbit is a degenerate problem − the same solution may be assigned to a low luminosity ratio system where the primary component moves little, but carries with it most of the system's light, or to a high luminosity ratio system where both components have a large motion about the barycenter, but because the difference in luminosity between the two components is small the photocenter is only slightly offset from the barycenter. Figure 7.1(a) could therefore correspond to an equal luminosity binary or to a single star. In the same manner, Figure 7.1(b) could correspond to a system in which the two components' masses and luminosities are only slightly different, or to a very low mass and luminosity ratio system where one component clearly dominates the photocenter[1].

As outlined in e.g., McCarthy et al. (1991), the degeneracy discussed above can be broken and a unique solution for the system's mass ratio can be obtained if the system's luminosity ratio and projected physical separation are known at a single epoch, so long as the photocentric orbit is also known. Suppose that in a resolved image the components' separation, p, is measured, as well as the fluxes of the two components. The following quantities can then be defined:

$$\beta = \frac{F_2}{F_1 + F_2}$$

where F_1 and F_2 are the fluxes of the primary and secondary components, respectively.

[1]Overluminosity is often detected in a color-magnitude diagram. In the equal luminosity case, the offset is 0.7 mag.

Similarly, we define the secondary's fractional mass as

$$B = \frac{M_2}{M_1 + M_2}$$

and ρ as the system's photocentric perturbation at the epoch at which p was measured. The ratio p/ρ is then a scaling factor between the photocentric orbit and the barycentric orbit. The system's mass ratio B can then be related to the known luminosity ratio β by the equation

$$\frac{p}{\rho} = \frac{1}{B - \beta}.$$

We can then solve for B and apply the previous equation in combination with Kepler's third law to yield the masses of the individual components.

The fractional luminosity ratio β should in principle be measured in the same band that was used for mapping the photocentric orbit. In practice, the trigonometric parallax observations are performed in one of the optical bands V, R, or I, and the Gemini/NIRI observations were performed through bands J, H, and K_s, or their narrow band equivalents in cases where the targets were too bright for observing through broad bands. The flux ratios measured in the Gemini/NIRI observations can be converted to optical flux ratios using the relations in Table 6.5, with care taken to propagate the uncertainties associated with each relation.

7.3 Gemini/NIRI Observations

Data were collected through observing programs GN-2009A-Q-94, GN-2009B-Q-10, GN-2010B-Q-9, and GN-2011A-Q-26. In total, 19.2 hours of Gemini time were allocated through NOAO. Observations were carried out in queue mode. In most cases the science target was bright enough to serve as its own natural guide star. The targets ranged in brightness from $K \sim 5.0$ to $K \sim 11.0$, making some of the targets extremely bright for an 8 meter telescope. Fortunately, the NIRI array allows exposures as short as 0.020 s to be added in non-destructive co-adds, thus allowing for very high signal-to-noise while preventing saturation. The plate scale achieved with the f/32 camera is $0.0219''$ pixel^{-1} and the field of view is $11.2''$. Observations were taken using a 3×3 dither pattern with $4.0''$ steps through filters J, H, and K_s. For bright targets, narrow band filters were used to avoid saturation. The full observing sequence for a single target lasted from 15 to 40 minutes, including overheads.

Adaptive Optics correction was done using the ALTAIR facility level AO system, which sends a wavefront corrected beam to NIRI. ALTAIR can use the science target as a guide star for full wavefront sensing in cases where V $\lesssim$15, and requires the use of the Laser Guide Star for fainter optical magnitudes. The laser guide star was used for 12 out of the 37 targets observed. The typical FWHM for a well-exposed PSF in the K band is $\sim 0.065''$ in Natural Guide Star observations. The image quality is somewhat worse and more variable (FWHM $\sim 0.07''$ to $\sim 0.1''$) when the Laser Guide Star is used.

7.4 Searching for Companions

Because most observations consisted of co-adding very short exposures, the resulting images often had strong speckle patterns. Figure 7.2 shows the unresolved image of LHS 1050. The speckle pattern around the image often mimics the profile of real companions, making companion identification difficult for low signal to noise observations. The situation can be ameliorated by looking at the individual dither images before they are coadded, and trying to determine whether or not a potential companion is constantly appearing in all nine images. The speckle pattern and NIRI's PSF are wavelength dependent, so even if a particular image artifact is present in several co-adds, it should shift places when comparing images taken with different bands, whereas a real astronomical source will stay in the same position. If a potential companion is detected, we then checked wide field images and traced the primary target's proper motion to make sure that the detection was not a background star.

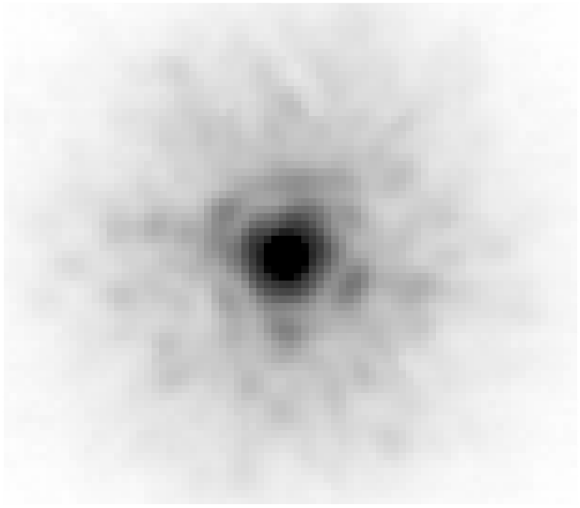

Figure 7.2 Gemini/NIRI image for LHS 1050, an unresolved source. The central image is surrounded by speckles and image artifacts that may mimic the profiles of faint companions.

Given NIRI's f/32 plate scale of 0.0219″ pixel^{-1} and the ∼0.065″ resolution typically achieved with AO correction, a low contrast companion could be unambiguously detected if its centroid was three pixels away from the primary source so that a saddle point of at least one pixel existed between the two sources. Because ALTAIR's performance varies from image to image, it is not possible to assume a generic PSF for PSF subtraction, as done in the HST/NICMOS case (§3.3), to probe to closer separations that ∼0.065″. The sensitivity to high contrast companions is more difficult to generalize due to the presence of speckles, which are present to a varying degree depending on exposure time and ALTAIR performance. As discussed in §7.5 we were able to detect companions with contrast as high as ΔK ∼4.6 mag at a separation of 0.25″; however, this case should not be taken as a generalization of the search's detection capability − every AO image is unique.

7.5 Results

Table 7.1 lists the results for all 31 targets that have been analyzed, with those targets for which a companion was detected listed first. All separations and delta magnitudes listed in Table 7.1 are approximate and are pending final reductions.

Table 7.1: Gemini AO Results

Name	R. A.	Dec.	Joint Spectral Type	V mag.	Archive Code	Guide Star Type[a]	Filter Type[b]	Companion Detected?	First Detection?	Separation (arcsec)	ΔK
GJ 1005AB	00 15 28	−16 08 01	M3.5V	11.48	GN-2009B-Q-10-200	N	Na	Yes	No	0.24	1.1
GJ 2005BC	00 24 44	−27 08 24	M5.5V	15.28	GN-2009B-Q-10-208	L	B	Yes	No	0.46	0.2
GJ 65AB	01 39 01	−17 57 01	M5.0V	12.96	GN-2009B-Q-10-218	N	Na	Yes	No	2.10	0.1
LHS 1630AB	04 07 20	−24 29 13	M3.5V	12.38	GN-2009B-Q-10-241	N	B	Yes	No	0.98	0.3
GJ 234AB	06 29 24	−02 48 00	M4.0V	11.12	GN-2009B-Q-10-253	N	Na	Yes	No	1.02	1.6
GJ 2069AED	08 31 37	+19 23 39	M4.0V	11.93	GN-2009B-Q-10-265	N	Na	Yes	No	0.62	3.1
GJ 2069BC	08 31 37	+19 23 49	M4.0V	14.83	GN-2009B-Q-10-429	N	B	Yes	No	0.97	0.5
LHS 2071AB	08 55 20	−23 52 15	M4.0V	13.88	GN-2009B-Q-10-273	N	B	Yes	Yes	0.22	1.3
LHS 6167AB	09 15 36	−10 35 47	M4.5V	13.82	GN-2009B-Q-10-277	N	B	Yes	No	0.18	∼0.0
WT 1827AB	10 43 02	−09 12 41	M5.5V	15.10	GN-2009B-Q-10-282	L	B	Yes	No	0.40	0.4
LHS 2397AAB	11 21 49	−13 13 08	M7.5V	19.58	GN-2010B-Q-9-40	L	B	Yes	No	0.27	2.4
GJ 473AB	12 33 17	+09 01 15	M5.0V	12.47	GN-2009B-Q-10-292	N	Na	Yes	No	0.44	∼0.0
GJ 1215ABC	17 17 44	+11 40 11	M5.0V	15.07	GN-2009B-Q-10-306	L	B	Yes	Yes	0.25	4.6
LTT 7434AB	18 45 58	−28 54 54	M4.0V	12.69	GN-2009B-Q-10-323	N	B	Yes	Yes	0.12	3.5
LHS 501AC	20 55 37	−14 02 08	M4.0V	12.49	GN-2009B-Q-10-328	N	Na	Yes	Yes	0.07	0.2

Continued on next page

Name	R. A.	Dec.	Joint Spectral Type	V mag.	Archive Code	Guide Star Type[a]	Filter Type[b]	Companion Detected?	First Detection?	Separation (arcsec)	ΔK
GJ 831AB	21 31 18	−09 47 26	M4.0V	12.02	GN-2009B-Q-10-335	N	Na	Yes	No	0.24	1.1
LHS 3738AB	21 58 49	−32 26 27	M4.5V	15.80	GN-2009B-Q-10-341	N	B	Yes	Yes	0.11	1.0
GJ 866AB	22 38 33	−15 17 59	M5.0V	12.39	GN-2009B-Q-10-346	N	Na	Yes	No	0.13	0.4
LHS 4009AB	23 45 31	−16 10 18	M4.5V	14.38	GN-2010B-Q-9-43	N	B	Yes	No	0.55	0.1
LHS 1050	00 15 49	+13 33 22	M3.0V	12.62	GN-2009B-Q-10-213	N	Na	No	···	···	···
BRI 0021-0214	00 24 24	−01 58 20	M9.0V	19.88	GN-2010B-Q-9-100	L	B	No	···	···	···
LHS 1302	01 51 04	−06 07 05	M4.5V	14.49	GN-2009B-Q-10-419	N	B	No	···	···	···
LHS 1582	03 43 22	−09 33 51	M4.5V	14.69	GN-2009B-Q-10-424	N	B	No	···	···	···
LHS 1604	03 51 00	−00 52 45	M7.0V	18.07	GN-2009B-Q-10-234	L	B	No	···	···	···
G 99-049	06 00 03	+02 42 23	M3.5V	11.31	GN-2009B-Q-10-246	N	B	No	···	···	···
SCR 1107-3420B	11 07 50	−34 20 59	WD	13.66	GN-2009B-Q-10-287	N	B	No	···	···	···
GJ 433	11 35 26	−32 32 23	M2.0V	9.82	GN-2009A-Q-94-42	N	Na	No	···	···	···
GJ 494	13 00 46	+12 22 32	M1.0V	9.73	GN-2009B-Q-10-300	N	Na	No	···	···	···
GJ 678.1	17 30 22	+05 32 54	M1.0V	9.32	GN-2009B-Q-10-311	N	Na	No	···	···	···
LHS 3376	18 18 57	+66 11 33	M4.5V	13.46	GN-2009A-Q-94-79	N	B	No	···	···	···
LP 876-010	22 48 04	−24 22 07	M4.0V	12.59	GN-2009B-Q-10-353	N	B	No	···	···	···

Of the 19 multiples we were able to resolve, five have been resolved for the first time, and hence their multiplicity is confirmed through this program. The newly resolved multiples are: LHS 2071AB, GJ 1215ABC, LTT 7434AB, LHS 501AC, and LHS 3738AB. The remaining previously known resolved multiples were placed in this observing program so that ΔJHK_s could be established. In a future phase of this project, having ΔJHK_s will enable the estimation of each component's optical magnitudes by using the relations listed in Table 6.5, thus providing the luminosity ratios necessary for obtaining individual component masses from the photocentric orbits (§7.2.1).

We now discuss the five newly confirmed binaries.

7.5.1 LHS 2071AB

LHS 2071AB was first reported as a photocentric astrometric binary in Riedel et al. (2010). That work estimated a period of 16.4±2.8 years for this system but noted that because the orbit had not finished a complete cycle the estimate was highly uncertain. Figure 7.3 shows

[a]L = Laser Guide Star. N = Natural Guide Star

[b]B = Regular (broad band) JHK_s. Na = Narrow band equivalents.

an updated astrometric perturbation as well as the resolved K_s band image from Gemini. The joint spectral type is M4.0V. From the estimated $\Delta K_s \sim 1.3$ and the joint magnitude of $K_s = 8.20$ from 2MASS, we estimate $K_s = 9.8$ for the secondary companion. Given the system's trigonometric parallax of 68.81 mas (14.53 pc, Riedel et al. 2010), the secondary's absolute K magnitude is 9.0. This absolute magnitude puts the companion in the M9V to L0 spectral type range. The projected angular separation for the resolved image is $\sim 0.22''$, which translates to a projected physical separation of 3.2 AU. As shown in 7.3(a), the system has now been monitored for $\sim$13 years. If the period suggested by Riedel et al. (2010) is correct, we should be able to derive dynamical masses in an additional $\sim$4 years, once the orbit wraps in our data.

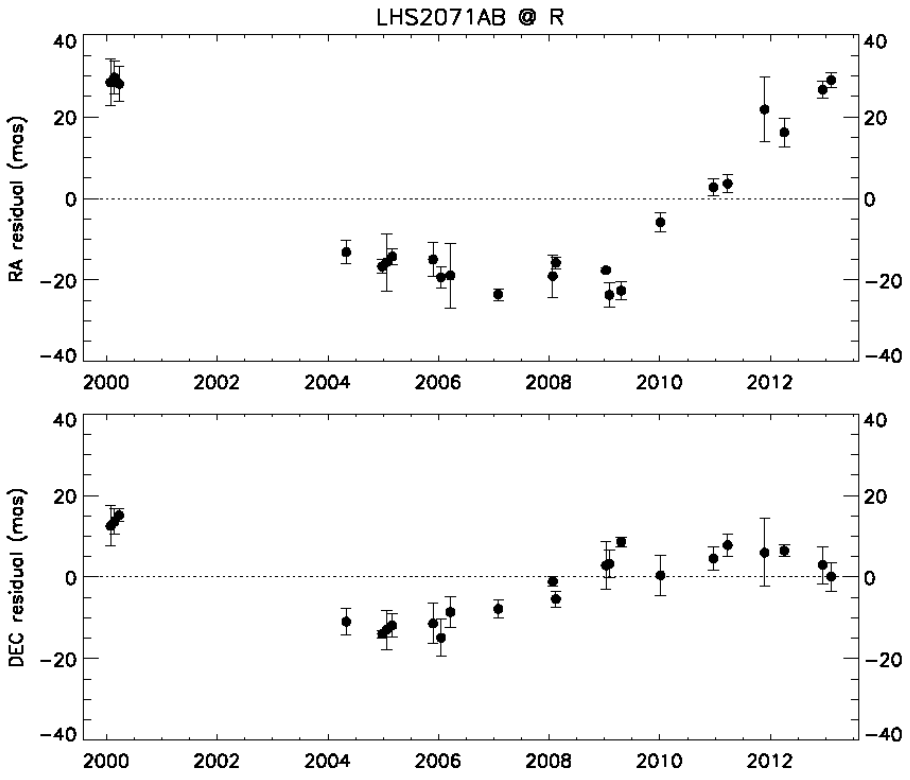

(a)

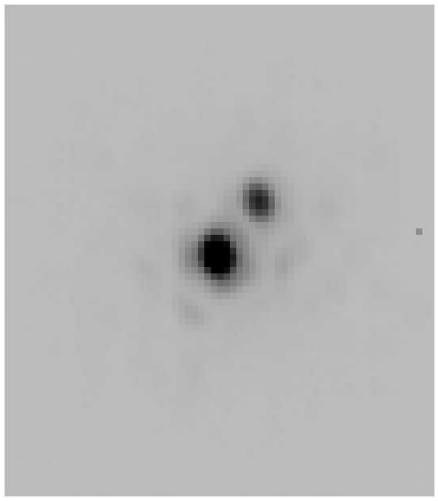

(b)

Figure 7.3 (a) Astrometric perturbation and (b) resolved K_s band image for LHS 2071AB. The separation is approximately $0.22''$ and $\Delta K_s \sim 1.3$. From the astrometric perturbation, Riedel et al. (2010) estimate a period of 16.4±2.8 years.

7.5.2 GJ 1215 ABC

GJ 1215 is an M5.0V (joint) star with a large and clear astrometric perturbation shown in Figure 7.1(b). The trigonometric parallax of 79.76 mas (CTIOPI/RECONS, unpublished) places the star at 12.54 pc. While the astrometric perturbation shown in Figure 7.1(b) is unequivocal, detecting the companion proved difficult, with both HST/FGS and infrared and optical speckle observations yielding null results. Although initial analysis of the Gemini AO images also seemed to show no companion, a more careful examination of the image revealed what is likely a triple system with two closely separated components orbiting the primary at a projected separation of $\sim$0.25″, or 3.1 AU. Figure 7.4 shows the results. The duplicity of the secondary component was inferred in most of the nine individual images taken through each band before co-adding them, thus lending a high degree of confidence to the existence of the C component. The projected separation between components B and C is $\sim$0.076″, or $\sim$1.0 AU. Approximating the luminosities of both components as equal and approximating $\Delta K_{s(A-BC)} \sim 4.6$, the B and C components would have absolute magnitudes of $M_k \sim 12.3$, making them mid to late L dwarfs. The perturbation in Figure 7.1(b) has a period of $\sim$9.5 yr, and is now sufficiently sampled for mapping the orbit of the joint BC component around the A component. Once the orbits of the B and C components are mapped, that orbit will provide an independent verification of the total mass of the BC component. We will propose for more AO observations to continue to map the orbits of this exciting triple system, with emphasis on determining the orbits of the B and C components.

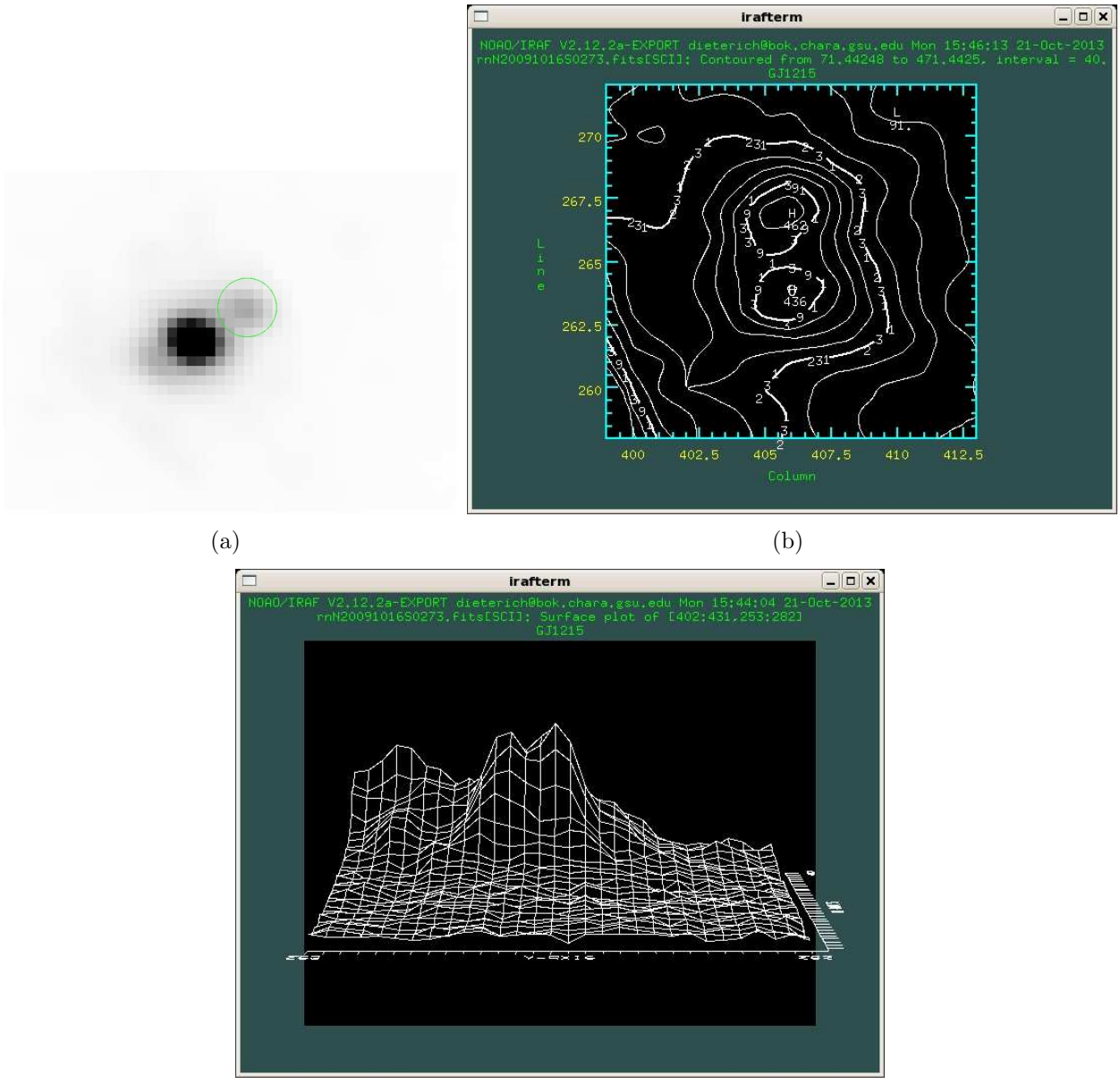

Figure 7.4 Discovery images for GJ 1215 BC. Figure (a) is a K_s band image showing the unresolved BC component enclosed with a circle. Figure (b) shows the contour plot in the H band, indicating a peak flux difference of $\sim$6% between the B and C components. The A component is off the plot to the lower left. Figure (c) shows the H band surface plot, where the peaks of the B and C components are visible in front of the rise in flux caused by the A component. The A-BC projected separation is $\sim$0.25″, or $\sim$3.1 AU. The B-C projected separation is $\sim$0.076″, or $\sim$1.0 AU.

7.5.3 LTT 7434AB

LTT 7434 is an M4.0V (joint) star for which we compute a parallax of 54.92 mas (18.21 pc, CTIOPI/RECONS, unpublished). The parallax residuals are shown in Figure 7.5, where a long term astrometric perturbation is visible. Unfortunately, the system was not monitored between 2004 and 2010. The perturbation is therefore still in the early stages of being mapped and a characterization of the orbit is still not possible.

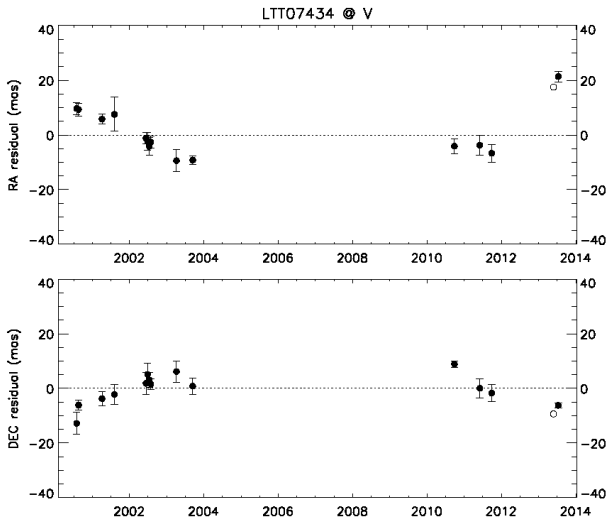

Figure 7.5 Astrometric perturbation for LTT 7434AB. Unfortunately, the system was not monitored between 2004 and 2010. While the perturbation is evident in both axes, more observations are needed to constrain the period and other orbital properties.

The Gemini AO observations revealed a faint companion at a projected separation of $\sim$0.12″ (2.2 AU), $\Delta J \sim 2.5$, and $\Delta H \sim 3.5$. The companion was not detected in the K_s band. The small separation and relatively high contrast of this system hinders the precise determination of flux ratio, and there is a large uncertainty in the magnitude differences quoted here. Assuming these values, we calculate $J - H \sim -0.6$ for the companion. The blue $J - H$,

color along with the non-detection in the K_s band suggest that the companion is a T dwarf. Figure 7.6 shows the image and plots for the system. The low signal-to-noise of the detection is evident in the surface plot. We will propose for further AO imaging of this system with longer exposure times in the hope of obtaining a better signal-to-noise for the companion, and detecting orbital motion.

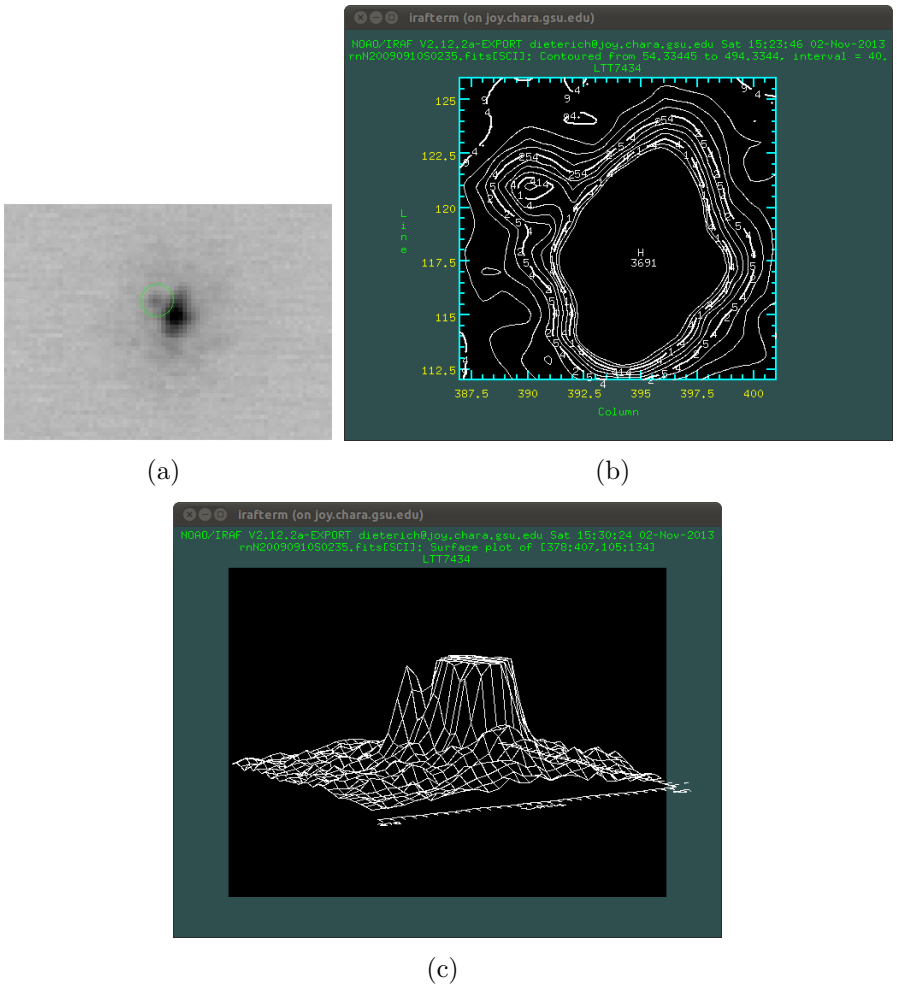

Figure 7.6 Discovery images for LTT 7434AB. Figure (a) is a J band image showing the faint B component enclosed with a circle. Figure (b) shows the contour plot in the J band with the flux ceiling set just above the B component's peak flux to facilitate viewing. Figure (c) shows the J band surface plot, also with a low flux ceiling. The low signal-to-noise for the companion is evident from Figure (c).

7.5.4 LHS 501AC

LHS 501A is an M4.0V star with a new parallax of 81.82 mas (12.22 pc, CTIOPI/RECONS, unpublished). The system is a known wide binary, with the B component (LHS 500, M5.0V) located at a projected separation of 107″, or ∼1300 AU. The trigonometric parallax of the A component has a perturbation indicative of a close binary. The Gemini AO images revealed a very close and relatively bright companion, with projected separation ∼0.07″ (0.9 AU), and $\Delta\ JHK_s \sim 0.3$. The separation is close to the diffraction limit for Gemini and the peaks of each component are only 3 pixels apart, thus making the value for separation very uncertain. Figure 7.7 shows the astrometric perturbation, the contour plot, and the surface plot for the system. Like LTT 7434AB, there is a gap in the astrometric coverage that makes determining the orbital period still not possible, although the declination axis hints at a period of ∼2 years. The relatively small and almost constant flux ratio indicates that the companion is likely a mid to late M dwarf.

7.5.5 LHS 3738AB

An astrometric perturbation for the M4.5V star LHS 3738 was first reported in Riedel et al. (2010). That work reported a parallax of 50.87 mas (19.67 pc) and a preliminary period of 5.8±0.2 years for the photocentric orbit. LHS 3738 is itself a member of a wider system in which LHS 3739 (M3.5V) is the primary component, thus making this system a hierarchical triple system. Riedel et al. (2010) reported a projected separation of 113.1″, or 2225 AU, between LHS 3739 and LHS 3738. We were able to resolve the LHS 3738 system into its

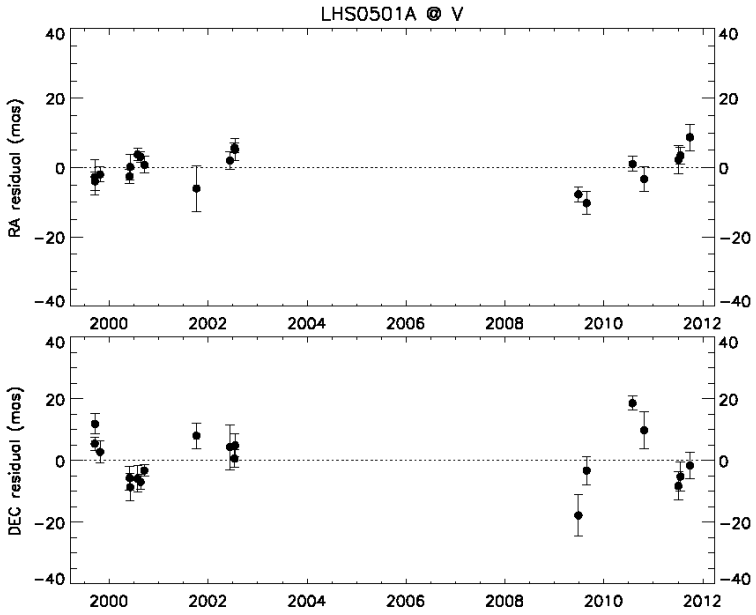

(a)

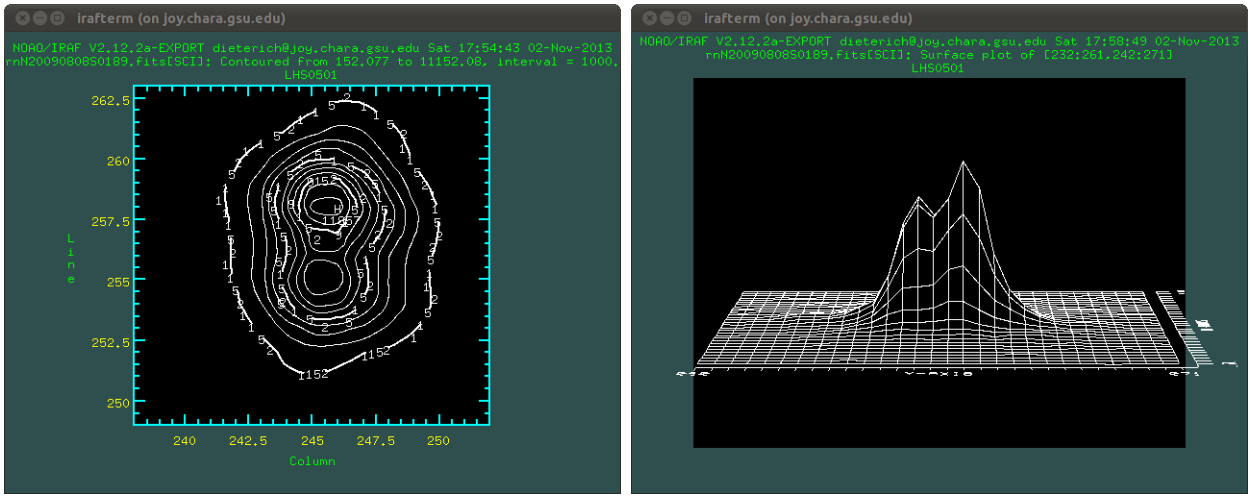

(b) (c)

Figure 7.7 (a) Astrometric perturbation, (b) contour plot, and (c) surface plot for LHS 501AC. The astrometric perturbation has a large gap in monitoring between 2003 and 2009. The declination axis shows hints of a period of ∼2 years, but more repetitions are needed to determine the a reliable period. The projected separation is only ∼0.07″ (0.9 AU), which makes determining the exact location of each peak difficult. Figure (c) is rotated 90° from Figure (b) so that the companion can be seen.

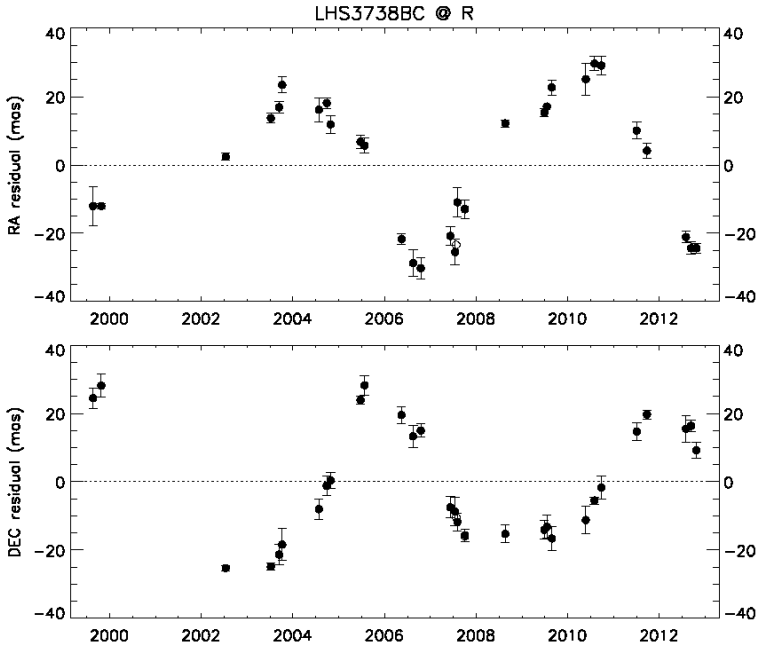

(a)

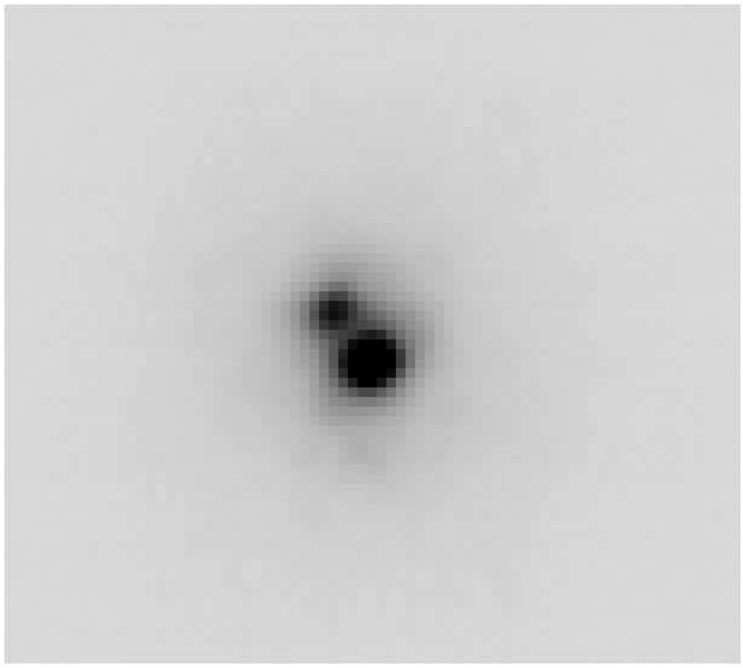

(b)

Figure 7.8 (a) Astrometric perturbation and (b) K_s band resolved image for LHS 3738BC. From the astrometric perturbation, Riedel et al. (2010) estimate an orbital period of 5.8±0.2 years. The projected separation is $\sim 0.11''$, or 2.2 AU. As can be seen from (a), the system has been monitored for more than two orbital periods, thus making it ripe for dynamical mass determination.

A and B components in all three bands, and estimate a projected separation of $\sim 0.11''$, or 2.2 AU. Figure 7.8 shows an updated version of the astrometric perturbation first reported in Riedel et al. (2010) and the resolved K_s band image. We estimate $\Delta JHK_s \sim 1.0$, which would make the companion a mid to late M dwarf.

As can be seen if Figure 7.8(a), the photocentric orbit of LHS 3738AB has already been monitored for more than two orbital periods and is therefore an ideal case for the derivation of dynamical masses using the procedures outlined in §7.2.1. The work to derive definite orbital parameters and masses for this system will commence soon and we plan to publish individual masses in a future paper.

7.6 The Future of the Gemini AO Project

In this chapter we provided an overview of the motivation for combining astrometric monitoring through trigonometric parallax observations with high resolution imaging in order to obtain dynamical masses. We also confirmed the existence of companions to five systems that were resolved for the first time as a result of this project. All measurements we report here are preliminary and are pending a more thorough reduction of the AO images and formal orbital fitting in the cases where enough astrometric coverage exists to determine orbital parameters. The next steps depend on the nature of each target with regard to what is already known about it and what can be known given the current data. For this purpose, it is useful to group the targets of this study into three broad categories: (1) the five systems that have been resolved for the first time as a result of this study, (2) previously

resolved systems that do not yet have dynamical masses determined, and (3) systems that already have dynamical masses. We now briefly examine what can be done to maximize the scientific potential of each of these groups. The scientific issues listed below will be addressed in an upcoming paper that will also provide a general overview of the project. After that, smaller papers that further characterize individual systems will follow as the dynamical masses become available.

7.6.1 First Detections

These five targets were presented in the preceding section. While only GJ 1215ABC and LHS 3738AB have enough astrometric coverage to yield dynamical masses at this point, there is intrinsic value in the publication of all five systems because they have been confirmed for the first time as a result of this study. The fact that we now have resolved JHK_s photometry also means that the near infrared colors of the components can be used to give further insight into their properties.

7.6.2 Previously Resolved Systems with no Dynamical Masses

Seven of the 19 systems resolved in this program had been previously resolved through other means, and yet still lack dynamical masses. They are: LHS 1630AB, GJ 2069AED, GJ 2069BC, LHS 6167AB, WT 1827AB, GJ 831AB and LHS 4009AB. The other targets have orbits that are in diverse states of completion, depending on the orbital period. We will investigate the extent to which it may be possible to estimate orbital parameters for orbits that seem nearly complete; however, experience dictates that such estimates must be

done with extreme caution. We also expect that several of these orbits will have complete coverage in the next few years. The majority of systems in this category were resolved previously using HST/FGS (e.g., Henry et al. 1999), which provides differential photometry in a bandpass that closely approximates the V band. Even if masses cannot yet be derived, combining the resolved JHK_s photometry and resolved V band photometry from HST/FGS greatly enhances the potential for photometric characterization of the companions. It is now possible to fit them into our newly derived color-magnitude relations (§6.4, Table 6.5) and to compare the companions to spectroscopically characterized objects that are good color matches.

7.6.3 Systems with Previously Known Dynamical Masses

Seven of the systems resolved in this study are systems for which dynamical masses already exist or have been published by others during the course of the study. These systems are: GJ 2005ABC, GJ 234AB, LHS 2397aAB, GJ 473AB, GJ 1005AB, GJ 65AB, and GJ 866ABC. Systems with well constrained masses, such as GJ 234AB, will serve as important checks on our methodology. It is also possible that for some systems our results will further reduce the errors associated with the mass measurements. Because dynamical masses for VLM stars and brown dwarfs can only be established for very closely separated systems, we often know very little about the atmospheric properties of the objects we use as benchmarks in the MLR. Indeed, the current MLRs are best described as Mass-Absolute Magnitude relations in the sense that they use a single photometric band as a proxy for luminosity (Henry & McCarthy 1993; Henry et al. 1999; Delfosse et al. 2000). As is the case with the systems described in

§7.6.2 above, knowledge of resolved JHK_s photometry will now allow us to better understand these important benchmarks and move in the direction of a true MLR where the benchmark objects are fully characterized.

CHAPTER 8

Conclusions

The work presented in this dissertation has connections to several topics in low mass star and brown dwarf research. In this concluding chapter, we review the highlights of the work. More importantly, we ask the question: *"How has the work presented here advanced the science of astronomy?"* The answer to this broad question can be used as the metric of the merit of any scientific work. This is especially true for the large and detailed projects that so often form the bulk of graduate dissertation work.

8.1 Stellar/Substellar Multiplicity

After a brief outline of the background knowledge that is most important for motivating this dissertation, we addressed the topic of M dwarf multiplicity, with an emphasis on stellar/substellar multiplicity, in Chapters 3 and 4. The conclusions from this study, in the form of multiplicity fractions for different scenarios, are listed in Table 4.2. By comparing our results to that of several other studies, we discuss "a current map of the brown dwarf desert" in §4.4. Our principal conclusion is that the scarcity of substellar companions orbiting stars seems to be a universal property of stellar populations. From the other studies we site in §4.4 we see that the brown dwarf desert exists regardless of the separations and ages of the systems in questions, and that the desert also prevails for a wide range of masses, but with the more massive component always significantly more massive than the secondary (primary of spectral types K or earlier). The work presented here finished the portrait of the brown dwarf desert by probing mass ratios approaching unity, where the stellar companion may be

only slightly more massive than the substellar companion. We find essentially the same result as the previous searches with more massive primaries, which state that the stellar/substellar multiplicity fraction is best characterized as being on the order of a few percent (Table 4.2). This finding excludes the possibility that mass ratio is the primary factor controlling the formation of stellar/substellar binaries, and points to the nature of the secondary companion as playing the primary role. In other words, we can now say with good confidence that regardless of the properties of the primary star, *Nature dislikes brown dwarfs as companions to stars.* The causes for this selection effect in the binary formation process are not clear. We discuss the implications of our findings in light of the leading stellar and brown dwarf formation theoretical scenarios in §4.6.2. Any theoretical prediction of the results of the stellar formation process must now replicate the multiplicity fractions stated in Table 4.2 and the general idea of a mostly invariant brown dwarf desert, if it is to be deemed valid.

Looking toward the future of this line of research, we note that the overall results in Table 4.2 are statistically robust, with uncertainties of only a few percent, and that given the size of our survey and those discussed in §4.4, little statistical robustness can be gained unless very large surveys for close substellar companions, on the order of thousands of targets, are implemented. Even then the value of such surveys may have more to do with the characteristics of individual objects and the presence of individual companions than in improving population properties. What could be improved is the connection between binary properties and precise masses at the extreme low mass end of the stellar main sequence. In Figure 4.5 and §4.6 we note that there is currently a gap in the companion mass coverage between 0.2

and 0.1 $M_{\odot}$. This mass range is important because it is where the onset of nearly equal mass multiplicity appears to take place. Making more dynamical masses available in that mass range will also improve the overall robustness of the MLR, which will improve our understanding of multiple systems as well as isolated objects (Chapter 7).

8.2 The HR Diagram at the End of the Stellar Main Sequence

In what is perhaps the most important aspect of this dissertation, we have conducted a photometric and astrometric survey of 63 objects thought to lie close to the stellar/substellar boundary, ranging in spectral types from M6V to L4. The methodology of this survey is discussed in Chapter 5 and its results are discussed in Chapter 6. The main result of this survey is the creation of the first HR diagram for these spectral types that is based on very broad photometric SED coverage ($\sim$97%), precise trigonometric distance measurements, and the latest model atmospheres for $T_{\rm eff}$ determination. The HR diagram is shown in Figure 6.3 and discussed in §6.3. By examining luminosity-radius (Figure 6.12) and temperature-radius (Figure 6.15) trends, we identify what is likely the minimum radius star at the end of the stellar main sequence and the subsequent jump to larger radii at cooler temperatures for brown dwarfs. We compare our findings to the predictions of several theoretical evolutionary models (§6.7.3) and find that none of the models adequately fit the data, but that the discrepancy is in the direction that is expected, given the recent revision of the solar metallicity values used to calibrate the models. We have checked our radii predictions against radii directly measured with long baseline optical interferometry and have achieved

good results for hotter stars (Figure 5.4). It is currently not possible to check our technique directly against measured radii for late M and L dwarfs. However, we are confident that the *BT-Settl* model atmospheres we are using work well in the late M and L temperature range because the uncertainties we obtain in the temperature derivations are no larger than the ones obtained for hotter objects. Should these results hold up to further scrutiny, this would be a significant discovery in the sense that it answers fundamental questions about the nature of the stellar population of the Galaxy, and what objects are or are not stars in the VLM domain. This research also highlighted the importance of optical photometry when studying cool stars and brown dwarfs.

There are still 19 objects in this project that do not have finished trigonometric parallaxes. We will include them in our HR diagram and publish them in a future publication. In the future, we must look for ways to test the results and the atmospheric models used to derive the effective temperatures, which are then used to derive radii. Direct comparison of model spectra to observed spectra in this temperature range is one way in which the models could be tested, thus accessing the validity of our results.

8.3 New Astrometric Binaries

The effort to obtain dynamical masses for VLM stars and brown dwarfs is necessarily a long term effort due to the orbital periods of the binary systems suitable for dynamical mass determination. Binaries for which the components can be resolved using high resolution imaging tend to have periods of several years in the VLM regime. In Chapter 7, we described

observations done as part of a pilot project to resolve several binaries for which we noticed astrometric perturbations in the trigonometric parallax solutions. By resolving five binary systems for the first time, we have confirmed their multiplicity, determined their separations as well as their flux ratios, all of which are necessary for dynamical mass determinations.

Mass is the most fundamental property of any astronomical object, and the dynamical masses we will obtain as a result of this long term project will allow for a thorough comparison of stellar properties to model predictions. As a result of this project we will be able to populate the HR diagram of Figure 6.3 with benchmark binaries, refine the MLR, constrain rates of substellar cooling, and provide the data needed to finally understand the physics of these low mass objects in detail.

8.4 Final Thoughts

I have spent the last eight years of my life learning and teaching astronomy, and in particular, absorbing and producing knowledge about our faintest Galactic neighbors and their fundamental properties. Only time will tell if the specific results presented in this dissertation are or are not a significant contribution to human knowledge. Regardless of specific results, I will be satisfied if looking back at this work I can say that it has broadened our perception of the Universe in a small way, and helped shift our vision from one that is Earth-centered to one that provides a broader understanding of our place in the Galaxy. As I look back, in the future, I hope to remember what exciting times these were for astronomy and physics. During the course of my graduate studies NASA's Kepler mission discovered hundred of

extrasolar planets, the Hubble Space Telescope was saved by a daring servicing mission, an SUV-sized rover landed on Mars, we were treated to a transit of Venus, a Nobel Prize was awarded for the discovery of the acceleration of the expansion of the Universe, and the existence of the Higgs Boson was confirmed at the Large Hadron Collider at CERN.

As I write this, the United States is slowly emerging from the Great Recession that started in 2008, and science spending is being cut in all areas. And yet, there is so much potential for discovery that did not exist even a decade ago. As astronomy reaches for the depths of the cosmos with projects such as the Dark Energy Survey and approaches the point where we can seriously consider the possibility of life in other planets, many of which may soon be imaged in detail, it is easy to see that we are on the verge of a potential revolution is astronomy the likes of which have not been seen before. I hope whoever reads this will be able to say that the People realized that they had too much to lose by not investing in science and chose to fund its true potential. As for me, I am grateful to have been a part of this exciting time, in no matter how small a manner.

REFERENCES

Allard, F., Hauschildt, P. H., Alexander, D. R., Tamanai, A., & Schweitzer, A. 2001, ApJ, 556, 357

Allard, F., Hauschildt, P. H., Baraffe, I., & Chabrier, G. 1996, ApJ, 465, L123

Allard, F., Homeier, D., Freytag, B., Schaffenberger, W., & Rajpurohit, A. S. 2013, ArXiv e-prints

Allard, F., Homeier, D., Freytag, B., & Sharp, C. M. 2012, in EAS Publications Series, Vol. 57, EAS Publications Series, ed. C. Reylé, C. Charbonnel, & M. Schultheis, 3–43

Allen, P. R. 2007, ApJ, 668, 492

Allen, P. R., Burgasser, A. J., Faherty, J. K., & Kirkpatrick, J. D. 2012, AJ, 144, 62

Allen, P. R., Koerner, D. W., McElwain, M. W., Cruz, K. L., & Reid, I. N. 2007, AJ, 133, 971

Allen, P. R., Koerner, D. W., Reid, I. N., & Trilling, D. E. 2005, ApJ, 625, 385

Allen, P. R., & Reid, I. N. 2008, AJ, 135, 2024

Allers, K. N., & Liu, M. C. 2013, ApJ, 772, 79

Andrei, A. H. et al. 2011, AJ, 141, 54

Antonova, A., Doyle, J. G., Hallinan, G., Golden, A., & Koen, C. 2007, A&A, 472, 257

Apai, D., Radigan, J., Buenzli, E., Burrows, A., Reid, I. N., & Jayawardhana, R. 2013, ApJ, 768, 121

Bailer-Jones, C. A. L., & Mundt, R. 2001, A&A, 367, 218

Baraffe, I., Chabrier, G., Allard, F., & Hauschildt, P. H. 1995, ApJ, 446, L35

——. 1998, A&A, 337, 403

——. 2002, A&A, 382, 563

Baraffe, I., Chabrier, G., Barman, T. S., Allard, F., & Hauschildt, P. H. 2003, A&A, 402, 701

Basri, G., Mohanty, S., Allard, F., Hauschildt, P. H., Delfosse, X., Martín, E. L., Forveille, T., & Goldman, B. 2000, ApJ, 538, 363

Bate, M. R. 2009, MNRAS, 392, 590

——. 2011, MNRAS, 417, 2036

Becklin, E. E., & Zuckerman, B. 1988, Nature, 336, 656

Berger, E. 2002, ApJ, 572, 503

Berger, E. et al. 2010, ApJ, 709, 332

Bessel, M. S. 1990, A&AS, 83, 357

Bessell, M., & Murphy, S. 2012, PASP, 124, 140

Bessell, M. S. 1995, PASP, 107, 672

Biller, B. A. et al. 2007, ApJS, 173, 143

Binney, J., Dehnen, W., & Bertelli, G. 2000, MNRAS, 318, 658

Blake, C. H., Charbonneau, D., & White, R. J. 2010, ApJ, 723, 684

Bochanski, J. J., Hawley, S. L., Covey, K. R., West, A. A., Reid, I. N., Golimowski, D. A., & Ivezić, Ž. 2010, AJ, 139, 2679

Bonnell, I. A., Clark, P., & Bate, M. R. 2008, MNRAS, 389, 1556

Bouy, H. et al. 2008, A&A, 486, 877

Bowler, B. P., Liu, M. C., & Dupuy, T. J. 2010, ApJ, 710, 45

Boyajian, T. S. et al. 2012, ApJ, 757, 112

Burgasser, A. J. 2004, ApJS, 155, 191

Burgasser, A. J. et al. 2002, ApJ, 564, 421

Burgasser, A. J., Kirkpatrick, J. D., Liebert, J., & Burrows, A. 2003a, ApJ, 594, 510

Burgasser, A. J., Kirkpatrick, J. D., & Lowrance, P. J. 2005, AJ, 129, 2849

Burgasser, A. J., Kirkpatrick, J. D., Reid, I. N., Brown, M. E., Miskey, C. L., & Gizis, J. E. 2003b, ApJ, 586, 512

Burgasser, A. J., Looper, D. L., Kirkpatrick, J. D., Cruz, K. L., & Swift, B. J. 2008a, ApJ, 674, 451

Burgasser, A. J., McElwain, M. W., Kirkpatrick, J. D., Cruz, K. L., Tinney, C. G., & Reid, I. N. 2004, AJ, 127, 2856

Burgasser, A. J., Reid, I. N., Siegler, N., Close, L., Allen, P., Lowrance, P., & Gizis, J. 2007, Protostars and Planets V, 427

Burgasser, A. J., Vrba, F. J., Lépine, S., Munn, J. A., Luginbuhl, C. B., Henden, A. A., Guetter, H. H., & Canzian, B. C. 2008b, ApJ, 672, 1159

Burgasser, A. J., Witte, S., Helling, C., Sanderson, R. E., Bochanski, J. J., & Hauschildt, P. H. 2009, ApJ, 697, 148

Burrows, A., Heng, K., & Nampaisarn, T. 2011, ApJ, 736, 47

Burrows, A., Hubbard, W. B., Lunine, J. I., & Liebert, J. 2001, Reviews of Modern Physics,

73, 719

Burrows, A., Hubbard, W. B., Saumon, D., & Lunine, J. I. 1993, ApJ, 406, 158

Burrows, A. et al. 1997, ApJ, 491, 856

Caballero, J. A. 2007, ApJ, 667, 520

Caffau, E., Ludwig, H.-G., Steffen, M., Freytag, B., & Bonifacio, P. 2011, Sol. Phys., 268, 255

Chabrier, G., & Baraffe, I. 1997, A&A, 327, 1039

——. 2000, ARA&A, 38, 337

Chabrier, G., Baraffe, I., Allard, F., & Hauschildt, P. 2000, ApJ, 542, 464

Chabrier, G., Baraffe, I., Allard, F., & Hauschildt, P. H. 2005, ArXiv Astrophysics e-prints

Chabrier, G., Baraffe, I., Leconte, J., Gallardo, J., & Barman, T. 2009, in American Institute of Physics Conference Series, Vol. 1094, 15th Cambridge Workshop on Cool Stars, Stellar Systems, and the Sun, ed. E. Stempels, 102–111

Clark, B. M., Blake, C. H., & Knapp, G. R. 2012, ApJ, 744, 119

Close, L. M., Siegler, N., Freed, M., & Biller, B. 2003, ApJ, 587, 407

Close, L. M. et al. 2007, ApJ, 660, 1492

Cohen, M., Wheaton, W. A., & Megeath, S. T. 2003, AJ, 126, 1090

Comerón, F., Testi, L., & Natta, A. 2010, A&A, 522, A47

Costa, E., Méndez, R. A., Jao, W.-C., Henry, T. J., Subasavage, J. P., Brown, M. A., Ianna, P. A., & Bartlett, J. 2005, AJ, 130, 337

Crifo, F., Phan-Bao, N., Delfosse, X., Forveille, T., Guibert, J., Martín, E. L., & Reylé, C.

2005, A&A, 441, 653

Cruz, K. L., Kirkpatrick, J. D., & Burgasser, A. J. 2009, AJ, 137, 3345

Cruz, K. L. et al. 2007, AJ, 133, 439

Cruz, K. L., Reid, I. N., Liebert, J., Kirkpatrick, J. D., & Lowrance, P. J. 2003, AJ, 126, 2421

Cushing, M. C. et al. 2011, ApJ, 743, 50

Cushing, M. C., Looper, D., Burgasser, A. J., Kirkpatrick, J. D., Faherty, J., Cruz, K. L., Sweet, A., & Sanderson, R. E. 2009, ApJ, 696, 986

Cushing, M. C. et al. 2008, ApJ, 678, 1372

Cushing, M. C., Saumon, D., & Marley, M. S. 2010, AJ, 140, 1428

Dahn, C. C. et al. 2002, AJ, 124, 1170

Delfosse, X. et al. 2004, in Astronomical Society of the Pacific Conference Series, Vol. 318, Spectroscopically and Spatially Resolving the Components of the Close Binary Stars, ed. R. W. Hilditch, H. Hensberge, & K. Pavlovski, 166–174

Delfosse, X., Forveille, T., Ségransan, D., Beuzit, J.-L., Udry, S., Perrier, C., & Mayor, M. 2000, A&A, 364, 217

Dieterich, S. B., Henry, T. J., Golimowski, D. A., Krist, J. E., & Tanner, A. M. 2012, AJ, 144, 64

Dieterich, S. B., Henry, T. J., Jao, W.-C., & Riedel, A. R. 2011, in Astronomical Society of the Pacific Conference Series, Vol. 448, 16th Cambridge Workshop on Cool Stars, Stellar Systems, and the Sun, ed. C. Johns-Krull, M. K. Browning, & A. A. West, 849

Duchêne, G., & Kraus, A. 2013, ARA&A, 51, 269

Dupuy, T. J., & Liu, M. C. 2012, ApJS, 201, 19

Dupuy, T. J., Liu, M. C., & Ireland, M. J. 2009, ApJ, 699, 168

Duquennoy, A., & Mayor, M. 1991, A&A, 248, 485

Enoch, M. L., Brown, M. E., & Burgasser, A. J. 2003, AJ, 126, 1006

Evans, T. M. et al. 2012, ApJ, 744, 120

Faherty, J. K., Burgasser, A. J., Cruz, K. L., Shara, M. M., Walter, F. M., & Gelino, C. R. 2009, AJ, 137, 1

Faherty, J. K. et al. 2012, ApJ, 752, 56

Faherty, J. K., Burgasser, A. J., West, A. A., Bochanski, J. J., Cruz, K. L., Shara, M. M., & Walter, F. M. 2010, AJ, 139, 176

Fischer, D. A., & Marcy, G. W. 1992, ApJ, 396, 178

Forveille, T. et al. 2004, A&A, 427, L1

Freed, M., Close, L. M., & Siegler, N. 2003, ApJ, 584, 453

Gatewood, G., & Coban, L. 2009, AJ, 137, 402

Geballe, T. R. et al. 2002, ApJ, 564, 466

Gelino, C. R., Marley, M. S., Holtzman, J. A., Ackerman, A. S., & Lodders, K. 2002, ApJ, 577, 433

Gizis, J. E., Monet, D. G., Reid, I. N., Kirkpatrick, J. D., Liebert, J., & Williams, R. J. 2000, AJ, 120, 1085

Gizis, J. E., & Reid, I. N. 1997, PASP, 109, 849

Gizis, J. E., Reid, I. N., & Hawley, S. L. 2002, AJ, 123, 3356

Gizis, J. E., Reid, I. N., Knapp, G. R., Liebert, J., Kirkpatrick, J. D., Koerner, D. W., & Burgasser, A. J. 2003, AJ, 125, 3302

Golimowski, D. A. et al. 2004a, AJ, 128, 1733

——. 2004b, AJ, 127, 3516

Golimowski, D. A., Minniti, D., Henry, T. J., & Ford, H. C. 2006, in Bulletin of the American Astronomical Society, Vol. 38, American Astronomical Society Meeting Abstracts #208, 83

Golimowski, D. A., Minniti, D., Henry, T. J., & Ford, H. C. 2007, in IAU Symposium, Vol. 240, IAU Symposium, ed. W. I. Hartkopf, P. Harmanec, & E. F. Guinan, 329

Graham, J. A. 1982, PASP, 94, 244

Grether, D., & Lineweaver, C. H. 2006, ApJ, 640, 1051

Grevesse, N., Noels, A., & Sauval, A. J. 1993, A&A, 271, 587

Harding, L. K., Hallinan, G., Boyle, R. P., Butler, R. F., Sheehan, B., & Golden, A. 2011, in Astronomical Society of the Pacific Conference Series, Vol. 448, 16th Cambridge Workshop on Cool Stars, Stellar Systems, and the Sun, ed. C. Johns-Krull, M. K. Browning, & A. A. West, 219

Hawley, S. L. et al. 2002, AJ, 123, 3409

Hayashi, C., & Nakano, T. 1963, Progress of Theoretical Physics, 30, 460

Heinze, A. N. et al. 2013, ApJ, 767, 173

Henry, T. J. 1991, PhD thesis, Arizona Univ., Tucson.

Henry, T. J., Franz, O. G., Wasserman, L. H., Benedict, G. F., Shelus, P. J., Ianna, P. A., Kirkpatrick, J. D., & McCarthy, Jr., D. W. 1999, ApJ, 512, 864

Henry, T. J., Jao, W.-C., Subasavage, J. P., Beaulieu, T. D., Ianna, P. A., Costa, E., & Méndez, R. A. 2006, AJ, 132, 2360

Henry, T. J., & McCarthy, Jr., D. W. 1990, ApJ, 350, 334

——. 1993, AJ, 106, 773

Henry, T. J., Subasavage, J. P., Brown, M. A., Beaulieu, T. D., Jao, W.-C., & Hambly, N. C. 2004, AJ, 128, 2460

Hester, J. J. et al. 1996, AJ, 111, 2349

Hinz, J. L., McCarthy, Jr., D. W., Simons, D. A., Henry, T. J., Kirkpatrick, J. D., & McGuire, P. C. 2002, AJ, 123, 2027

Iben, Jr., I., & Laughlin, G. 1989, ApJ, 341, 312

Jao, W.-C., Henry, T. J., Subasavage, J. P., Brown, M. A., Ianna, P. A., Bartlett, J. L., Costa, E., & Méndez, R. A. 2005, AJ, 129, 1954

Jao, W.-C., Henry, T. J., Subasavage, J. P., Winters, J. G., Riedel, A. R., & Ianna, P. A. 2011, AJ, 141, 117

Jarrett, T. H. et al. 2011, ApJ, 735, 112

Jayawardhana, R., Ardila, D. R., Stelzer, B., & Haisch, Jr., K. E. 2003, AJ, 126, 1515

Jenkins, J. S., Ramsey, L. W., Jones, H. R. A., Pavlenko, Y., Gallardo, J., Barnes, J. R., & Pinfield, D. J. 2009, ApJ, 704, 975

Kendall, T. R., Mauron, N., Azzopardi, M., & Gigoyan, K. 2003, A&A, 403, 929

Khandrika, H., Burgasser, A. J., Melis, C., Luk, C., Bowsher, E., & Swift, B. 2013, AJ, 145, 71

Kirkpatrick, J. D. 2005, ARA&A, 43, 195

Kirkpatrick, J. D., Barman, T. S., Burgasser, A. J., McGovern, M. R., McLean, I. S., Tinney, C. G., & Lowrance, P. J. 2006, ApJ, 639, 1120

Kirkpatrick, J. D. et al. 2008, ApJ, 689, 1295

——. 2012, ApJ, 753, 156

Kirkpatrick, J. D., Henry, T. J., & Irwin, M. J. 1997, AJ, 113, 1421

Kirkpatrick, J. D., Henry, T. J., & Liebert, J. 1993, ApJ, 406, 701

Kirkpatrick, J. D. et al. 1999, ApJ, 519, 802

——. 2000, AJ, 120, 447

Knapp, G. R. et al. 2004, AJ, 127, 3553

Koen, C. 2003, MNRAS, 346, 473

——. 2004, MNRAS, 354, 378

——. 2005, MNRAS, 360, 1132

Koen, C., Matsunaga, N., & Menzies, J. 2004, MNRAS, 354, 466

Konopacky, Q. M., Ghez, A. M., Barman, T. S., Rice, E. L., Bailey, III, J. I., White, R. J., McLean, I. S., & Duchêne, G. 2010, ApJ, 711, 1087

Kraus, A. L., Ireland, M. J., Martinache, F., & Hillenbrand, L. A. 2011, ApJ, 731, 8

Kraus, A. L., Ireland, M. J., Martinache, F., & Lloyd, J. P. 2008, ApJ, 679, 762

Kraus, A. L., White, R. J., & Hillenbrand, L. A. 2005, ApJ, 633, 452

Krist, J. E., Golimowski, D. A., Schroeder, D. J., & Henry, T. J. 1998, PASP, 110, 1046

Krist, J. E., & Hook, R. N. 1997, in The 1997 HST Calibration Workshop with a New Generation of Instruments, ed. S. Casertano, R. Jedrzejewski, T. Keyes, & M. Stevens, 192–+

Kumar, S. S. 1963, ApJ, 137, 1121

Landolt, A. U. 1992, AJ, 104, 340

——. 2007, AJ, 133, 2502

——. 2009, AJ, 137, 4186

Law, N. M., Dhital, S., Kraus, A., Stassun, K. G., & West, A. A. 2010, ApJ, 720, 1727

Leggett, S. K., Allard, F., Burgasser, A. J., Jones, H. R. A., Marley, M. S., & Tsuji, T. 2005, in ESA Special Publication, Vol. 560, 13th Cambridge Workshop on Cool Stars, Stellar Systems and the Sun, ed. F. Favata, G. A. J. Hussain, & B. Battrick, 143

Leggett, S. K., Hauschildt, P. H., Allard, F., Geballe, T. R., & Baron, E. 2002, MNRAS, 332, 78

Liu, M. C., & Leggett, S. K. 2005a, ApJ, 634, 616

——. 2005b, ApJ, 634, 616

Lodieu, N., Scholz, R.-D., McCaughrean, M. J., Ibata, R., Irwin, M., & Zinnecker, H. 2005, A&A, 440, 1061

Lodieu, N., Zapatero Osorio, M. R., Martín, E. L., Solano, E., & Aberasturi, M. 2010, ApJ, 708, L107

Looper, D. L. et al. 2008, ApJ, 686, 528

Lowrance, P. J. et al. 2005, AJ, 130, 1845

Luhman, K. L. 2012, ARA&A, 50, 65

Luhman, K. L., McLeod, K. K., & Goldenson, N. 2005, ApJ, 623, 1141

Marcy, G. W., & Butler, R. P. 2000, PASP, 112, 137

Martín, E. L., Delfosse, X., Basri, G., Goldman, B., Forveille, T., & Zapatero Osorio, M. R. 1999, AJ, 118, 2466

Masciadri, E., Mundt, R., Henning, T., Alvarez, C., & Barrado y Navascués, D. 2005, ApJ, 625, 1004

McCarthy, C., & Zuckerman, B. 2004, AJ, 127, 2871

McCarthy, Jr., D. W., Henry, T. J., McLeod, B., & Christou, J. C. 1991, AJ, 101, 214

McGovern, M. R., Kirkpatrick, J. D., McLean, I. S., Burgasser, A. J., Prato, L., & Lowrance, P. J. 2004, ApJ, 600, 1020

Metchev, S. A., & Hillenbrand, L. A. 2009, ApJS, 181, 62

Nakajima, T., Oppenheimer, B. R., Kulkarni, S. R., Golimowski, D. A., Matthews, K., & Durrance, S. T. 1995, Nature, 378, 463

Oppenheimer, B. R., Golimowski, D. A., Kulkarni, S. R., Matthews, K., Nakajima, T., Creech-Eakman, M., & Durrance, S. T. 2001, AJ, 121, 2189

Phan-Bao, N. et al. 2008, MNRAS, 383, 831

Radigan, J., Jayawardhana, R., Lafrenière, D., Artigau, É., Marley, M., & Saumon, D. 2012, ApJ, 750, 105

Raghavan, D. et al. 2010, ApJS, 190, 1

Rajpurohit, A. S., Reylé, C., Allard, F., Homeier, D., Schultheis, M., Bessell, M. S., & Robin, A. C. 2013, ArXiv e-prints

Rebolo, R., Martin, E. L., & Magazzu, A. 1992, ApJ, 389, L83

Reid, I. N., Cruz, K. L., Burgasser, A. J., & Liu, M. C. 2008, AJ, 135, 580

Reid, I. N. et al. 2003, AJ, 125, 354

Reid, I. N., & Gizis, J. E. 1997, AJ, 113, 2246

Reid, I. N., Hawley, S. L., & Gizis, J. E. 1995, AJ, 110, 1838

Reid, I. N., Lewitus, E., Allen, P. R., Cruz, K. L., & Burgasser, A. J. 2006, AJ, 132, 891

Reiners, A., & Basri, G. 2009, ApJ, 705, 1416

Reipurth, B., & Clarke, C. 2001, AJ, 122, 432

Reylé, C., Scholz, R.-D., Schultheis, M., Robin, A. C., & Irwin, M. 2006, MNRAS, 373, 705

Riedel, A. R. et al. 2010, AJ, 140, 897

Rosenthal, E. D., Gurwell, M. A., & Ho, P. T. P. 1996, Nature, 384, 243

Salpeter, E. E. 1955, ApJ, 121, 161

Saumon, D., Chabrier, G., & van Horn, H. M. 1995, ApJS, 99, 713

Schmidt, S. J., Cruz, K. L., Bongiorno, B. J., Liebert, J., & Reid, I. N. 2007, AJ, 133, 2258

Schmidt, S. J., West, A. A., Hawley, S. L., & Pineda, J. S. 2010, AJ, 139, 1808

Scholz, R.-D., Lodieu, N., Ibata, R., Bienaymé, O., Irwin, M., McCaughrean, M. J., & Schwope, A. 2004, MNRAS, 347, 685

Seifahrt, A., Reiners, A., Almaghrbi, K. A. M., & Basri, G. 2010, A&A, 512, A37

Shkolnik, E., Liu, M. C., & Reid, I. N. 2009, ApJ, 699, 649

Shkolnik, E. L., Hebb, L., Liu, M. C., Reid, I. N., & Collier Cameron, A. 2010, ApJ, 716, 1522

Shu, F. H., Lizano, S., & Adams, F. C. 1987, in IAU Symposium, Vol. 115, Star Forming Regions, ed. M. Peimbert & J. Jugaku, 417–433

Sivarani, T., Lépine, S., Kembhavi, A. K., & Gupchup, J. 2009, ApJ, 694, L140

Skrutskie, M. F. et al. 2006, AJ, 131, 1163

Sorahana, S., Yamamura, I., & Murakami, H. 2013, ApJ, 767, 77

Stamatellos, D., Maury, A., Whitworth, A., & André, P. 2011, MNRAS, 413, 1787

Stassun, K. G., Mathieu, R. D., & Valenti, J. A. 2006, Nature, 440, 311

Subasavage, J. P., Jao, W.-C., Henry, T. J., Bergeron, P., Dufour, P., Ianna, P. A., Costa, E., & Méndez, R. A. 2009, AJ, 137, 4547

Thies, I., & Kroupa, P. 2007, ApJ, 671, 767

Thies, I., Kroupa, P., Goodwin, S. P., Stamatellos, D., & Whitworth, A. P. 2010, ApJ, 717, 577

Tinney, C. G. 1996, MNRAS, 281, 644

Tinney, C. G., Burgasser, A. J., Kirkpatrick, J. D., & McElwain, M. W. 2005, AJ, 130, 2326

Tinney, C. G., Reid, I. N., Gizis, J., & Mould, J. R. 1995, AJ, 110, 3014

Torres, G. 2013, Astronomische Nachrichten, 334, 4

van Altena, W. F., Lee, J. T., & Hoffleit, D. 1995, VizieR Online Data Catalog, 1174, 0

van Leeuwen, F., ed. 2007, Astrophysics and Space Science Library, Vol. 350, Hipparcos, the New Reduction of the Raw Data

Whitworth, A. P., & Zinnecker, H. 2004, A&A, 427, 299

Williams, K. A., Bolte, M., & Koester, D. 2009, ApJ, 693, 355

Wright, E. L. et al. 2010, AJ, 140, 1868

York, D. G. et al. 2000, AJ, 120, 1579

Zapatero Osorio, M. R., Martín, E. L., Béjar, V. J. S., Bouy, H., Deshpande, R., & Wainscoat, R. J. 2007, ApJ, 666, 1205

APPENDIX – IDL Codes for Determining Effective Temperature and SED Fits

This appendix contains all code used to determine the effective temperature, luminosity, and radius of objects based on the *BT-Settl* models. The motivation and physics behind the procedures is explained in §§5.5 and 5.6. The codes are transcribed here "as used", and several of them could be improved. The explanations accompanying every code are meant in part to provide a step by step description of the pipeline.

All codes were run using IDL version 7.0.

A Formatting Input Spectral Templates

The *BT-Settl* synthetic spectra are provided in a wavelength scale that varies according to the region of the spectrum and increments are generally smaller than 1 Å. This precision is not needed for calculating photometric magnitudes. Computations are greatly simplified if the spectra are smoothed using a 1Å scale, so that integrating over wavelength can be done by counting array elements. This simplification avoids the use of "for" loops, and makes the code ran considerably faster.

The following code takes a list of file names containing *BT-Settl* spectra and outputs the spectra in those files using a 1Å scale running from 4,000Å to 30μm. This is the wavelength range that will be used for all calculations.

```
pro formatspectra,infile

readcol,infile,filenames,format='a'
```

```
size=n_elements(filenames)

intwave =lindgen(296000)+4000
for i=0,size-1 do begin
    print,""
    print, "Working on ",filenames[i]
    readcol,filenames[i],wave,logflux,format="d,d"
    flux=10.^logflux
    intflux = interpol(flux,wave,intwave)
    smoothintflux = smooth(intflux,20)
    openw,unit,'int'+filenames[i],/get_lun
    for j=0L,295999 do printf,unit,intwave[j],smoothintflux[j]
    free_lun, unit
endfor
end
```

B Obtaining Colors From Synthetic Spectra

Once spectra are formatted, it is necessary to obtain the synthetic colors for all combinations of bands V, R, I, J, H, K_s, $W1$, $W2$, and $W3$ for each synthetic spectrum. This is done using the tabulated photometric zero points for each band and the filter response function for each band. The input is a one column text file with a list of file names for the synthetic spectra. The output is one text file consisting of a large table. The first column of the output is the file name, and the others are the 36 possible colors.

```
pro synthcolors,infile

colorset
readcol,infile,filenames,format="a"
howmanyfiles = n_elements(filenames)

readcol,"V_curve.txt",vwave,vtrans,format="L,d", /silent
readcol,"R_curve.txt",rwave,rtrans,format="L,d", /silent
readcol,"I_curve.txt",iwave,itrans,format="L,d", /silent
readcol,"J_RSR_curve.txt",jwave,jtrans,format="L,d", /silent
readcol,"H_RSR_curve.txt",hwave,htrans,format="L,d", /silent
readcol,"Ks_RSR_curve.txt",kswave,kstrans,format="L,d", /silent
readcol,"intw1curve.txt",w1wave,w1trans,format="L,d", /silent
readcol,"intw2curve.txt",w2wave,w2trans,format="L,d", /silent
readcol,"w3curve.txt",w3wave,w3trans,format="L,d", /silent
readcol,"w4curve.txt",w4wave,w4trans,format="L,d",/silent

;; The effective wavelengths for the bands are:
veffwave = 5455. ;Angstroms, Bessel and Murphy 2012 PASP 124,140, table 3
reffwave = 6426.
ieffwave = 7939.
jeffwave = 1.235e4  ;Angstroms, Cohen et al. 2003 AJ 126,1096, table 2
heffwave = 1.662e4
kseffwave = 2.159e4
w1effwave = 3.353e4 ;Angstroms, Jarrett et al 2011, ApJ 735,112, table 4
w2effwave = 4.603e4
w25effwave = 8.05e4   ; mean of w2 and w3. covers gap for polynomial
```

```
w3effwave = 1.156e5
w34effwave = 1.682e5
w4effwave = 2.208e5


wave = lindgen(296000)+4000+5
sizelongwave=n_elements(wave)
longflux =    fltarr(sizelongwave)
longvtrans =  fltarr(sizelongwave)
longrtrans =  fltarr(sizelongwave)
longitrans =  fltarr(sizelongwave)
longjtrans =  fltarr(sizelongwave)
longhtrans =  fltarr(sizelongwave)
longkstrans = fltarr(sizelongwave)
longw1trans = fltarr(sizelongwave)
longw2trans = fltarr(sizelongwave)
longw3trans = fltarr(sizelongwave)
longw4trans = fltarr(sizelongwave)


minvwave=min(vwave)
minrwave=min(rwave)
miniwave=min(iwave)
minjwave=min(jwave)
minhwave=min(hwave)
minkswave=min(kswave)
minw1wave=min(w1wave)
minw2wave=min(w2wave)
minw3wave=min(w3wave)
minw4wave=min(w4wave)

sizevwave=n_elements(vwave)
sizerwave=n_elements(rwave)
sizeiwave=n_elements(iwave)
sizejwave=n_elements(jwave)
sizehwave=n_elements(hwave)
sizekswave=n_elements(kswave)
sizew1wave=n_elements(w1wave)
sizew2wave=n_elements(w2wave)
sizew3wave=n_elements(w3wave)
sizew4wave=n_elements(w4wave)
```

```
for i=0L, sizelongwave-1 do begin ; this loop will create the long
                                  ; band arrays
    if wave[i] eq minvwave then begin
        for j=0L,sizevwave-1 do longvtrans[i+j] =vtrans[j]
    endif
    if wave[i] eq minrwave then begin
        for j=0L,sizerwave-1 do longrtrans[i+j] =rtrans[j]
    endif
    if wave[i] eq miniwave then begin
        for j=0L,sizeiwave-1 do longitrans[i+j] =itrans[j]
    endif
    if wave[i] eq minjwave then begin
        for j=0L,sizejwave-1 do longjtrans[i+j] =jtrans[j]
    endif
    if wave[i] eq minhwave then begin
        for j=0L,sizehwave-1 do longhtrans[i+j] =htrans[j]
    endif
    if wave[i] eq minkswave then begin
        for j=0L,sizekswave-1 do longkstrans[i+j] =kstrans[j]
    endif
    if wave[i] eq minw1wave then begin
        for j=0L,sizew1wave-1 do longw1trans[i+j] =w1trans[j]
    endif
    if wave[i] eq minw2wave then begin
        for j=0L,sizew2wave-1 do longw2trans[i+j] =w2trans[j]
    endif
    if wave[i] eq minw3wave then begin
        for j=0L,sizew3wave-1 do longw3trans[i+j] =w3trans[j]
    endif
    if wave[i] eq minw4wave then begin
        for j=0L,sizew4wave-1 do longw4trans[i+j] =w4trans[j]
    endif
endfor


openw,unit,"colors.jao.out.2",/get_lun, width=500

for a=0, howmanyfiles-1 do begin
    c = double(2.998e10)        ; speed of light in cm/s
    h = double(6.626e-27)       ; planck's constant in erg*sec
```

```
  ;; The photometric zero points for VRI are calculated
  ;; based on Bessel and Murphy 2012 (PASP 124,140)
  ;; starting from equations A2 and A4, plug in zero points
  ;; and effective wavelengths from Table 3 to calculate
  ;; zero points in units of photons/s/cm2.

  zpv  = double(1.01464e11) ;photons/s/cm2
  zpr  = double(7.15579e10) ;photons/s/cm2
  zpi  = double(4.71718e10) ;photons/s/cm2

  ;; While Bessel reports zero points in terms of offsets,
  ;; 2MASS (Cohen et al 2003, AJ 126,1096, table 2) and
  ;; WISE (Jarrett et al 2011, ApJ 735,112, table 4)
  ;; report them in terms of an isophot flux in energy units
  ;; which must then be convolved with the RSRs to get the total
  ;; zero point flux. This only needs to be done once, and was done
  ;; by the lines that are commented out below.
  ;; The tabulated isophotal fluxes in W/cm2/micron are:
  ;;     J         H          Ks         W1        W2          W3
  ;; 3.129e-13  1.133e-13  4.283e-14  8.179e-15  2.415e-15  6.515e-17
  ;; to go from  W/cm2/micron to erg/s/cm2/Ang multiply by 10^(7-4)=10^3

  zpjiso  =  3.129e-13 *10.^3.
  zphiso  =  1.133e-13 *10.^3.
  zpksiso =  4.283e-14 *10.^3.
  zpw1iso =  8.179e-15 *10.^3.
  zpw2iso =  2.415e-15 *10.^3.
  zpw3iso =  6.515e-17 *10.^3.
  zpw4iso =  5.090e-18 *10.^3.

  zpj =  total((zpjiso/(h*c))*(longjtrans   *wave)) / (total(longjtrans))
  zph =  total((zphiso/(h*c))*(longhtrans   *wave)) / (total(longhtrans))
  zpks = total((zpksiso/(h*c))*(longkstrans *wave)) / (total(longkstrans))
  zpw1 = total((zpw1iso/(h*c))*(longw1trans *wave)) / (total(longw1trans))
  zpw2 = total((zpw2iso/(h*c))*(longw2trans *wave)) / (total(longw2trans))
  zpw3 = total((zpw3iso/(h*c))*(longw3trans *wave)) / (total(longw3trans))

;   openr,specfile,filenames[a],/get_lun
;   flux =0d
;   while not eof(specfile) do begin
```

```
 ;       readf,specfile, x,y
 ;       flux=[flux,y]
 ;   endwhile

 readcol,filenames[a],flux,format="x,d"

;      help,flux
;; Step 5 - Change spectrum to units of photon/s/cm2/A.
;; This minimizes the color terms when comparing it to
;; the zero point (vega).


      fluxinphotons = double(flux *(wave/(h*c)))
      help,fluxinphotons
      print, total(fluxinphotons)
;      plot,wave,flux,xrange=[6000,50000]
       newvflux = (total((longvtrans*fluxinphotons)) / (total(longvtrans)))
       print, total(longvtrans*fluxinphotons)
       help,newvflux
       newrflux = total((longrtrans*fluxinphotons)) / (total(longrtrans))
       help,newrflux
       newiflux = total((longitrans*fluxinphotons)) / (total(longitrans))
       help,newiflux

       newjflux = total((longjtrans*fluxinphotons)) / (total(longjtrans))
       newhflux = total((longhtrans*fluxinphotons)) / (total(longhtrans))
       newksflux = total((longkstrans*fluxinphotons)) / (total(longkstrans))

       neww1flux = total((longw1trans*fluxinphotons)) / (total(longw1trans))
       neww2flux = total((longw2trans*fluxinphotons)) / (total(longw2trans))
       neww3flux = total((longw3trans*fluxinphotons)) / (total(longw3trans))



        v =  ((-2.5)*(alog10(newvflux/zpv)  ))
        r =  ((-2.5)*(alog10(newrflux/zpr)  ))
        i =  ((-2.5)*(alog10(newiflux/zpi)  ))

        j =  ((-2.5)*(alog10(newjflux/zpj)  ))
        h =  ((-2.5)*(alog10(newhflux/zph)  ))
        k = ((-2.5)*(alog10(newksflux/zpks)))
```

```
        w1 = ((-2.5)*(alog10(neww1flux/zpw1)))
        w2 = ((-2.5)*(alog10(neww2flux/zpw2)))
        w3 = ((-2.5)*(alog10(neww3flux/zpw3)))

        print,''
        print,filenames[a],v,r,i,j,h,k,w1,w2,w3
        print,''
        print,filenames[a],v-r,v-i,v-j,v-h,v-k,v-w1,v-w2,v-w3,$
                                   r-i,r-j,r-h,r-k,r-w1,r-w2,r-w3,$
                                       i-j,i-h,i-k,i-w1,i-w2,i-w3,$
                                           j-h,j-k,j-w1,j-w2,j-w3,$
                                               h-k,h-w1,h-w2,h-w3,$
                                                   k-w1,k-w2,k-w3,$
                                                        w1-w2,w1-w3,$
                                                              w2-w3

        printf,unit,filenames[a],    v-r,v-i,v-j,v-h,v-k,v-w1,v-w2,v-w3,$
                                   r-i,r-j,r-h,r-k,r-w1,r-w2,r-w3,$
                                       i-j,i-h,i-k,i-w1,i-w2,i-w3,$
                                           j-h,j-k,j-w1,j-w2,j-w3,$
                                               h-k,h-w1,h-w2,h-w3,$
                                                   k-w1,k-w2,k-w3,$
                                                        w1-w2,w1-w3,$
                                       w2-w3, format='(a,36(f11.5))'


endfor

free_lun, unit

end
```

C Calculating the Effective Temperature of Science Objects

Now that we know the colors for all synthetic spectra, we can match these colors to the colors of a given science object to obtain the science object's effective temperature. This is done by comparing the colors of the science objects against the colors of *all* synthetic spectra, one at a time, and then interpolating the comparison to the point of zero residual. Each color is compared independently, so this code effectively provides multiple independent determinations of the effective temperature. The mean of these values is adopted as the effective temperature and the 1σ dispersion as the uncertainty. The code automatically excludes colors that did not interpolate well and gives the user the option to further discard colors that are deemed to be outliers. See §5.5 for a discussion of the methodology.

The input is the name of the object followed by its photometric magnitudes and their uncertainties. The output is the the graphical representation seen in Figure 5.2 as well as written output of the object's effective temperature and error. The output file also contains the name of the best matching spectral template, which will be used later as a starting point to calculate the SED, and the same photometry that was used as input.

```
pro automatch3,outfile1,outfile2,id,spt,objname,v,verr,r,rerr,i,ierr, $
j,jerr,h,herr,k,kerr,w1,w1err,w2,w2err,w3,w3err

set_plot, 'x'

vmag = v
rmag = r
imag = i
jmag = j
hmag = h
```

```
kmag = k
w1mag = w1
w2mag = w2
w3mag = w3

readcol,"colors.2011.out", lineid,filename,temp,$


                                    neglogg,logm,vmr,vmi,vmj,vmh,vmk,vmw1,$
                                    vmw2,vmw3,$
                                    rmi,rmj,rmh,rmk,rmw1,rmw2,rmw3,$
                                    imj,imh,imk,imw1,imw2,$
                        format="i,a", /silent




readcol,"colors.2011.out",imw3,jmh,jmk,jmw1,jmw2,jmw3,hmk,hmw1,hmw2,hmw3,$
                      kmw1,kmw2,kmw3,w1mw2,w1mw3,w2mw3,$
          format="x,x,x,x,x,x,x,x,x,x,x,x,x,x,x,x,x,x,x,x,x,x,x,x,x", /silent



repeatstar = 0
while repeatstar eq 0 do begin
                                  ;The following variables are augmented
                                  ;throughout the program, and need to
                                  ;be undefined for every do-over.
   if n_elements(foundbadindex)    ne -1 then undefine,foundbadindex
   if n_elements(whereselect)      ne -1 then undefine,whereselect
   if n_elements(goodindices)      ne -1 then undefine,goodindices
   if n_elements(badindices)       ne -1 then undefine,badindices
   if n_elements(goodintindices)   ne -1 then undefine,goodintindices
   if n_elements(badintindices)    ne -1 then undefine,goodintindices
   if n_elements(whichindex)       ne -1 then undefine,whichindex
   if n_elements(goodtemps)        ne -1 then undefine,goodtemps
   if n_elements(goodresiduals)    ne -1 then undefine,goodresiduals
   if n_elements(badtemps)         ne -1 then undefine,badtemps
   if n_elements(badresiduals)     ne -1 then undefine,badresiduals


   photcolors = [vmag-jmag,vmag-hmag,vmag-kmag,vmag-w1mag,vmag-w2mag, $
```

```
                vmag-w3mag, $
                rmag-jmag,rmag-hmag,rmag-kmag,rmag-w1mag,rmag-w2mag,$
                imag-jmag,imag-hmag,imag-kmag,imag-w1mag,imag-w2mag];, $
;                                             jmag-hmag,jmag-kmag]

   colornames = ['v-j','v-h','v-k','v-w1','v-w2','v-w3', $
                 'r-j','r-h','r-k','r-w1','r-w2',        $
                 'i-j','i-h','i-k','i-w1','i-w2'        ];, $
;                'j-h','j-k']

   howmanyspec = n_elements(lineid)
   residuals = fltarr(16,howmanyspec)

   speccolor = fltarr(16,howmanyspec)

   for z=0,howmanyspec-1 do begin ; this populates the model colors array
 ;      speccolor[0,z]=vmr[z]
 ;      speccolor[1,z]=vmi[z]
       speccolor[0,z]=vmj[z]
       speccolor[1,z]=vmh[z]
       speccolor[2,z]=vmk[z]
       speccolor[3,z]=vmw1[z]
       speccolor[4,z]=vmw2[z]
       speccolor[5,z]=vmw3[z]
;       speccolor[8,z]=rmi[z]
       speccolor[6,z]=rmj[z]
       speccolor[7,z]=rmh[z]
       speccolor[8,z]=rmk[z]
       speccolor[9,z]=rmw1[z]
       speccolor[10,z]=rmw2[z]
 ;      speccolor[13,z]=rmw3[z]
       speccolor[11,z]=imj[z]
       speccolor[12,z]=imh[z]
       speccolor[13,z]=imk[z]
       speccolor[14,z]=imw1[z]
       speccolor[15,z]=imw2[z]
 ;      speccolor[19,z]=imw3[z]
;;       speccolor[20,z]=jmh[z]
;;       speccolor[21,z]=jmk[z]
;;       speccolor[23,z]=jmw1[z]
;;       speccolor[24,z]=jmw2[z]
;;       speccolor[25,z]=jmw3[z]
```

```
;;       speccolor[26,z]=hmk[z]
;;       speccolor[27,z]=hmw1[z]
;;       speccolor[28,z]=hmw2[z]
;;       speccolor[29,z]=hmw3[z]
;;       speccolor[30,z]=kmw1[z]
;;       speccolor[31,z]=kmw2[z]
;;       speccolor[32,z]=kmw3[z]
;;       speccolor[33,z]=w1mw2[z]
;;       speccolor[34,z]=w1mw3[z]
;;       speccolor[35,z]=w2mw3[z]
   endfor


   for i=0, 15 do begin ;loop over all colors for calculating residuals
       for j=0, howmanyspec-1 do residuals[i,j] = photcolors[i] - $
       speccolor[i,j]
   endfor

   absresiduals = abs(residuals)
   meanresallcolors = fltarr(howmanyspec)
   for j = 0, howmanyspec-1  do meanresallcolors[j] = mean(absresiduals[*,j])

   sortbyresidual = sort(meanresallcolors)
   help,sortbyresidual
   ;;now print the best 15 lines
   print,''
   print,"The following 15 spectra have the lowest residuals."
   print,"    LINE      TEMP         LOG(G)      METALLICITY  RESIDUAL"
   for j=0,15 do print,lineid[sortbyresidual[j]],temp[sortbyresidual[j]], $
                   -neglogg[sortbyresidual[j]],logm[sortbyresidual[j]], $
                     meanresallcolors[sortbyresidual[j]]


   ;Now calculate residuals for each magnitude
   meanvres  = fltarr(howmanyspec)
   meanrres  = fltarr(howmanyspec)
   meanires  = fltarr(howmanyspec)
   meanjres  = fltarr(howmanyspec)
   meanhres  = fltarr(howmanyspec)
   meankres  = fltarr(howmanyspec)
   meanw1res = fltarr(howmanyspec)
   meanw2res = fltarr(howmanyspec)
```

```
  meanw3res = fltarr(howmanyspec)
;                              0    1      2     3      4      5
;  colornames = [            'v-j','v-h','v-k','v-w1','v-w2','v-w3', $
;                              6     7     8      9     10
;                            'r-j','r-h','r-k','r-w1','r-w2',      , $
;                             11     12    13    14     15
;                            'i-j','i-h','i-k','i-w1','i-w2'         $
;;;


  for j=0, howmanyspec-1 do begin
      meanvres[j] = mean([absresiduals[0,j],absresiduals[1,j],$
      absresiduals[2,j],$
      absresiduals[3,j],absresiduals[4,j],absresiduals[5,j]])
      meanrres[j] = mean([absresiduals[6,j],absresiduals[7,j], $
      absresiduals[8,j],$
      absresiduals[9,j],absresiduals[10,j]])
      meanires[j] = mean([absresiduals[11,j],absresiduals[12,j], $
      absresiduals[13,j],$
      absresiduals[14,j],absresiduals[15,j]])
      meanjres[j] = mean([absresiduals[0,j],absresiduals[6,j], $
      absresiduals[11,j]])
      meanhres[j] = mean([absresiduals[1,j],absresiduals[7,j], $
      absresiduals[12,j]])
      meankres[j] = mean([absresiduals[2,j],absresiduals[8,j],$
      absresiduals[13,j]])
     meanw1res[j] = mean([absresiduals[3,j],absresiduals[9,j], $
     absresiduals[14,j]])
     meanw2res[j] = mean([absresiduals[4,j],absresiduals[10,j], $
     absresiduals[15,j]])
     meanw3res[j] = absresiduals[5,j]

  endfor

  print, "Mean residuals for each band"
  for j=0,14 do print,lineid[sortbyresidual[j]], $
  meanvres[sortbyresidual[j]],$
    meanrres[sortbyresidual[j]],meanires[sortbyresidual[j]],$
    meanjres[sortbyresidual[j]], $
    meanhres[sortbyresidual[j]],meankres[sortbyresidual[j]], $
    meanw1res[sortbyresidual[j]],meanw2res[sortbyresidual[j]], $
     meanw3res[sortbyresidual[j]]
```

```
read,"Use the residuals above to pick the best log g: ",bestlogg
read,"Use the residuals above to pick the best [M/H]: ",bestmet
read,"Enter the number for the line with overall best match: ",bestline

bestfile = ''
bestfile = filename[where(lineid eq bestline)]

;Now let's make another master array for the synthetic photometry, but
;only with the chosen log g and metallicity. Also make an array
;for the residuals.


selectspeccolor = fltarr(20,howmanyspec) ; all elements not matching
                                         ; log g and
                                         ; metallicity will be left
                                         ; as zero
selectresiduals = fltarr(20,howmanyspec)
selectlines     = fltarr(howmanyspec)
;selectmeanres   = fltarr(howmanyspec)
for j=0, howmanyspec-1 do begin
    if neglogg[j] eq -bestlogg and logm[j] eq bestmet then begin
        selectlines[j] = lineid[j]
        for i=0, 15 do begin
            selectspeccolor[i,j] =speccolor[i,j]
            selectresiduals[i,j] =residuals[i,j]
        endfor
;        selectmeanres[j] = mean(abs(selectresiduals[*,j]))
    endif
endfor

whereselect = where(selectlines ne 0.)
howmanyselect = n_elements(whereselect)

print,"Number of spectra matching criteria: ", howmanyselect
;sortedselecindices = sort(selectlines)

shortselectspeccolor = fltarr(20,howmanyselect)
shortselectresiduals = fltarr(20,howmanyselect)
shortselectlines = fltarr(howmanyselect)
shortselecttemp  = fltarr(howmanyselect)
```

```
shortselectfiles = strarr(howmanyselect)

for j=0, howmanyselect-1 do begin
    shortselectlines[j]     = selectlines[whereselect[j]]
    shortselecttemp[j]      = temp[whereselect[j]]
    shortselectfiles[j]      = filename[whereselect[j]]
    for i=0, 19 do begin
    shortselectresiduals[i,j] = selectresiduals[i,whereselect[j]]
    shortselectspeccolor[i,j] = selectspeccolor[i,whereselect[j]]
    endfor
endfor


plot, shortselecttemp,shortselectresiduals[0,*], psym=3,yrange=[-3,3], $
xrange=[1400,4000],xtitle="Temperature", $
ytitle="Residuals", $
title="Effective Temperature Matches for 22 Good Colors", $
subtitle="Dots indicate model values. Diamonds indicate interpolation.",$
 xstyle=1,ystyle=1

oplot,[0,4000],[0,0],linestyle=2
for i=1,15 do oplot,shortselecttemp,shortselectresiduals[i,*],$
psym=3,symsize=1.5

;Now interpolate the temp and the residuals 36 times, one for each
;color
inttemp = fltarr(16)
intresidual = fltarr(16)

for i =0, 15 do begin
    inttemp[i]     = interpol(shortselecttemp,shortselectspeccolor[i,*],$
     photcolors[i])
    intresidual[i] = interpol(shortselectresiduals[i,*], $
    shortselecttemp, $
    inttemp[i])

endfor

goodintindices = where(inttemp ge 1500 and inttemp le 4000 and $
   abs(intresidual) $
 lt .2) ;sometimes interpol produces crazy numbers if
                          ; the colors are not monotoninc.
```

```
badintindices  = where(inttemp lt 1500 or inttemp gt 4000 or $
 abs(intresidual) ge .2)
goodinttemp     = fltarr(n_elements(goodintindices))
goodintresidual = fltarr(n_elements(goodintindices))
goodintcolornames  = strarr(n_elements(goodintindices))

badinttemp = fltarr(n_elements(badintindices))
badintresidual = fltarr(n_elements(badintindices))
badintcolornames = strarr(n_elements(badintindices))


for i =0,n_elements(goodintindices)-1 do begin
    goodinttemp[i]     = inttemp[goodintindices[i]]
    goodintresidual[i] = intresidual[goodintindices[i]]
    goodintcolornames[i] = colornames[goodintindices[i]]
endfor

if badintindices[0] ne -1 then begin
    for i=0, n_elements(badintindices)-1 do begin
        badinttemp[i] = inttemp[badintindices[i]]
        badintresidual[i] = intresidual[badintindices[i]]
        badintcolornames[i] = colornames[badintindices[i]]
    endfor
endif


if badintindices[0] ne -1 then begin
    print,"The following colors had bad interpolations: ", $
   colornames[badintindices]
    originalcolornames = colornames
endif else print,"All 19 colors interpolated okay."


inttemp     = goodinttemp        ;reassigning names here makes it easier
intresidual = goodintresidual    ;because the above for loop was
                                 ;written after
colornames  = goodintcolornames  ;the rest of the program below.

oplot,inttemp,intresidual,psym=4,symsize=1.5
if badintindices[0] ne -1 then begin
    oplot,badinttemp,badintresidual,psym=4,symsize=1.5
    oplot,badinttemp,badintresidual,psym=7,symsize=1.5
```

```
endif

meantemp=mean(inttemp)
sigmatemp = stddev(inttemp)

oplot,[meantemp-sigmatemp,meantemp-sigmatemp],[-2,2],linestyle=2
oplot,[meantemp+sigmatemp,meantemp+sigmatemp],[-2,2],linestyle=2
oplot,[meantemp,meantemp],[-1.5,1.5],linestyle=2

;;print,"Color    int. temp     frac sigma"; uncoment this line is
;;using line 224.
fracsigma = fltarr(n_elements(colornames))

for i=0,n_elements(colornames)-1 do  begin
    fracsigma[i] = (inttemp[i]-meantemp)/sigmatemp
;;    print,colornames[i],inttemp[i],fracsigma[i]
endfor
;;;;;;;;;;;;;;;;;;;;;;;;;;;;;;;;;;;;;;;;;;;;;;;;;;;;;;;;;;;;;;;;;;;;;;;;;;;;;;;
;; Now use mouse to toss bad ones and re-compute
print,''
print, "Preliminary Results"
print, "Effective temperature: ",meantemp
print, '1 sigma uncertainty:   ',sigmatemp
print,''
doagain = 1
colorselect = 0
print,"Click on any point to see color name."
print,"Click again to exclude color."
print,"Click away from any point to exit."
firstlap = 1
;badindices = 0
while doagain eq 1 do begin
    closetoapoint = 0
    cursor, x, y, /down
    for i=0,n_elements(colornames)-1 do begin
        if abs(x-inttemp[i]) lt 10. and abs(y-intresidual[i])lt 0.1 $
         then closetoapoint = 1
    endfor
    if closetoapoint eq 0 then doagain = 0 else begin
        whichtemp = abs(x - inttemp)
        whichindex = where(whichtemp eq min(whichtemp))
        if colorselect eq 0 then begin        ;This block selects $
```

```
          a color and prints it.
              print,"Selected color: ",colornames[whichindex]
              print,"Selected temp.: ",inttemp[whichindex]
           ;   print, "index: ",whichindex
             colorselect = 1
              selectedindex = whichindex
          endif else begin  ; this block deletes a selected color.
              if whichindex eq selectedindex then begin
                  oplot, inttemp[whichindex],intresidual[whichindex], $
                  psym= 7,symsize=2
                  if (n_elements(badindices) eq 0) then badindices = $
                 whichindex else badindices = [badindices, whichindex]
              endif; else colorselect = 0
              colorselect =0
          endelse
       endelse
  endwhile

  ;;badindices are bad indices of the inttemp array.
  ;;must now create the arrays
  ;;goodtemps,goodresiduals,badtemps,badresiduals
;  if n_elements(badindices) eq -1 then badindices = -9
  for i=0, n_elements(inttemp)-1 do begin
      foundbadindex = where(i eq badindices) ;is this particular index of $
       inttemp bad?
      if foundbadindex[0] eq -1 then begin
          if n_elements(goodtemps) eq 0 then goodtemps = inttemp[i] $
          else goodtemps = [goodtemps,inttemp[i]]
          if n_elements(goodresiduals) eq 0 then goodresiduals = $
          intresidual[i] else goodresiduals = [goodresiduals,intresidual[i]]
      endif else begin
          if n_elements(badtemps) eq 0 then badtemps = inttemp[i] else $
          badtemps = [badtemps,inttemp[i]]
          if n_elements(badresiduals) eq 0 then badresiduals = $
          intresidual[i] $
          else badresiduals = [badresiduals,intresidual[i]]
      endelse
  endfor

  ;;;;;;;;;;;;;;;;;;;;;;;;;;;;;;;;;;;;;;;;;;;;;;;;;;;;;;;;;;;;;;;;;;;;;;;;;;
  ;oplot, badtemps,badresiduals,psym=7
```

```
   goodmeantemp  = mean(goodtemps)
   goodsigmatemp = stddev(goodtemps)

   oplot,[goodmeantemp-goodsigmatemp,goodmeantemp-goodsigmatemp],[-2,2],$
   linestyle=3
   oplot,[goodmeantemp+goodsigmatemp,goodmeantemp+goodsigmatemp],[-2,2],$
   linestyle=3
   oplot,[goodmeantemp,goodmeantemp],[-1.5,1.5],linestyle=3

   print,"Colors excluded: ",colornames[badindices]
   print,''
   print,"FINAL RESULTS FOR ",objname
   print, "Effective Temperature: ",goodmeantemp
   print, '1 sigma uncertainty:   ',goodsigmatemp
   read,"Enter (0) to try again, (1) to save and move on, (2) to save but  $
      comment out the line, (3) to move on without saving: ",repeatstar
endwhile

if repeatstar eq 1 or repeatstar eq 2 then begin
    openu,unit1,outfile1,/append,/get_lun,width=500
    spc = '   ' ;space string variable, because idl output is stupid.
    if repeatstar eq 1 then  printf,unit1,id,spc,objname,spc,spt,spc, $
    bestfile,spc, $
    goodmeantemp,goodsigmatemp,vmag,verr,rmag,rerr,imag,ierr,jmag,jerr, $
    hmag,herr, $
                            kmag,kerr,w1mag,w1err,w2mag,w2err,w3mag,w3err,$
    format ='(a,a,a,a,a,a,a,a,20(f9.2))'
    if repeatstar eq 2 then begin
        comout = '##'
        comstring = ' '
        read,"Enter a SHORT comment: ",comstring
        printf,unit1,comout,spc,id,spc,objname,spc,spt,spc,bestfile,spc, $
        goodmeantemp,goodsigmatemp,vmag,verr,rmag,rerr,imag,ierr,jmag,jerr, $
        hmag,herr, $
                            kmag,kerr,w1mag,w1err,w2mag,w2err,w3mag,w3err, $
              spc,comstring, format ='(a,a,a,a,a,a,a,a,a,a,20(f9.2),a,a)'
    endif

    ;Now compute/collect the sigmas for
    ;all 36 colors and print them to a
    ;separate file.
```

```
; help,inttemp
  intindex = 0
; help,goodintindices
; print, goodintindices

 tempsigmas = fltarr(16)
 for i =0, 15 do begin
     interpolgood = where(i eq goodintindices)
     if interpolgood ne -1 then begin
         tempsigmas[i] = (inttemp[intindex] - goodmeantemp) /goodsigmatemp
         intindex ++
     endif else tempsigmas[i] = -99
;     print, tempsigmas[i]
 endfor

 openu,unit2,outfile2,/append,/get_lun,width=1000
 if repeatstar eq 1 then  printf,unit2,id,spc,objname,spc,spt, $
 goodmeantemp,$
 goodsigmatemp,tempsigmas
 if repeatstar eq 2 then  printf,unit2,comout,spc,id,spc,objname,spc, $
 spt, $
 goodmeantemp,goodsigmatemp,tempsigmas

 free_lun,unit1
 free_lun,unit2

 ;; Now re-construct and save the final plot
 set_plot,'ps'
 device, filename=objname+".plot2.ps", /landscape
 plot, shortselecttemp,shortselectresiduals[0,*], psym=3,yrange=[-3,3], $
 xrange=[1400,4000],xtitle="Temperature", $
ytitle="Residuals",title=objname+" -- Effective Temperature Matches for $
  20 Good Colors", $
subtitle="Dots indicate model values. Diamonds indicate interpolation.",$
  xstyle=1,ystyle=1, $
 charthick=2, thick=2, xthick=2, ythick=2

 oplot,[0,4000],[0,0],linestyle=2,thick=2
 for i=1,15 do oplot,shortselecttemp,shortselectresiduals[i,*],psym=3, $
     symsize=1.2,thick=2

 oplot,inttemp,intresidual,psym=4,symsize=1.2,thick=2
```

```
    if badintindices[0] ne -1 then begin
       oplot,badinttemp,badintresidual,psym=4,symsize=1.2,thick=2
       oplot,badinttemp,badintresidual,psym=7,symsize=1.2,thick=2
    endif

    oplot,[meantemp-sigmatemp,meantemp-sigmatemp],[-2,2],linestyle=2,thick=2
    oplot,[meantemp+sigmatemp,meantemp+sigmatemp],[-2,2],linestyle=2,thick=2
    oplot,[meantemp,meantemp],[-1.5,1.5],linestyle=2,thick=2
    if badindices[0] ne -1 then oplot, inttemp[badindices], $
    intresidual[badindices],psym= 7,symsize=1.2,thick=2

    oplot,[goodmeantemp-goodsigmatemp,goodmeantemp-goodsigmatemp],[-2,2],$
       linestyle=3,thick=2
    oplot,[goodmeantemp+goodsigmatemp,goodmeantemp+goodsigmatemp],[-2,2],$
     linestyle=3,thick=2
    oplot,[goodmeantemp,goodmeantemp],[-1.5,1.5],linestyle=3,thick=2

    xyouts, 1500,2.6, 'Best Temperature (K): '
    xyouts, 1500,2.4, '1 Sigma Error (K):    '
   if badintindices[0] ne -1 then xyouts, 1500,-2.3,'Bad Interpolations: ' $
       else xyouts, 1500,-2.3, 'All colors interpolated okay.'
    if badindices[0] ne -1 then    xyouts, 1500,-2.5,'Bad Fits: ' $
       else xyouts, 1500,-2.5, 'All colors had good fits.'
    xyouts, 2000,2.6, goodmeantemp
    xyouts, 2000,2.4, goodsigmatemp
    if badintindices[0] ne -1 then begin
       for i=0, n_elements(badintindices)-1 do xyouts, (2000 + (i*150)), $
              -2.3, originalcolornames[badintindices[i]]
   endif
    if badindices[0] ne -1 then begin
        for i=0, n_elements(badindices)-1 do xyouts, (1750 + (i*150)),  $
         -2.5, colornames[badindices[i]]
    endif
    if repeatstar eq 2 then xyouts, 2500, 2.5, "WARNING: This result was $
       commented out."

    device, /close

endif

end
```

The previous code required the parameters for each objects to be entered in the code call line, which is burdensome given the fact that each object has nine magnitudes and nine errors to be entered. The next code executes the previous code for each line in a file so that the input can be tabulated. After each object is calculated, the code gives the user the option of stopping or moving on to the next object.

```
pro automatch,infile,outfile1,outfile2

readcol,infile,id,spt,name,vmag,verr,rmag,rerr,imag,ierr,jmag,jerr,$
   hmag,herr,kmag,kerr,w1mag,w1err,w2mag,w2err,w3mag,w3err, $
       format="i,a,a,f,f,f,f,f,f,f,f,f,f,f,f,f,f,f,f,f,f"

howmanystars = n_elements(name)
colorset
plot,[100,200],[100,200],xrange=[0,10],yrange=[0,10]
anykey = ''
read,'Use the mouse to re-size the graph window to facilitate viewing. $
 Press ENTER when done.',anykey
print,''
Read,"Start on line: ",startline

startindex = where(id eq startline)

for i = startindex[0], howmanystars-1 do begin
    print,''
    print, 'Now working on star ',id[i],', ',name[i]
    if vmag[i] eq 0 then begin
        Read,'Enter an estimate for V: ',vmag[i]
        verr[i] = 0.2
    endif
automatch3,outfile1,outfile2,id[i],spt[i],name[i],vmag[i],verr[i],rmag[i] $
,rerr[i],imag[i],ierr[i],jmag[i],jerr[i],hmag[i],herr[i], $
          kmag[i],kerr[i],w1mag[i],w1err[i],w2mag[i],w2err[i],w3mag[i],$
         w3err[i]
endfor
print,''
print, 'END'
end
```

D Calculating Luminosity and Radius

In the previous section, code "automatch3.pro" selected which of the *BT-Settl* synthetic spectra was an overall best match to the colors of each science target. We will now tweak that template based on the differences between the observed photometry and photometry from the synthetic template so as to produce a template that more closely matches the true SED of the science object. The reasoning behind the procedure is described in §5.6. The input for this procedure is the output from the previous procedure, with added columns for trigonometric parallax and its error. The output is a text line containing the luminosity and radius in several units, and the associated errors. This procedure produces Figure 5.3.

```
pro calsed8,objid,objname,spt,template,prlx,perr,pcode,teff,tefferr,$
            vmag,vmagerr,rmag,rmagerr,imag,imagerr,$
            jmag,jmagerr,hmag,hmagerr,ksmag,ksmagerr,w1mag,w1magerr,$
            w2mag,w2magerr,w3mag,w3magerr,outfile,$
            vwave,vtrans,rwave,rtrans,iwave,itrans,jwave,jtrans,hwave, $
            htrans,kswave,kstrans,w1wave,w1trans,$
            w2wave,w2trans,w3wave,w3trans

set_plot,'ps'
device,filename=objname+'.calsed.pub.8order.ps'

;openu,outunit,outfile,/get_lun,/append
print,"Now working on ",objname,", spectral type ",spt
print, "Now reading SED template."
readcol,template,wave,flux,format="L,d",/silent

;;The Allard model spectra are calculated as flux at the stellar
;;surface, which is a very high number. This code was originally
;; designed to work with observed templates, i.e., units of
;; flux at the telescope. This gives the calibration routine a hard
;; time. To correct for this, lets convert the total
;; flux to a typical observed bolometric flux of
```

```
;; ~ 10^-10 erg/s/cm^2

modeltotal = double(total(flux))
flux = flux * (double(1e-10)/modeltotal)
;;;;; change the factor in the next line if the coeficients for the
;;;;; first polynomial fit are too big.
flux = flux * 30d

;; Step 3 - modify RSRs array to match dimensions of flux template.
;; This makes all arrays run out to 30 microns (300,000 A)

;; The effective wavelengths for the bands are:
veffwave = 5455. ;Angstroms, Bessel and Murphy 2012 PASP 124,140, table 3
reffwave = 6426.
ieffwave = 7939.
jeffwave = 1.235e4  ;Angstroms, Cohen et al. 2003 AJ 126,1096, table 2
heffwave = 1.662e4
kseffwave = 2.159e4
w1effwave = 3.353e4 ;Angstroms, Jarrett et al 2011, ApJ 735,112, table 4
w2effwave = 4.603e4
w25effwave = 8.05e4   ; mean of w2 and w3. covers gap for polynomial
w3effwave = 1.156e5

longwave = wave
longflux = flux

minwave = min(wave)
;;; longwave =   findgen(300000 - minwave+1)+minwave

sizelongwave=n_elements(longwave)
;;; longflux =    fltarr(sizelongwave)
longvtrans =  fltarr(sizelongwave)
longrtrans =  fltarr(sizelongwave)
longitrans =  fltarr(sizelongwave)
longjtrans =  fltarr(sizelongwave)
longhtrans =  fltarr(sizelongwave)
longkstrans = fltarr(sizelongwave)
longw1trans = fltarr(sizelongwave)
longw2trans = fltarr(sizelongwave)
longw3trans = fltarr(sizelongwave)
```

```
minvwave=min(vwave)
minrwave=min(rwave)
miniwave=min(iwave)
minjwave=min(jwave)
minhwave=min(hwave)
minkswave=min(kswave)
minw1wave=min(w1wave)
minw2wave=min(w2wave)
minw3wave=min(w3wave)


sizevwave=n_elements(vwave)
sizerwave=n_elements(rwave)
sizeiwave=n_elements(iwave)
sizejwave=n_elements(jwave)
sizehwave=n_elements(hwave)
sizekswave=n_elements(kswave)
sizew1wave=n_elements(w1wave)
sizew2wave=n_elements(w2wave)
sizew3wave=n_elements(w3wave)


sizeflux = n_elements(flux)
;;; for i=0L, sizeflux-1 do longflux[i] = flux[i] ; creates long
                                                  ; template array
for i=0L, sizelongwave-1 do begin ; this loop will create the
                                  ; long band arrays
    if longwave[i] eq minvwave then begin
        for j=0L,sizevwave-1 do longvtrans[i+j] =vtrans[j]
    endif
    if longwave[i] eq minrwave then begin
        for j=0L,sizerwave-1 do longrtrans[i+j] =rtrans[j]
    endif
    if longwave[i] eq miniwave then begin
        for j=0L,sizeiwave-1 do longitrans[i+j] =itrans[j]
    endif
    if longwave[i] eq minjwave then begin
        for j=0L,sizejwave-1 do longjtrans[i+j] =jtrans[j]
    endif
    if longwave[i] eq minhwave then begin
        for j=0L,sizehwave-1 do longhtrans[i+j] =htrans[j]
```

```
    endif
    if longwave[i] eq minkswave then begin
        for j=0L,sizekswave-1 do longkstrans[i+j] =kstrans[j]
    endif
    if longwave[i] eq minw1wave then begin
        for j=0L,sizew1wave-1 do longw1trans[i+j] =w1trans[j]
    endif
    if longwave[i] eq minw2wave then begin
        for j=0L,sizew2wave-1 do longw2trans[i+j] =w2trans[j]
    endif
    if longwave[i] eq minw3wave then begin
        for j=0L,sizew3wave-1 do longw3trans[i+j] =w3trans[j]
    endif
endfor


;; Step 5 - Change spectrum to units of photon/s/cm2/A.
;; This minimizes the color terms when comparing it to
;; the zero point (vega).

c = double(2.998e10)  ; speed of light in cm/s
h = double(6.626e-27) ; planck's constant in erg*sec

fluxinphotons = longflux *(longwave/(h*c))
;plot, longwave,fluxinphotons, /xlog
;; The photometric zero points for VRI are calculated
;; based on Bessel and Murphy 2012 (PASP 124,140)
;; starting from equations A2 and A4, plug in zero points
;; and effective wavelengths from Table 3 to calculate
;; zero points in units of photons/s/cm2.

zpv  = double(1.01464e11) ;photons/s/cm2
zpr  = double(7.15579e10) ;photons/s/cm2
zpi  = double(4.71718e10) ;photons/s/cm2

;; While Bessel reports zero points in terms of offsets,
;; 2MASS (Cohen et al 2003, AJ 126,1096, table 2) and
;; WISE (Jarrett et al 2011, ApJ 735,112, table 4)
;; report them in terms of an isophot flux in energy units
;; which must then be convolved with the RSRs to get the total
;; zero point flux. This only needs to be done once, and was done
;; by the lines that are commented out below.
```

```
;; The tabulated isophotal fluxes in W/cm2/micron are:
;;     J         H          Ks         W1        W2          W3
;; 3.129e-13  1.133e-13  4.283e-14  8.179e-15  2.415e-15  6.515e-17
;; to go from  W/cm2/micron to erg/s/cm2/Ang multiply by 10^(7-4)=10^3

zpjiso  =  3.129e-13 *10.^3.
zphiso  =  1.133e-13 *10.^3.
zpksiso =  4.283e-14 *10.^3.
zpw1iso =  8.179e-15 *10.^3.
zpw2iso =  2.415e-15 *10.^3.
zpw3iso =  6.515e-17 *10.^3.


zpj =  total((zpjiso/(h*c))*(longjtrans   *longwave)) / (total(longjtrans))
zph =  total((zphiso/(h*c))*(longhtrans   *longwave)) / (total(longhtrans))
zpks = total((zpksiso/(h*c))*(longkstrans *longwave)) / (total(longkstrans))
zpw1 = total((zpw1iso/(h*c))*(longw1trans *longwave)) / (total(longw1trans))
zpw2 = total((zpw2iso/(h*c))*(longw2trans *longwave)) / (total(longw2trans))
zpw3 = total((zpw3iso/(h*c))*(longw3trans *longwave)) / (total(longw3trans))




;print, "Zero points in photons for 2mass and wise: ",zpj,zph,zpks,zpw1,$
        zpw2,zpw3

;; Step 6 - While loop
residuals = 'bad'

newvmag = 0.
newrmag = 0.
newimag = 0.
newjmag = 0.
newhmag = 0.
newksmag = 0.
neww1mag = 0.
neww2mag = 0.
neww3mag = 0.



anykey = ' '
```

```
itcounter = 0.
;; Read, "Enter maximum error for convergence: ",maxerr

maxerr = 0.03
;;set_plot, 'ps'
;; filenamestring = ' '
;; read, "File name for plots: ",filenamestring
;;device, filename=objname+"calsed.plot.ps", /landscape
print,' '
;;printf,1,' '
print,objname
;;printf,1,objname
firstiter = 1 ;for first iteration, stores original magnitudes
while residuals eq 'bad' do begin
             ;customize next line(s) to change error tolerance
    If abs(newvmag - vmag) gt maxerr or abs(newrmag - rmag) gt maxerr or $
       abs(newimag - imag) gt maxerr or abs(newjmag - jmag) gt maxerr or $
       abs(newhmag - hmag) gt maxerr or abs(newksmag - ksmag) gt maxerr or $
       abs(neww1mag - w1mag) gt maxerr or abs(neww2mag - w2mag) gt $
       maxerr or $
       abs(neww3mag - w3mag) gt maxerr then begin

       newvflux = total((longvtrans*fluxinphotons)) / (total(longvtrans))
       newrflux = total((longrtrans*fluxinphotons)) / (total(longrtrans))
       newiflux = total((longitrans*fluxinphotons)) / (total(longitrans))

       newjflux = total((longjtrans*fluxinphotons)) / (total(longjtrans))
       newhflux = total((longhtrans*fluxinphotons)) / (total(longhtrans))
       newksflux = total((longkstrans*fluxinphotons)) / (total(longkstrans))

       neww1flux = total((longw1trans*fluxinphotons)) / (total(longw1trans))
       neww2flux = total((longw2trans*fluxinphotons)) / (total(longw2trans))
       neww3flux = total((longw3trans*fluxinphotons)) / (total(longw3trans))

        newvmag =  ((-2.5)*(alog10(newvflux/zpv)  ))
        newrmag =  ((-2.5)*(alog10(newrflux/zpr)  ))
        newimag =  ((-2.5)*(alog10(newiflux/zpi)  ))

        newjmag =  ((-2.5)*(alog10(newjflux/zpj)  ))
        newhmag =  ((-2.5)*(alog10(newhflux/zph)  ))
        newksmag = ((-2.5)*(alog10(newksflux/zpks)))
```

```
    neww1mag = ((-2.5)*(alog10(neww1flux/zpw1)))
    neww2mag = ((-2.5)*(alog10(neww2flux/zpw2)))
    neww3mag = ((-2.5)*(alog10(neww3flux/zpw3)))

    if firstiter eq 1 then begin
        origvmag = newvmag
        origrmag = newrmag
        origimag = newimag
        origjmag = newjmag
        orighmag = newhmag
        origksmag = newksmag
        origw1mag = neww1mag
        origw2mag = neww2mag
        origw3mag = neww3mag
    endif
    firstiter = 0

;   print, "the new magnitudes are ",newvmag,newrmag,newimag,newjmag,$
    newhmag, $
    newksmag,neww1mag,neww2mag,neww3mag,neww4mag
;   anykey = ' '
;   read,"Press any key to continue: ",anykey

    vfluxfac =  10.^(-(vmag-newvmag)/2.5)
    rfluxfac =  10.^(-(rmag-newrmag)/2.5)
    ifluxfac =  10.^(-(imag-newimag)/2.5)
    jfluxfac =  10.^(-(jmag-newjmag)/2.5)
    hfluxfac =  10.^(-(hmag-newhmag)/2.5)
    ksfluxfac = 10.^(-(ksmag-newksmag)/2.5)
    w1fluxfac = 10.^(-(w1mag-neww1mag)/2.5)
    w2fluxfac = 10.^(-(w2mag-neww2mag)/2.5)
    w3fluxfac = 10.^(-(w3mag-neww3mag)/2.5)

    cumvfluxfac  = 10.^(-(newvmag-origvmag)/2.5)
    cumrfluxfac  = 10.^(-(newrmag-origrmag)/2.5)
    cumifluxfac  = 10.^(-(newimag-origimag)/2.5)
    cumjfluxfac  = 10.^(-(newjmag-origjmag)/2.5)
    cumhfluxfac  = 10.^(-(newhmag-orighmag)/2.5)
    cumksfluxfac = 10.^(-(newksmag-origksmag)/2.5)
    cumw1fluxfac = 10.^(-(neww1mag-origw1mag)/2.5)
    cumw2fluxfac = 10.^(-(neww2mag-origw2mag)/2.5)
    cumw3fluxfac = 10.^(-(neww3mag-origw3mag)/2.5)
```

```
        print, "The flux factors are: ",vfluxfac,rfluxfac,ifluxfac, $
        jfluxfac,hfluxfac, $
        ksfluxfac,w1fluxfac,w2fluxfac,w3fluxfac
;        print, "The cumulative factors are: ",cumvfluxfac,cumrfluxfac

        w25fluxfac = (w2fluxfac +w3fluxfac)/2. ; mean of w2 and w3 to $
                                               ;  cover polynomial gap


        effwave = [min(longwave),veffwave,reffwave,ieffwave, $
        jeffwave,heffwave, $
        kseffwave,w1effwave,w2effwave,w25effwave,w3effwave, $
        200000L,max(longwave)]
        fluxfac = [vfluxfac,vfluxfac,rfluxfac,ifluxfac,jfluxfac, $
        hfluxfac,ksfluxfac, $
         w1fluxfac,w2fluxfac,w25fluxfac,w3fluxfac,w3fluxfac,w3fluxfac]


        if itcounter eq 0 then begin
            initialmaxflux = max(fluxinphotons)
            if max(fluxfac) ge 1 then begin
               plot,effwave,fluxfac,psym=1,yrange=[0,max(fluxfac)+0.2], $
               xstyle=1,/xlog,title="SED Calibration for "+objname, $
                      xtitle="Wavelength in Angstroms", $
                      ytitle="Normalized Photon Flux", charsize=1.2, $
                      xcharsize=1.2,ycharsize=1.2, $
                     charthick=4,thick=4,xthick=4,ythick=4

;;    subtitle="Dashed Lines Indicate Polynomial Fits. Dotted Spectrum $
           is the Original Template"

            endif else plot,effwave,fluxfac,psym=1,yrange=[0,1.2], $
               xstyle=1,/xlog,title="SED Calibration for "+objname, $
                                    xtitle="Wavelength in Angstroms", $
                 ytitle="Normalized Photon Flux", charsize=1.2, $
                 xcharsize=1.2,ycharsize=1.2, $
                 charthick=4,thick=4,xthick=4,ythick=4

;           oplot, longwave,fluxinphotons/initialmaxflux,linestyle=1
```

```
        oplot, longwave,fluxinphotons/max(fluxinphotons),linestyle=5
 endif  else oplot,effwave,fluxfac,psym=1

  ;  print, "The flux factors are ",vfluxfac,rfluxfac,ifluxfac, $
jfluxfac,hfluxfac,ksfluxfac,w1fluxfac,w2fluxfac,w3fluxfac,w4fluxfac

    polyresult = poly_fit(alog10(effwave/(10.^4)),fluxfac,9)
    fluxmultarray =  polyresult[0] + polyresult[1]* $
    (alog10(longwave/1.e4)) $
    + polyresult[2]*(alog10(longwave/1.e4))^2. + $
    polyresult[3]*(alog10(longwave/1.e4))^3. + $
    polyresult[4]*(alog10(longwave/1.e4))^4. + $
    polyresult[5]*(alog10(longwave/1.e4))^5. + $
    polyresult[6]*(alog10(longwave/1.e4))^6. + $
    polyresult[7]*(alog10(longwave/1.e4))^7. + $
    polyresult[8]*(alog10(longwave/1.e4))^8. + $
    polyresult[9]*(alog10(longwave/1.e4))^9.


   ; print,"polynomial coeficients: ",polyresult
    oplot,longwave,fluxmultarray,linestyle=3
    fluxinphotons = fluxinphotons * fluxmultarray  ;$
              ;  applies multiplicative factor
    itcounter ++
  ;  print,"End of iteration number ",itcounter
  ;  print, ' '
  ;  print, objname
endif else begin
    residuals = 'good'
    oplot, longwave,fluxinphotons/max(fluxinphotons)
    print,"SED calibration solution converged after ", $
      itcounter," iterations."
    print, "The final flux factors are ",vfluxfac,rfluxfac, $
    ifluxfac,jfluxfac,hfluxfac,ksfluxfac,w1fluxfac,w2fluxfac,w3fluxfac
endelse
if itcounter ge 99 then begin
   oplot, longwave,fluxinphotons/max(fluxinphotons)
   residuals = 'good'
   print,"WARNING! SED calibration residuals did not converge. $
   Stopping at 100 iterations."
   print, "The final flux factors are ",vfluxfac,rfluxfac,ifluxfac, $
   jfluxfac,hfluxfac,ksfluxfac,w1fluxfac,w2fluxfac,w3fluxfac
```

```
   endif
endwhile

cumvfluxfac  = cumvfluxfac  / cumhfluxfac
cumrfluxfac  = cumrfluxfac  / cumhfluxfac
cumifluxfac  = cumifluxfac  / cumhfluxfac
cumjfluxfac  = cumjfluxfac  / cumhfluxfac
cumksfluxfac = cumksfluxfac / cumhfluxfac
cumw1fluxfac = cumw1fluxfac / cumhfluxfac
cumw2fluxfac = cumw2fluxfac / cumhfluxfac
cumw3fluxfac = cumw3fluxfac / cumhfluxfac
cumhfluxfac  = cumhfluxfac  / cumhfluxfac
print,''
print, "The cumulative fractional changes are: ",cumvfluxfac,cumrfluxfac, $
cumifluxfac,cumjfluxfac,cumhfluxfac,cumksfluxfac,cumw1fluxfac,$
cumw2fluxfac, $
cumw3fluxfac
print,''

fluxergcal = double(fluxinphotons*((h*c)/longwave))

obsflux = double(total(fluxergcal))

;;; Now calculate the uncertainties. To do that,
;;; first calculate the final flux through each filter.

;;;
;print,"First element of longwave ",longwave[0]


finalvflux  = double(total(fluxergcal[4800-4000:6500-4000]))
finalrflux  = double(total(fluxergcal[5500-4000:8500-4000]))
finaliflux  = double(total(fluxergcal[7000-4000:9000-4000]))

finaljflux  =  double(total(fluxergcal[11000-4000:13500-4000]))
finalhflux  =  double(total(fluxergcal[15000-4000:18000-4000]))
finalksflux =  double(total(fluxergcal[19500-4000:23500-4000]))

finalw1flux = double(total(fluxergcal[28000-4000:40000-4000]))
finalw2flux = double(total(fluxergcal[40000-4000:53000-4000]))
finalw3flux = double(total(fluxergcal[75000-4000:170000-4000]))
```

```
fluxcoveredfrac = (finalvflux + finalrflux +finaliflux + finaljflux  $
             +finalksflux + $
                   finalw1flux + finalw2flux + finalw3flux)/obsflux
print, "Fraction of SED sampled by photometry: ",fluxcoveredfrac

photfluxerr = ((vmagerr*finalvflux)^(2d)+(rmagerr*finalrflux)^(2d)+ $
              (imagerr*finaliflux)^(2d) + $
               (jmagerr*finaljflux)^(2d)+(hmagerr*finalhflux)^(2d)+ $
               (ksmagerr*finalksflux)^(2d) + $
               (w1magerr*finalw1flux)^(2d)+(w2magerr*finalw2flux)^(2d)+ $
               (w3magerr*finalw3flux)^(2d))^(1d/2d)

photfluxerr = photfluxerr / fluxcoveredfrac

print, "fluxes in each band: "




print, "photometry error: ",photfluxerr


;;Define the fractional residuals
vfluxres  = double(vfluxfac -1.)
rfluxres  = double(rfluxfac -1.)
ifluxres  = double(ifluxfac -1.)
jfluxres  = double(jfluxfac -1.)
hfluxres  = double(hfluxfac -1.)
ksfluxres = double(ksfluxfac -1.)
w1fluxres = double(w1fluxfac -1.)
w2fluxres = double(w2fluxfac -1.)
w3fluxres = double(w3fluxfac -1.)

;;Correct the flux by adding the residuals


obsflux = obsflux + ((vfluxres * finalvflux) + (rfluxres * finalrflux) $
       + (ifluxres * finaliflux) + $
       (jfluxres * finaljflux) + (hfluxres * finalhflux) + $
       (ksfluxres * finalksflux) + $
       (w1fluxres * finalw1flux) + (w2fluxres * finalw2flux) + $
       (w3fluxres * finalw3flux))
```

```
fitfluxerr = ((vfluxres * finalvflux)^(2d) + (rfluxres * finalrflux)^(2d) $
            + (ifluxres * finaliflux)^(2d) + $
              (jfluxres * finaljflux)^(2d) + (hfluxres * finalhflux)^(2d) $
             + (ksfluxres * finalksflux)^(2d) + $
              (w1fluxres * finalw1flux)^(2d) + (w2fluxres * $
              finalw2flux)^(2d) $
            + (w3fluxres * finalw3flux)^(2d))^(1d/2d)

fitfluxerr = fitfluxerr / fluxcoveredfrac

obsfluxerr = (photfluxerr^(2d) + fitfluxerr^(2d))^(1d/2d)  ;;$
  This is the final flux error on earth

print,"The flux from 0.4 to 30 microns is             ",obsflux," $
 erg/s/cm2 +- ",(obsfluxerr/obsflux)*100,'   percent.'

;read,"Press any key to continue: ",anykey
;;;;;;;;;;;;;;;;;;;;;;;;;;;;;;;;;;;;;;;;;;;;;;;;;;;;;;;;;;;;;;;;;;;
;;;;;;;;;;;;;; PART 2 -- BLACKBODY FIT ;;;;;;;;;;;;;;;
;;;;;;;;;;;;;;;;;;;;;;;;;;;;;;;;;;;;;;;;;;;;;;;;;;;;;;;;;;;;;;;;;;;

;; The luminosity is L = 4 * pi * obsflux * d^2,
;; where d is the distance to the star in cm.
;; 1 pc = 3.086e18 cm

print, "The parallax is ",prlx
print, "the distance is ",1./prlx

luminosity = double(4d * double(!pi) *  $
obsflux *(double(3.086e18)/double(prlx))^2d)
help,luminosity
print, luminosity
;;The solar luminosity is 3.827e33 erg/sec

;;The luminosity error is calculated by
print,'parallax error ',perr


lumerr = double(4d * double(!pi)*(double(3.086e18)^(2d)) * $
(((1d/(prlx^(2d)))*obsfluxerr)^(2d) + $
((-2d*obsflux/(prlx^(3d)))*perr)^(2d))^(1d/2d))
```

```
lumsolunit = double(luminosity/(3.827e33))

lumsoluniterr = double(lumerr/(3.827e33))

print,"Luminosity error (ergs)",lumerr
print,"Luminosity error (percent) ", (lumerr/luminosity)*100.


;;The stellar radius is calculated by R = (L/(4*pi*sb))^(1/2)*1/(Teff^2)
;;where sb is the stephan-Boltzman constant, sb = 5.67e-5 erg/cm^2/K^4/sec

sb = 5.67e-5

radiuscm = double(((luminosity/(4. * !pi * sb))^(1./2.))*(1./(teff^2.)))

radiuscmerr = double((1./(4.*!pi*sb))^(1./2.) *  $
((lumerr/(2.*luminosity^(1./2.) * teff^2.))^2. + $
((-2.*luminosity^(1./2.)*tefferr)/(teff^3.))^2.)^(1./2.))



radiussol = double(radiuscm/(6.96e10))
radiussolerr = double(radiuscmerr/(6.96e10))
radiusjup = double(radiuscm/(7.1492e9))
radiusjuperr = double(radiuscmerr/(7.1492e9))

print,"radius errors (cm,sol,jup) ",radiuscmerr,radiussolerr,radiusjuperr
print,"percent radius error ",(radiuscmerr/radiuscm)*100.
print,'      '
print,objid,'  ',objname,'  ',spt,teff,luminosity,lumsolunit,radiussol, $
radiusjup
print,' '

 read,"Enter (1) to save results, (2) to save but comment out the line, or $
(3) to discard: ",savestatus

;;;savestatus = 3
 if savestatus eq 1 or savestatus eq 2 then begin
     openu,unit1,outfile, /get_lun, /append, width=500

     space = '  '
```

```
     commentout = '## '
     if savestatus eq 1 then printf,unit1,objid,space,objname,space,spt, $
    teff, $
tefferr,luminosity,lumerr,lumsolunit,lumsoluniterr,radiussol,radiussolerr, $
radiusjup,radiusjuperr
     if savestatus eq 2 then printf,unit1,commentout,objid,space,objname,$
     space, $
spt,teff,tefferr,luminosity,lumerr,lumsolunit,lumsoluniterr,radiussol, $
radiussolerr,$
radiusjup,radiusjuperr
     free_lun,unit1
 endif

device, /close
end
```

The previous code required each object to be entered separately. The following code automates it by reading the input lines from a file.

```
pro autocalsed,infile,outfile
colorset
longreadcol,infile,objid,objname,spt,template,prlx,perr,pcode,teff, $
tefferr,vmag,verr,rmag,rerr,imag,ierr,jmag,jerr,hmag,herr,kmag,kerr,$
 w1mag,w1err,w2mag,w2err,w3mag,w3err,format='i,a,a,a,f,f,i,f,f,f,f,f, $
 f,f,f,f,f,f,f,f,f,f,f,f,f,f,f', /silent

;; readcol,infile,w2mag,w2err,w3mag,w3err,format='x,x,x,x,x,x,x,x,x, $
 x,x,x,x,x,x,x,x,x,x,x,x,x,f,f,f,f', /silent


listsize = n_elements(objid)

print, "Now reading band transfer functions."
 readcol,"V_curve.txt",vwave,vtrans,format="L,d", /silent
 readcol,"R_curve.txt",rwave,rtrans,format="L,d", /silent
 readcol,"I_curve.txt",iwave,itrans,format="L,d", /silent
 readcol,"J_RSR_curve.txt",jwave,jtrans,format="L,d", /silent
 readcol,"H_RSR_curve.txt",hwave,htrans,format="L,d", /silent
 readcol,"Ks_RSR_curve.txt",kswave,kstrans,format="L,d", /silent
 readcol,"intw1curve.txt",w1wave,w1trans,format="L,d", /silent
 readcol,"intw2curve.txt",w2wave,w2trans,format="L,d", /silent
 readcol,"w3curve.txt",w3wave,w3trans,format="L,d", /silent

read,"Enter number ID of first object: ",firstline
beginhere = where(objid eq firstline)

for i=beginhere[0],listsize-1 do begin
;;;;; On the next line, use calsed7 for screen graphics, calsed8 to
;;;;; save as postscript, or calsed9 to save publication quality,
;;;;; calsed10 for one iteration only.
;;;;; calsed9 broke. clased8 will now do publication quality.

    calsed8,objid[i],objname[i],spt[i],template[i],prlx[i],perr[i], $
    pcode[i],teff[i],tefferr[i],vmag[i],verr[i],rmag[i],rerr[i],imag[i], $
    ierr[i],$
            jmag[i],jerr[i],hmag[i],herr[i],kmag[i],kerr[i],w1mag[i], $
```

```
            w1err[i],w2mag[i],w2err[i],w3mag[i],w3err[i],outfile,$
            vwave,vtrans,rwave,rtrans,iwave,itrans,jwave,jtrans,hwave, $
            htrans,kswave,kstrans,w1wave,w1trans,$
            w2wave,w2trans,w3wave,w3trans

    anykey = ' '
  ;  read,'Press ENTER to continue.',anykey
print, ' '
print, ' '
endfor

end
```